

# Bimetallic Copper Complexes for Bioinspired Dioxygen Activation and Catalytic Water Oxidation

**DISSERTATION**

zur Erlangung des  
mathematisch-naturwissenschaftlichen Doktorgrades

„Doctor rerum naturalium“

der Georg-August-Universität Göttingen

im Promotionsprogramm Biometals  
der Georg-August-University Göttingen School of Science (GAUSS)

vorgelegt von

**ALEXANDER BRINKMEIER**

aus Northeim

Göttingen 2017

### Betreuungsausschuss

Prof. Dr. Franc Meyer, Institut für Anorganische Chemie, Georg-August-Universität Göttingen

Prof. Dr. Sven Schneider, Institut für Anorganische Chemie, Georg-August-Universität Göttingen

Prof. Dr. Ebbe Nordlander, Chemical Physics, Lund University

### Mitglieder der Prüfungskommission

#### *Referent:*

Prof. Dr. Franc Meyer, Institut für Anorganische Chemie, Georg-August-Universität Göttingen

#### *Korreferent:*

Prof. Dr. Sven Schneider, Institut für Anorganische Chemie, Georg-August-Universität Göttingen

#### *Weitere Mitglieder der Prüfungskommission:*

Prof. Dr. Lutz Ackermann, Institut für Organische und Biomolekulare Chemie, Georg-August-Universität Göttingen

Prof. Dr. Dietmar Stalke, Institut für Anorganische Chemie, Georg-August-Universität Göttingen

Prof. Dr. Ricardo Mata, Institut für Physikalische Chemie, Georg-August-Universität Göttingen

Jun. Prof. Selvan Demir, Institut für Anorganische Chemie, Georg-August-Universität Göttingen

Tag der mündlichen Prüfung: 08.01.2018

## TABLE OF CONTENTS

---

<b>1 General Introduction .....</b>	<b>1</b>
<b>2 Natural Copper Sites.....</b>	<b>2</b>
2.1 Type I and Type II Active Sites	2
2.2 Type III Active Sites	3
2.2.1 The Mechanism of Dioxygen Activation in Type III Active Sites	4
2.3 Type IV Active Sites	5
<b>3 Synthetic Copper Complexes .....</b>	<b>7</b>
3.1 <sup>T</sup> P complexes	11
3.2 <sup>S</sup> P Complexes	12
3.3 Hydroperoxo Complexes	13
3.4 Superoxo Complexes	14
<b>4 Physical Methods in bioinorganic chemistry.....</b>	<b>17</b>
4.1 UV/vis Absorption Spectroscopy	17
4.1.1 Franck-Condon-Principle	18
4.1.2 Vibronic Coupling	19
4.2 Resonance Raman Spectroscopy	20
4.2.1 Physical Principles of Raman and Infrared Spectroscopy	20
4.2.2 Resonance Enhancement	23
<b>5 Motivation of the Present Work .....</b>	<b>24</b>
<b>6 Results and Discussion.....</b>	<b>26</b>
6.1 A Dicopper(II)-Peroxo Intermediate	26
6.1.1 Formation in solution	26
6.1.2 Solid State Structure	28
6.1.3 Solid State Resonance Raman and UV/vis Reflectance Spectroscopy	30
6.1.4 Elemental Analysis	32
6.1.5 Magnetism	33
6.1.6 Electron Paramagnetic Resonance Spectroscopy	36
6.1.7 DFT calculations	39
6.1.8 Summary and Conclusion	42

6.2	Interaction with Alkali Metal Ions	43
6.2.1	Adduct formation in Solution	43
6.2.2	Solution State Resonance Raman Spectroscopy	49
6.2.3	Solid State Structures	52
6.2.4	Solid State UV/vis Spectroscopy	58
6.2.5	Solid State Resonance Raman Spectroscopy	60
6.2.6	Magnetism	63
6.2.7	DFT Calculations	67
6.2.8	Summary and Conclusion	73
6.3	A Dinuclear Cupric Hydroperoxo Complex	74
6.3.1	Formation and $pK_a$ Determination	74
6.3.2	Summary and Conclusion	88
6.4	A Dinuclear Cupric Superoxo Complex	89
6.4.1	Electrochemical and Chemical Generation	90
6.4.2	First Solid State Structure of a Dinuclear Copper(II) Superoxo Complex	94
6.4.3	DFT Calculations	95
6.4.4	EPR Spectroscopy and SQUID Magnetometry	98
6.4.5	Substrate Reactivity	102
6.4.6	Modulation of the Redox Potential <i>via</i> Interaction with Alkali Metal Ions	115
6.4.7	Summary and Conclusion	119
6.5	A Decomposition Product – Recycling and Formation	120
6.5.1	Formation of <b>5</b> from Hydroperoxo Complex <b>2+H<sup>+</sup></b>	127
6.5.2	Summary and Conclusion	132
6.6	Electrocatalytic Water Oxidation	134
6.6.1	Towards Electrocatalytic Water Oxidation	137
6.6.2	DFT Calculations	146
6.6.3	Summary and Conclusion	149
6.7	Towards a Synthetic Type IV Copper Active Site	150
6.7.1	Summary and Conclusion	153
6.8	A Novel Dicopper(II)-Peroxo Adduct – First Results	154
6.8.1	Interaction with Alkali Metal Ions	157
6.8.2	Summary and Conclusion	158
<b>7</b>	<b>Experimental Section .....</b>	<b>159</b>
7.1	General Synthetic Methods and Materials	159

7.2	UV/vis Spectroscopy	159
7.2.1	$pK_a$ Determination <i>via</i> UV/vis Titration Experiments	159
7.2.2	Determination of Association Constants <i>via</i> UV/vis Titration Experiments	160
7.3	Magnetic Measurements	161
7.4	Resonance Raman Spectroscopy	161
7.5	Electrochemistry	162
7.5.1	Cyclic voltammetry	162
7.5.2	Controlled Potential Coulometry	162
7.6	Spectro-Electrochemistry	162
7.7	X-Ray Diffraction	163
7.8	EPR Spectroscopy	169
7.9	NMR Spectroscopy	169
7.10	IR Spectroscopy	170
7.11	Elemental Analysis	170
7.12	Substrate Reactivity	170
7.13	Syntheses	171
7.13.1	$[L^1Cu_2]BPh_4$ ( <b>1</b> )	171
7.13.2	$[L^1Cu_2(O_2)]BPh_4 \cdot Et_2O, 0.5$ acetone ( <b>2</b> )	171
7.13.3	$[L^1Cu_2(O_2)(LiOTf)]_2(BPh_4)_2$ ( <b>2+Li<sup>+</sup></b> )	172
7.13.4	$[L^1Cu_2(O_2)((CH_3)_2CO)(KOTf)]_2(OTf)_2 \cdot 0.5 H_2O$ ( <b>2+K<sup>+</sup></b> )	172
7.13.5	$[L^1Cu_2(O_2)] [(BPh_4)(SbF_6)]$ ( <b>4</b> )	172
7.13.6	$[L^1Cu_2(OH)(H_2O)](ClO_4)_2$ ( <b>5</b> )	173
7.13.7	Preparation of <b>HL<sup>3</sup></b>	173
7.13.8	$[L_3Cu_2]BPh_4$ ( <b>12</b> )	174
7.14	List of Complexes	175
<b>8</b>	<b>References</b> .....	<b>176</b>
<b>9</b>	<b>Abbreviations</b> .....	<b>184</b>
<b>11</b>	<b>Acknowledgements</b> .....	<b>186</b>
<b>12</b>	<b>Curriculum Vitae</b> .....	<b>187</b>









# 1 GENERAL INTRODUCTION

---

With the development of various advanced physical methods such as electronic absorption, resonance Raman (rR) and electron paramagnetic resonance (EPR) spectroscopy, the field of bioinorganic chemistry became an independent and highly interdisciplinary research area in the last 60 years.<sup>1</sup> The word “bioinorganic” is related to the fact that approximately 40% of the to date known enzymes contain one or multiple metal atoms in their active sites that play a key role in the enzyme’s activity.<sup>1,2</sup> These metalloenzymes combine catalytic power with a high degree of specificity, enabling a huge number of different substrate conversions at mild reaction conditions.<sup>3,4</sup> The role of the bioinorganic coordination chemist is now to understand this interplay of organic framework and metal ion in order to design synthetic model complexes that help to understand the mechanisms of action of such active sites, and to develop bioinspired catalysts.<sup>1</sup>

Next to the elements iron (Fe) and zinc (Zn), the late transition metal copper (Cu) is one of the most important metal atoms incorporated in metalloenzymes and is mainly functioning as the Cu<sup>I</sup>/Cu<sup>II</sup> redox couple that enables various processes such as metal ion uptake, electron transfer, O<sub>2</sub>-transport and catalysis.<sup>5,6,7,8</sup> Presently, seven classes of copper containing enzymes are known, whereat the class of type III copper active sites is the most extensively studied.<sup>7</sup>

The following sections will focus on a selected number of these active sites and will further introduce the reader to the main issues of this thesis.

## 2 NATURAL COPPER SITES

### 2.1 Type I and Type II Active Sites

The family of type I active sites, most commonly known as blue copper proteins, enables the long range transfer of electrons in biological systems.<sup>9,10</sup> The name “blue copper site” is thereby related to the intense blue color of the oxidized form, originating from a ligand to metal charge transfer transition (LMCT) from a cysteine sulfur atom to the  $\text{Cu}^{\text{II}}$  ion.<sup>9,11</sup> X-ray crystallographic analyses show the central atom to feature a strongly distorted tetrahedral geometry which is believed to accelerate the electron transfer due to a lower reorganization energy of the active site.<sup>12,13</sup> The coordination sphere is provided by two nitrogen donor atoms (histidine), one cysteine ligand and by one methionine sulfur donor in case of Plastocyanin (see Figure 1, left).<sup>14,10</sup> The most common representatives of type I copper sites are Plastocyanin, Azurin and Amicyanin.<sup>12,7,15</sup>

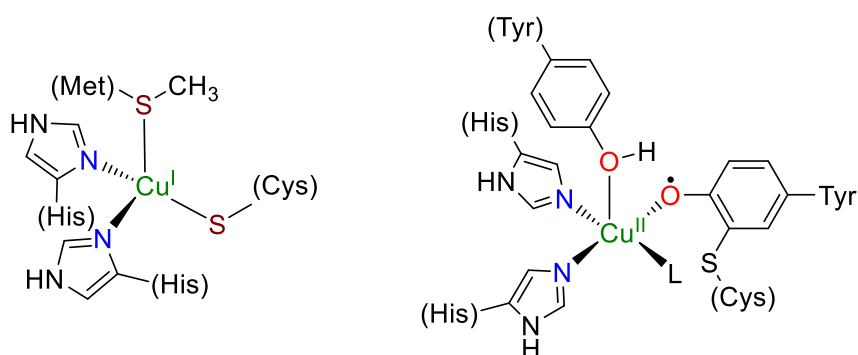
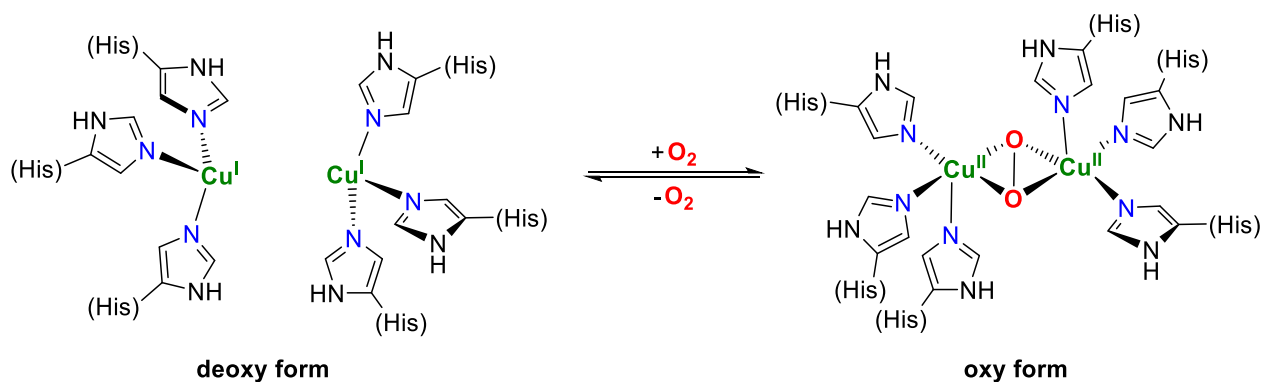


**Figure 1.** Molecular structures of the reduced Plastocyanin active site (left) and of Galactose oxidase in its oxidized form (right); L = water (pH = 7) or acetate (pH = 4.5).<sup>12,7,16</sup>

The class of type II active sites, also known as “normal” copper proteins, is represented by Galactose oxidase (see Figure 1, right) and Copper-zinc superoxide dismutase (SOD).<sup>7,11</sup> Both mononuclear copper sites contain nitrogen and oxygen donor atoms in a distorted tetragonal or square planar geometry and show EPR features similar to common copper(II) complexes, containing an N,O chromophore with a tetragonal geometry.<sup>7,10</sup> Their slightly blue color in the oxidized form originates from d–d transitions and does not arise from ligand to metal charge transfer processes as in type I active sites.<sup>17,7</sup> The active site of Galactose oxidase combines the type II copper(II) metal center with a coordinated tyrosyl radical.<sup>7</sup> This metalloradical complex functions as a two electron redox unit at which the overall catalysis is divided into two half-reactions – the oxidation of a primary alcohol and the reduction of molecular oxygen to hydrogen peroxide.<sup>18,19</sup>

## 2.2 Type III Active Sites

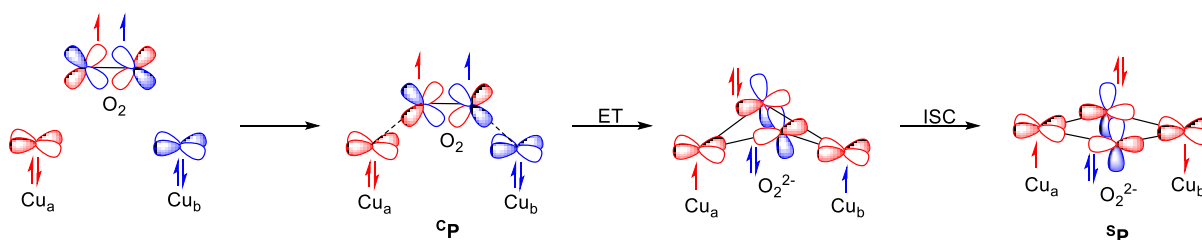
The family of type III active sites is represented by the three proteins Tyrosinase, Catechol oxidase and Hemocyanin.<sup>7</sup> Whereas Tyrosinase and Catechol oxidase catalyze substrate conversion, Hemocyanin is an oxygen-transport protein that can be isolated from mollusks and arthropods.<sup>20,21,22,23</sup> All three enzymes are featuring the same active site. The major difference between the catalytically active proteins and Hemocyanin is the access of the potential substrate to the dicopper core.<sup>8</sup> Whereas the substrate binding pockets in Tyrosinase and Catechol oxidase are accessible for the corresponding substrates, the binding site in Hemocyanin is shielded by a phenylalanine residue of the protein framework, and consequently the exclusive role of Hemocyanin is dioxygen binding and transport.<sup>23,24</sup> In Hemocyanin as well as in Tyrosinase and Catechol oxidase, three histidine nitrogen atoms are coordinating each copper ion (see Scheme 1).<sup>25</sup> The Cu-Cu distance in the reduced form of Hemocyanin (deoxy form) was determined to 3.5 – 4.6 Å, where the copper atoms exhibit a distorted trigonal planar geometry.<sup>26,27</sup> Upon dioxygen binding the two Cu<sup>I</sup> ions are oxidized, resulting in two strongly antiferromagnetically coupled Cu<sup>I</sup> ions, featuring a total  $S = 0$  ground state.<sup>7</sup> The central atoms were found to have a square pyramidal coordination geometry with a Cu-Cu distance of ca. 3.6 Å.<sup>26</sup> The enzyme which is colorless in the reduced form, changes color to intense blue in the oxy form, and in doing so, two characteristic absorption maxima at 345 ( $\epsilon = 19 \text{ mM}^{-1} \text{ cm}^{-1}$ ) and at 600 nm ( $\epsilon = 1000 \text{ M}^{-1} \text{ cm}^{-1}$ ) emerge, which are related to  $\text{O}_2^{2-} \rightarrow \text{Cu}^{\text{II}}$  charge transfer transitions (see Section 3 for details).<sup>28</sup>



**Scheme 1.** Reversible dioxygen uptake by the Hemocyanin active site.<sup>25</sup>

## 2.2.1 The Mechanism of Dioxygen Activation in Type III Active Sites

The mechanism of dioxygen binding at type III active sites is still a subject of ongoing debate. Since dioxygen features a triplet ground state, the two-electron reduction at the diamagnetic active site is principally spin forbidden.<sup>29,26,30</sup> Detailed computational calculations on the basis of molecular structures of the oxy and deoxy form of Hemocyanin assume the dioxygen molecule to interact in a certain way with the enzymes active site, in overcoming the spin forbidden nature of this reaction.<sup>26,31</sup> At early stages of O<sub>2</sub>-reduction, the molecule approaches the bimetallic copper(I) site and simultaneously interacts with both of its perpendicular  $\pi^*$ -orbitals with the dicopper site (see Scheme 2).<sup>26,32</sup>



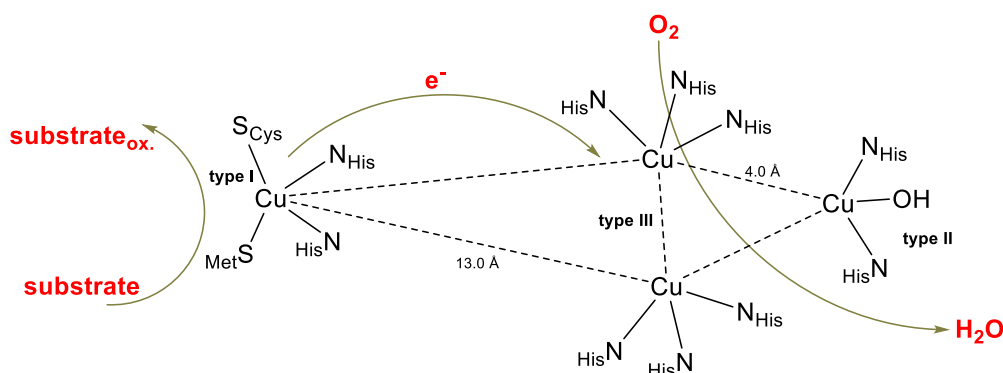
**Scheme 2.** Proposed mechanism of O<sub>2</sub> reduction at type III copper sites.<sup>26</sup>

One of the oxygen  $\pi^*$  orbitals exclusively interacts with one of the Cu<sup>I</sup> ions, whereas the perpendicular oxygen  $\pi^*$  orbital simultaneously interacts with the other copper site, in lowering the energy difference between triplet and singlet state of the system (see Scheme 2).<sup>33</sup> Finally, two electrons of the same spin are synchronously transferred from the copper atoms into the two oxygen centered  $\pi^*$ -orbitals, resulting in two ferromagnetically coupled Cu<sup>II</sup> ions.<sup>31,26</sup> The butterfly structure then progresses into a more planar geometry, where a superexchange pathway between the two Cu<sup>II</sup> ions *via* the peroxide molecule is observed.<sup>33,31</sup> This pathway is stabilizing the overall singlet state of the system, enabling the inter system crossing (ISC) to the experimentally observed  $S = 0$  ground state.<sup>26</sup> This mechanism involves a <sup>3</sup>P Cu<sub>2</sub>/O<sub>2</sub> binding mode (see Scheme 2). Recently, two synthetic examples have been published, supporting the above described trajectory of dioxygen activation at type III active sites (see Section 5 for details).<sup>31,34</sup>

## 2.3 Type IV Active Sites

Another family of copper containing proteins is represented by type IV copper active sites, which combine a type III and a type II active site in forming a triangular shaped trinuclear cluster.<sup>35,36,11</sup> Multicopper oxidases additionally contain at least one type I copper ion, in order to couple the reduction of dioxygen to water with the oxidation of selected substrates (see Scheme 3).<sup>37</sup> In the enzyme's resting state, all four copper atoms are featuring the oxidation states +II.<sup>35,36</sup> Finally, all copper ions are reduced to the oxidation state +I upon substrate conversion.<sup>35,36</sup> The fully reduced tetranuclear copper site then transfers in total four electrons on the dioxygen molecule, whereat the actual mechanism of action is still under debate.<sup>33</sup>

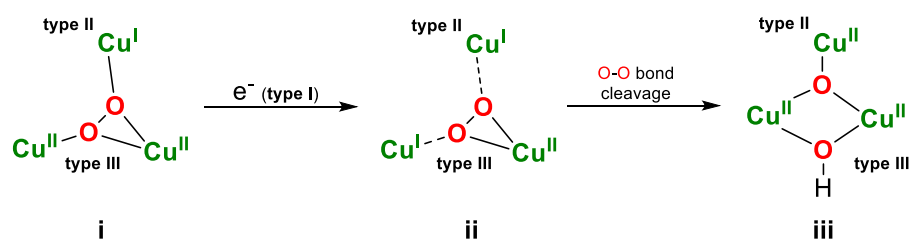
The coordination environment of the type III subsite in its reduced form is similar to that found in Hemocyanin (see Section 2.2), but changes in the resting state, with an additional hydroxide ligand bridging the two antiferromagnetically coupled Cu<sup>II</sup> ions.<sup>37</sup>



**Scheme 3.** Schematic representation of substrate conversion at multi copper oxidase active site.<sup>33</sup>

Several groups studied the nature of resting and reduced states of the trinuclear copper site, in which open coordination positions have been identified in the center of the cluster.<sup>33</sup> These vacant coordination positions are believed to be relevant during the mechanism of dioxygen binding.<sup>33</sup> The mechanistic details of dioxygen reduction at multicopper oxidases are still under debate, but various experiments suggest a sequence of two concerted steps to occur.<sup>33</sup> The initial stage is assumed to be a two electron reduction of dioxygen to a peroxide at the trinuclear cluster. The resulting intermediate would then be a trinuclear copper peroxo core, featuring two copper ions in the +II oxidation and one copper atom in the +I oxidation state.<sup>33</sup> Interestingly, dioxygen is not reduced at a type II site depleted form, pointing at a remarkable difference of the type III site in multicopper oxidases compared to that in Hemocyanin.<sup>38,33</sup> However, dioxygen reduction still takes place when the type I active site is replaced instead of the type II site.<sup>33</sup> This experiment shows the initial step in the four electron reduction of dioxygen to water to be the two electron reduction at the trinuclear cluster. This reaction is independent of the presence of the type I site, but requires the triangular arrangement.<sup>33</sup> However, the

resulting peroxy species shows different spectroscopic features than the side-on peroxy species in Hemocyanin, which is due to the presence of the type II site in multicopper oxidases that additionally interacts with the peroxide, in affecting both binding geometry and electronic structure (see Scheme 4).<sup>33,39,40</sup> The postulated next step in full O<sub>2</sub> reduction is the one-electron transfer from the type I site to the trinuclear cluster, in forming a trinuclear Cu-peroxy core with two Cu atoms in the +I oxidation state.<sup>41,33</sup> Detailed computational calculations underline the importance of this unusual trinuclear copper-peroxide core, where two Cu ions exist in the +I oxidation state.<sup>40</sup> This arrangement is believed to enable the final two electron reduction of the peroxide with a low energy barrier, with the Cu<sup>I</sup> bound peroxide acting as a Lewis acid.<sup>33</sup> This interaction is believed to lower the O<sub>2</sub><sup>2-</sup> σ\* orbital in energy, thus enabling the final concerted 2e<sup>-</sup> transfer from both Cu<sup>I</sup> ions.<sup>33,39,41</sup> Besides two electrons, also a proton is postulated to be transferred in this final reduction.<sup>40</sup> This partial proton coupled electron transfer (PCET) gives rise to intermediate **iii** that subsequently reacts into the enzymes resting state (see Scheme 4).<sup>40</sup>



**Scheme 4.** Schematic representation of postulated mechanism of reductive O-O bond cleavage of peroxo intermediate **i** at multicopper oxidase active site.<sup>33,40</sup>

This unique example shows that the trinuclear copper core in multicopper oxidases combines the redox activity of the Cu<sup>I</sup>/Cu<sup>II</sup> couple with an additional structural relevance of one of the copper ions, in functioning as a Lewis acid.<sup>33,39,41</sup> This abnormal behavior allows the enzyme to fine tune the redox potential of the final concerted two electron reduction of the peroxo intermediate.<sup>33</sup> A synthetic model complex, describing the unique intermediate **i** has however not been isolated to date but is a topic of recent studies (see Section 6.7).

### 3 SYNTHETIC COPPER COMPLEXES

Within the last 60 years of research in the field of bioinorganic chemistry, the synthesis of copper containing model complexes has been extensively studied, since a huge number of metalloenzymes contain the  $\text{Cu}^{\text{I}}/\text{Cu}^{\text{II}}$  redox couple, which enables *i.a.* substrate conversion and  $\text{O}_2$  transport (see Sections 2.1 - 2.3).<sup>6,7,42</sup> Although copper containing enzymes show highly diverse reactivity, most of the to date known species are postulated to form different reactive copper oxygen intermediates, being involved in the enzymes mechanism of action.<sup>43</sup> These natural archetypes are extensively studied for already half a century and a huge number of ligand systems has been employed.<sup>42,6</sup> Next to mononuclear copper complexes with mainly two, three and four nitrogen donor atoms coordinating the copper ion, also dinucleating ligand systems have been developed (see Figure 2).<sup>42</sup>

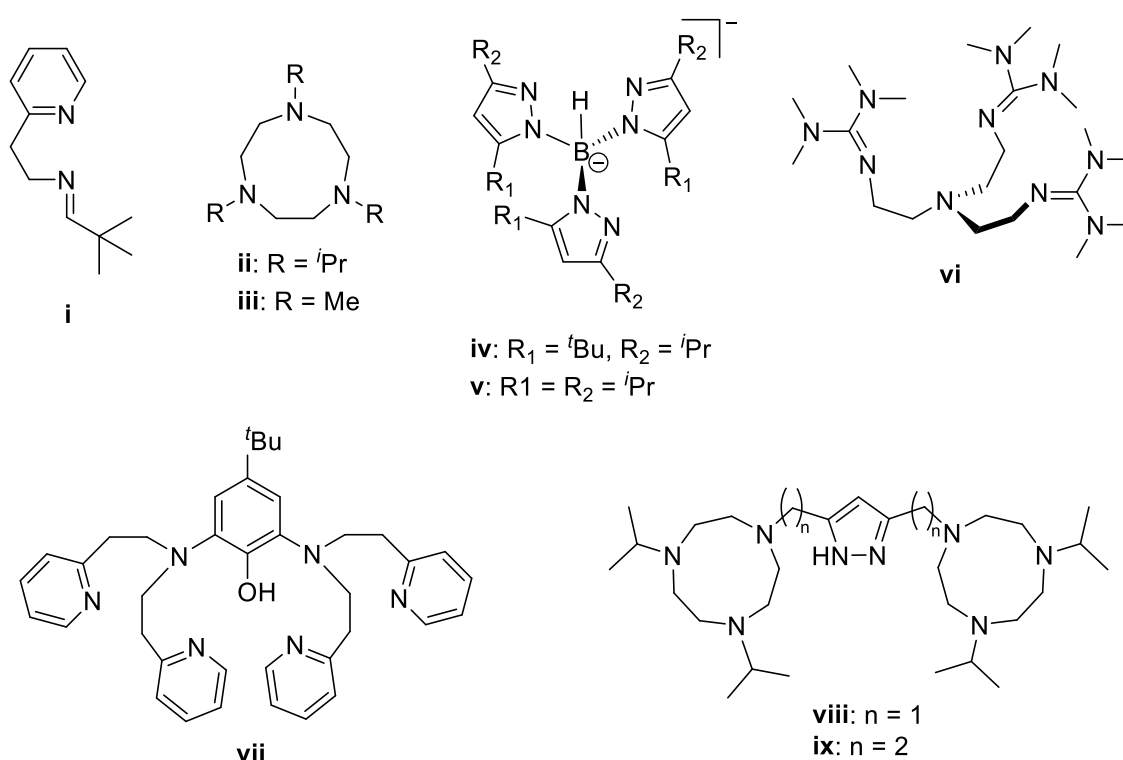


**Figure 2.** Different nitrogen donor ligands for mono- and dinuclear copper complexes.<sup>42</sup>

Upon reaction of the copper(I) precursor complexes with dioxygen, a variety of copper oxygen intermediates has been isolated, of which most of them are currently discussed to be also relevant in natural copper active sites (see Figure 3).<sup>42,44</sup> The nature of these copper oxygen species is mainly defined by the special ligand design being applied, which enables both steric and/or electronic control.<sup>44</sup> However, TOLMAN *et al.* showed that also the solvent has an influence on the nature of the copper oxygen binding mode.<sup>45,46</sup>

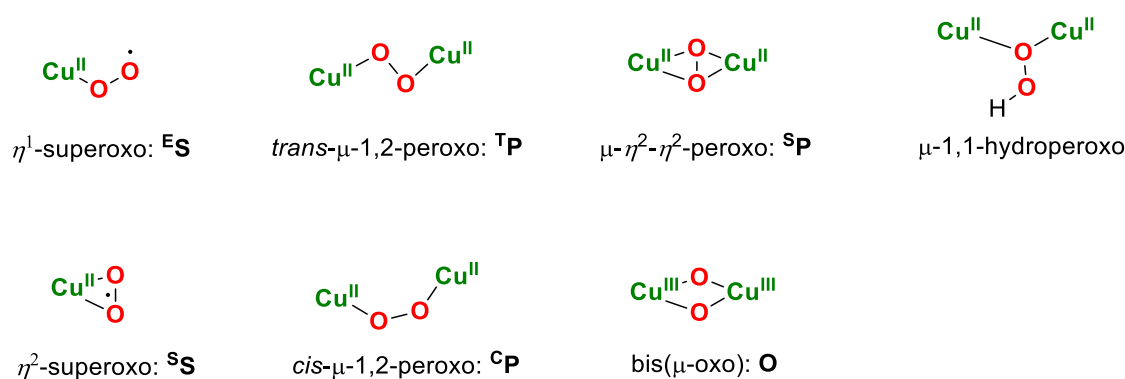


**Figure 3.** Overview of structurally characterized copper oxygen species.<sup>44,31,47</sup>

The in Figure 3 depicted copper oxygen binding motifs all show characteristic spectroscopic features, reflecting the different electronic structures of these copper oxygen cores.<sup>44,31,47</sup> In the following, a principal description of such interactions will be provided with respect to molecular orbital (MO) theory. A general MO diagram of a mononuclear Cu<sup>II</sup>  $\eta^1$ -peroxo complex is depicted in Figure 4.<sup>33,44</sup> This binding mode represents a simplified interaction of copper- and oxygen-centered orbitals and will be considered first, although this species has not been characterized structurally. Upon binding of the peroxide end-on to the Cu<sup>II</sup> ion, one of the oxygen-centered  $\pi^*$  orbitals is stabilized by a  $\sigma$ -interaction with the copper(II) magnetic  $d_{x^2-y^2}$  orbital which is in turn destabilized.<sup>48,33</sup>

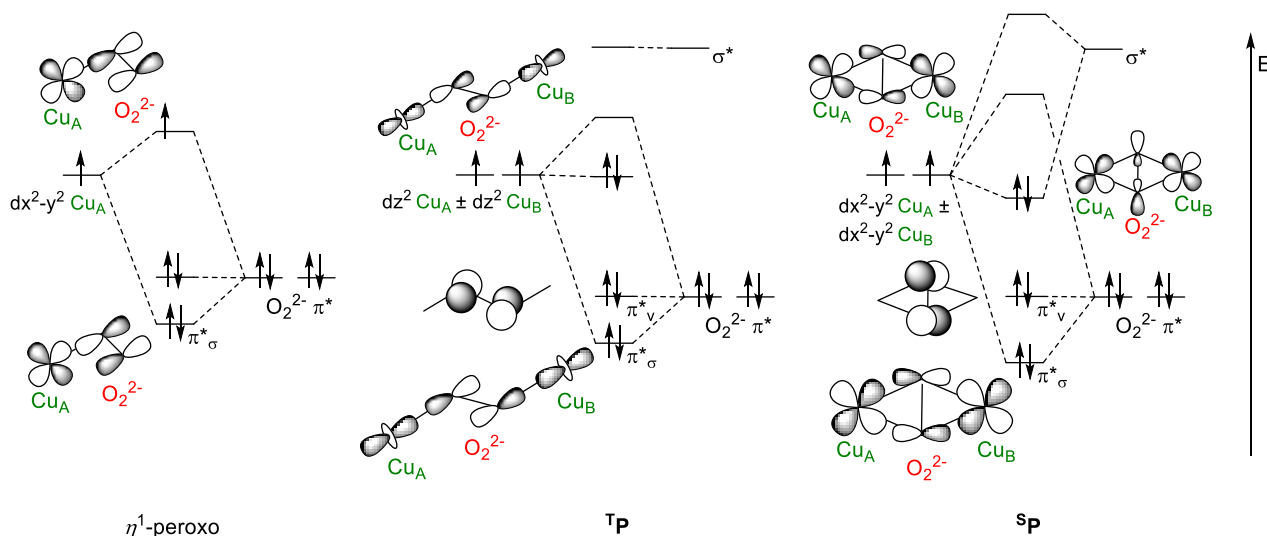


**Figure 4.** Approximate MO diagrams of different possible copper oxygen intermediates, the  $\eta^1$ -peroxo intermediate has not been isolated until now and is only shown for demonstrative reasons; the copper-centered orbitals are drawn at same energy.<sup>33,44</sup>

This interaction can be monitored *via* UV/vis absorption spectroscopy, since it produces a characteristic in-plane  $O_2^{2-} \pi_\sigma^* \rightarrow Cu^{II}$  charge transfer (CT) transition in the visible region.<sup>49,33,11</sup> The intensity as well as the relative energy of this CT transition generally quantify the magnitude of the peroxide donor interaction with the Cu<sup>II</sup> ion (see Section 4.1 for further details).<sup>33,50</sup> With respect to MO theory, a diminished overlap of copper- and oxygen-centered orbitals is directly related to the decreased



intensity of the corresponding CT transition, since the probability of this excitation to occur is a direct function of orbital overlap.<sup>50</sup> The intensity of a CT transition additionally depends on the temperature and on the solvent, but this aspect will be discussed in Section 4.1.<sup>51</sup> If the magnitude of overlap between copper- and oxygen-centered orbitals is reconsidered, this interaction is additionally reflected in the relative energy of the corresponding CT transition, since also the energy splitting between oxygen  $\pi^*$  and the copper-centered magnetic orbital is a function of orbital overlap.<sup>50</sup>

If a second  $\text{Cu}^{\text{II}}$  ion is involved in this type of interaction, different binding modes such as the  $^{\text{T}}\text{P}$  or  $^{\text{S}}\text{P}$  structures can be obtained (see Figure 3).<sup>44,31,47</sup> In  $^{\text{T}}\text{P}$  systems, the two oxygen  $\pi^*$  orbitals can be differentiated in  $\sigma$ - and  $\pi$ -bonding orbitals when interacting with the copper centered orbitals.<sup>44</sup> One of the two peroxide  $\pi^*$  orbitals interacts with the symmetric combination of the two copper magnetic orbitals in a  $\sigma$  bonding interaction, in splitting the two copper centered orbitals in energy.<sup>33</sup> If the resulting energy difference between the two copper-centered magnetic orbitals is large enough to overcome electron-electron repulsion, both copper centered electrons will couple their spin and a singlet ground state will be observed.<sup>52,33</sup> The bridging peroxide then provides a so-called superexchange pathway that is the reason for antiferromagnetically coupled binuclear copper sites (see Section 6.1.5 for a detailed description).<sup>53,54</sup> The  $\sigma$  bonding interaction again is the origin of an in-plane  $\text{O}_2^{2-} \pi_{\sigma}^* \rightarrow \text{Cu}^{\text{II}}$  CT transition that now arises at dual intensity compared to the mononuclear  $\eta^1$ -peroxo complex.<sup>33</sup> The simultaneous interaction of the peroxide with two copper atoms doubles the probability of an electronic transition to occur, with respect to the overlap integral of excited and ground state wave functions (see Section 4.1).<sup>33</sup> Next to this CT transition, a second but less intense absorption maximum at lower energy can be found in the UV/vis absorption spectra of both mononuclear and dinuclear peroxo complexes.<sup>44</sup> This absorption band results from another CT transition from the second peroxide  $\pi^*$  orbital, which is vertical to the copper oxygen plane.<sup>33</sup> This out-of-plane  $\pi_{\nu}^* \rightarrow \text{Cu}^{\text{II}}$  CT transition is much less intense than the in-plane CT transition, which is due to a diminished overlap of copper and oxygen centered orbitals.<sup>42</sup>

If the MO diagram of this  $^{\text{T}}\text{P}$  binding motif is compared with that of the  $^{\text{S}}\text{P}$  motif, significant differences can be observed which are also reflected by the UV/vis absorption spectra.<sup>55</sup> In  $^{\text{S}}\text{P}$  systems, the peroxo ligand is bound side-on ( $\mu\text{-}\eta^2\text{:}\eta^2$ ) to both copper ions, with one of the two oxygen  $\pi^*$  orbitals strongly overlapping with the symmetric combination of the copper  $d_{x^2-y^2}$  orbitals in a  $\sigma$ -bonding interaction.<sup>56</sup> The peroxide has now four donor interactions with the two copper atoms, indicated by a two times more intense in-plane CT transition compared to  $^{\text{T}}\text{P}$  species.<sup>33</sup> The two copper ions are strongly antiferromagnetically coupled ( $-2J \geq 600 \text{ cm}^{-1}$ ), substantiating the intense donor interaction between the copper and oxygen atoms.<sup>57</sup> The splitting of both formerly degenerated copper magnetic orbitals is further enlarged by an additional interaction that only occurs in  $^{\text{S}}\text{P}$  species due to the specific geometry of the copper oxygen core.<sup>33</sup> The  $\text{O}_2^{2-} \sigma^*$  orbital overlaps with the copper centered HOMO and a

significant amount of electron density is donated *via* this back bonding interaction into the oxygen centered  $\sigma^*$  orbital.<sup>33,55</sup> This interaction is significantly weakening the peroxide bond since, with respect to the O-O bond, an antibonding orbital is populated.<sup>33,44</sup> On the contrary, the aforementioned interactions describe the donation of electron density from the antibonding oxygen centered  $\pi^*$  orbitals, in stabilizing the O-O bond.<sup>33</sup>

Although these considerations are rather qualitative, they enable a fundamental understanding of the electronic structure of copper oxygen motifs. A more detailed discussion with respect to the interplay of orbital overlap and the corresponding electronic structure in dinuclear  $\text{Cu}_2/\text{O}_2$  complexes will be provided in Sections 6.1.5 and 6.2.3.

### 3.1 $^1P$ complexes

Although the  $^1P$  motif has only been isolated from synthetic copper complexes, its relevance for understanding the mechanism of action in natural copper sites cannot be excluded.<sup>31,44</sup> The first synthetic  $^1P$  complex that was also crystallographically characterized, has been published in the early 90s and is a dimer of two mononuclear copper(II) complexes, being stabilized by tetradentate nitrogen donor ligands (see Figure 5, complex **x**).<sup>58,59</sup> Next to this original example, several other  $^1P$  complexes were characterized, all showing similar spectroscopic features.<sup>60,44</sup> Two selected  $^1P$  complexes are depicted in Figure 5.<sup>60,58</sup> Both complexes are dimers of monomeric copper(II) complexes, being bridged by the peroxo ligand.

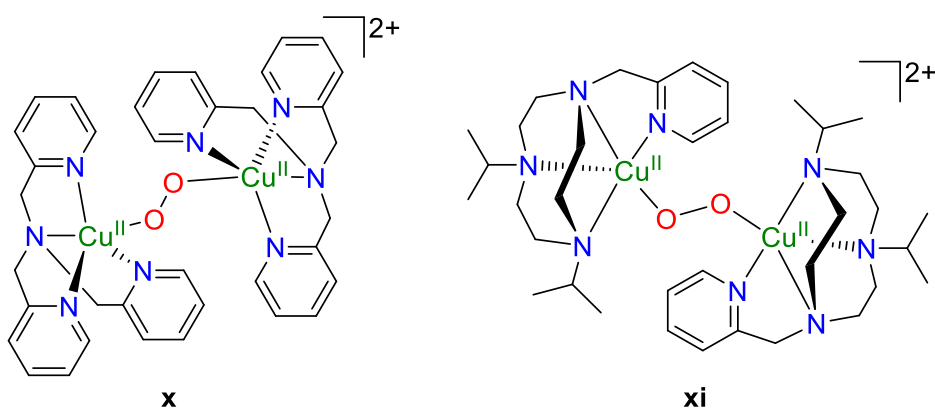


**Figure 5.** Structurally characterized  $^1P$  complex **x** and proposed structure of  $^1P$  species **xi**.<sup>60,58</sup>

The purple color of these complexes originates from two CT transitions (see Section 3) and the corresponding resonance Raman (rR) spectra (for more details concerning rR spectroscopy see Section 4.2) consistently show two oxygen isotope sensitive features at ca. 830  $\text{cm}^{-1}$  and at ca. 550  $\text{cm}^{-1}$ .<sup>61,60</sup> The band at higher energy attributes to the O-O stretching vibration, whereas the signal at ca. 550  $\text{cm}^{-1}$  can be assigned to a Cu-O stretch.<sup>44</sup> Although all proposed  $^1P$  complexes are extensively studied *via* UV/vis absorption and rR spectroscopy, only few examples are also magnetically characterized, which is due to a pronounced instability of these species.<sup>44</sup> All magnetically characterized examples feature a  $S = 0$  ground state with a singlet-triplet splitting of  $-2J \geq 600 \text{ cm}^{-1}$ , reflecting the strong bonding interaction of copper and oxygen atoms.<sup>62,43</sup>

## 3.2 $^5\text{P}$ Complexes

Within the last three decades several synthetic  $^5\text{P}$  complexes were synthesized.<sup>44</sup> The different model compounds all show similar spectroscopic features which are similar to those obtained for the oxy form of Hemocyanin, supporting the proposed  $^5\text{P}$  motif for this copper site.<sup>44</sup> The UV/vis absorption spectra are dominated by two CT transitions (see Section 3) at ca. 345 nm ( $\epsilon = 21 \text{ mM}^{-1} \text{ cm}^{-1}$ ) and at ca. 540 nm ( $\epsilon = 800 \text{ M}^{-1} \text{ cm}^{-1}$ ).<sup>44</sup> The corresponding rR spectra show oxygen isotope sensitive O-O stretching vibrations at ca.  $745 \text{ cm}^{-1}$ .<sup>26,44</sup> The molecular structures of the two synthetic compounds **xii** and **xiii** show the desired  $^5\text{P}$  motif (see Figure 6).<sup>63,64</sup> The O-O bond lengths were determined to ca.  $1.4 \text{ \AA}$ , which is typical for a peroxo species.<sup>64,63</sup> The  $\text{Cu}^{\text{II}}$  ions are coordinated by three nitrogen donor atoms and two peroxide oxygen atoms in a distorted square pyramidal geometry.<sup>64,63</sup> These structural parameters correlate with those of the solid state structure of oxy Hemocyanin, isolated from *Limulus Polyphemus*<sup>65,66</sup> and *Octopus dofleini*,<sup>67</sup> confirming the proposed  $^5\text{P}$  binding mode in these enzymes.

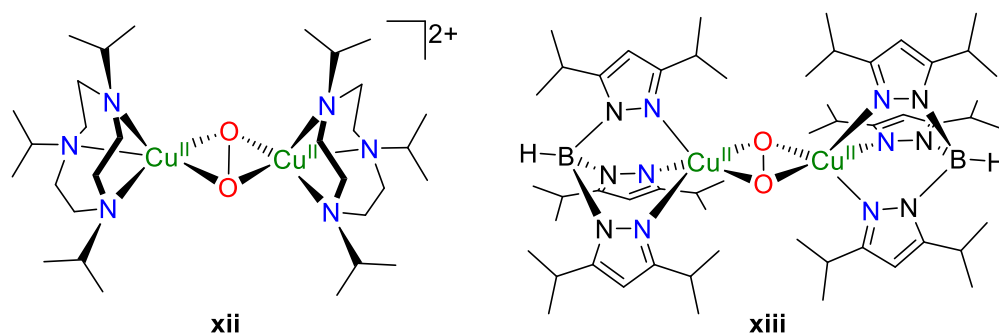


**Figure 6.** Selected examples of structurally characterized  $^5\text{P}$  complexes.<sup>63,64</sup>

The electronic structure of both synthetic and natural  $^5\text{P}$  compounds has been also investigated *via* DFT calculations, revealing the strong bonding interactions of copper and oxygen atoms.<sup>63,52</sup> The good overlap of copper- and oxygen-centered orbitals is thereby reflected by the intense UV/vis absorption spectra, and consequently the  $\text{Cu}^{\text{II}}$  ions in  $^5\text{P}$  complexes are strongly antiferromagnetically coupled.<sup>44</sup> The singlet-triplet splitting (for more details regarding the magnetism in dinuclear copper-oxygen complexes see Section 6.1.5) in oxy Hemocyanin was determined to  $-2J > 600 \text{ cm}^{-1}$  and could also be confirmed by its synthetic counterparts.<sup>57,26,68,62</sup>

### 3.3 Hydroperoxo Complexes

Besides few examples,<sup>47,69,70</sup> most of the to date known synthetic mono- and dinuclear copper hydroperoxo complexes are formed by the reaction of copper(II) precursors with H<sub>2</sub>O<sub>2</sub>.<sup>71,72,73</sup> With one exception<sup>74</sup> all of these complexes are highly thermally unstable, making a full spectroscopic and structural characterization difficult.<sup>47,69,70</sup> To date only two fully characterized examples are known (see Figure 7).<sup>74,47</sup> Although such motifs have not been isolated from natural copper sites, certain relevance is discussed in dopamine  $\beta$ -monooxygenase (D $\beta$ M) and galactose oxidase.<sup>75,74</sup> Figure 7 shows a summary of the to date structurally characterized synthetic hydroperoxo sites, which have been published over a period of almost 20 years, highlighting the rareness of these compounds.<sup>74,47</sup> In contrast to the mononuclear hydroperoxide **xiv**, complex **xv** can be reversibly generated from a peroxo precursor by addition of 2,6-lutidinium triflate. A pK<sub>a</sub> value of approximately 22.2 (MeCN, T = -20 °C) was determined *via* UV/vis back titration experiments of **xv** with 1,1,3,3-Tetramethylguanidine (TMG, pK<sub>a</sub> = 23.3 (MeCN, T = 25 °C)).<sup>47</sup>

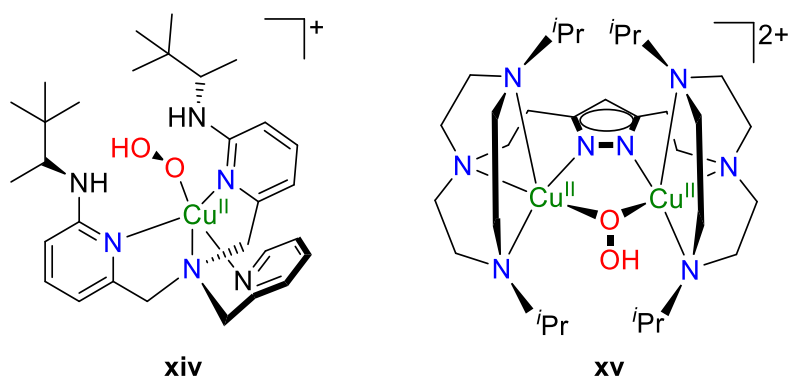
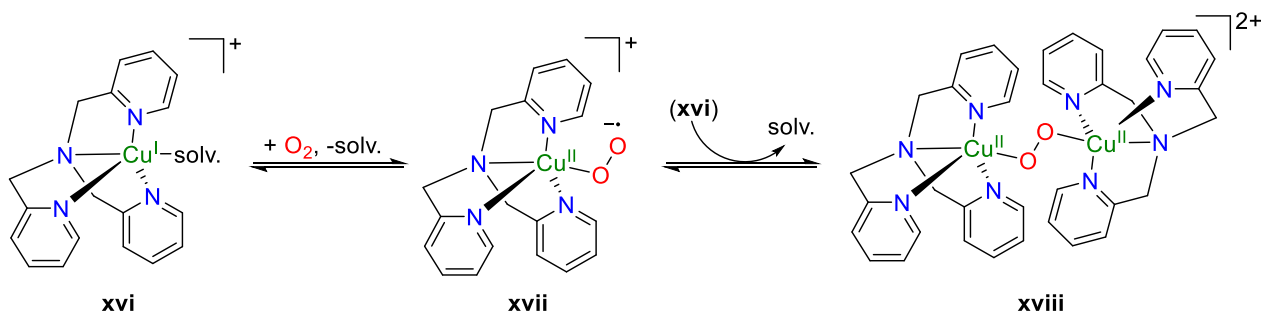


**Figure 7.** To date structurally characterized mono- and dinuclear copper hydroperoxo complexes.<sup>74,47</sup>

The UV/vis absorption spectrum of **xv** shows an intense band at ca. 420 nm ( $\epsilon = 5700 \text{ M}^{-1} \text{ cm}^{-1}$ ) and a much weaker feature at ca. 600 nm ( $\epsilon = 300 \text{ M}^{-1} \text{ cm}^{-1}$ ). These two absorption maxima are characteristic for hydroperoxo complexes and can be also found in their mononuclear counterparts.<sup>69,74</sup> Resonance Raman data of the structurally characterized complexes **xiv** and **xv** show one oxygen isotope sensitive band at ca.  $860 \text{ cm}^{-1}$  ( $\Delta(^{16}\text{O}_2\text{-}^{18}\text{O}_2) = \text{ca. } 46 \text{ cm}^{-1}$ ), which is at almost the same energy as the O-O stretching vibration of free H<sub>2</sub>O<sub>2</sub> (ca.  $870 \text{ cm}^{-1}$ ;  $\Delta(^{16}\text{O}_2\text{-}^{18}\text{O}_2) = 40 \text{ cm}^{-1}$ ).<sup>74,47</sup> The EPR spectrum of complex **xiv** is typical for a trigonal bipyramidal mononuclear copper(II) complex, whereat complex **xv** is EPR silent.<sup>74,47</sup> The two Cu<sup>II</sup> ions in **xv** were found to be strongly antiferromagnetically coupled ( $-2J = 1076 \text{ cm}^{-1}$ ) with the hydroperoxide providing an efficient superexchange pathway.<sup>74,47</sup>

### 3.4 Superoxo Complexes

In contrast to dinuclear copper(II) peroxy complexes, which are intensively described in the literature (see Sections 3.1 and 3.2), the one-electron reduction of O<sub>2</sub> to the corresponding superoxo complex at mono- or at dinuclear synthetic copper sites is rarely observed.<sup>76,77,78</sup> However, synthesis and a detailed spectroscopic characterization of such compounds are of high interest, since mononuclear superoxo intermediates are being discussed as relevant in several natural copper sites such as peptidylglycine α-hydroxylating monooxygenase (PHM) and dopamine β-monooxygenase (DβM).<sup>77,79,80</sup> Mononuclear copper(II) superoxo complexes are postulated to be usually formed as an intermediate during the synthesis of dinuclear peroxy/oxo systems by reacting mononuclear copper(I) precursors with dioxygen (see Scheme 5).<sup>44,81,82,83</sup> Detailed kinetic investigations based on low temperature stopped-flow UV/vis absorption experiments support the in Scheme 5 proposed mechanism, but until to date definite structural evidence of the mononuclear cupric superoxo intermediate **xvii** is still lacking.<sup>44,82,83</sup>



**Scheme 5.** Proposed mechanism of O<sub>2</sub> reduction by mononuclear copper(I) sites *via* superoxo intermediate **xvii**.<sup>83</sup>

However, several mononuclear copper(II) superoxo complexes have been synthesized by introducing sterically demanding ligands that prevent the mononuclear copper(II) superoxo complex from reacting with a second equivalent of the copper(I) complex.<sup>44</sup> Figure 8 summarizes all to date structurally characterized examples of mononuclear copper superoxo sites. The superoxide was found to either bind in an end-on (<sup>E</sup>S) or in a side-on (<sup>S</sup>S) fashion to the copper ion.<sup>84,85,80,86,87,88</sup>

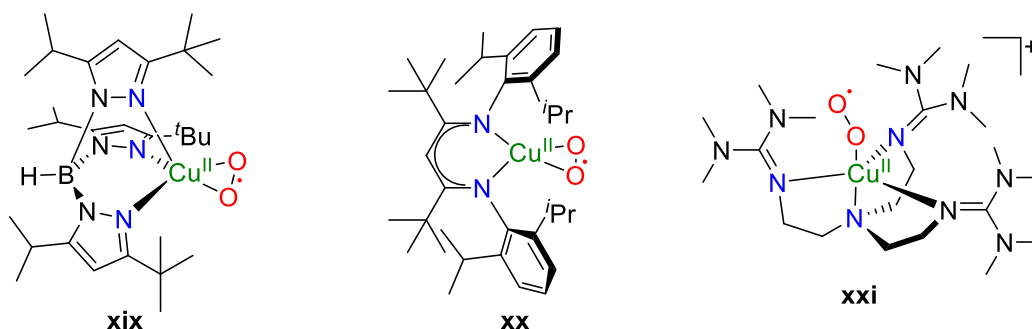


**Figure 8.** Summary of structurally characterized synthetic mononuclear copper superoxo complexes.<sup>45,84,88</sup>

Whereas  ${}^5\text{S}$  complexes are diamagnetic due to a singlet ground state,  ${}^E\text{S}$  complexes feature a triplet ground state.<sup>89,80,45</sup> These differences become obvious if the principle MO diagrams of  ${}^5\text{S}$  and  ${}^E\text{S}$  motifs are studied (see Figure 9).<sup>80,76</sup>

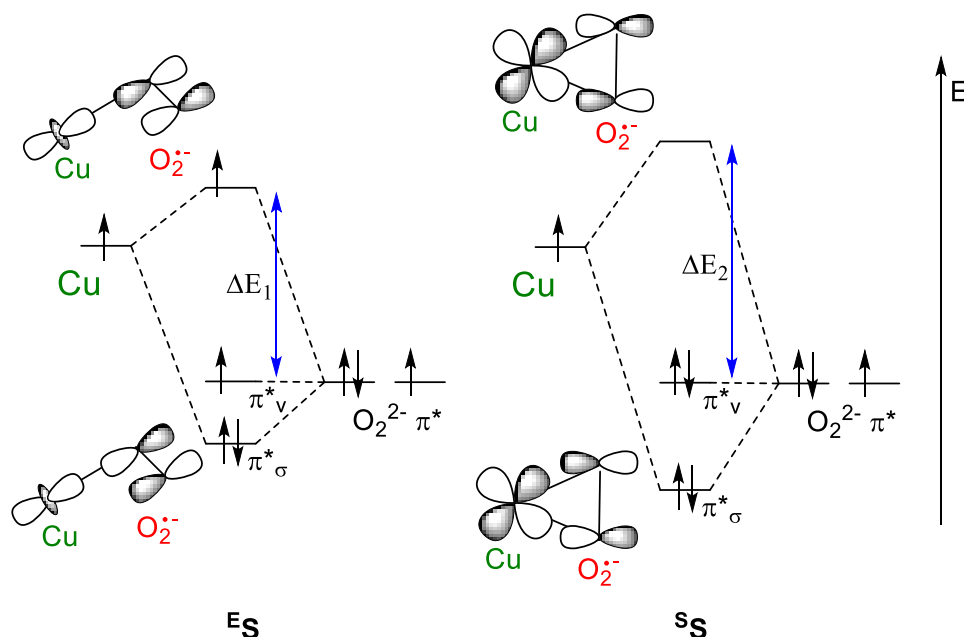


**Figure 9.** Approximate MO diagrams of paramagnetic  ${}^E\text{S}$  and diamagnetic  ${}^5\text{S}$  motifs; copper and oxygen centered orbitals are drawn at same energy.<sup>76,80</sup>

The superoxide delivers in total three electrons in the doubly degenerate  $\pi^*$ -orbitals of which one  $\pi^*$ -orbital is interacting in a sigma fashion ( $\pi^*_\sigma$ ) with the metal centered magnetic orbital.<sup>80</sup> The second oxygen  $\pi^*$  orbital is vertical to the copper superoxo plane ( $\pi^*_\nu$ ) and consequently non-bonding.<sup>80</sup> The magnitude of energy difference  $\Delta E$  (see Figure 9) between  $\pi^*_\nu$  and the copper centered orbital principally defines the magnetic ground state of the mononuclear superoxo species.<sup>76,80</sup> In  ${}^5\text{S}$  complexes the copper oxygen bond has a highly covalent character, resulting in a  $\Delta E$  that is large enough to overcome the spin pairing energy of both formerly unpaired electrons and consequently  ${}^5\text{S}$  complexes are diamagnetic.<sup>76</sup> In  ${}^E\text{S}$  complexes the superoxide is bound end-on to the copper atom, leading to a different bonding geometry compared to  ${}^5\text{S}$  sites.<sup>88</sup> DFT calculations predict a significantly smaller overlap of copper- and oxygen-centered orbitals.<sup>80</sup> With respect to Figure 9, the corresponding  $\Delta E$  is smaller compared to  ${}^5\text{S}$  complexes. Thus,  ${}^E\text{S}$  complexes are paramagnetic compounds that feature a  $S = 1$  ground state.<sup>88,80</sup> This discussion is indeed rather qualitative but reliably describes the magnetic properties of both independent binding motifs. Whereas  ${}^E\text{S}$  complexes show a characteristic EPR spectrum,  ${}^5\text{S}$  compounds were found to be EPR silent without exception.<sup>80,88,76</sup>

The different electronic structures of  ${}^5\text{S}$  and  ${}^E\text{S}$  systems can be further monitored *via* UV/vis absorption spectroscopy. The aforementioned interaction of copper- and oxygen-centered orbitals in  ${}^5\text{S}$  systems is found to have a strong covalent character, consequently splitting oxygen centered  $\pi^*_\sigma$  and copper

centered orbitals stronger in energy compared to the  ${}^E\text{S}$  motif (see Figure 9).<sup>76,80</sup> Thus,  ${}^E\text{S}$  species exhibit an intense CT transitions at ca. 400 nm ( $\text{O}_2^{2-} \pi_\sigma^* \rightarrow \text{Cu}^{\text{II}}$ ,  $\epsilon = 3000\text{-}8000 \text{ M}^{-1} \text{ cm}^{-1}$ ), which is shifted towards higher energies for  ${}^S\text{S}$  complexes ( $\lambda_{\text{max}} = \text{ca. } 300 \text{ nm}$ ).<sup>44</sup> The corresponding rR spectra of  ${}^S\text{S}$  and  ${}^E\text{S}$  sites show a characteristic O-O stretching vibration at ca.  $970 - 1100 \text{ cm}^{-1}$ , which is at a typical energy for superoxo complexes.<sup>88,78,44</sup>

However, this section only deals with mononuclear copper superoxo complexes, although also synthetic dinuclear copper superoxo analogs are postulated.<sup>77,90</sup> Till this date no structural evidence of such a species has been published. Nevertheless, the first structurally characterized dinuclear superoxo complex will be exclusively introduced in this thesis (see Section 6.4).



## 4 PHYSICAL METHODS IN BIOINORGANIC CHEMISTRY

---

### 4.1 UV/vis Absorption Spectroscopy

UV/vis absorption spectroscopy is one of the most frequently applied spectroscopic methods in probing electronic structure.<sup>91</sup> The relevance of this field of molecular spectroscopy is discussed in Section 3, and also major experimental parts of this thesis are based on this method. In general, UV/vis absorption spectroscopy deals with the interaction of molecules with electromagnetic radiation, inducing a transition from one stationary electronic energy level into another.<sup>91</sup> The excitation from a stationary energy level  $E_m$  into an energetically higher state  $E_n$  however only is observed if a significant number of particles is located at the energy level  $E_m$ .<sup>51</sup> The number of particles  $N_i$  being located at energy level  $E_i$  is thereby described by the Boltzmann equation:<sup>51</sup>

$$1) \quad N_i \propto N e^{-E_i/kT}$$

Consequently, the population of an energy level  $E_i$  increases with decreasing energy of the state  $E_i$  and increasing temperature  $T$ . The interaction of a molecule with an incident photon is described by the transition moment,  $\vec{R}_{mn}$ :<sup>51</sup>

$$2) \quad \vec{R}_{mn} = \int \psi_m^*(x) \hat{\mu} \psi_n(x) dx$$

One fundamental requirement of an interaction of the molecule with the electric light wave is the oscillation of an electric dipole within the molecule, since otherwise the transition moment would be zero.<sup>91</sup> Apart from the classical approach, quantum theory predicts a change in charge distribution during the absorption process to be the fundamental requirement for the excitation to occur.<sup>92</sup> The transition moment further contains the wave functions of ground and excited energy states, which leads to the selection rule of symmetry.<sup>93</sup> Since the dipole operator is an ungerade component, only transitions between wave functions of different symmetry (*i.e.* of gerade and ungerade symmetry) are allowed.<sup>91</sup> However, energy transfer only occurs if the molecule can resonate with the electric field of the light wave.<sup>94,51</sup>

$$3) \quad E_n - E_m \approx h\nu$$

The energy difference between the two states, being involved in the electronic transition, must equal the energy of the incident photon.<sup>94,95</sup> Commonly, electronic transitions occur in a wide range from 120 to 1300 nm (8000 – 80000  $\text{cm}^{-1}$ ).<sup>95</sup> Consequently, electronic transitions are accompanied by vibronic and rotational transitions, which is the reason for usually broad absorption spectra.<sup>91</sup> If the electronic absorption spectrum of sodium is considered, straight lines are observed due to the absence of rotational and vibrational degrees of freedom.<sup>95</sup> Electronic transitions, being accompanied by vibronic and rotational transitions, are described by the Franck-Condon-principle.<sup>91,95</sup>

### 4.1.1 Franck-Condon-Principle

Electronic transitions are generally coupled to vibronic and rotational transitions, which is one reason for usually broad electronic absorption spectra.<sup>91,95</sup> The intensity of such transitions is described by the Franck-Condon-principle which defines the intensity of an electronic transition to depend on the overlap of ground and excited state wave functions.<sup>92</sup> Both ground state and electronically excited state can be described with a Morse potential (for a detailed description see Section 4.2.1), featuring the equilibrium bond distance  $r_e$ .<sup>91,96</sup> The excited state equilibrium bond distance can be equal to that of the electronic ground state (see Figure 10-a), or it may be larger (and in principle also smaller) than the ground state equilibrium bond distance (see Figure 10-b).<sup>91,95</sup>

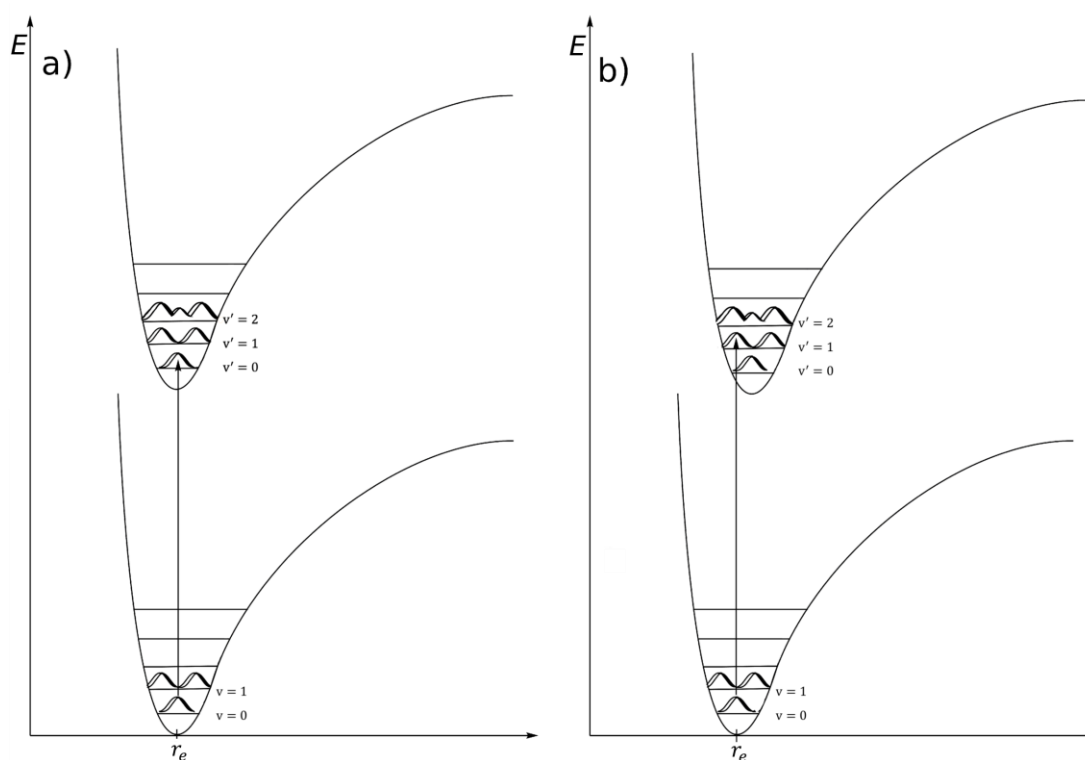


**Figure 10.** Schematic illustration of Franck-Condon-principle: Excitation from electronic ground state into electronically excited state under a): maintaining of the equilibrium bond distance and under b): elongating of the equilibrium bond distance  $r_e$ .<sup>95</sup>

In general, the molecule can be excited into different vibronic energy levels of the excited state, but not all of these transition occur with the same intensity.<sup>95</sup> In Figure 10-a, the transition into the first vibronic energy level of the electronically excited state occurs with the highest intensity, since the overlap of both wave functions is maximal in this case.<sup>95</sup> The transitions into the states corresponding to  $v' = 1$  and  $v' = 2$  are also observed, but with significantly lower intensity.<sup>95</sup> However, if the equilibrium bond distance is elongated within the excited state (see Figure 10-b), the transition into the vibronic state corresponding to  $v' = 0$  is not the most intense anymore. With respect to Figure 10-b the

transition into the vibronic state corresponding to  $v' = 1$  becomes the most intense, due to maximal overlap of ground and excited state wave functions.<sup>91,95</sup>

Since each vibronic state further contains several rotational energy levels, ideal absorption spectra typically show a broad profile, whereat the maximum of an absorption band (referred to as  $\lambda_{\max}$ ) corresponds to the most probable excitation with respect to the Franck-Condon-principle.<sup>94</sup>

#### 4.1.2 Vibronic Coupling

According to equation 4), an electronic transition is only allowed if the integral of the type

$$4) \quad \langle \psi_m | d | \psi_n \rangle$$

is nonzero, with  $d$  representing one part of the dipole operator.<sup>91</sup> If equation 4) does not contain the totally symmetric representation, the transition becomes orbitally forbidden and will not be observed within the absorption profile.<sup>91</sup> However, electronic transitions are generally coupled to vibronic transitions, leading to an elimination of the above-mentioned symmetry constraint.<sup>91,93</sup> If an electronically forbidden transition from ground state  $\psi_0$  to excited state  $\psi_1$  is considered, this transition may gain intensity from the electronically allowed transition from ground state  $\psi_0$  to e.g. excited state  $\psi_2$  by vibronic coupling.<sup>91</sup> This mechanism requires the symmetry of  $\psi_1$  to change due to displacement along the vibrational coordinate, in which  $\psi_1$  is mixing with  $\psi_2$ .<sup>91</sup> One prominent example is the closed shell complex  $[\text{PtCl}_4]^{2-}$ , which is featuring a square planar geometry.<sup>91</sup> The excitation of an electron from the  $d_{z^2}$  orbital into the  $d_{xy}$  orbital is principally Laporte forbidden, due to the gerade-gerade character of ground state and excited state wave functions.<sup>91</sup> However, this excitation becomes vibronically allowed if it occurs in conjunction with a vibration, distorting the center of symmetry.<sup>91</sup>

## 4.2 Resonance Raman Spectroscopy

In previous sections, several natural and synthetic mono- and dinuclear copper oxygen sites have been introduced, most of which are intensively colored due to mainly electric dipole allowed LMCT transitions from the dioxygen ligand to the metal center(s). A detailed understanding of both nature and origin of these transitions not only allows an insight into the general structure of the corresponding copper oxygen motif, but also can deliver detailed information about the excited state geometry.<sup>96</sup> For that purpose, a laser can be tuned to the wavelength of such an electric dipole allowed CT transition. With this setup certain vibrational modes, imaging the excited state distortion, can be selectively enhanced and the position of these Raman bands can be used to illustrate the electronic structure within the copper oxygen core.<sup>96</sup> The following section will focus on the principles of infrared and Raman spectroscopy. Finally, the mechanism of resonance enhancement will be introduced and its relevance in the field of bioinorganic chemistry will be pointed out.

### 4.2.1 Physical Principles of Raman and Infrared Spectroscopy

Although different physical mechanism are involved, both infrared (IR) and Raman processes describe the excitation of molecular vibrations within chemical compounds and provide valuable chemical information in using relatively simple experimental setups.<sup>96</sup> If a simple diatomic molecule is considered, the frequency of vibration is described as:<sup>97</sup>

$$5) \quad \nu_0 = \frac{1}{2\pi} \sqrt{\frac{k}{\mu}}$$

Since equation 5) reflects the vibration of a diatomic molecule, the vibration of two individual masses is replaced by the vibration of one reduced mass  $\mu$ .<sup>96</sup> The frequency additionally depends on the magnitude of force constant  $k$ , which is also called "spring constant".<sup>97</sup> The classical vibration of a diatomic molecule is described by the harmonic oscillator (see Figure 11), which contains stationary states of certain energy.<sup>97</sup> The spacing between two different energy levels corresponds to the amount of energy that is required to enable this transition.<sup>96</sup> Each stationary state is described by a corresponding eigenvalue of energy:<sup>97</sup>

$$6) \quad E(v) = h\nu_0(v + \frac{1}{2})$$

However, the harmonic oscillator only roughly describes the vibration of a diatomic molecule, since this simple model neglects the experimentally observed dissociation of the molecule at high displacement from the equilibrium distance  $r_e$ .<sup>96</sup> Additionally, the harmonic oscillator underrates the Coulomb repulsion between both atoms and even allows a negative bond distance at high oscillating amplitudes.<sup>97</sup> The empiric Morse potential (see Figure 11) provides a much more realistic description in

incorporating both coulomb interaction and dissociation limit.<sup>96</sup> The potential energy of the Morse potential thus is defined as:<sup>97,96</sup>

$$7) \quad V = D_e [1 - e^{\beta(r-r_e)}]^2$$

The parameter  $\beta$  contains the reduced mass  $\mu$ , the dissociation energy  $D_e$  and further physical constants and was found empirically.<sup>97,96</sup> In contrast to the harmonic oscillator, the different energy levels of the Morse potential are not equally spaced.<sup>97</sup>

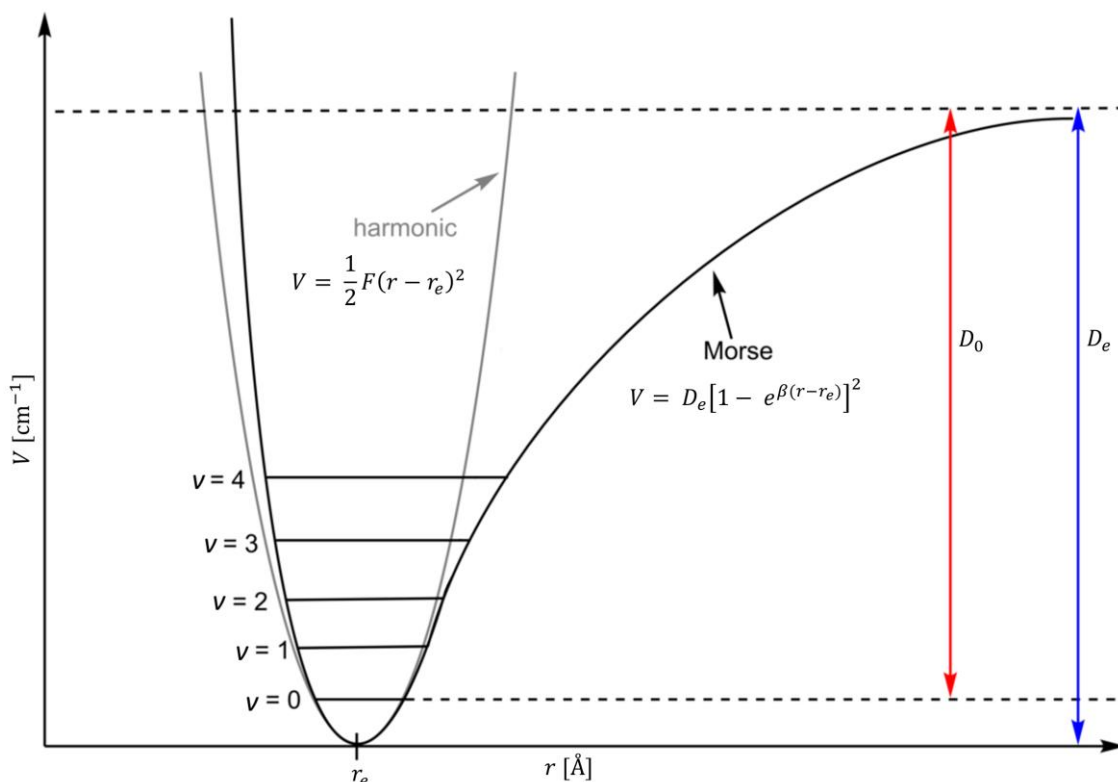


**Figure 11.** Potential curves of harmonic oscillator (grey curve) and of Morse potential (black curve).<sup>96</sup>

With the basic theoretical background in hand, the different selection rules in IR and Raman spectroscopy will be introduced. Homonuclear diatomic molecules feature no permanent dipole moment and are IR inactive since the transition moment is zero (see Section 4.1 for details).<sup>96,98</sup>

However, in the 1920s RAMAN discovered a phenomenon that enabled a novel method of vibrational spectroscopy - Raman spectroscopy.<sup>98</sup> This method empowers spectroscopists to collect vibrational data of IR inactive compounds and is based on the so called Raman-effect.<sup>98</sup> In IR spectroscopy an excitation of a molecular vibration requires a change of the dipole moment  $\mu$  with respect to the vibrational coordinate,  $Q$ .<sup>96</sup>

$$8) \quad I_{IR} \propto (\partial\mu/\partial Q)^2$$

On the contrary, the Raman-effect deals with the fluctuating dipole moment  $P$ , which is induced by the incident photon.<sup>96</sup>

$$9) \quad I_R \propto P^2 = (\alpha'E)^2; \quad \alpha' = (\partial\alpha/\partial Q)_0 Q$$

A fluctuating dipole moment is only induced, if a change in the molecule's polarizability (denoted as  $\alpha'$ ) occurs with respect to the vibrational coordinate.<sup>96</sup>

Whereas in IR spectroscopy a transition to a vibrationally excited state requires the direct absorption of a photon providing the exact energy difference of ground and excited state (see Section 4.1, equation 3) for details), the Raman process describes the same transition accessed *via* inelastic scattering of a photon.<sup>96,98</sup> The scattered photon then emerges with different energy. If the energy of the photon is reduced, the process is referred to as Stokes radiation.<sup>96</sup> Alternatively, the same transition can be induced by a photon being scattered at the corresponding vibrationally excited state, which is referred to as Anti-Stokes radiation.<sup>96</sup> The Raman-effect however is only weakly observed and the corresponding vibrations are in principal less intense compared those studied by IR spectroscopy (one exception is resonance Raman spectroscopy, see Section 4.2.2).<sup>96</sup> This effect is due to the phenomenon of Rayleigh-scattering, since only a small fraction of the incident photons is interacting with the molecule.<sup>98</sup> Of this small fraction again only a certain portion is being inelastically scattered, giving rise to the corresponding Raman spectrum.<sup>98</sup>

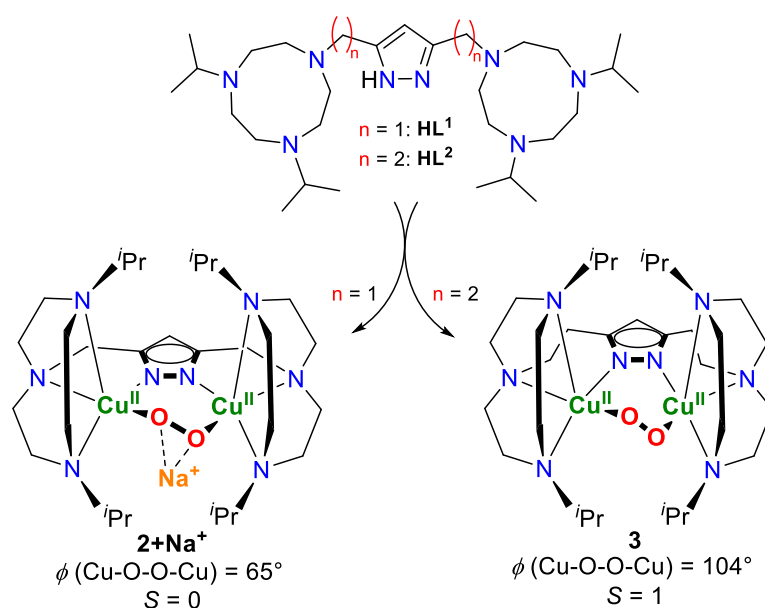
## 4.2.2 Resonance Enhancement

In Section 3 different copper oxygen binding motifs are discussed, which have been isolated from synthetic and also partly from natural copper sites. All of these complexes are featuring intense CT transitions, which have been identified to originate from the peroxide ligands.<sup>44</sup> In general, CT transitions additionally enhance stretching modes within the metal-ligand framework, of which the O-O stretching vibration for instance is IR inactive.<sup>96</sup> However, especially the relative energy of the O-O stretch contains valuable chemical information concerning the electronic structure within the copper oxygen core.<sup>6</sup> Thus, the method of resonance Raman spectroscopy is applied in order to collect chemical information of the molecule's electronically excited state.

Since the intense CT transitions in Type III active sites arise from the peroxo ligand, especially the O-O stretch is enhanced within this transfer. Consequently, the polarizability of this bond changes within this electronic transition, inducing a fluctuating dipole moment within the molecule.<sup>96,98</sup> If now a laser is tuned to the resonance conditions of this electric dipole allowed CT transition, the Raman active O-O vibration is strongly enhanced.<sup>96</sup> All other Raman active modes that are not directly related to this electronic transition are not significantly intensified.<sup>96,98</sup> This method allows bioinorganic chemists to analyze samples of much lower concentrations as required for normal Raman experiments and enables an insight into the molecule's excited state geometry.<sup>96</sup> The to date well established <sup>5</sup>P binding mode in oxy Hemocyanin for instance has been intensively studied *via* UV/vis absorption and rR spectroscopy, since these methods require relatively low sample concentrations. The combination of rR spectroscopy and DFT calculations predicted the presence of a peroxide ligand within oxy Hemocyanin, long before a molecular structure of this active site finally revealed the <sup>5</sup>P motif.<sup>52</sup>

## 5 MOTIVATION OF THE PRESENT WORK

The specific design of ligand **HL**<sup>1</sup> was established in prior studies (see Scheme 6).<sup>99,31,32</sup> The fusion of a central pyrazole unit with two triazacyclononane (TACN) side arms *via* a methylene spacer enables the synthesis of the corresponding dicopper(I) compound. This complex is featuring a particular binding pocket, to subsequently bind dioxygen in a distinct motif (see Scheme 6). The anticipated binding mode may be best described as  $\mu$ -1,2-*cis* peroxo dicopper(II) site, and is believed to be a possible key step in understanding the mechanism of dioxygen activation in natural type III active sites such as Tyrosinase and Hemocyanin (see Section 2.2.1 for details).<sup>31,100,26</sup> However, the synthesis of single crystalline and consequently clean material of the dicopper(I) precursor was a major challenge and has been quite recently developed.<sup>10</sup> When unpurified material of this complex is exposed to dioxygen the formation of the desired *cis*- $\mu$ - $\eta^1$ : $\eta^1$ -peroxo species (**6P**) is anyhow observed. The solid state structure of this compound is the first example of this unique binding mode and additionally contains a sodium ion, interacting with the peroxide. The sodium ion thereby originates from the synthesis of the Cu(I) precursor.<sup>31</sup>



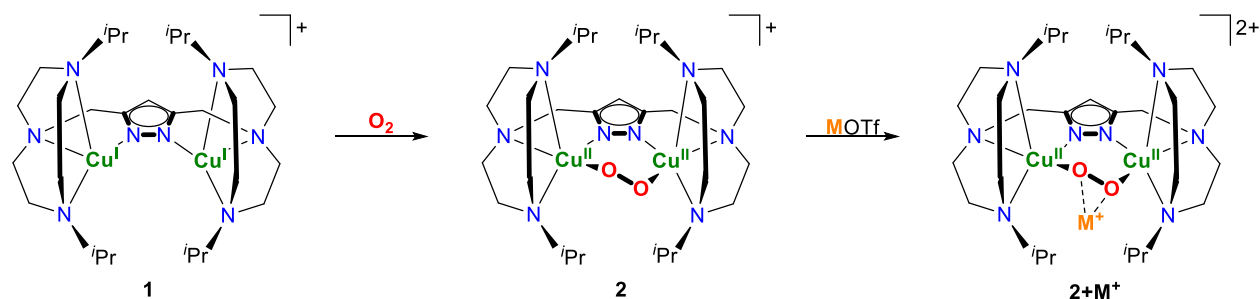
**Scheme 6.** Structurally characterized Cu<sub>2</sub>/O<sub>2</sub> complexes of relevance for this work.<sup>31,34</sup>

Next to this remarkable interaction, which was also quantified in solution *via* UV/vis titration experiments, the complex was found to exhibit a singlet ground state but with a reduced antiferromagnetic coupling of  $-2J = 144 \text{ cm}^{-1}$ .<sup>31</sup> The relatively weak antiferromagnetic coupling compared to all synthetic **6P** species ( $-2J \geq 600 \text{ cm}^{-1}$ ) was mainly attributed to the Cu-O-O-Cu torsion angle of 65°, accounting for a diminished overlap of oxygen- and copper-centered orbitals in partly suppressing the superexchange pathway between both copper atoms.<sup>31,101,62</sup> This superexchange pathway is believed to break down at a Cu-O-O-Cu torsion angle close to 90° (see Section 6.1.5) and



consequently the concept of intentional ligand design was again applied to synthesize a ligand that promotes such coordination chemistry.<sup>34</sup> The methylene spacer in **HL**<sup>1</sup> was exchanged by an ethylene unit to form ligand **HL**<sup>2</sup>.<sup>34</sup> The additional CH<sub>2</sub>-group was introduced to shorten the Cu...Cu distance of the corresponding peroxodicopper(II) complex, in order to enable a higher Cu-O-O-Cu torsion angle.<sup>34</sup> The molecular structure of the isolated peroxy compound **3** indeed shows a significantly higher Cu-O-O-Cu torsion angle of 104°. Both copper ions are ferromagnetically coupled ( $-2J = -140 \text{ cm}^{-1}$ ).<sup>34</sup> Since the structure of the Cu<sub>2</sub>/O<sub>2</sub> core lies close to the midpoint between the planar <sup>6</sup>P (e.g.  $\phi(\text{Cu}_2\text{O}_2) = 0^\circ$ ) and <sup>7</sup>P (e.g.  $\phi(\text{Cu}_2\text{O}_2) = 180^\circ$ ) binding modes, this motif is referred to as orthogonal- $\mu$ - $\eta^1$ : $\eta^1$ -peroxy binding mode, <sup>0</sup>P.

However, complex **2+Na**<sup>+</sup> differs from **3** in that a sodium ion is interacting with the peroxy moiety, raising the question of how this cation affects the electronic structure of this <sup>6</sup>P species. The interaction of Lewis acidic metal ions with metal-oxo and metal-peroxy complexes is a topic of recent studies.<sup>102</sup> A non-haem iron(III) peroxy complex was reported to interact with several redox-inert metal ions such as Ca<sup>2+</sup> and Sc<sup>3+</sup>, giving insight into the role of Ca<sup>2+</sup> in the function of the oxygen evolving complex in photosystem II.<sup>102,103</sup> Since not only Ca<sup>2+</sup> but also the alkali metal ion Na<sup>+</sup> is ubiquitous and abundant in the natural environment, the influence of the Na<sup>+</sup> ion on the nature of the copper-oxygen core in **2+Na**<sup>+</sup> is of considerable interest. This thesis therefore focuses on the synthesis and on the characterization of the parent <sup>6</sup>P complex **2** (see Scheme 7), followed by a controlled reaction with the alkali metal ions Li<sup>+</sup>, Na<sup>+</sup> and K<sup>+</sup>.



**Scheme 7.** Synthesis of complex **2** and controlled formation of corresponding alkali metal adducts **2+M**<sup>+</sup>.

The influence of the alkali metal ions on the electronic structure of the copper oxygen core will be discussed. Further investigations towards the redox chemistry of these unique peroxy alkali metal ion adducts as well as relevant conclusions concerning the relevance of such interactions for synthetic and natural copper oxygen intermediates will be drawn.

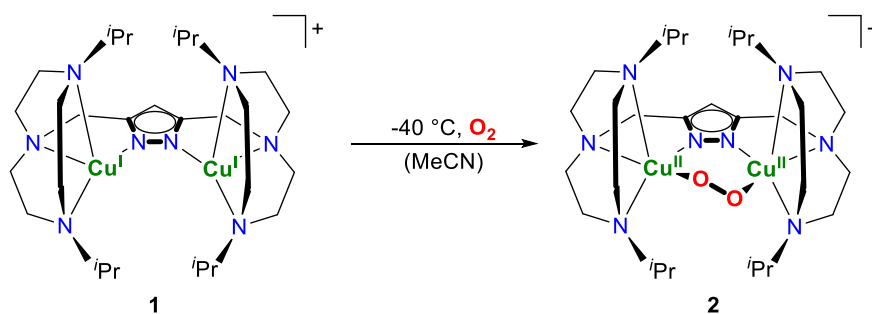
## 6 RESULTS AND DISCUSSION

### 6.1 A Dicopper(II) Peroxo Intermediate

The following chapter will focus on the synthesis as well as on the spectroscopic characterization of peroxo complex **2**, featuring a <sup>c</sup>P binding mode. The unusual geometry of the copper oxygen core is thereby induced by the specific ligand design (see Section 5). The electronic structure of this species will be discussed in both solid and solution state and further investigated with the support of DFT calculations. The effect of structural parameters such as Cu-O-O-Cu torsion angle  $\phi$  on the magnitude of magnetic exchange coupling between the Cu<sup>II</sup> ions and on the nature of the corresponding electronic absorption spectrum of this complex will be presented. Finally, a comparison with the structurally related peroxo complex **3**<sup>34</sup> will be drawn and the interplay of Cu-O-O-Cu torsion angle  $\phi$  and magnetic ground state will be discussed in providing relevant information for the proposed trajectory of O<sub>2</sub>-binding in type III active sites.

#### 6.1.1 Formation in solution

In previous work,<sup>10</sup> a synthetic route for generating single crystalline material of the dinuclear copper(I) precursor **1** has been developed. Generally, ca. 200 mg of ligand **HL**<sup>1</sup> have been reacted with NaO<sup>t</sup>Bu, [Cu(MeCN)<sub>4</sub>]ClO<sub>4</sub> and NaBPh<sub>4</sub>. The desired complex was isolated after carrying out Et<sub>2</sub>O diffusion into a concentrated solution of acetone in moderate yields (see Section 7.13.1). Complex **1** readily reacts with molecular dioxygen in e.g. MeCN by forming an intense purple solution, which was observed to be stable on the UV/vis timescale at temperatures below 250 K (Scheme 8).



**Scheme 8.** Schematic presentation of reaction of precursor **1** with O<sub>2</sub> in forming <sup>c</sup>P species **2**.

The corresponding UV/vis absorption spectrum (see Figure 12) shows two maxima in absorbance at 527 nm ( $\epsilon = 5.0 \text{ mM}^{-1} \text{ cm}^{-1}$ ) and at 648 nm ( $\epsilon = 3.9 \text{ M}^{-1} \text{ cm}^{-1}$ ) and a shoulder at 456 nm ( $\epsilon = 2.6 \text{ M}^{-1} \text{ cm}^{-1}$ ).<sup>10</sup> The electronic absorption spectrum thereby looks very similar to that of related *trans*-peroxo systems, whose electronic structure has been investigated in detail *via* computational studies.<sup>82,104,50</sup> However, the spectrum of **2** is two times less intense than the electronic absorption spectra of related <sup>T</sup>P complexes, reflecting the unique bonding situation in this <sup>c</sup>P species (this outcome

will be discussed in more detail in Section 6.2.3).<sup>44</sup> The major transition at 527 nm arises from one of the two peroxide  $\pi^*$  orbitals, interacting with the Cu-centered magnetic orbitals *via* a  $\sigma$ -interaction ( $\pi^*_\sigma$ ) (see Figure 12). The second CT transition at 648 nm arises from the other peroxide  $\pi^*$  orbital that shows no significant overlap with the Cu-centered orbitals. With respect to a planar arrangement of the  $\text{Cu}_2/\text{O}_2$  core, this  $\pi^*$  orbital would be vertical to the  $\text{Cu}_2/\text{O}_2$  plane and is thus denoted to as  $\pi^*_\nu$ . It should be noted that complex **2** is featuring a significant torsion of the  $\text{Cu}_2/\text{O}_2$  core (see Section 6.1.2) and thus no planar arrangement of the  $\text{Cu}_2/\text{O}_2$  moiety is observed. However, this electronic transition appears with lower intensity compared to the former due to a minor overlap with the copper- and oxygen-centered orbitals and will still be denoted as  $\text{O}_2^{2-} \pi^*_\nu \rightarrow \text{Cu}^{\text{II}}$  CT.<sup>50</sup>

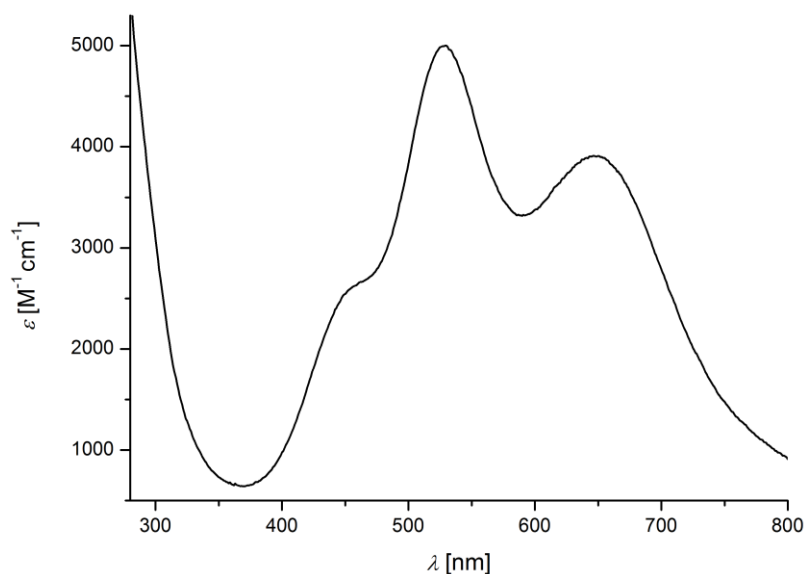


**Figure 12.** UV/vis absorption spectrum of complex **2** (MeCN,  $T = -40\text{ }^\circ\text{C}$ ).

The origin of the broad shoulder at 456 nm cannot be assigned clearly. The corresponding TD-DFT singlet-to-singlet calculations (see Section 6.1.7), exclusively predict the experimentally observed CT transitions at 527 and 648 nm. This indicates spin-forbidden character of the transition at 456 nm for which full-scale spin-orbit TD-DFT would be needed. However, this method is technically not possible at the moment, since **2** is featuring a antiferromagnetically coupled ground state (for more details see Section 6.1.7).<sup>105</sup>

The corresponding solution state rR spectrum (EtCN,  $T = -30\text{ }^\circ\text{C}$ ,  $\lambda_{\text{exc}} = 633\text{ nm}$ ) shows two intensive oxygen isotope sensitive signals at  $784\text{ cm}^{-1}$  and  $809\text{ cm}^{-1}$ , collapsing into one signal upon labeling with  $^{18}\text{O}_2$  ( $\tilde{\nu}_{18\text{O}-18\text{O}} = 760\text{ cm}^{-1}$ ).<sup>32,10</sup> The origin of this doublet may be explained with the Fermi resonance phenomenon, which is described in more detail in Section 6.1.3. Nevertheless, the O-O stretch is at typical energy for a  $\mu$ -1,2 peroxide, supporting the assumed formation of a dicopper peroxy species.<sup>44</sup>

### 6.1.2 Solid State Structure

A major challenge was the isolation of single crystalline material of compound **2**. Whereas the structurally related complexes **2+M<sup>+</sup>** (see Section 6.2.3) could be isolated within a few months by selectively testing multiple crystallization conditions, complex **2** has been isolated after more than one year of intensive screening. Many different solvents such as MeCN, EtCN or Acetone, combined with diffusion and layering techniques (Et<sub>2</sub>O or MTBE) have been applied at variable temperatures ( $T = -26, -36, -80$  °C). Finally, single crystalline material of **2** was obtained after Et<sub>2</sub>O diffusion into a solution of the oxygenated complex in a mixture of acetone and Et<sub>2</sub>O at  $-26$  °C. Since **2** has been observed to slowly decompose during the crystallization process, the solubility of **2** was decreased in using a mixture of acetone and Et<sub>2</sub>O. This procedure enabled the isolation of single crystalline material within two weeks of Et<sub>2</sub>O diffusion. However, single crystals were only obtained from quite diluted solutions of complex **2** (see Section 7.13.2). The solid state structure of the oxygen adduct **2** is depicted in Figure 13.

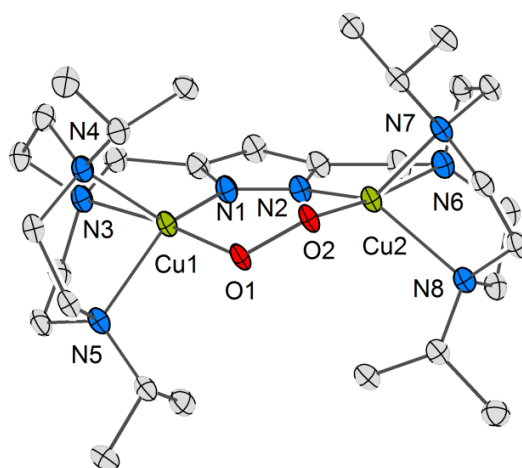


**Figure 13.** Molecular structure of **2** with thermal displacement ellipsoids given at 30% probability. Hydrogen atoms, counterion BPh<sub>4</sub><sup>-</sup>, and additional solvent molecules are omitted for clarity; for selected bond lengths and angles see Section 7.7.

The molecular structure of **2** shows two Cu<sup>II</sup> ions in a distorted trigonal bipyramidal coordination environment ( $\tau(\text{Cu1}) = 0.63$ ,  $\tau(\text{Cu2}) = 0.60$ )<sup>106</sup>, provided by four nitrogen donor atoms of TACN side arm and the pyrazolate unit, and by one oxygen atom of the peroxo ligand. The Cu-pyrazolate bond lengths are substantially shorter (Cu1-N1 = 1.91 Å, Cu2-N2 = 1.90 Å) than those of the copper atoms to the TACN side arm nitrogen donor atoms (Cu1-N3,4,5 = 2.18-2.26 Å). The Cu...Cu separation decreased to 3.74 Å upon O<sub>2</sub> binding (complex **1**:  $d(\text{Cu-Cu}) = 4.15$  Å). The O-O bond length was determined to 1.44 Å, which is typical for <sup>T</sup>P and <sup>C</sup>P complexes.<sup>44,34</sup> The Cu<sub>2</sub>/O<sub>2</sub> core is featuring a <sup>C</sup>P geometry with a Cu-O-O-Cu torsion angle of 55.3°, which is by 10.1° smaller compared to that of the previously reported sodium ion adduct, **2+Na<sup>+</sup>** (this outcome will be discussed in Section 6.2.3). A space-filling model of compound **2** is depicted in Figure 14, highlighting the easy accessibility of the peroxide. In comparison

to the structurally related  $\text{C}^{\text{P}}$  complex **3**<sup>34</sup> (see Section 5), the peroxide is not fully shielded by the  $i\text{Pr}$  groups of the TACN side arms. This unique cavity enables subsequent interaction of the peroxy moiety with e.g. alkali metal ions such as  $\text{Na}^+$  (see Section 6.2) and explains why this peroxide has been initially isolated as the sodium adduct, **2**+ $\text{Na}^+$ . The corresponding precursor contained sodium ions from the previous synthesis, which can easily access the peroxy moiety in forming the corresponding alkali metal adduct (see Section 5). Since now clean starting material of **1** is available, the interaction of the peroxy moiety with e.g.  $\text{Na}^+$  can be selectively studied which will be demonstrated in Section 6.2.

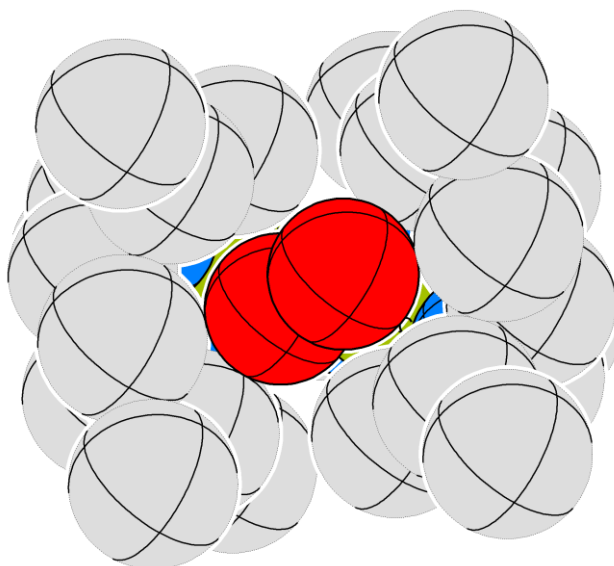


**Figure 14.** Space-filling model of complex **2**.

### 6.1.3 Solid State Resonance Raman and UV/vis Reflectance Spectroscopy

The single crystalline material of complex **2** was further analyzed *via* solid state UV/vis and solid state rR spectroscopy. The corresponding UV/vis reflectance spectrum (see Figure 15, for experimental details see Section 7.2) matches with the UV/vis absorption spectrum of this species in solution, demonstrating that the molecular structure determined crystallographically is largely preserved in solution. However, a more detailed discussion of the solid and solution state UV/vis spectra of **2** and of its alkali metal adducts **2+M<sup>+</sup>** is provided in Section 6.2.4.

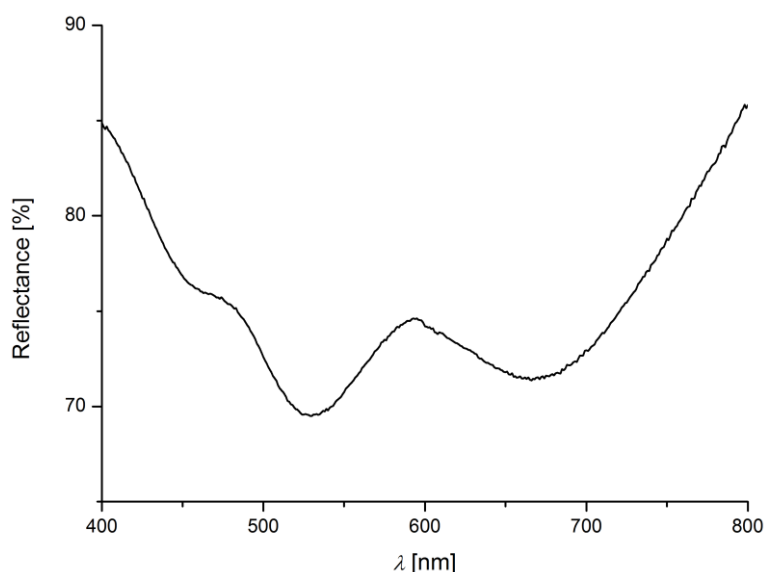


**Figure 15.** Solid state UV/vis spectrum of crystalline material of **2**.

The rR spectrum of crystalline material of **2** (see Figure 16) is also similar to that recorded in solution, further reflecting the comparable electronic structures in both solid and solution state. The spectrum shows two oxygen isotope sensitive features at  $780\text{ cm}^{-1}$  and at  $805\text{ cm}^{-1}$  (solution:  $784\text{ cm}^{-1}$ ,  $809\text{ cm}^{-1}$ ), collapsing into one signal upon labeling with  $^{18}\text{O}_2$  ( $\tilde{\nu}_{^{18}\text{O}-^{18}\text{O}} = 760\text{ cm}^{-1}$ ). The origin of this doublet may be explained with the Fermi resonance phenomenon, which describes the mixing of two vibrational levels of same symmetry and of almost same energy in combining the two vibrational wave functions (in this case the O-O stretching vibration and another, not clearly assignable vibration).<sup>107,108</sup> Due to the quantum mechanical mixing of both modes, the higher energy mode shifts to higher and the lower energy mode shifts to lower energy, which makes the exact determination of the  $^{16}\text{O}-^{16}\text{O}$  stretching vibration energy difficult.<sup>108,109</sup> Upon labeling with  $^{18}\text{O}_2$ , the  $^{18}\text{O}-^{18}\text{O}$  stretching vibration in **2** shifts to lower energy compared to the  $^{16}\text{O}_2$  normal mode. Consequently, the energy difference between  $^{18}\text{O}_2$  normal mode and the second mode that would form the Fermi doublet increases (it is assumed that the unassigned mode, being resonance enhanced within the Fermi doublet, is not as much affected by the  $^{18}\text{O}_2$  labeling as the O-O normal mode). As a result of an increasing energy difference between  $^{18}\text{O}_2$

labeled normal mode and the second mode, both vibrations are not anymore resonance enhanced together and the observed doublet collapses into a singlet that accounts for the pure  $^{18}\text{O}$ - $^{18}\text{O}$  stretching vibration.<sup>107</sup> This observation has been furthermore made for related  $\text{TP}$  systems, where the proposed Fermi doublet is also collapsing into one band upon labeling with  $^{18}\text{O}_2$ .<sup>78,109</sup> A second but much less intense oxygen isotope sensitive feature can be found at  $415\text{ cm}^{-1}$  that can be assigned to a Cu-O stretching vibration, shifting to higher energy upon labeling with  $^{18}\text{O}_2$  ( $\tilde{\nu}_{\text{Cu-O}} = 439\text{ cm}^{-1}$ ). The same trend can be also seen in the solution state rR spectra and is further predicted by DFT calculations (see Section 6.2.7). However, the origin of this unusual behavior is still a subject of ongoing discussion. Besides these oxygen isotope sensitive stretches, other features at ca. 270, 330, 350 and at  $1002\text{ cm}^{-1}$  can be found, presumably corresponding to the counterion  $\text{BPh}_4^-$ , the Cu-N stretches of the central pyrazole unit and of the TACN sides arms.<sup>109,50</sup>

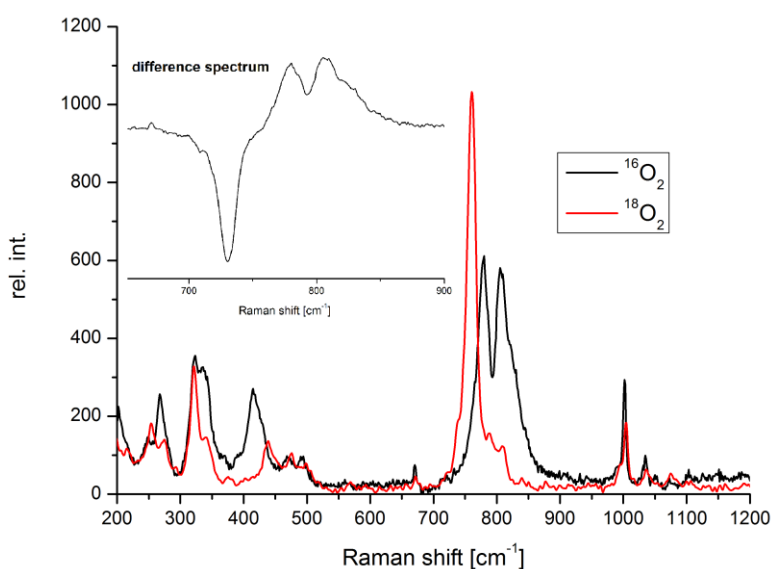


**Figure 16.** Solid state resonance Raman spectrum of  $^{18}\text{O}$  labeled (red line) and unlabeled (black line) single crystalline material of complex **2**,  $\lambda_{\text{exc}} = 633\text{ nm}$ .

#### 6.1.4 Elemental Analysis

In order to verify the proper chemical composition of complex **2**, single crystalline material of this compound has been studied *via* elemental analysis (EA). Based on the crystal structure, the unit cell is known to further contain two different solvent molecules (acetone and Et<sub>2</sub>O), which originate from the crystallization process (see Section 7.13.2 for details).

Complex **2** has been prepared freshly (see Section 7.13.2 for instructions) and was directly submitted to the EA. Furthermore, the unit cell parameters of one selected crystal have been determined prior to the measurement. The unit cell parameters were found to match with those of the crystal structure of **2** (see Figure 13 for molecular structure). The isolated crystalline material was split into two samples, of which two independent measurements have been performed. The first measurement already shows significant deviations from the expected composition (see Table 1). The second measurement, which was performed a few minutes after the first one, shows even larger differences. One explanation may be the loss of solvent molecules, being partly replaced by water. Table 1 shows the data obtained from the two independent measurements and in addition the corresponding calculated chemical compositions of complex **2** and of possible analogs, where the solvent molecules have been partly replaced by water. However, this comparison is only qualitative, since a definite reason for the deviation of experimental and calculated chemical composition cannot be assigned. Another possibility may be an additional decomposition of the peroxo moiety, in gradually releasing solvent molecules from the single crystal. However, the EA experiments demonstrate the single crystals of complex **2** to be much more sensitive towards external influences than crystalline material of its structural related alkali metal adducts (see Section 6.2), which may also be due to a shielding of the peroxide unit by the different alkali metal ions.

**Table 1.** Results of EA of one selected batch of single crystalline material of complex **2**. The second measurement was performed subsequent to the first one. The calculated possible chemical compositions are depicted below the experimental values.

	C [%]	H [%]	N [%]
<b>Found during 1. measurement</b>	<b>61.34</b>	<b>7.79</b>	<b>10.76</b>
<b>Found during 2. Measurement</b>	<b>60.73</b>	<b>7.60</b>	<b>10.62</b>
Calculated for <b>2</b> : [L <sup>1</sup> Cu <sub>2</sub> O <sub>2</sub> ]BPh <sub>4</sub> · Et <sub>2</sub> O, 0.5 acetone	63.92	8.25	10.19
Calculated for [L <sup>1</sup> Cu <sub>2</sub> O <sub>2</sub> ]BPh <sub>4</sub> · Et <sub>2</sub> O, H <sub>2</sub> O	62.91	8.24	10.30
Calculated for [L <sup>1</sup> Cu <sub>2</sub> O <sub>2</sub> ]BPh <sub>4</sub> · 0.5 acetone, H <sub>2</sub> O	62.75	7.92	10.74
Calculated for [L <sup>1</sup> Cu <sub>2</sub> O <sub>2</sub> ]BPh <sub>4</sub> · 2H <sub>2</sub> O	61.67	7.91	10.86
Calculated for [L <sup>1</sup> Cu <sub>2</sub> O <sub>2</sub> ]BPh <sub>4</sub>	63.9	7.79	11.25



## 6.1.5 Magnetism

The magnetic properties of compound **2** have been intensively studied *via* SQUID magnetometry (for representative example see Figure 17).

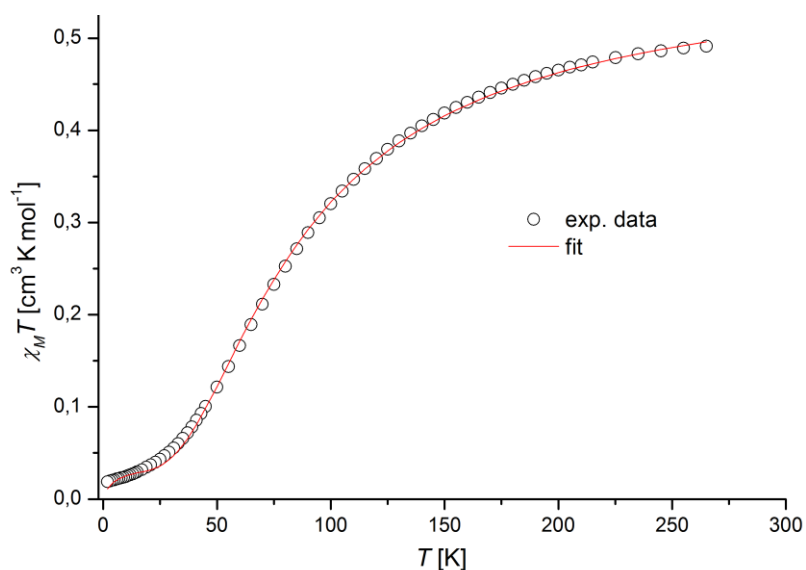


**Figure 17.** Temperature dependence of  $\chi_M T$  of complex **2** in the range between 295 K and 2 K. The red line represents the best fit (see Section 7.3 for details). Parameters obtained:  $J = -53.7 \text{ cm}^{-1}$ ,  $g = 1.81$ , PI = 10.0 %, TIP =  $510 \times 10^{-6} \text{ cm}^3 \text{ mol}^{-1}$ .

The samples have been prepared from freshly isolated single crystalline material (see Section 7.13.2 for instructions), of which the unit cell parameters have been determined *via* X-ray diffraction before each magnetic measurement. The cell parameters of the crystals were always found to coincide with those obtained during prior analysis and thus the magnetic data can be related to the derived structural parameters such as Cu-O-O-Cu torsion angle  $\phi$  and the coordination geometry of the Cu<sup>II</sup> ions (the influence of the coordination geometry on the magnitude of magnetic exchange coupling will be discussed in Section 6.2.6). However, the single crystalline material of **2** was observed to be much more sensitive than that of its structural analogues **2+M<sup>+</sup>** (see Section 6.1.4). Hence, magnetic data have been determined in multiple experiments from independently synthesized batches of single crystalline material of complex **2**. All experiments consistently show the same magnetic parameters, of which especially the  $g$ -value of  $g = 1.8$  is rather unusual. From previous work<sup>10</sup>, amorphous material of complex **2** is known to partly release dioxygen from the surface under vacuum, in forming the diamagnetic dicopper(I) complex **1**. Although single crystalline material of **2** was used during the magnetic measurements, this behavior would explain the observed  $g$ -value, since the SQUID measurement is performed under vacuum. However, the single crystalline material of complex **2** would only release dioxygen at the surface, which is small compared to the overall volume of the single crystals. In order to verify this hypothesis, a SQUID measurement of single crystalline material of **2** has been performed under He-atmosphere. Nevertheless, a  $g$ -value of ca. 1.8 has been determined again,

disproving the above-mentioned hypothesis. The abnormally low  $g$ -value must therefore originate from another diamagnetic impurity, which has not been determined until to date.

The magnetic susceptibility data (see Figure 17) predict a  $S = 0$  ground state with a low singlet-triplet splitting of  $-2J = 107 \text{ cm}^{-1}$ , which is even lower than the singlet-triplet splitting of the already characterized sodium adduct  $\mathbf{2} + \text{Na}^+$  (this outcome will be reconsidered in Section 6.2.6).<sup>31</sup> For better understanding of the magnetic properties of complex  $\mathbf{2}$ , the theory of exchange coupling in dinuclear complexes will be introduced. The two  $\text{Cu}^{\text{II}}$  ions in  $\mathbf{2}$ , both having an independent set of d-orbitals, are featuring a  $d^9$ -configuration and thus one of the five d-orbitals is singly occupied. These singly occupied magnetic orbitals, denoted as SOMOs (Singly Occupied Molecular Orbitals), will magnetically exchange couple *via* the peroxide and the pyrazolate bridges.<sup>110</sup> For reasons of clarity, only the interaction *via* the peroxy moiety will be considered at first.

The principal interaction of copper- and oxygen-centered orbitals in dinuclear copper-oxygen complexes has been introduced in Section 3 and will be exclusively discussed for  $^{\text{C}}\mathbf{P}$  complexes in Section 6.1.7. However, regardless of which dinuclear peroxy dicopper species is considered, this interaction gives rise to a molecular spin singlet ( $S = 0$ ) and a molecular spin triplet ( $S = 1$ ).<sup>111</sup> The energy difference between singlet and triplet state thereby is a function of overlap of copper- and oxygen-centered orbitals and is conventionally denoted by  $2J$ .<sup>111,112,110</sup> The interaction is defined to be antiferromagnetic, if the ground state is the singlet state ( $2J < 0$ ).<sup>111</sup> The interaction is considered to be ferromagnetic if a triplet ground state is observed ( $2J > 0$ ).<sup>111</sup> However, the energy difference  $2J$  always has a ferromagnetic ( $J_{\text{F}}$ ) and an antiferromagnetic ( $J_{\text{AF}}$ ) contribution:<sup>110</sup>

$$10) \quad J = J_{\text{F}} + J_{\text{AF}}$$

The ferromagnetic contribution can be approximately described as the Coulomb repulsion of the two electrons, favoring the high spin state.<sup>111</sup>  $J_{\text{F}}$  is thus counteracting  $J_{\text{AF}}$  that depends on the overlap integral of the magnetic orbitals with the bridging peroxy moiety.<sup>111</sup> If positive and negative zones of the overlap density exactly compensate each other, then the overlap integral becomes zero and  $J$  exclusively contains the ferromagnetic contribution,  $J_{\text{F}}$ .<sup>111,112</sup> Since in dinuclear copper(II) peroxy complexes the two copper atoms are bridged *via* a peroxy moiety, the copper SOMOs are delocalized over the whole peroxide. Consequently, the overlap integral depends on the Cu-O-O-Cu torsion angle  $\phi$ .<sup>6,101,111</sup> If the copper oxygen core is planar, the overlap of copper- and oxygen-centered orbitals is large, with  $J_{\text{AF}}$  representing the dominating contribution and thus both  $\text{Cu}^{\text{II}}$  ions are antiferromagnetically coupled. The related  $^{\text{T}}\mathbf{P}$  systems show such a planar arrangement of the copper oxygen core. As a result, both  $\text{Cu}^{\text{II}}$  ions are strongly antiferromagnetically coupled ( $-2J \geq 600 \text{ cm}^{-1}$ ).<sup>57,26,68</sup> In contrast to the planar  $^{\text{T}}\mathbf{P}$  systems, the copper oxygen core in complex  $\mathbf{2}$  is not planar but features a Cu-O-O-Cu torsion angle of  $55^\circ$ . Due to this non-planar arrangement, the overlap of copper- and oxygen-centered orbitals is significantly diminished in compound  $\mathbf{2}$ , giving rise to a much smaller

antiferromagnetic contribution compared to the related  $T^{\text{P}}$  systems. Thus, the two  $\text{Cu}^{\text{II}}$  ions in **2** are much weaker antiferromagnetically coupled ( $-2J = 107 \text{ cm}^{-1}$ ) than in other dinuclear copper oxygen sites.<sup>44</sup> The above-mentioned theory of exchange coupling predicts the magnetic ground state of complex **2** to change from  $S = 0$  to  $S = 1$ , if the Cu-O-O-Cu dihedral angle would approach  $90^\circ$ .<sup>113,114,6,101</sup> Next to complex **2**, a second  $C^{\text{P}}$  moiety has been recently published prior to this work, featuring a Cu-O-O-Cu torsion angle of  $104^\circ$  (see Figure 18).<sup>34</sup> This complex is structurally similar to compound **2** (see Section 5) and the dihedral angle is imposed by the specific ligand design applied.<sup>34</sup> Complex **3** is indeed featuring a  $S = 1$  ground state ( $-2J = -140 \text{ cm}^{-1}$ ).<sup>34</sup> With the magnetic data of both complexes in hand, the interplay of Cu-O-O-Cu dihedral angle  $\phi$  and magnetic ground state is illustrated, supporting the theoretical description of this superexchange mechanism. However, this discussion is rather qualitative and will be further continued on the basis of DFT calculations on compound **2** and the alkali metal adducts  $\mathbf{2} + \mathbf{M}^+$  in Section 6.2.7.

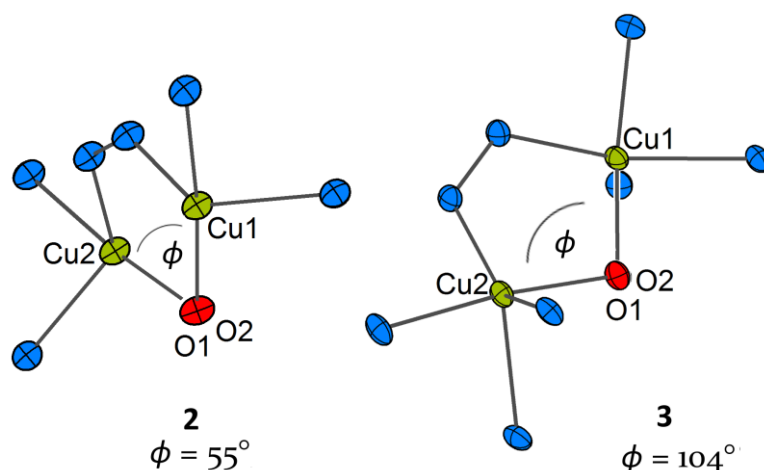


**Figure 18.** Comparison of the core structures of complexes **2** (left) and **3** (right); The Cu-O-O-Cu torsion angle is presented in looking down the O-O bond.<sup>34</sup>

The peroxo moiety in complexes **2** and **3** is not the only pathway, mediating superexchange between the two copper(II) ions. The pyrazolate bridges in **2** and **3** are also providing a possible superexchange pathway between the two metal ions, and thus the corresponding Cu-N-N-Cu torsion angle has to be considered additionally. However, if both pyrazolate and peroxide mediated exchange pathways are compared, the contribution of the magnetic coupling *via* the peroxide bridge is reported to be predominant, whereas dinuclear copper complexes with a pyrazolate ligand, representing the only bridging unit, show only weak magnetic coupling ( $-2J = 30\text{-}70 \text{ cm}^{-1}$ ).<sup>44,115,116</sup> The contribution of the pyrazolate bridge to the overall observed magnetic interaction is therefore neglected in this discussion.

## 6.1.6 Electron Paramagnetic Resonance Spectroscopy

The magnetic properties of **2** have been studied *via* SQUID magnetometry and are presented in the previous section. The two Cu<sup>II</sup> ions are weakly antiferromagnetically coupled ( $-2J = 107 \text{ cm}^{-1}$ ) and complex **2** features a  $S = 0$  ground state. However, the singlet-triplet splitting is rather small compared to other dinuclear peroxo sites and the energetically higher  $S = 1$  spin state is thus considerably populated even at 140 K (see Figure 19).<sup>6,57,32</sup>

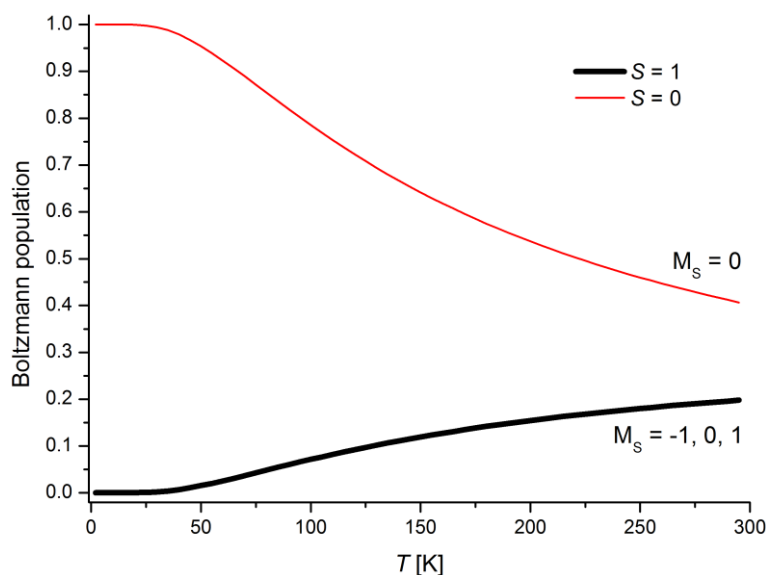


**Figure 19.** Boltzmann population of  $S = 1$  excited state of peroxo complex **2**;  $\Delta E = |2J|$  ( $J = -54 \text{ cm}^{-1}$ ).

According to the temperature dependence of the Boltzmann population of the  $S = 1$  excited state depicted in Figure 19, **2** is expected to show an EPR spectrum at e.g. 140 K, although it might be weak. With respect to this assumption, the properties of **2** have been further investigated *via* EPR spectroscopy. Figure 20 shows one representative example of a frozen solution of **2**, which has been recorded at 143 K. The different samples have been prepared freshly (see Section 7.8 for instructions) from independent batches of single crystalline material of precursor **1**. All spectra consistently show the same signal pattern. One selected sample additionally has been stored over several weeks at  $-80 \text{ }^\circ\text{C}$  and was again measured in yielding the same spectrum as obtained during the first experiment. Thus, the samples of complex **2** are assumed to exclusively contain this species, since a contamination with decomposition products or other impurities would result in at least slightly different EPR spectra.

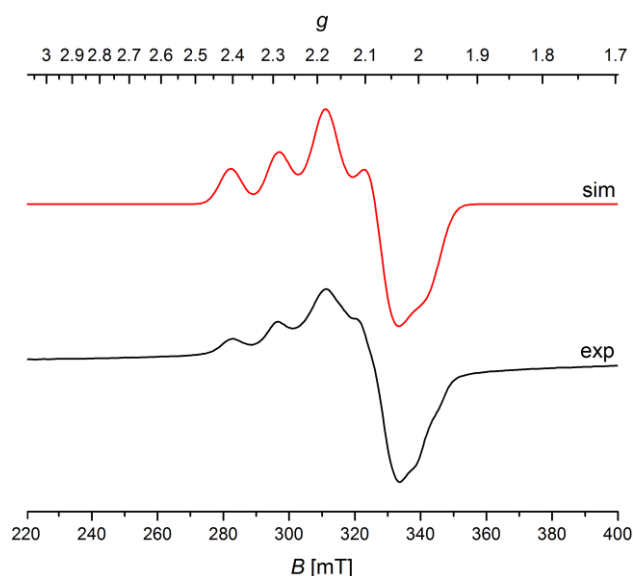


**Figure 20.** X-band EPR spectrum (black line) and corresponding simulation<sup>117</sup> (red line) of 0.01 M frozen solution of **2** in MeCN recorded at 143 K.

The EPR spectrum of complex **2** was recorded in a solution of frozen MeCN at 143 K. The corresponding  $g$ -values ( $g_1 = 2.22$ ,  $g_2 = 2.12$ ,  $g_3 = 2.01$ ) can be simulated with the software package easyspin<sup>117</sup>, running under Matlab®. The simulated spectrum ( $S = 1$ ,  $g$ -strains were applied) matches with the experimental data. Possible zero field splitting was not included into the simulation. The experimental spectrum furthermore shows a weak half-field signal at ca. 161 mT, which is not considered during the simulation (see Figure 21, left).

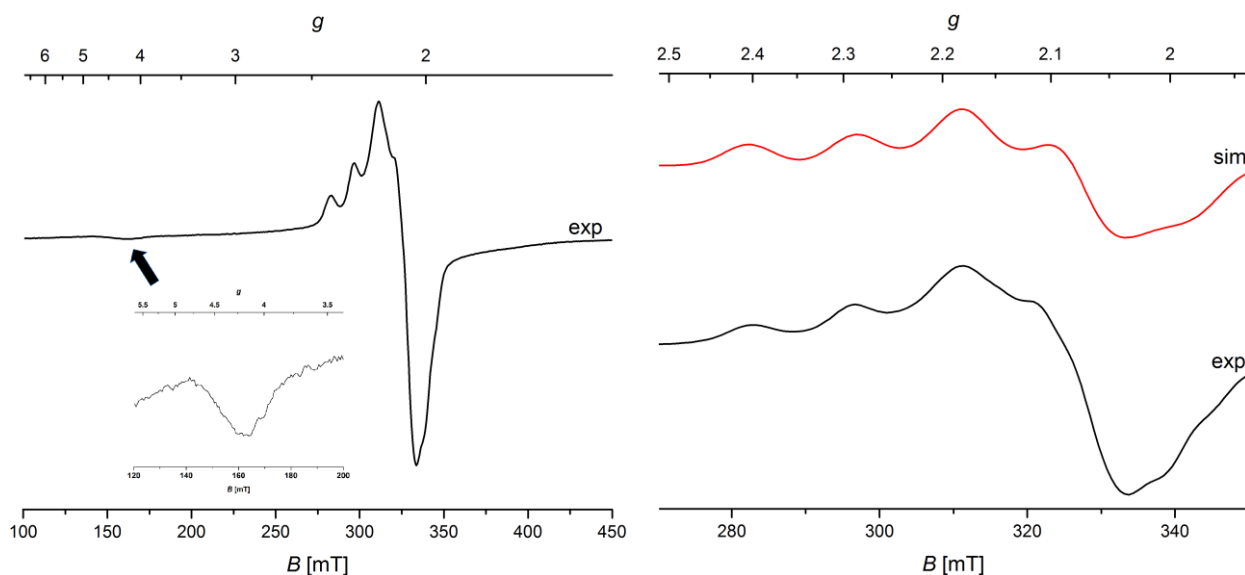


**Figure 21.** Left: ERP spectrum of frozen 0.01 M solution of **2** in MeCN recorded at 143 K in the range of 100 – 450 mT (inset shows half-field signal at ca.161 mT); right: close-up view of experimental and simulated<sup>117</sup> spectra ( $a_1 = 80$  G,  $a_2 = 130$  G,  $a_3 = 440$  G).

The experimentally observed half-field signal at 161 mT supports the thermal population of the  $S = 1$  state depicted in Figure 19. Since the experimental spectrum matches with the simulation, the half-field

signal at 161 mT is attributed to complex **2**, of which a small amount exists in the  $S = 1$  excited state. Thus, the EPR experiment supports the magnetic susceptibility data presented in Section 6.1.5, predicting a weakly antiferromagnetically coupled dicopper site.

## 6.1.7 DFT calculations

With the structural data of complex **2** in hand, density functional theory (DFT) calculations were carried out in cooperation with the working group of SWART<sup>118</sup> on both the optimized geometry as well as on the molecular structure determined *via* X-ray crystallography. A more detailed discussion of the corresponding results including those of the structurally related alkali metal adducts **2+M<sup>+</sup>** is provided in Section 6.2.7, while this chapter will exclusively focus on a computational description of the bonding between copper atoms and peroxide in **2**. On the basis of the optimized structure (BP86 functional<sup>119,120</sup>, including dispersion corrections according to GRIMME<sup>121</sup> (DFT-D3), TZP basis set<sup>122,118</sup>), a MO diagram for **2** could be developed (see Figure 22, for more computational details see ref.<sup>105</sup>). It should be noted that the results presented in this Section are only preliminary.

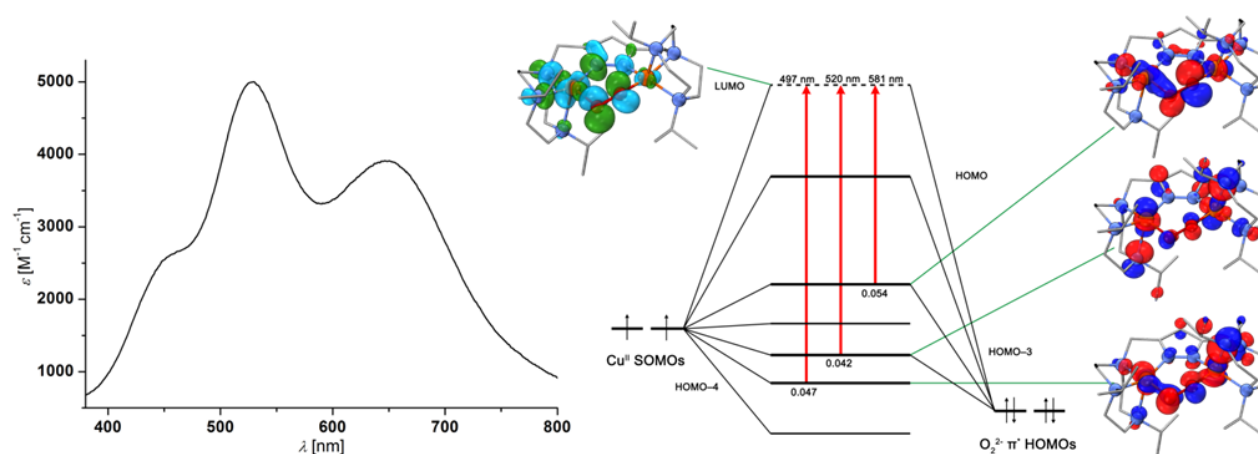


**Figure 22.** Experimental electronic absorption spectrum (left) and calculated MO diagram including corresponding  $\alpha$ -spin MOs obtained from geometry optimized data of complex **2** (right).<sup>118</sup>

The major transition of the experimental spectrum at 527 nm thereby arises from HOMO-3, the peroxide  $\pi^*$  orbital that interacts with the Cu-centered orbitals via a  $\sigma$ -interaction ( $\pi^*_\sigma$ ) to the LUMO which is located mainly on the peroxide and on the ligand. The transition at 648 nm arises from a second peroxide  $\pi^*$  orbital that is denoted as HOMO-1 (denoted as  $\pi^*_\nu$  in Section 6.1.1). The broad shoulder at 465 nm is not observable in the TD-DFT singlet-to-singlet spectrum, but it is however noticed in the experimental data. This most likely indicates spin-forbidden character for which full-scale spin-orbit TD-DFT would be needed, which is at the moment technically impossible in ADF (Amsterdam Density Functional) due to the antiferromagnetically coupled open-shell ground state.<sup>123,124</sup> However, next to TD-DFT calculations based on the optimized geometry of **2**, a second approach based on X-ray constrained geometries which were performed under the unrestricted formalism for open-shell singlet and triplet states except for the excitation energies, for which only singlet states were considered.<sup>118</sup> The corresponding calculated MO diagram is depicted in Figure 23, b). The MO diagram thereby looks similar to that obtained from the first approach (see Figure 23, a)), although all CT

transitions are shifted to lower energy compared to the calculations based on the fully optimized geometries (see Table 2 for details).

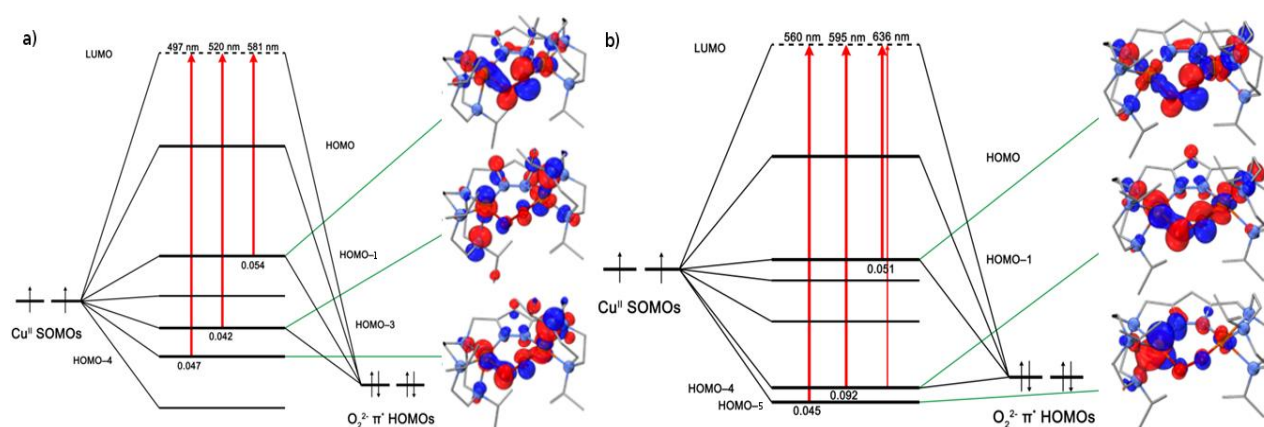


**Figure 23.** Calculated MO diagrams and corresponding  $\alpha$ -spin MOs based on a): optimized geometry and from b): X-ray constrained point coordinates of complex **2**.

**Table 2.** Summary of TD-DFT-calculated excitation energies and dominant transitions obtained from 1): geometry optimized structural coordinates and 2): from single point optimized coordinates.<sup>118</sup>

approach	energy [nm]	oscillator strength [f]	transition (to LUMO) <sup>c</sup>
1) geometry optimization <sup>a</sup>	497	0.047	HOMO-4
	520	0.042	HOMO-3
	581	0.054	HOMO-1
2) single point calculations <sup>b</sup>	560	0.045	HOMO-5
	595	0.092	HOMO-4
	636	0.051	HOMO-1

<sup>a</sup>geometry optimization: BP86 functional<sup>119,120</sup>, inclusion of Grimme's<sup>121</sup> dispersion energy (DFT-D3), TZ2P basis set<sup>122</sup>; excitation energies were calculated by using the S12g functional<sup>125</sup> in conjunction with a TZ2P basis set (S12g/TZ2P); single point final energies were calculated by using different XC functionals (see ref.<sup>105</sup> for more details). Calculations were performed under the unrestricted formalism for open-shell singlet and triplet states (except for the excitation energies, here only singlet states were considered). <sup>b</sup>molecular structure determined by X-ray diffraction was optimized with constraints in order to locate hydrogen atoms; for computational details see: <sup>a</sup>geometry optimization. <sup>c</sup>Only the dominating transition is reported here, for more details see Section 6.2.7, Table 11 and ref.<sup>105</sup>.

In summary, the DFT calculations show that the electronic structure of the copper oxygen core in **2** is principally similar to that of the structurally related **TP** systems.<sup>44</sup> Two main interactions are giving rise to a characteristic electronic absorption spectrum, while a most likely spin forbidden transition is the origin of the experimentally observed shoulder at 465 nm.



Consequently, this work delivers a first preliminary computational description of this unique  $\epsilon$ P binding mode obtained from synthetic copper complexes and may also deliver important results for further investigations of the relevance of this binding mode during the mechanism of dioxygen activation at type III active copper sites.

### 6.1.8 Summary and Conclusion

The selective synthesis of peroxo complex **2** was presented in this chapter. In screening various crystallization conditions, single crystalline material was obtained and a molecular structure of this  ${}^{\text{C}}\text{P}$  species could be determined. The solid state structure of **2** highlights the easy accessibility of the copper oxygen core, which is induced by the specific ligand design. This cavity enables the peroxo moiety to interact with e.g. alkali metal ions, which will be discussed in Section 6.2.

The spectroscopic properties of **2** have been studied in both solution and solid state. The solid and solution state UV/vis and rR data were found to agree and thus the structural parameters such as Cu-O-O-Cu torsion angle  $\phi$  were also used to interpret the electronic structure of the  ${}^{\text{C}}\text{P}$  species in solution.

The magnetic properties of **2** have been intensively analyzed by SQUID magnetometry, highlighting the unique bonding situation of the copper oxygen core. **2** is featuring a  $S = 0$  ground state, whereas the weak antiferromagnetic coupling ( $-2J = 107 \text{ cm}^{-1}$ ) between the  $\text{Cu}^{\text{II}}$  ions is attributed to a diminished overlap of copper- and oxygen-centered orbitals, which is induced by a Cu-O-O-Cu torsion angle of  $55^\circ$ . The weak antiferromagnetic coupling in **2** was additionally demonstrated *via* EPR spectroscopy, showing weak signals corresponding to a thermal population of the energetically higher  $S = 1$  state.

The magnetic properties of **2** have been furthermore compared to those of the structurally related  ${}^{\text{O}}\text{P}$  species, **3**. Complex **3** is thereby featuring a  $S = 1$  ground state, promoted by a Cu-O-O-Cu dihedral angle of  $104^\circ$ . With these two complexes in hand, the interplay of Cu-O-O-Cu torsion angle  $\phi$  and magnetic ground state could be demonstrated. Thus, complex **2** represents a snapshot of the discussed trajectory of dioxygen binding in type III active sites and delivers valuable insight into the mechanism of  $\text{O}_2$  activation.

First preliminary DFT calculations were performed<sup>105</sup> in order to analyze the unique bonding situation in complex **2**. While the origin of the two CT transitions in the electronic absorption spectrum of **2** could be identified, the origin of the experimentally observed shoulder at 456 nm is still unclear. The shoulder most likely originates from a spin forbidden transition. However, this thesis provides first computational insight into the bonding in  ${}^{\text{C}}\text{P}$  complexes which is another milestone towards the understanding of the mechanism of dioxygen activation at type III active copper sites.

## 6.2 Interaction with Alkali Metal Ions

### 6.2.1 Adduct formation in Solution

With clean material of **1** in hand, peroxo complex **2** can be selectively synthesized (see Section 6.1) and the corresponding alkali metal ion adducts  $\mathbf{2}+\mathbf{M}^+$  ( $\mathbf{M} = \text{Li, Na, K}$ ) can be directly generated in situ, while monitoring the formation of these adducts *via* e.g. UV/vis absorption spectroscopy. Compound  $\mathbf{2}+\mathbf{Na}^+$  has been isolated already prior to this work under different starting conditions (see Section 5). Since a selective generation from clean starting material is now possible, the formation of  $\mathbf{2}+\mathbf{Na}^+$  has been examined once again in this work.<sup>31</sup> The nature of the adducts  $\mathbf{2}+\mathbf{K}^+$  and  $\mathbf{2}+\mathbf{Li}^+$  has been studied in detail *via* various spectroscopic methods and will be compared with the data obtained for  $\mathbf{2}+\mathbf{Na}^+$ . Additionally, the solid state structures of all three adducts will be discussed (Section 6.2.3), highlighting the in all three cases very similar binding motifs that however do not reflect the differences monitored by especially solution and solid state UV/vis spectroscopy. Consequently, DFT calculations have been performed in order to quantify the influence of the different alkali metal ions on the electronic structure of the copper oxygen core (see Section 6.2.7). Figure 24 shows the formation of adduct  $\mathbf{2}+\mathbf{Li}^+$  monitored by UV/vis absorption spectroscopy. In this titration experiment a solution of LiOTf has been added in substoichiometric amounts (in steps of 0.05 eq. with overall 2.00 eq. being added) to a solution of **2** in MeCN at  $-40\text{ }^\circ\text{C}$ . An isosbestic point at 487 nm indicates a clean conversion.

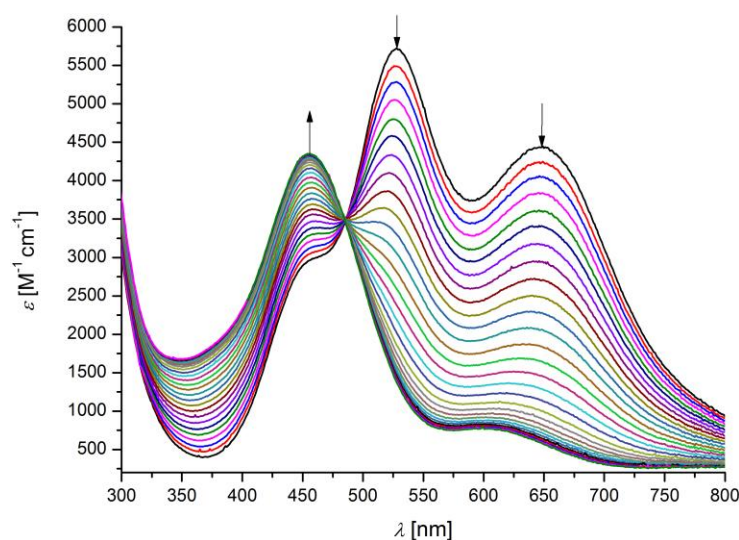
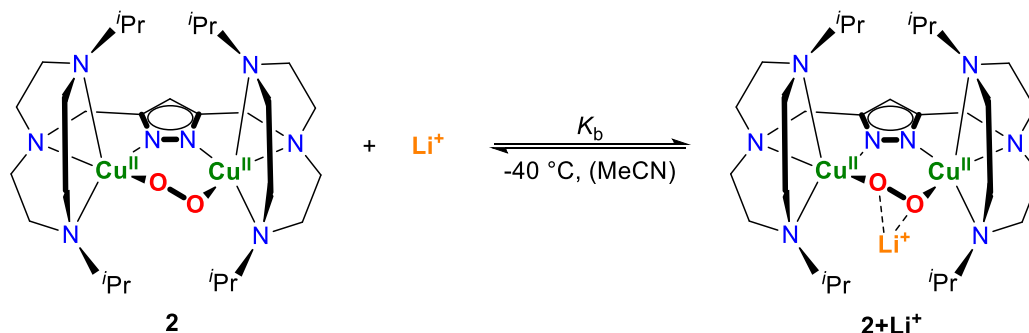


**Figure 24.** Titration of complex **2** with LiOTf in steps of 0.05 eq., with overall 2.00 eq. of titrant being added. The isosbestic point at 487 nm indicates a clean conversion (MeCN,  $T = -40\text{ }^\circ\text{C}$ ).

Whereat the absorption maxima of **2** at 527 and at ca. 650 nm simultaneously decrease during the addition of the first 0.80 equivalents of LiOTf, the stepwise addition of further LiOTf induces only minor conversion of **2** into the lithium adduct  $\mathbf{2}+\mathbf{Li}^+$ , which has two absorption maxima at 456 nm ( $\epsilon = 3.9\text{ mM}^{-1}\text{ cm}^{-1}$ ) and at 595 nm ( $\epsilon = 0.7\text{ mM}^{-1}\text{ cm}^{-1}$ ). Complex **2** can be described as a host complex, forming the

corresponding host-guest complex  $2+Li^+$  (see Scheme 9).<sup>126,127</sup> The formation of  $2+Li^+$  can be described with an binding constant  $K_b$ :

$$11) \quad K_b = \frac{[2+Li^+]c^0}{[2][Li^+]}; \quad c^0 = 1 \text{ mol} \cdot \text{L}^{-1}$$



**Scheme 9.** Host-guest complex formation monitored *via* UV/vis absorption spectroscopy.

The 1:1 stoichiometry of host and guest has been determined *via* the mole ratio method (see Figure 25) and is further supported by the structural data determined *via* X-ray diffraction for complex  $2+Li^+$  (see Section 6.2.3 for details).<sup>128</sup> The equilibrium between host, guest and host-guest complex has been analyzed by a software package provided by THORDARSON<sup>128</sup> (see Section 7.2.2 for further details), in fitting  $K_b$  by correlating changes in the absorbance of **2** with a substoichiometric addition of LiOTf, until no further significant change in absorbance of the final spectrum was observed (see Figure 26). With this procedure, the association constants for  $2+Na^+$  and for  $2+K^+$  have been determined as well (see Table 3).

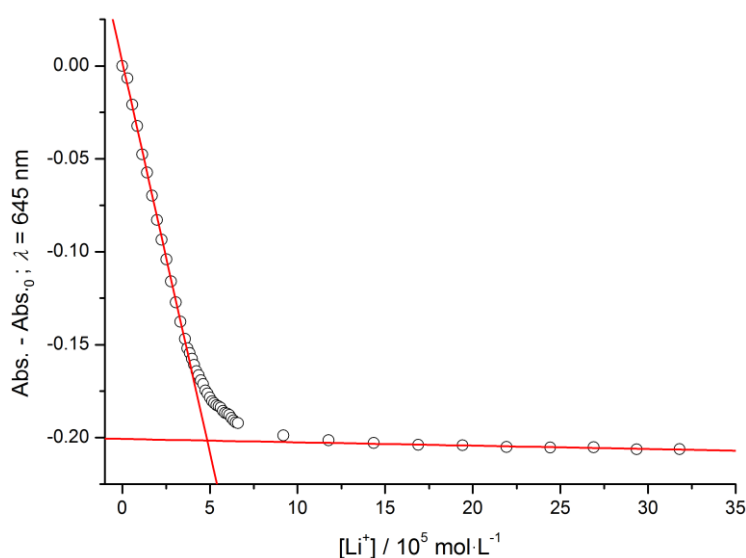


**Figure 25.** Selected example of determination of host-guest stoichiometry *via* mole ratio method.<sup>128</sup> A  $[Li^+]_0/[2]_0$  stoichiometric ratio of ca. 0.9 was determined which by approximation corresponds to a 1:1 host-guest stoichiometry;  $[2]_0 = 58 \mu\text{M}$ .<sup>128</sup>

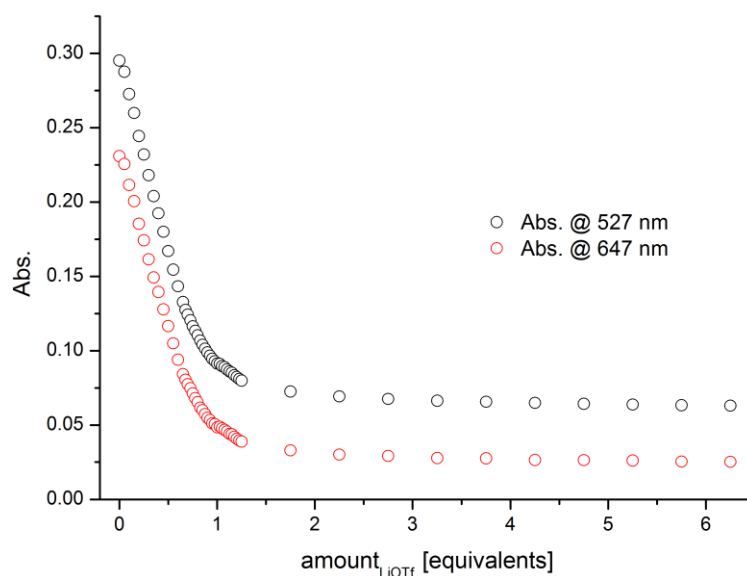


**Figure 26.** Changes in Absorbance of two selected wavelengths during a titration experiment of **2** with LiOTf used for determination of  $K_b$ . LiOTf has been added stepwise in different concentrations. At first LiOTf was added in steps of 0.05 eq. (from 0 - 0.65 eq.), followed by steps of 0.025 eq. (from 0.65 - 1.25 eq.), followed by steps of 0.5 eq. (from 1.25 - 6.25 eq.); (MeCN,  $T = -40\text{ }^\circ\text{C}$ ).

**Table 3.** Association constants of all three adducts determined *via* UV/vis titration experiments.<sup>128</sup>

complex	eq. of MOTf added	$K_b$
<b>2+K<sup>+</sup></b>	48.0	$64 \pm 5.6\%$
<b>2+Na<sup>+</sup></b>	15.0	$70 \times 10^1 \pm 6.2\%$
<b>2+Li<sup>+</sup></b>	6.25	$69 \times 10^4 \pm 23\%$

A clear trend can be observed when the association constants and the required total equivalents of alkali metal ion, which have been added to complex **2** during the titration experiment, are compared. The total amount of alkali metal ion, being required for an almost complete conversion of **2** into the desired host-guest complex, increases from LiOTf (ca. 2 eq.) over NaOTf (ca. 14 eq.) to KOTf (ca. 50 eq.). Since Lewis acidic alkali metal ions interact with the Lewis basic peroxy unit, a decreasing strength of this interaction is expected from  $\text{Li}^+$  over  $\text{Na}^+$  to  $\text{K}^+$  in terms of the HSAB concept (Hard and Soft (Lewis) Acids and Bases).<sup>129</sup> Consequently, a higher amount of e.g.  $\text{Na}^+$  compared to  $\text{Li}^+$  is required to convert **2** into the respective alkali metal adduct (see Figure 26 and Figure 27). The obtained association constants (see Table 3) indeed agree with the HSAB concept. The binding constant for the formation of **2+K<sup>+</sup>** is by far the smallest ( $64 (\pm 6\%)$ ), whereas the adduct **2+Li<sup>+</sup>** is formed with an association constant of  $K_b > 10^5$ .

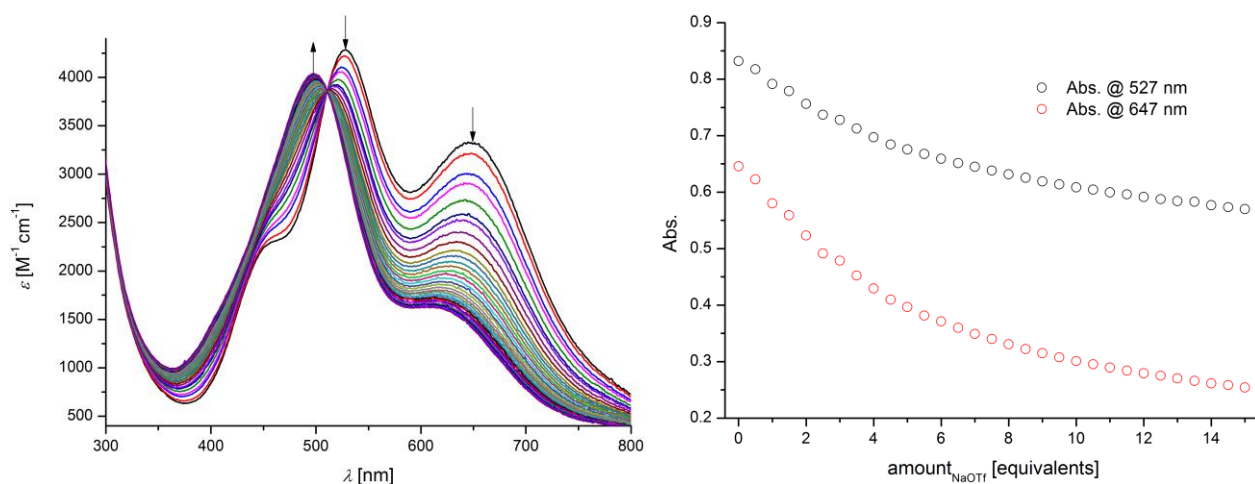


**Figure 27.** Left: titration of complex **2** with NaOTf in steps of 0.5 eq., with overall 15.0 eq. added. The isosbestic point at 511 nm indicates a clean conversion. Right: changes in absorbance during titration experiment used for determination of the association constant.

However, this derived sequence only reflects a rough trend since the different solvation energies of the alkali metal ions in MeCN are not considered within the fitting procedure.<sup>130</sup> The solvation of  $\text{Li}^+$  in e.g. MeOH is significantly stronger than the solvation of  $\text{Na}^+$  and  $\text{K}^+$ .<sup>130,131</sup> The association constants describing the aforementioned adduct formation are thus also affected by the different solvation energies of the alkali metal ions.<sup>127</sup>

If the three association constants are further compared, the exceptionally high error for the binding constant of  $\mathbf{2}+\text{Li}^+$  becomes apparent. In general, larger errors are involved within the determination of binding constants  $> 10^5$  in contrast to association constants in the range of  $10^2 - 10^4$ .<sup>128</sup> However, the association constant determined for  $\mathbf{2}+\text{Li}^+$  is by three orders of magnitude larger than the binding constant for e.g.  $\mathbf{2}+\text{Na}^+$ . In order to verify the derived association constant for  $\mathbf{2}+\text{Li}^+$ , a solution of complex **2** has been titrated with a solution of the 15-crown-5 adduct of  $\text{Li}^+$  (see Figure 28), which has a comparable binding constant in MeCN ( $10^{3.8} - 10^{5.3}$ ,  $T = 25\text{ }^\circ\text{C}$ ) (see Scheme 10).<sup>132,133,134</sup> Since the association constant for  $\mathbf{2}+\text{Li}^+$  is higher than that of the corresponding 15-crown-5 adduct of  $\text{Li}^+$ , **2** should abstract the  $\text{Li}^+$  ion from 15-crown-5.

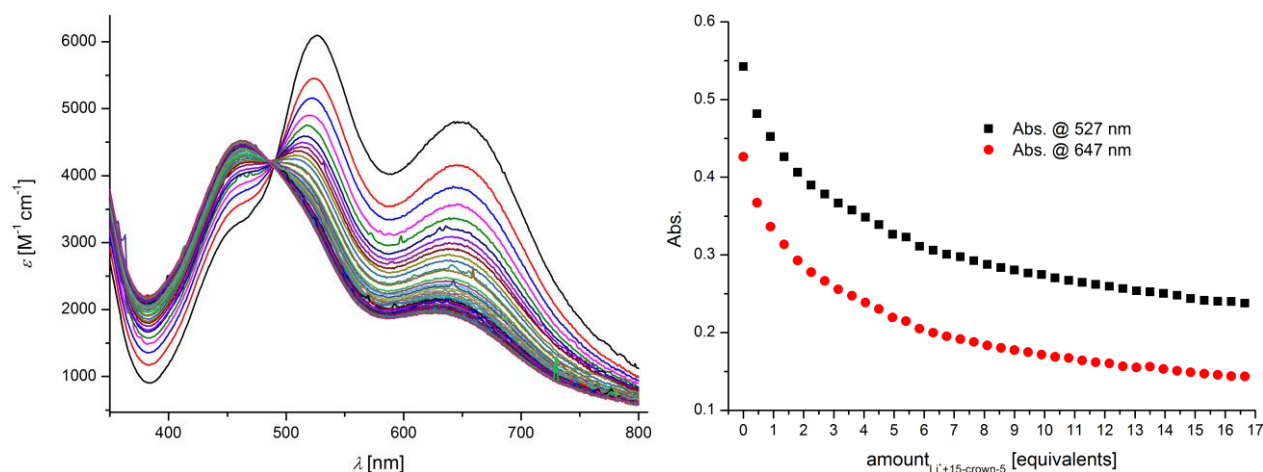
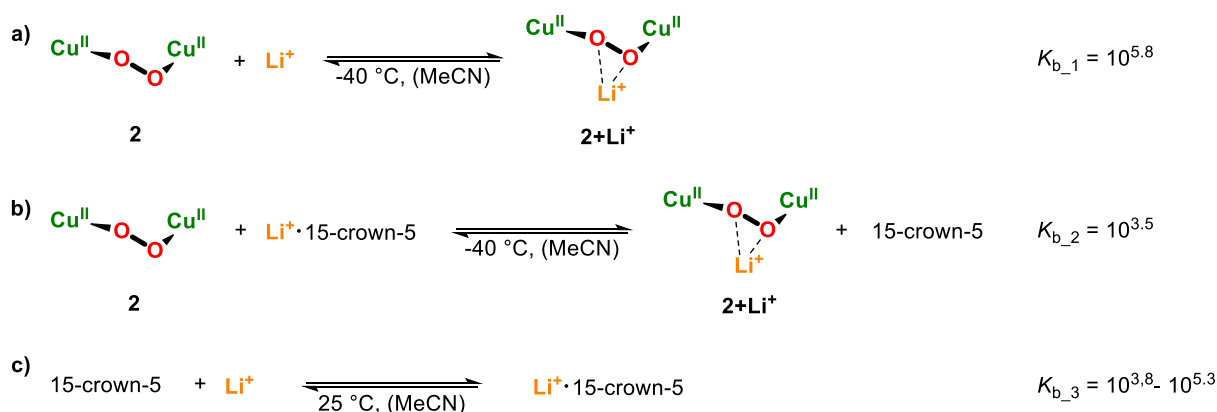


**Figure 28.** Left: Titration of **2** with a solution of  $\text{Li}^+\cdot\text{15-crown-5}$  in steps of 0.45 eq. (MeCN,  $T = -40^\circ\text{C}$ ); the isosbestic point at 489 nm indicates a clean conversion. Right: Changes in Absorbance at two selected wavelength during the titration experiment.



**Scheme 10.** a): formation of  $\mathbf{2+Li}^+$  and experimentally derived association constant  $K_{b_1}$  (denoted as  $K_b$  in Table 3); b): control experiment of titration of **2** with  $\text{Li}^+\cdot\text{15-crown-5}$  and corresponding association constant  $K_{b_2}$ ; c): formation of adduct  $\text{Li}^+\cdot\text{15-crown-5}$  and corresponding association constant  $K_{b_3}$ .

Complex **2** was indeed found to abstract the  $\text{Li}^+$  cation from the corresponding 15-crown-5 adduct and an association constant of  $K_{b_2} = 10^{3.5}$  ( $\pm 10\%$ ) has been determined with the THORDARSON software package.<sup>128</sup> This experiment qualitatively confirms the magnitude of the derived association constant for  $\mathbf{2+Li}^+$ , since complex **2** binds the  $\text{Li}^+$  cation with a higher affinity than 15-crown-5 and thus  $K_{b_1} > K_{b_3}$ . However, the alkali metal ions not only form the corresponding host-guest complexes in different strength, but also affect the electronic structure of the peroxo dicopper core. This outcome will be discussed in detail in Sections 6.2.3 and 6.2.7, while this chapter will primarily focus on a qualitative description of this phenomenon. Within stepwise addition of substoichiometric amounts of the different alkali metal ions to the peroxo unit, the two maxima of **2** (referred to as  $\lambda_{\text{max}_1}$  and  $\lambda_{\text{max}_2}$ ; see Table 4 for details) undergo a significant blue-shift (see Figure 29).

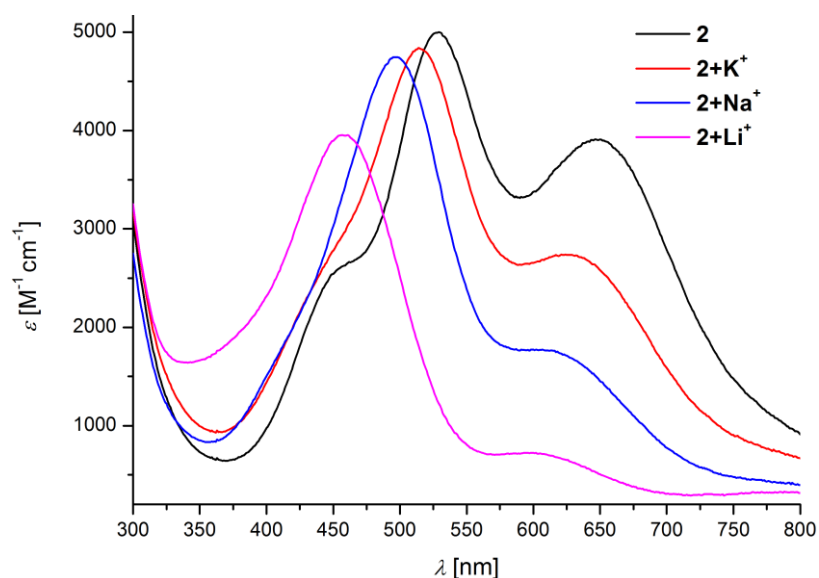


**Figure 29.** UV/vis absorption spectra of complex **2** and of corresponding alkali metal adducts **2+M<sup>+</sup>**. All complexes have been prepared from the same stock solution of precursor **1**, to enable comparable conditions (MeCN,  $T = -40$  °C).

The absolute blue-shift of both maxima increases from **2+K<sup>+</sup>** over **2+Na<sup>+</sup>** to **2+Li<sup>+</sup>** (see Table 4), which goes along with a decrease of their intensities (see Table 4). Interestingly, the intensity of the absorption maximum  $\lambda_{\max_2}$  of **2** is much more affected during the host-guest complex formation, but this outcome will be discussed in Section 6.2.5.

**Table 4.** Summary of characteristic data of complex **2** and its alkali metal ion adducts **2+M<sup>+</sup>**, obtained from the titration experiments.

complex	$\lambda_{\max_{1,2}}$ [nm]	$\Delta\varepsilon$ (@ $\lambda_{\max_{1,2}}$ ) [%]	$K_b$
<b>2</b>	527, 649	-	-
<b>2+K<sup>+</sup></b>	515, 624	-3, -30	$64 \pm 5.6\%$
<b>2+Na<sup>+</sup></b>	497, 612	-5, -56	$70 \times 10^1 \pm 6.2\%$
<b>2+Li<sup>+</sup></b>	456, 595	-21, -81	$69 \times 10^4 \pm 23\%$



## 6.2.2 Solution State Resonance Raman Spectroscopy

The in Section 6.2.1 described UV/vis spectra of the different  ${}^{\text{C}}\text{P}$  species show two main maxima in absorbance, denoted as  $\lambda_{\text{max}_1}$  and  $\lambda_{\text{max}_2}$ . If the solution state sample of e.g.  $\mathbf{2}+\text{Li}^+$  is irradiated by a He:Ne-laser ( $\lambda_{\text{exc}} = 633 \text{ nm}$ ,  $\lambda_{\text{max}_2}(\mathbf{2}+\text{Li}^+) = 595 \text{ nm}$ ), an oxygen isotope sensitive feature corresponding to the O-O stretching vibration of the peroxide is observed (see Figure 30). A summary of the rR data regarding the O-O stretching vibration of  $\mathbf{2}$  and of its corresponding alkali metal adducts  $\mathbf{2}+\text{M}^+$  is listed in Table 5. Of all species both solid and solution state rR spectra have been recorded, whereat the solid state rR spectra will be discussed in detail in Section 6.2.5. The solution state spectra of  $\mathbf{2}$ ,  $\mathbf{2}+\text{Na}^+$  and  $\mathbf{2}+\text{K}^+$  have been already collected in previous work.<sup>10,32</sup> The corresponding rR spectrum of  $\mathbf{2}+\text{Li}^+$  looks similar to those of the other alkali metal adducts and is depicted in Figure 30. Except for  $\mathbf{2}+\text{Li}^+$ , an accurate determination of the O-O stretching frequencies is hampered due to Fermi resonance (see Section 6.1.3 for detailed description) and thus the average frequency of the Fermi doublet is shown in Table 5. Interestingly, excitation with a diode-laser ( $\lambda_{\text{exc}} = 457 \text{ nm}$ ), did not result in any resonance enhancement for any of the three adducts. Even for  $\mathbf{2}+\text{Li}^+$  which is featuring an intense absorption maximum at 456 nm, no oxygen isotope sensitive vibration is observed (this outcome will be discussed in Section 6.2.5).

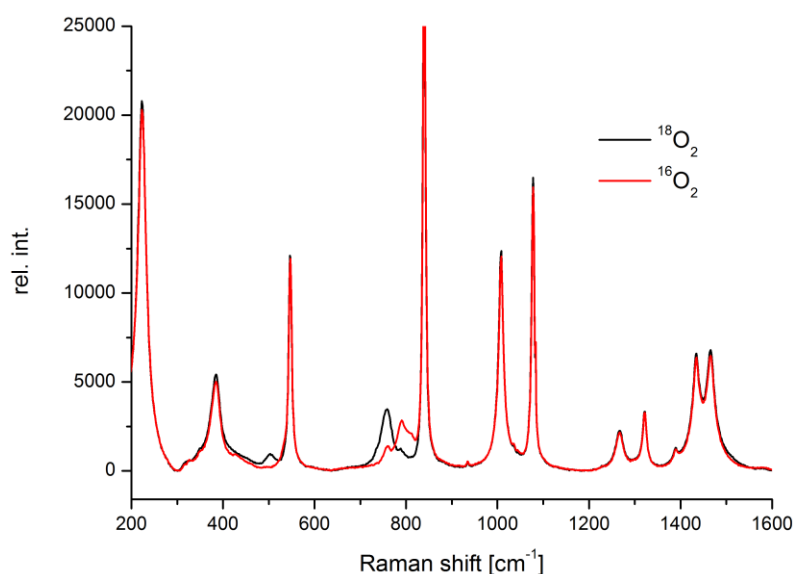


**Figure 30.** Solution state resonance Raman spectrum of  $\mathbf{2}+\text{Li}^+$  in EtCN at  $-30 \text{ }^\circ\text{C}$  ( $c = 1 \times 10^{-2} \text{ M}$ ,  $\lambda_{\text{exc}} = 633 \text{ nm}$ ).

If the solution state rR spectra of all  ${}^{\text{C}}\text{P}$  complexes are compared, several trends can be observed which will be discussed in the following. The O-O stretching vibration of  $\mathbf{2}$  has been detected at  $797 \text{ cm}^{-1}$  (see Section 6.1.1 for details), and is shifting towards lower energies in the series of alkali metal adducts from  $\mathbf{2}+\text{K}^+$  to  $\mathbf{2}+\text{Li}^+$ , albeit marginally. The absolute shifts for  $\mathbf{2}+\text{K}^+$  and for  $\mathbf{2}+\text{Na}^+$  are almost identical ( $\Delta\tilde{\nu}_{\text{O-O}}(\mathbf{2} - \mathbf{2}+\text{M}^+) = 1 \text{ cm}^{-1}$  ( $\text{M} = \text{K}$ ),  $2 \text{ cm}^{-1}$  ( $\text{M} = \text{Na}$ )). The absolute shift of the O-O stretch in the rR spectrum of  $\mathbf{2}+\text{Li}^+$  is only slightly different ( $\Delta\tilde{\nu}_{\text{O-O}}(\mathbf{2} - \mathbf{2}+\text{Li}^+) = 6 \text{ cm}^{-1}$ ).

**Table 5.** Comparison of O-O stretching frequencies of the  ${}^{\text{C}}\text{P}$  complexes, observed during the solution state rR experiments ( $\lambda_{\text{exc}}=633$  nm,  $T = -30$  °C,  $c = 1 \times 10^{-2}$  M, EtCN).

complex	$\tilde{\nu}_{\text{O-O}}$ [ $\text{cm}^{-1}$ ]
<b>2</b>	797* ( $\Delta^{16}\text{O}_2\text{-}^{18}\text{O}_2 = 39$ )
<b>2+K<sup>+</sup></b>	796* ( $\Delta^{16}\text{O}_2\text{-}^{18}\text{O}_2 = 40$ )
<b>2+Na<sup>+</sup></b>	795* ( $\Delta^{16}\text{O}_2\text{-}^{18}\text{O}_2 = 41$ )
<b>2+Li<sup>+</sup></b>	791 ( $\Delta^{16}\text{O}_2\text{-}^{18}\text{O}_2 = 35$ )

\*exact determination of the O-O stretching frequency is complicated due to Fermi resonance.

However, the exact shifts in **2+K<sup>+</sup>** and in **2+Na<sup>+</sup>** are hard to determine in comparison to compound **2** due to the Fermi resonance phenomenon, which does not occur in **2+Li<sup>+</sup>** (this trend becomes even more apparent in the solid state spectra, see Section 6.2.5). The absence of a Fermi doublet in **2+Li<sup>+</sup>** may be explained with a lower energy of the O-O stretch compared to the other  ${}^{\text{C}}\text{P}$  species, since the Fermi resonance phenomenon describes the mixing of two vibrational state wave functions of *i.a.* similar energy.<sup>108,107</sup> With respect to the other  ${}^{\text{C}}\text{P}$  complexes the wave function expressing the O-O stretch and the wave function of another, but unknown stretching mode, are mixing. This condition may not be fulfilled in **2+Li<sup>+</sup>** anymore since the O-O stretch is shifted to lower wavenumbers, while the energy of the other vibrational mode is retained (for more details concerning Fermi resonance see Section 6.1.3).<sup>108,107</sup> Interestingly, the only minor differences in O-O stretching frequencies between **2** and its alkali metal adducts do not reflect the drastic changes of the UV/vis absorption spectrum of **2**, observed during alkali metal adduct formation. Figure 31 shows an overview of all solution state rR spectra, which have been recorded in EtCN at identical complex concentrations.<sup>32</sup> Parts of the in Figure 31 shown results have already been collected prior to this work.<sup>32</sup> Each spectrum has been referenced relative to the solvent signals of EtCN and thus the intensity of e.g. the O-O stretch of complex **2** can be directly contrasted with those of the alkali metal adducts. All oxygen isotope sensitive features are marked with an asterisk. If the O-O stretching vibrations at ca 800  $\text{cm}^{-1}$  are compared, a drastic loss of intensity is observed from **2** over **2+K<sup>+</sup>** to finally **2+Li<sup>+</sup>**. This sequence is further underlined by the overtone of the O-O stretch at ca. 1600  $\text{cm}^{-1}$ , which is quite intense for **2**, but could not be detected for **2+Li<sup>+</sup>**. With respect to the mechanism of resonance enhancement (see Section 4.2.2 for details), this observation can be qualitatively interpreted. The absorption maximum  $\lambda_{\text{max}_2}$  of **2** at ca. 650 nm corresponds to the  $\text{O}_2^{2-} \pi_{\text{v}}^* \rightarrow \text{Cu}^{\text{II}}$  charge transfer transition (see Sections 6.1.1 and 6.1.7 for details). If now a significant distortion of the O-O bond is involved with this electronic transition, the sample can be irradiated with a laser of adequate wavelength ( $\lambda_{\text{exc}} = 633$  nm) and the O-O stretch can be selectively enhanced within the rR experiment.<sup>96,98</sup>

The solution state rR spectrum of complex **2** shows an intense oxygen isotope sensitive feature (see Figure 31) corresponding to the O-O stretch, which is at typical energy for a peroxo motif.<sup>44</sup> The intensity of the O-O stretch is high compared to the other observed stretching modes. According to the mechanism of resonance enhancement, the absorption maximum  $\lambda_{\text{max}_2}$  is therefore coupled to significant distortion of the O-O bond. When comparing **2** with its alkali metal adducts **2+M<sup>+</sup>**, the absorption maximum of **2** at ca. 650 nm is blue-shifted (e.g. 624 nm for **2+K<sup>+</sup>**) and is simultaneously drastically losing intensity (see Section 6.2.1, Table 4). DFT calculations for the alkali metal adducts **2+M<sup>+</sup>** thereby revealed these bands to also correspond to a  $\text{O}_2^{2-} \pi_v^* \rightarrow \text{Cu}^{\text{II}}$  CT transitions (see Section 6.2.7). However, the laser excitation wavelength is retained at  $\lambda_{\text{exc}} = 633$  nm in all experiments. Since the resonance enhancement of the O-O stretch is coupled to the intensity of the  $\text{O}_2^{2-} \pi_v^* \rightarrow \text{Cu}^{\text{II}}$  CT transition (see Section 4.2 for details), the trend observed in the different UV/vis absorption spectra is also reproduced in the rR experiments.<sup>96</sup> This tendency is furthermore valid for the corresponding overtone, which is not detected for **2+Li<sup>+</sup>**.

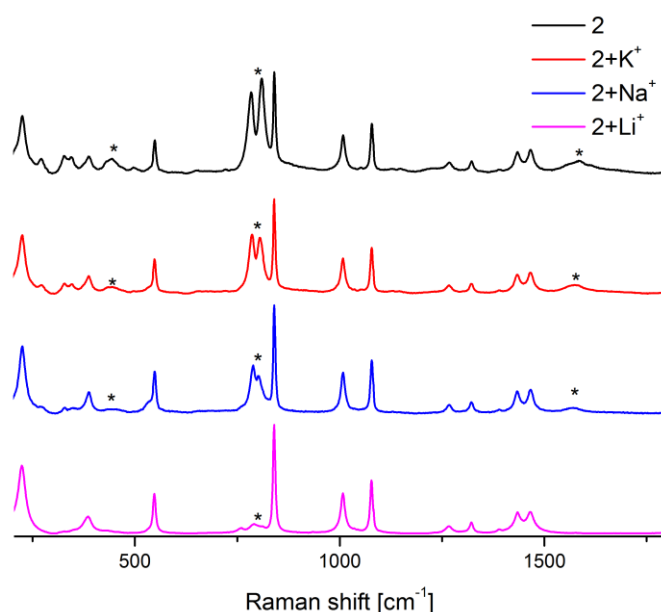


**Figure 31.** Resonance Raman spectra of **2+M<sup>+</sup>** in EtCN at -30 °C ( $c = 1 \times 10^{-2}$  M,  $\lambda_{\text{exc}} = 633$  nm). <sup>18</sup>O sensitive signals are labeled (\*); the spectra have been scaled relative to the solvent signal at 840  $\text{cm}^{-1}$ .<sup>32</sup>

Next to the O-O stretch and its corresponding overtone, a third oxygen isotope sensitive feature at ca. 450  $\text{cm}^{-1}$  is observed for all **C<sup>o</sup>P** complexes. The relatively weak signal corresponds to a Cu-O stretch, which is also coupled to the excited state distortion of the O-O bond.<sup>96</sup> However, an accurate determination of the Cu-O stretching frequencies is complicated due to a broad line shape and a low intensity. A more detailed discussion of Cu-O stretches is provided in Section 6.2.7. Besides these oxygen isotope sensitive stretches, other features at ca. 270, ca. 330 and at ca 350  $\text{cm}^{-1}$  can be found, which also lose intensity in the above-mentioned order. These signals presumably correspond to Cu-N stretches of the central pyrazole unit and of the TACN side arms (see Section 6.2.7 for details).<sup>50,109</sup>

### 6.2.3 Solid State Structures

The molecular structures of the alkali metal adducts  $\mathbf{2}+\mathbf{M}^+$  consistently feature a  ${}^{\text{C}}\mathbf{P}$  motif, with slight variations in O-O bond length, Cu-O-O-Cu torsion angle  $\phi$  and coordination environment of the  $\text{Cu}^{\text{II}}$  ions (see Table 6). In this chapter, the structural differences of all three adducts will be discussed and further compared to the parameters obtained from the molecular structure of complex  $\mathbf{2}$ . This chapter will additionally provide a qualitative basis for the computational investigation of the influence of the alkali metal ions on the electronic structure of the copper oxygen core, discussed in Section 6.2.7.

The complexes  $\mathbf{2}+\mathbf{K}^+$  and  $\mathbf{2}+\mathbf{Li}^+$  have been crystallized under quite similar conditions from acetone and  $\text{Et}_2\text{O}$  at  $-26\text{ }^\circ\text{C}$  (see Sections 7.13.3 and 7.13.4). The molecular structures of  $\mathbf{2}+\mathbf{K}^+$  and of  $\mathbf{2}+\mathbf{Na}^+$  have already been reported previously.<sup>31,32</sup> However, most of the spectroscopic data of  $\mathbf{2}+\mathbf{K}^+$  have not been collected during the pioneering work due to low yields and impurities of the isolated crystalline material.<sup>32</sup> Since in this work single crystalline material of precursor  $\mathbf{1}$  was available,  $\mathbf{2}+\mathbf{K}^+$  has been selectively generated in high yields and high purity (see Section 7.13.4 for details). Although more than 50 equivalents of KOTf are necessary to almost quantitatively generate  $\mathbf{2}+\mathbf{K}^+$  from its precursor  $\mathbf{2}$  in solution (see Section 6.2.1), only 1.5 equivalents of KOTf are required to crystallize  $\mathbf{2}+\mathbf{K}^+$  in 90% yield from acetone/ $\text{Et}_2\text{O}$ . A solid state structure of  $\mathbf{2}+\mathbf{K}^+$  has been determined and matches with the previously reported one.<sup>32</sup>

Figure 32 shows the molecular structure of  $\mathbf{2}+\mathbf{Li}^+$  which is a centrosymmetric dimer of two  ${}^{\text{C}}\mathbf{P}$  units. Each  $\text{Cu}_2/\text{O}_2$  site binds a  $\text{Li}^+$  which is bridged to the neighboring  $\text{Li}^+$  *via* two triflate ions. This packing is similarly observed in the other adducts  $\mathbf{2}+\mathbf{K}^+$  and  $\mathbf{2}+\mathbf{Na}^+$ .<sup>32,31</sup>

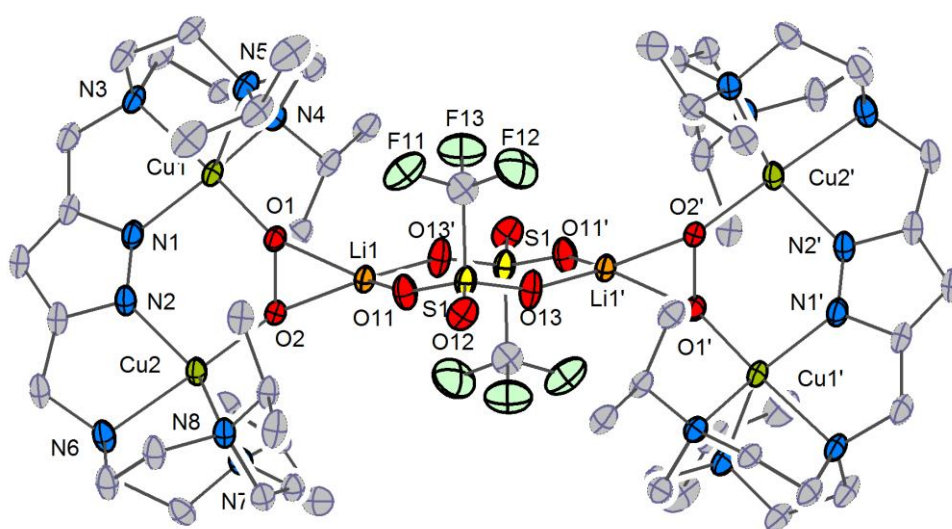


**Figure 32.** Molecular structure of  $\mathbf{2}+\mathbf{Li}^+$  with thermal displacement ellipsoids given at 30% probability. Hydrogen atoms, counterion  $\text{BPh}_4^-$ , and additional solvent molecules are omitted for clarity; for selected bond lengths and angles see Section 7.7.

The coordination sphere of each Cu<sup>II</sup> ion lies between an ideal square pyramidal and trigonal bipyramidal geometry ( $\tau(\text{Cu1}) = 0.57$ ;  $\tau(\text{Cu2}) = 0.54$ ) and is provided by four nitrogen donor atoms of a TACN side arm and the pyrazolate unit, and by one oxygen atom of the peroxo ligand. The Cu-pyrazolate bond lengths are substantially shorter (Cu1-N1 = 1.92 Å, Cu2-N2 = 1.93 Å) than those of the TACN side arm nitrogen donor atoms (2.12-2.21 Å). The Cu...Cu bond distance is 3.86 Å and is similar to those in the other alkali metal adducts (see Table 6). The O-O bond length in **2**+Li<sup>+</sup> was determined to 1.497 Å and is quite long compared to other literature known peroxide O-O bond distances.<sup>44</sup> Furthermore, the lithium cation is located in close proximity to the peroxide (Li1-O1 = 1.87 Å, Li1-O2 = 1.89 Å). The Li-O distances in **2**+Li<sup>+</sup> are much shorter than those in Li<sub>2</sub>O<sub>2</sub> (1.94-2.14 Å),<sup>135,136</sup> emphasizing the interaction of lithium cation and peroxo moiety in the solid state. The same trend was also observed in the molecular structures of the alkali metal adducts **2**+K<sup>+</sup> and **2**+Na<sup>+</sup>.<sup>32</sup> Whereat the alkali metal ions in **2**+K<sup>+</sup> and **2**+Na<sup>+</sup> are five coordinated by oxygen donor atoms of the triflate ions, the peroxo ligand and one additional acetone molecule, the Li<sup>+</sup> cation in **2**+Li<sup>+</sup> is only fourfold coordinated. This effect is due to the much larger ionic radii of Na<sup>+</sup> and of K<sup>+</sup>, enabling the coordination of a fifth oxygen donor ligand.<sup>137</sup> However, the different coordination numbers of the alkali metal ions have an effect on the crystal packing and thus may influence the structural parameters discussed in this section such as the Cu-O-O-Cu dihedral angle.

**Table 6.** Selected parameters of **2** and of alkali metal adducts **2**+M<sup>+</sup> obtained from the molecular structures.<sup>31</sup>

	$d \text{ O-O}$ [Å]	$d \text{ O-M}$ [Å] <sup>a</sup>	$\phi \text{ Cu-O-O-Cu}$ [°]	$d \text{ Cu-Cu}$ [Å]	$\tau(\text{Cu1}), \tau(\text{Cu2})$
<b>2</b>	1.441(2)	-	55.3(2)	3.7413(5)	0.63, 0.60
<b>2</b> +K <sup>+</sup>	1.483(4)	2.63(3)	66.8(2)	3.7894(7)	0.57, 0.54
<b>2</b> +Na <sup>+</sup>	1.498(7)	2.30(7)	65.2(5)	3.7966(12)	0.59, 0.57
<b>2</b> +Li <sup>+</sup>	1.497(3)	1.88(5)	71.1(2)	3.8562(9)	0.57, 0.54

<sup>a</sup>The average of both M-O distances is shown.

With the molecular parameters determined via X-ray crystallography of all alkali metal adducts in hand, the influence of the different redox inert cations on the structural parameters of the Cu<sub>2</sub>/O<sub>2</sub> core will be quantified in comparison to complex **2**. Furthermore, an introduction into a qualitative discussion with respect to the changes in O-O bond lengths and Cu-O-O-Cu dihedral angles  $\phi$  and the potential effects of the alkali metal ions on the electronic structure of the copper oxygen core will be provided. The interplay of Cu-O-O-Cu torsion angle and electronic structure of the copper oxygen unit will be in detail discussed in Sections 6.2.6 and 6.2.7.

The alkali metal ions are assumed to strongly interact with the peroxo moiety as indicated by the aforementioned short M-O distances (see Table 6). This kind of interaction will result in a withdrawal of

electron density from the oxygen centered  $\pi^*$  orbitals in stabilizing the O-O bond.<sup>138</sup> However, not only the alkali metal ions are affecting the electronic structure of the peroxide since this ligand is simultaneously interacting with the two  $\text{Cu}^{\text{II}}$  ions, which in turn also has an impact on the electronic structure of the peroxo moiety.<sup>50</sup> First evidence with respect to the electronic structure of the peroxide is provided by the O-O distances. The O-O bond lengths increase from 1.44 Å in **2** to 1.50 Å in **2+Li<sup>+</sup>**, but do not significantly differ between the alkali metal adducts (see Table 6). These results already suggest the actual mechanism behind this interaction to be quite complex since an exclusive interplay of peroxide and alkali metal ions would stabilize and thus shorten the O-O bond. However, besides the O-O bond distance also the Cu-O-O-Cu torsion angle as well as the coordination environment of the  $\text{Cu}^{\text{II}}$  ions is affected upon alkali metal binding. Generally, the dihedral angle increases from 55° in **2** to 71° in **2+Li<sup>+</sup>** (see Figure 33). With respect to MO theory the influence of the Cu-O-O-Cu torsion angle on the magnitude of interaction of copper- and oxygen-centered orbitals can be qualitatively explained. The Cu-O-O-Cu torsion angle in **2** is thereby induced by the specific ligand design applied (see Section 5) and increases in the presence of an alkali metal ion. However, the interplay of redox inert metal ion and peroxo moiety, in affecting the value of the Cu-O-O-Cu dihedral angle, is still unclear and could also not be explained even with the support of DFT calculations (see Section 6.2.7).

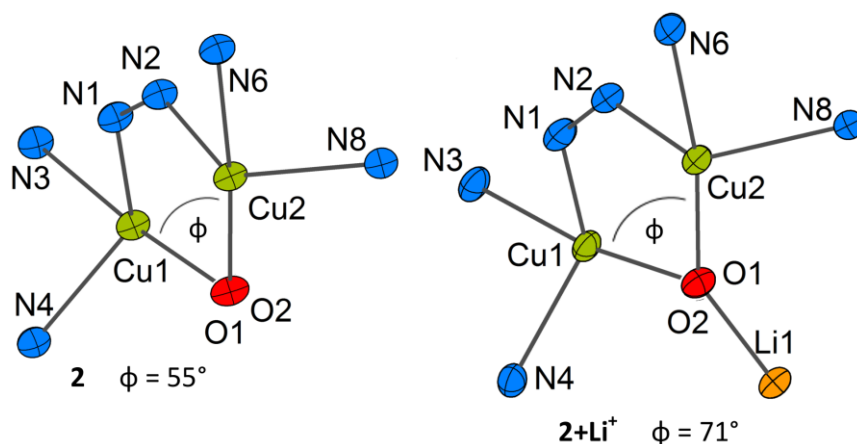


**Figure 33.** Copper oxygen cores of **2** and of **2+Li<sup>+</sup>**; the different Cu-O-O-Cu dihedral angles become apparent by looking down the O-O bond; the nitrogen donor atoms N5 and N7 are omitted for clarity in both structures.

Irrespective of the different torsion angles, all complexes are featuring a  $^6\text{P}$  binding mode. A significant torsion of the  $\text{Cu}_2/\text{O}_2$  plane is as well observed for complex **3**, featuring a Cu-O-O-Cu dihedral angle of 104° (see Sections 5 and 6.1.5).<sup>34</sup> Such a torsion of the copper oxygen core does not occur at the structurally related  $^1\text{P}$  systems, all showing a planar arrangement (*i.e.*  $\phi$  (Cu-O-O-Cu) = 180°).<sup>34,139,140</sup> Since the overlap of copper- and oxygen-centered orbitals strongly depends on the Cu-O-O-Cu dihedral angle, the extent of interaction between the  $\text{Cu}^{\text{II}}$  ions and the peroxide varies in **2** and its related adducts **2+M<sup>+</sup>**, as well as in **2** and the structurally related complex **3**.<sup>31,111</sup> The overlap of copper- and oxygen-centered orbitals in these complexes on the other hand must significantly deviate from that in

the planar  $\text{T}\mathbf{P}$  systems. For reasons of clarity this discussion will primarily focus on the contrasting juxtaposition of complex **2** and selected  $\text{T}\mathbf{P}$  species and will be finally transferred on the alkali metal adducts  $\mathbf{2}+\mathbf{M}^+$ .

Although this discussion is rather qualitative, several spectroscopic differences in  $\text{T}\mathbf{P}$ ,  $\text{C}\mathbf{P}$  and  $\text{O}\mathbf{P}$  complexes can be determined, which are a function of the aforementioned orbital overlap. Indeed also the ligand design has an effect on the spectroscopic characteristics of the copper oxygen core.<sup>44</sup> The described  $\text{C}\mathbf{P}$  and  $\text{T}\mathbf{P}$  systems are all based on nitrogen donor ligands (see Table 7).<sup>141,142,82,140,50</sup> Although neutral as well as anionic ligands are applied, the effect of the ligand design on the electronic structure of the copper oxygen core will be neglected in the following section.

**Table 7.** Selected structural and spectroscopic parameters of  $\text{T}\mathbf{P}$ ,  $\text{C}\mathbf{P}$  and  $\text{O}\mathbf{P}$  complexes.

Ligand <sup>a</sup>	mode	$d$ O-O [Å]	$\phi$ Cu-O-O-Cu [°]	$\lambda_{\text{max}}$ [nm]	$\epsilon$ [mM <sup>-1</sup> cm <sup>-1</sup> ]	ref.
L <sup>1</sup>	$\text{C}\mathbf{P}$	1.44	55	527, 648	5.0, 3.9	this work
L <sup>2</sup>	$\text{O}\mathbf{P}$	1.46	104	506, 600	4.8, 2.8	34
Bz <sub>3</sub> tren	$\text{T}\mathbf{P}$	1.45	180	518	14.9	141,142
Me <sub>6</sub> tren	$\text{T}\mathbf{P}$	1.37	180	552, 600	13.5, 9	82,140
TMPA	$\text{T}\mathbf{P}$	1.43	180	524, 615	11.3, 5.8	50

<sup>a</sup>Bz<sub>3</sub>tren = tris[2-(benzylamino)ethyl]amine, Me<sub>6</sub>tren = tris(2-dimethylaminoethyl)amine, TMPA = tris(2-methylpyridyl)amine.

The UV/vis absorption spectra of  $\text{T}\mathbf{P}$ ,  $\text{C}\mathbf{P}$  and  $\text{O}\mathbf{P}$  species look quite similar, featuring two main CT transitions.<sup>34,44</sup> These CT transitions can be identified as  $\text{O}_2^{2-} \pi_{\sigma}^* \rightarrow \text{Cu}^{\text{II}}$  and  $\text{O}_2^{2-} \pi_{\nu}^* \rightarrow \text{Cu}^{\text{II}}$  transitions (see Sections 3 and 6.2.7 for details). However, the absorption maxima of the  $\text{T}\mathbf{P}$  species are twice as intense than the corresponding maxima of the two literature known complexes **2** and **3** (see Table 7).<sup>34,44</sup> Consequently, the principal fashion of orbital interaction in e.g.  $\text{C}\mathbf{P}$  and  $\text{T}\mathbf{P}$  motifs is identical but the magnitude of overlap of copper- and oxygen-centered orbitals must be different. This assumption is further supported by DFT calculations and will be discussed in Section 6.2.7. Since the  $\text{C}\mathbf{P}$  and  $\text{O}\mathbf{P}$  compounds show a significant Cu-O-O-Cu torsion angle which is not the case for the  $\text{T}\mathbf{P}$  species, this aforementioned deviation is assumed to be the source of the different intensities in absorption. Due to a planar arrangement of the copper oxygen core in  $\text{T}\mathbf{P}$  complexes, the overlap of copper- and oxygen-centered orbitals is larger. The good overlap of copper- and oxygen-centered orbitals is reflected by the intense UV/vis absorption spectra, since the intensity of an electronic transition is, among other things, a function of overlap of electronic ground and excited state wave function (see Section 4.1).<sup>91,95</sup> The  $\text{C}\mathbf{P}$  and  $\text{O}\mathbf{P}$  complexes show similar interactions of copper- and oxygen-centered orbitals but are featuring a significant torsion angle along the Cu-O-O-Cu axis. This unusual arrangement diminishes the overlap of copper- and oxygen-centered orbitals and consequently the

absorption maxima are less intense compared to those of the  ${}^1\text{P}$  species (see Table 7). This trend is further observed in comparing **2** and its alkali metal adducts. The Cu–O–O–Cu dihedral angle is increasing from  $55^\circ$  in **2** to over  $71^\circ$  in **2+Li<sup>+</sup>** and the intensities of the corresponding CT transitions are decreasing in the same sequence. However, DFT calculations indicate the orbital interactions in the alkali metal adducts to slightly deviate from those in complex **2** and thus this comparison is rather qualitative (see Section 6.2.7). The absorption maxima of complex **2** are further shifting upon adduct formation, but also this outcome will be discussed in Section 6.2.7. The Cu–O–O–Cu dihedral angle is furthermore affecting the magnitude of magnetic exchange coupling of the two Cu<sup>II</sup> ions, which is discussed in Sections 6.1.3 and 6.2.6.

In comparing the molecular structures of complex **2** and its alkali metal adducts **2+M<sup>+</sup>** not only the Cu–O–O–Cu torsion angles but also the coordination environments of the Cu<sup>II</sup> ions are different. Whereat the  $\tau$  factors of the Cu<sup>II</sup> ions in the alkali metal adducts lie in the range of 0.54–0.59, the coordination environment of the Cu<sup>II</sup> ions in **2** is even more distorted towards a trigonal bipyramidal geometry ( $\tau(\text{Cu1}, \text{Cu2}) = 0.63, 0.60$ ). The distortion of the copper(II) coordination geometry from square pyramidal towards trigonal bipyramidal results in mixing of other d orbital character into the copper SOMOs.<sup>32,112,111</sup> The different orbital contributions change the overlap of magnetic copper atomic orbitals and the peroxide- and pyrazolate-centered orbitals, affecting the intensity of magnetic exchange coupling between both copper(II) units (see Section 6.2.6 for a detailed discussion).<sup>111</sup> If the overlap of copper- and oxygen-centered orbitals is generally diminished in going from a square pyramidal to a trigonal bipyramidal geometry, this interplay as well affects the intensities of the aforementioned CT transitions. However, this discussion is rather qualitative and will be continued in Section 6.2.7.

This discussion demonstrates the actual mechanism of action of the alkali metal ions and the peroxo moiety in affecting the electronic structure within the copper oxygen core to be quite complex. On the one hand the redox inert metal ions interact with the peroxide in stabilizing the O–O bond. On the other hand the peroxide is simultaneously interacting with the Cu<sup>II</sup> ions, which also has an influence on the electronic structure of the peroxide. Additionally, the molecular parameters such as Cu–O–O–Cu torsion angle and the coordination environment of the Cu<sup>II</sup> ions are changing upon adduct formation, complicating this discussion even more. A comparison of complex **2** with the structurally related  ${}^1\text{P}$  systems demonstrates the influence of the Cu–O–O–Cu dihedral angle on the intensities of the corresponding CT transitions observed during UV/vis absorption spectroscopy. This trend is furthermore observed in the alkali metal adducts **2+M<sup>+</sup>**.

However, the O–O bond lengths are similar in all three adducts although the electronic absorption spectra are drastically changing in going from **2+K<sup>+</sup>** to **2+Li<sup>+</sup>**. So far the structural parameters of the  ${}^6\text{P}$  sites have been compared with the data obtained from solution state UV/vis spectroscopy, raising the



question to what extent the solid state structures represent the electronic structures of these species in solution. Thus, solid state UV/vis reflectance spectra of single crystalline material of the alkali metal adducts were recorded, which will be discussed in the following section.

## 6.2.4 Solid State UV/vis Spectroscopy

Although the molecular structures of the alkali metal adducts consistently show a  ${}^{\text{C}}\text{P}$  motif, with only slight differences in Cu-O-O-Cu torsion angle, O-O bond length and coordination environment of the Cu(II) ions, the solution state UV/vis absorption spectrum of  $\mathbf{2}+\text{Li}^+$  significantly differs from those of  $\mathbf{2}+\text{K}^+$  and of  $\mathbf{2}+\text{Na}^+$ . Since the molecular structures of these species only reflect their structure in the solid state, a different structural motif in the solution state could be possible, which would explain the very different UV/vis absorption spectrum of  $\mathbf{2}+\text{Li}^+$ . From previous work<sup>31</sup>, the solid state UV/vis spectrum of  $\mathbf{2}+\text{Na}^+$  is known (see Figure 34), which shows the same absorption maxima as the solution state UV/vis absorption spectrum (see Table 8). Consequently, the molecular and electronic structure of  $\mathbf{2}+\text{Na}^+$  is similar in both solid and solution state and the molecular structure determined via X-ray diffraction can be assumed to approximately reflect the structure of this  ${}^{\text{C}}\text{P}$  motif in solution.

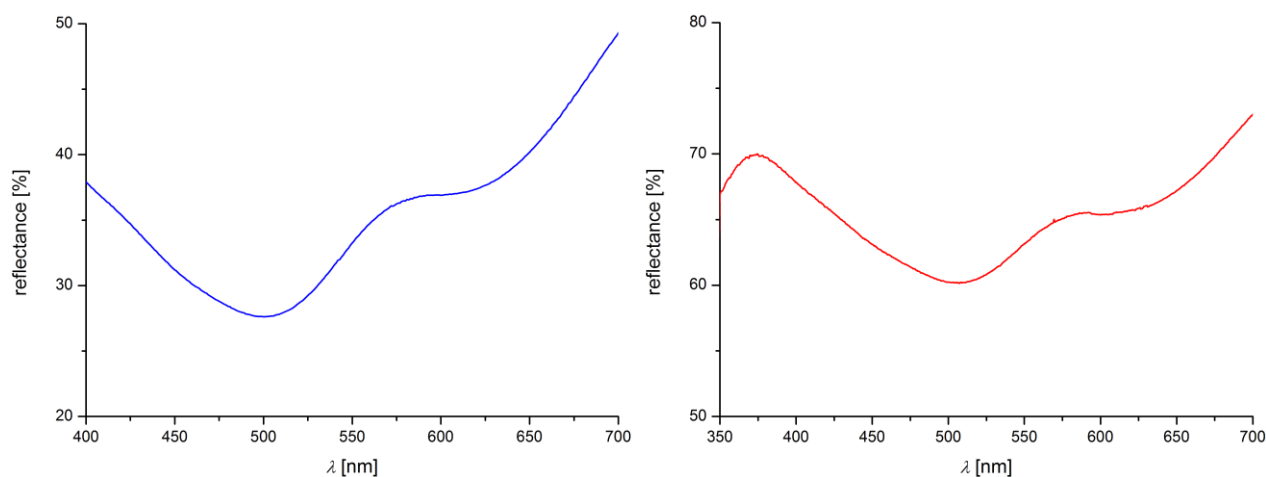


**Figure 34.** Solid state UV/vis spectra of  $\mathbf{2}+\text{Na}^+$  (left) and of  $\mathbf{2}+\text{K}^+$  (right).<sup>31</sup>

In order to shine light on the nature of especially  $\mathbf{2}+\text{Li}^+$ , solid state UV/vis spectra of crystalline material of  $\mathbf{2}+\text{Li}^+$  and of  $\mathbf{2}+\text{K}^+$  have been recorded (see Section 7.2 for details). The spectrum of  $\mathbf{2}+\text{Li}^+$  (see Figure 35) shows two minima in reflectance at ca. 460 nm and at ca. 600 nm, which are similar to the absorption maxima of this species in solution.

**Table 8.** UV/vis absorption maxima of all  ${}^{\text{C}}\text{P}$  complexes determined in solution and solid state. The solid state UV/vis spectra are quite broad, which makes an accurate assignment of the maxima difficult.<sup>31</sup>

complex	Solution: $\lambda_{\text{max}_{1,2}}$ [nm]	Solid: $\lambda_{\text{max}_{1,2}}$ [nm]
<b>2</b>	527, 649	529, 663
<b>2+K<sup>+</sup></b>	515, 624	511, 615
<b>2+Na<sup>+</sup></b>	497, 612	500, 609
<b>2+Li<sup>+</sup></b>	456, 595	463, 604

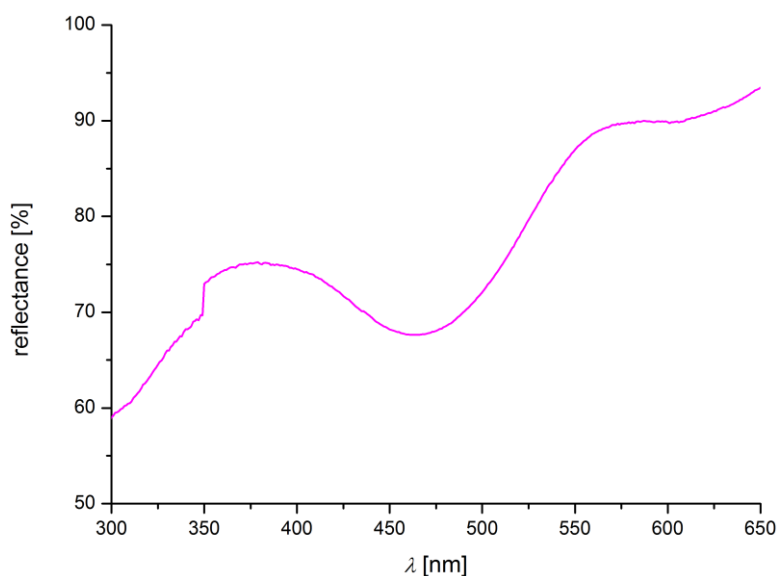


**Figure 35.** Solid state reflectance spectrum of  $2+Li^+$ .

Consequently, the molecular and electronic structure of this species is comparable in both solid and solution state. Also the solid state reflectance UV/vis spectrum of  $2+K^+$  matches with the data derived from the solution state (see Table 8). Since the  $K^+$  ion is observed to only weakly bind to the peroxy moiety in solution (see Section 6.2.1), the solid state UV/vis spectrum allows a conclusion of how the solution state UV/vis spectrum of the completely associated adduct would look like. The differences in both solution and solid state spectra are small and comparable to those of the other  $C_P$  complexes, confirming a nearly complete formation of the alkali metal adduct within the UV/vis titration experiment. However, the reflectance spectra of all  $C_P$  species are quite broad, complicating an accurate assignment of the minima in reflectance.

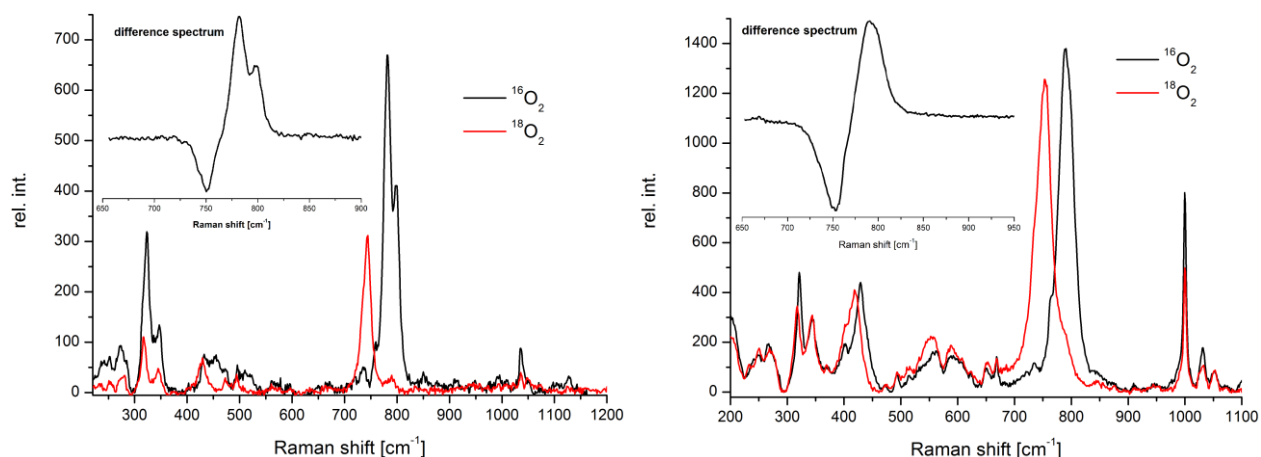
## 6.2.5 Solid State Resonance Raman Spectroscopy

Figure 33 shows the solid state rR spectra of the alkali metal adducts **2+K<sup>+</sup>** and **2+Li<sup>+</sup>** both showing an oxygen isotope sensitive feature at ca. 800 cm<sup>-1</sup>, which corresponds to the O-O stretching vibration of the peroxy moiety (see Table 9). All spectra have been recorded with laser excitation at 633 nm.

**Table 9.** Comparison of O-O stretching frequencies of the <sup>5</sup>P complexes observed during the solid state rR experiments ( $\lambda_{\text{exc}}=633$  nm).

complex	$\tilde{\nu}_{\text{O-O}}$ [cm <sup>-1</sup> ]
<b>2</b>	793 ( $\Delta^{16}\text{O}_2-^{18}\text{O}_2 = 41$ )
<b>2+K<sup>+</sup></b>	790 ( $\Delta^{16}\text{O}_2-^{18}\text{O}_2 = 46$ )
<b>2+Na<sup>+</sup></b>	789 ( $\Delta^{16}\text{O}_2-^{18}\text{O}_2 = 42$ )
<b>2+Li<sup>+</sup></b>	790 ( $\Delta^{16}\text{O}_2-^{18}\text{O}_2 = 36$ )

In general, the solid state rR spectra of the alkali metal adducts are similar to those recorded in solution (see Section 6.2.2), confirming identical molecular and electronic structures of these species in solution and solid state as already discussed in Section 6.2.4. The O-O stretching vibration is shifting slightly to lower wavenumbers with alkali metal ion binding, which matches with an increasing O-O bond length upon adduct formation. The absolute shifts for all three adducts are similar ( $\Delta\tilde{\nu}_{\text{O-O}}(\mathbf{2} - \mathbf{2+M}^+) = 3$  cm<sup>-1</sup> (M = K, Li), 4 cm<sup>-1</sup> (M = Na)), which coincides with nearly identical O-O bond lengths determined from the solid state structures.



**Figure 36.** Solid state rR spectra of **2+K<sup>+</sup>** (left) and of **2+Li<sup>+</sup>** (right),  $\lambda_{\text{exc}} = 633$  nm.

The rR spectra of **2+K<sup>+</sup>** and of **2+Na<sup>+</sup>** (the spectrum of **2+Na<sup>+</sup>** has been recorded in previous work<sup>32</sup>) are rather complex due to Fermi resonance. The spectrum of **2+Li<sup>+</sup>** shows the O-O stretching vibration as a single band at 790 cm<sup>-1</sup>. In contrast to the solution state spectrum where the O-O stretch is only weakly observed, the solid state spectrum of **2+Li<sup>+</sup>** reveals an intensive signal. This effect can be explained with

the use of crystalline material in such as the concentration of  $\mathbf{2+Li^+}$  is much higher during the measurement, compared to the spectrum recorded in solution.

If the corresponding solid or solution state UV/vis spectra of  $\mathbf{2+Li^+}$  are considered, the use of a laser excitation wavelength of 633 nm seems counterintuitive (see Figure 37). With respect to the mechanism of resonance enhancement an excitation with a diode-laser ( $\lambda_{\text{exc}} = 457 \text{ nm}$ ) should be preferred since the corresponding UV/vis spectrum of  $\mathbf{2+Li^+}$  shows an intense maximum in absorbance at 456 nm, whereas an excitation at 633 nm only involves a weak intensity in absorbance. The absorption maximum at 456 nm corresponds to a  $\text{O}_2^{2-} \pi_{\sigma}^* \rightarrow \text{Cu}^{\text{II}}$  CT transition whereas a  $\text{O}_2^{2-} \pi_{\nu}^* \rightarrow \text{Cu}^{\text{II}}$  CT transition is the origin of the band at ca 600 nm (see Section 6.2.7 for details). Consequently both transitions involve charge transfer from the peroxide and should provide suitable conditions for a rR experiment. Nevertheless, the  $\text{O}_2^{2-} \pi_{\sigma}^* \rightarrow \text{Cu}^{\text{II}}$  CT transition occurs with much higher probability and should be the preferred transition for the rR experiment.

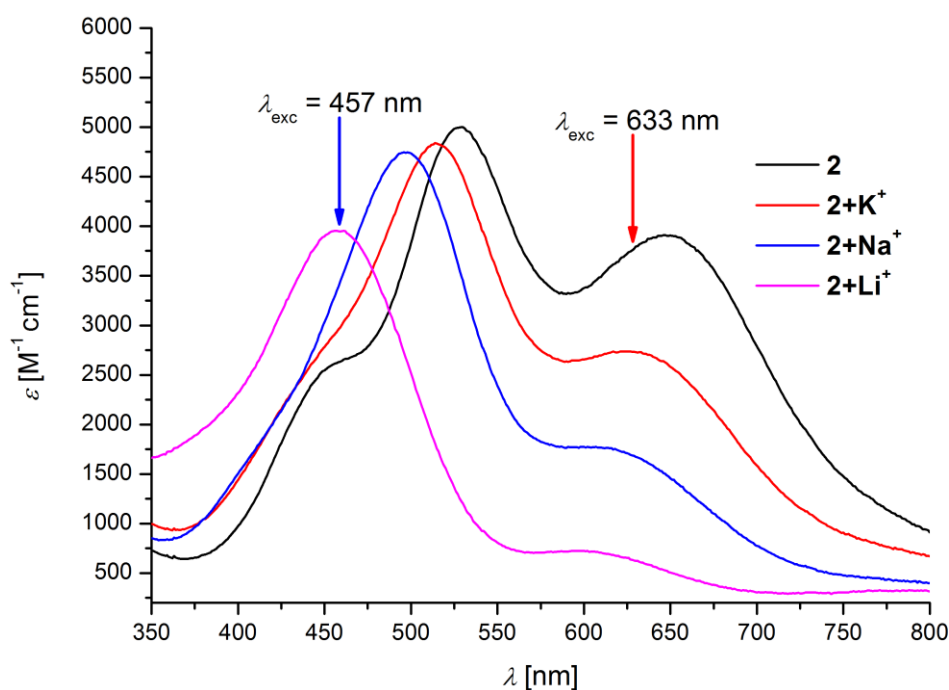


**Figure 37.** Solution state UV/vis absorption spectra of complex **2** and of its corresponding alkali metal adducts,  $\mathbf{2+M^+}$ ; the two different available excitation wavelengths are drawn with blue and red arrows.

However, if solution or solid state samples of  $\mathbf{2+Li^+}$  are irradiated with the diode-laser no oxygen isotope sensitive feature is observed. The same results have furthermore been observed for the other alkali metal adducts as well as for complex **2** which also shows oxygen isotope sensitive features only if the He:Ne-laser ( $\lambda_{\text{exc}} = 633 \text{ nm}$ ) is used for excitation. In order to understand this observation, the mechanism of resonance enhancement will be reconsidered (for further details concerning resonance enhancement see Section 4.2.2). The intensity of the enhanced Raman active O-O stretching mode is proportional to the excited state distortion along the normal mode, as well as to the intensity of the corresponding electronic transition.<sup>50,143,96</sup> The ground state  $\text{O}_2^{2-} \pi_{\sigma}^*$  orbital donates a significant

amount of electron density into the copper-oxygen bond and it consequently has less electron density with antibonding character in the intraperoxide region than the  $O_2^{2-} \pi_v^*$  orbital, which in turn donates significantly less electron density into the Cu-O bond (see Figure 38).<sup>50</sup> Thus, the  $O_2^{2-} \pi_v^* \rightarrow Cu^{II}$  CT transitions results in a greater distortion of the O-O bond and greater resonance enhancement of the O-O stretch relative to the low absorption intensity is observed.<sup>50</sup> This mechanism qualitatively explains why excitation with the He:Ne-laser gives rise the aforementioned rR spectra, while excitation with the diode-laser does not lead to any resonance enhancement of the O-O stretch.

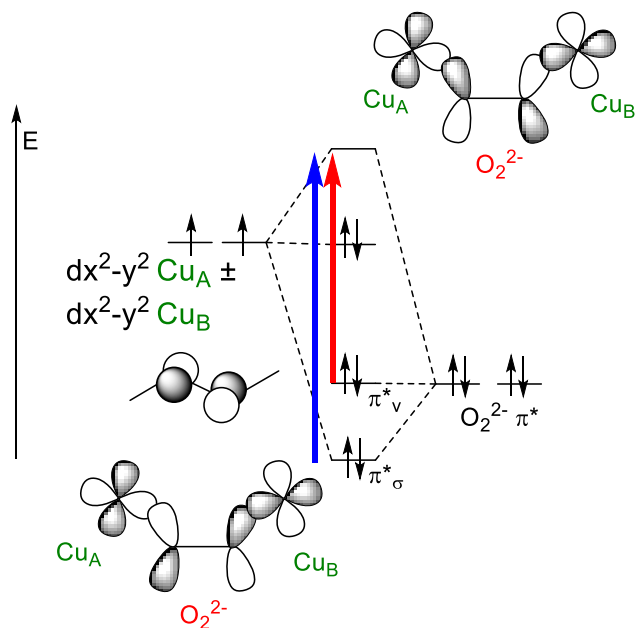


**Figure 38.** Qualitative MO diagram of  $Cu_2O_2$  motif.

## 6.2.6 Magnetism

The magnetic properties of all three alkali metal adducts were intensively studied by SQUID magnetometry, whereat the magnetism of complex **2+Na<sup>+</sup>** has been investigated prior to this work.<sup>31</sup> The samples of **2+K<sup>+</sup>** and of **2+Li<sup>+</sup>** were prepared from freshly isolated single crystalline material, of which the unit cell dimensions have been determined *via* X-ray diffraction before the magnetic measurements. The cell parameters of the crystals were consistently found to coincide with those obtained during prior analysis and thus the magnetic data can be related to the derived structural parameters such as Cu-O-O-Cu torsion angle  $\phi$  and the coordination geometry of the Cu<sup>II</sup> ions. Figure 39 shows the temperature dependence of  $\chi_M T$  of complex **2+K<sup>+</sup>**.

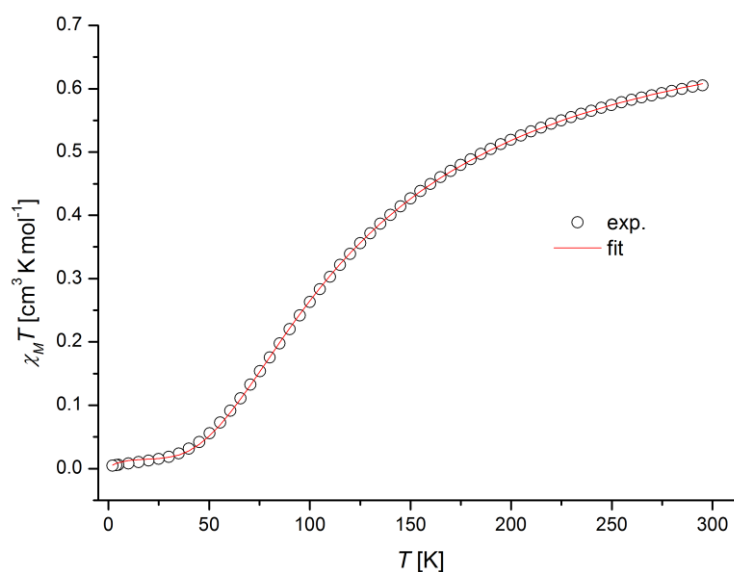


**Figure 39.** Temperature dependence of  $\chi_M T$  of complex **2+K<sup>+</sup>** in the range between 295 K and 2 K. The red line represents the best fit (see Section 7.3 for details). Parameters obtained:  $J = -77.2 \text{ cm}^{-1}$ ,  $g = 2.06$ , PI = 5.0 %, TIP =  $0.7 \times 10^{-4} \text{ cm}^3 \text{ mol}^{-1}$ .

The Cu<sup>II</sup> ions were found to be weakly antiferromagnetically coupled ( $-2J = 154 \text{ cm}^{-1}$ ). If the adducts **2+K<sup>+</sup>** and **2+Na<sup>+</sup>** are compared, both complexes are featuring similar magnetic properties with the Cu<sup>II</sup> ions in **2+K<sup>+</sup>** being slightly more antiferromagnetically coupled (see Table 10).

**Table 10.** Summary of relevant magnetic and structural parameters of complex **2** and of the alkali metal adducts **2+M<sup>+</sup>**.<sup>31</sup>

complex	$J \text{ [cm}^{-1}\text{]}$	$g$	$\phi \text{ Cu-O-O-Cu [}^\circ\text{]}$	$\tau(\text{Cu})$
<b>2</b>	-54	1.81	55.3(2)	0.62
<b>2+K<sup>+</sup></b>	-77	2.06	66.8(2)	0.56
<b>2+Na<sup>+</sup></b>	-72	2.00 (fixed)	65.2(5)	0.58
<b>2+Li<sup>+</sup></b>	-40	2.00	71.1(2)	0.56

The differences in magnetic coupling of both complexes are quite small and lie within the error of the experiment. However, antiferromagnetic coupling in **2+K<sup>+</sup>** should be weaker if one the Cu–O–O–Cu torsion angle, which is assumed to significantly affect the magnitude of magnetic exchange coupling (see Section 6.1.5 for a detailed description).<sup>31,111</sup> The Cu–O–O–Cu dihedral angle in **2+K<sup>+</sup>** is closer to the 90° arrangement (see Table 10), where the superexchange pathway between the two copper atoms is proposed to break down.<sup>110,111</sup> Since the observed dihedral angles only differ by 1.6°, this discussion is of course rather qualitative.

In the case of the adduct **2+Li<sup>+</sup>**, the corresponding Cu–O–O–Cu torsion angle was determined to 71°, which is significantly larger compared to the other alkali metal adducts. The temperature dependence of  $\chi_M T$  of complex **2+Li<sup>+</sup>** is shown in Figure 40.

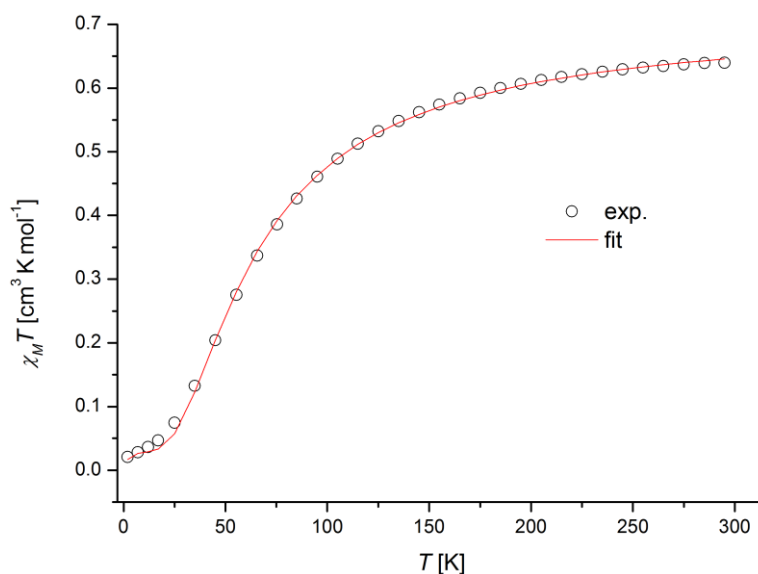


**Figure 40.** Temperature dependence of  $\chi_M T$  of complex **2+Li<sup>+</sup>** in the range between 295 K and 2 K. The red line represents the best fit (see Section 7.3 for details). Parameters obtained:  $J = -40.2 \text{ cm}^{-1}$ ,  $g = 2.00$ ,  $\text{PI} = 9.0 \%$ ,  $\text{TIP} = 3.1 \times 10^{-4} \text{ cm}^3 \text{ mol}^{-1}$ .

The antiferromagnetic coupling of the two Cu<sup>II</sup> ions in **2+Li<sup>+</sup>** is significantly weaker ( $-2J = 80 \text{ cm}^{-1}$ ) than in **2+K<sup>+</sup>** and **2+Na<sup>+</sup>**, illustrating the interplay of Cu–O–O–Cu dihedral angle and magnetic coupling of the Cu<sup>II</sup> ions. However, next to the Cu–O–O–Cu torsion angle also the coordination environment of the copper ions as well as the contribution of the pyrazolate bridge to the magnetic exchange coupling has to be considered. In Section 6.1.5 the effect of the pyrazolate bridge to the observed magnetic exchange coupling in complex **2** has been neglected, since these ligands only mediate weak magnetic exchange coupling.<sup>44,115,116</sup> The contribution of the pyrazolate ligands to the magnetic coupling in the alkali metal adducts will therefore also be neglected in this discussion.

Another structural parameter that influences the orbital overlap is the distortion of the copper(II) coordination geometry from square pyramidal towards trigonal bipyramidal. A progressive distortion from an ideal square pyramidal ( $\tau = 0$ ) towards a trigonal bipyramidal coordination environment ( $\tau = 1$ )



will mix the  $d_{x^2-y^2}$  and  $d_z^2$  magnetic orbitals of both idealized geometries.<sup>111</sup> A major distortion from a square pyramidal to a trigonal bipyramidal geometry consequently will diminish the overlap of the magnetic copper orbitals *via* the peroxide and pyrazolate centered orbitals, weakening the superexchange interaction.<sup>144,145</sup>

The coordination environment of the  $\text{Cu}^{\text{II}}$  ions is identical in  $\mathbf{2+K}^+$  and  $\mathbf{2+Li}^+$  and is increased towards a more trigonal bipyramidal geometry in complex **2** (see Table 10). Since both Cu-O-O-Cu torsion angle  $\phi$  and coordination geometry  $\tau$  are influencing the magnitude of magnetic exchange coupling, a direct comparison of the magnetic properties of **2** and of the alkali metal adducts  $\mathbf{2+M}^+$  is thus difficult.<sup>144,145</sup>

However, the  $\tau$  factors of the  $\text{Cu}^{\text{II}}$  ions in  $\mathbf{2+K}^+$  and  $\mathbf{2+Li}^+$  are identical and the contribution of the coordination geometry to the overall amount of exchange coupling is consequently not relevant compared to the Cu-O-O-Cu-dihedral angle. The Cu-O-O-Cu torsion angle  $\phi$  then remains as the only parameter determining the molecules singlet-triplet splitting. With respect to the structural and magnetic data of the alkali metal adducts  $\mathbf{2+K}^+$  and  $\mathbf{2+Li}^+$ , the interplay of Cu-O-O-Cu dihedral angle  $\phi$  and magnetic properties can then be confirmed. The Cu-O-O-Cu dihedral angle in  $\mathbf{2+Li}^+$  is closer to the  $90^\circ$  arrangement and thus the two  $\text{Cu}^{\text{II}}$  ions are more weakly antiferromagnetically coupled than in  $\mathbf{2+K}^+$ .

With this knowledge in hand, the magnetic properties of the complexes  $\mathbf{2+K}^+$  and  $\mathbf{2+Na}^+$  will be reconsidered. The two  $\text{Cu}^{\text{II}}$  ions in  $\mathbf{2+K}^+$  are slightly more antiferromagnetically coupled than the  $\text{Cu}^{\text{II}}$  ions in compound  $\mathbf{2+Na}^+$ , although the Cu-O-O-Cu torsion angle in  $\mathbf{2+K}^+$  is larger by  $1.6^\circ$ . With respect to the torsion angle  $\phi$ , the opposite magnetic behavior would be expected. However, the coordination environment of the  $\text{Cu}^{\text{II}}$  ions in  $\mathbf{2+Na}^+$  is more distorted towards trigonal bipyramidal geometry (see Table 10) and thus the overlap of copper- and oxygen-centered orbitals in  $\mathbf{2+Na}^+$  is smaller than that in  $\mathbf{2+K}^+$ . Consequently the magnetic exchange coupling in  $\mathbf{2+Na}^+$  is diminished with respect to coordination geometry of the  $\text{Cu}^{\text{II}}$  ions. This deviation may explain the opposite behavior with respect to the magnetism in these two adducts and also correlates with the magnetic properties observed for complex **2**.

Although the Cu-O-O-Cu torsion angle is the smallest in **2**, the two  $\text{Cu}^{\text{II}}$  ions are more weakly antiferromagnetically coupled than in  $\mathbf{2+K}^+$  and  $\mathbf{2+Na}^+$ . With respect to the dihedral angle  $\phi$ , the antiferromagnetic coupling of the copper atoms should be the strongest in **2**. However, the coordination geometry in **2** is more distorted towards a trigonal bipyramidal environment (see Table 10), thus diminishing the overlap of copper- and oxygen-centered orbitals, thus decreasing the corresponding superexchange interaction. This discussion is indeed rather qualitative, but is principally supported by DFT calculations performed on the molecular structures of **2** and its alkali metal adducts determined *via* X-ray diffraction (see Section 6.2.7). However, it should be noted that the absolute

differences in magnetic coupling of all complexes are quite small, which poses a challenge to the computational description of this interaction (see Section 6.2.7).

This discussion shows the magnetic properties of complex **2** and of its corresponding alkali metal adducts **2+M<sup>+</sup>** do not exclusively depend on the Cu–O–O–Cu dihedral angle. Furthermore, the coordination environment of the copper ions has to be considered, which complicates a quantitative evaluation of any magnetostructural correlation. Nevertheless, this section provides an insight into the magnetic properties of the different alkali metal adducts. The singlet-triplet splitting observed for peroxo complex **2** can be generally modified in adding different alkali metal ions. Such correlations have not yet been described for any other synthetic copper oxygen complex, raising the question if such interactions have to be also considered in understanding the mechanism of action of natural copper sites. With respect to the complexes **2+K<sup>+</sup>** and **2+Li<sup>+</sup>**, exclusively the Cu–O–O–Cu torsion angle is changing upon replacement of K<sup>+</sup> by Li<sup>+</sup>. As a result, the molecular triplet state in **2+Li<sup>+</sup>** becomes more populated compared to that in **2+K<sup>+</sup>** at e.g. physiological conditions. Since molecular spin states can be directly correlated to reactivity, the possible regulation of reactivity in natural copper sites by redox inert metal ions such as Na<sup>+</sup> or Ca<sup>2+</sup> has to be considered in future investigations.<sup>146,147</sup>

## 6.2.7 DFT Calculations

In order to elucidate the effect of alkali metal binding on the electronic structure of the copper oxygen core, DFT calculations were performed in cooperation with D'AMORE and SWART<sup>118</sup> on both the optimized geometries as well as on the molecular structures determined *via* X-ray crystallography of the adducts **2+M<sup>+</sup>** (for computational details see Section 6.1.7 and ref.<sup>105</sup>). This section will further compare the computational results for the alkali metal adducts to those obtained for complex **2**. The correlation between Cu-O-O-Cu torsion angle and magnitude of magnetic exchange coupling, which has been discussed in detail in Sections 6.1.5 and 6.2.6, will be further investigated. It however shall be noted that the absolute differences in antiferromagnetic coupling in the adducts are small and thus a computational description of the spin state splitting in the alkali metal adducts is ambiguous. It should be noted that the results presented in this Section are only preliminary.

In general, the DFT calculations reproduce the experimental data. In Section 6.2.1 the experimental solution state electronic absorption spectra of the alkali metal adducts **2+M<sup>+</sup>** were compared to the spectrum of peroxo complex **2**. The two main CT transitions were observed to undergo a blue-shift upon alkali metal binding. The absolute blue-shift of both maxima increases from **2+K<sup>+</sup>** over **2+Na<sup>+</sup>** to **2+Li<sup>+</sup>**, which goes along with a significant decrease in intensity, especially of the second transition. This trend is also qualitatively predicted by the corresponding TD-DFT calculations, with a decrease observed for the secondary transition in general agreement with the experimental findings (see Table 11 and Figure 41; for computational details see ref.<sup>105</sup>).

**Table 11.** Summary of TD-DFT-calculated excitation energies and dominant transitions (TD-DFT calculations are based on optimized geometries); oscillator strength is only reported for most dominant transitions.<sup>118</sup>

complex	energy [nm]	oscillator strength [f]	dominant transitions (to LUMO)
<b>2</b>	497	0.047	<b>HOMO-4(85%)</b> + HOMO-1(6%)+ HOMO-3(3%)
	520	0.042	<b>HOMO-3(76%)</b> + HOMO-4(9%)+ HOMO-1(8%)
	581	0.054	<b>HOMO-1(62%)</b> + HOMO-2(10%)+ HOMO-3(15%)
<b>2+K<sup>+</sup></b>	508	0.041	<b>HOMO-4(74%)</b> + HOMO-1(2%)+ HOMO-2(1%)
	585	0.028	<b>HOMO-3(76%)</b> + HOMO-2(14%)+ HOMO-1(6%)
	613	0.037	<b>HOMO-2(62%)</b> + HOMO-3(19%)+ HOMO-2(13%)
<b>2+Na<sup>+</sup></b>	503	0.057	<b>HOMO-4(93%)</b> + HOMO-2(2%)+ HOMO-1(1%)
	597	0.036	<b>HOMO-3(53%)</b> + HOMO-2(34%)+ HOMO-1(9%)
<b>2+Li<sup>+</sup></b>	485	0.055	<b>HOMO-4(95%)</b> + HOMO-2(2%)
	610	0.034	<b>HOMO-2(85%)</b> + HOMO-3(7%)+ HOMO-1(3%)

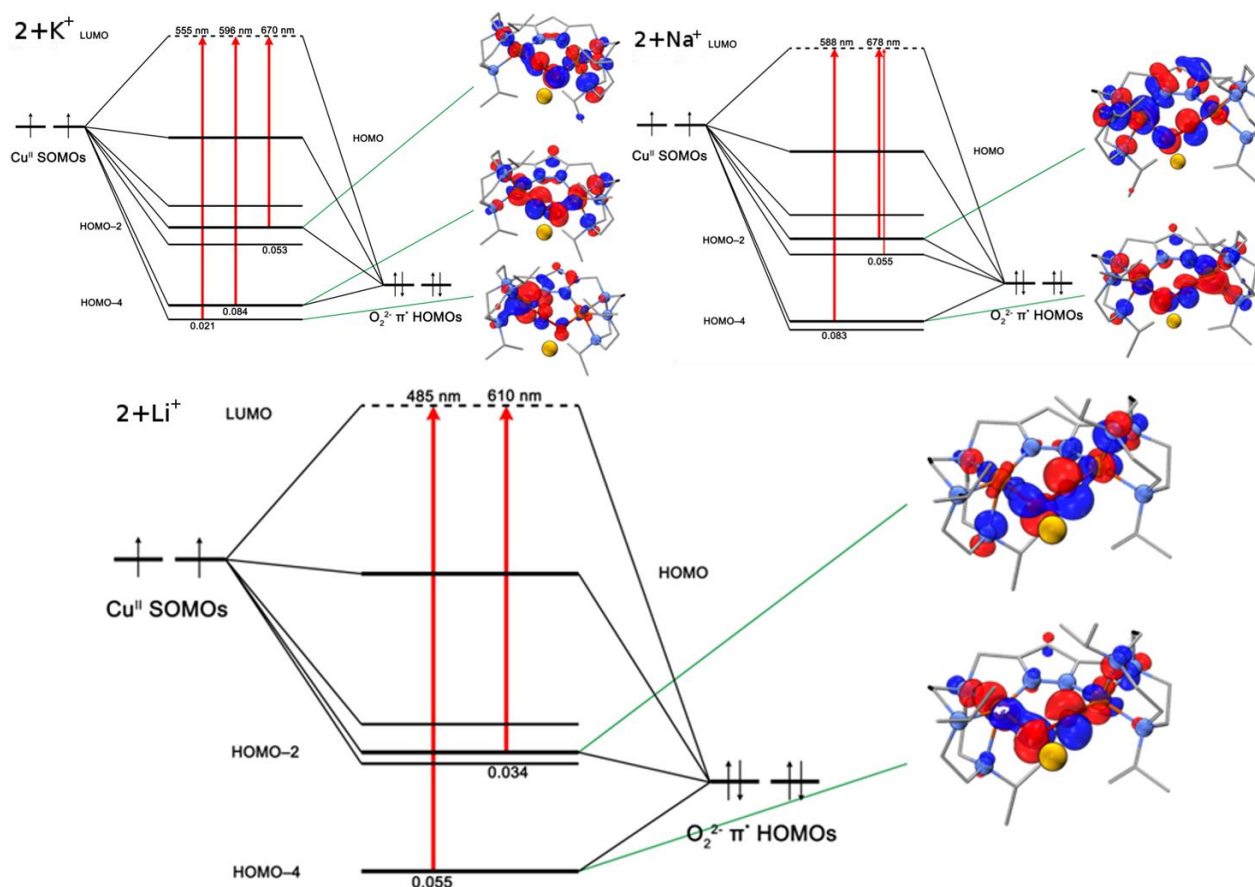


**Figure 41.** TD-DFT calculated MO diagram (based on fully optimized geometrie) of the adducts  $2+M^+$  and corresponding  $\alpha$ -spin MOs.<sup>118</sup>

If the CT transition corresponding to the longest wavelength for all alkali adducts is considered (e.g. the transition from HOMO-2  $\rightarrow$  LUMO for  $2+Li^+$ ), the calculated intensities of these CT transitions are considerably lower compared to the calculated intensity of the equivalent CT calculated for complex **2** (see Table 11). These findings are in agreement with the experimental results (see Section 6.2.1, Table 4 and Table 11 for details). Thus, in going from **2** to the corresponding adducts more electron density with antibonding character remains in the intraperoxide region, progressively weakening the O-O bond in the aforementioned order. These computational findings explain the experimentally observed differences in the rR spectra for **2** and the alkali metal adducts. The O-O stretch was experimentally observed to shift to lower wavenumbers upon alkali metal ion binding in both solid and solution state, which is furthermore supported by the computed frequencies (see Table 12, for computational details see ref.<sup>105</sup>). A shift of the O-O stretch to lower wavenumbers corresponds to a weakening of the O-O bond upon alkali metal binding. However, if only the pure interaction of peroxide and alkali metal ion is considered, this kind of adduct formation will lead to a withdrawal of electron density from the peroxide  $\pi^*$  orbitals, consequently stabilizing the O-O bond (see Section 6.2.3). Nevertheless, the peroxide is additionally interacting with the copper atoms and the DFT calculations in combination with the experimental rR data show that this interaction is predominant. In summary, the interaction of the

peroxo moiety with alkali metal ions leads to an increasing electron density at the peroxide due to diminished donor interactions of peroxide and copper atoms.

The DFT calculations additionally predict the intensity of the O-O stretch to drastically decrease in the order from **2** to **2+Li<sup>+</sup>**, which has also been observed experimentally (see Table 12). A detailed evaluation of this trend is provided in Sections 6.2.2 and 6.2.5, whereas the computational findings support this discussion.

**Table 12.** Summary of experimental (solid state,  $\lambda_{\text{exc}}=633$  nm) and calculated geometry optimized O-O stretching frequencies.<sup>118</sup>

complex	exp. $\tilde{\nu}_{\text{O-O}}$ [ $\text{cm}^{-1}$ ]	calc. <sup>a</sup> $\tilde{\nu}_{\text{O-O}}$ [ $\text{cm}^{-1}$ ]	intensity [ $\text{km mol}^{-1}$ ]
<b>2</b>	793	890	82
<b>2+K<sup>+</sup></b>	790	796	34
<b>2+Na<sup>+</sup></b>	789	764	32
<b>2+Li<sup>+</sup></b>	790	755	26

<sup>a</sup>frequency calculations were performed at the BP86-D<sub>3</sub>/TZ2P level of theory.<sup>148</sup>

Moreover, the computational results will be used to reinvestigate the Cu-O stretches, which are only weakly observed in the experimental rR spectra. An exact determination is complicated due to low intensity and thus only the solid state rR spectra allow a rough estimation of the exact Cu-O stretching frequencies (see Table 13). Interestingly, the DFT calculations predict two Cu-O stretching modes for **2+Li<sup>+</sup>**, of which one originates from coupling to a Li-O stretch. This coupling is enabled by the specific Li-O bond distance in **2+Li<sup>+</sup>**, which is significantly shorter than the corresponding alkali-O distances in the other adducts (see Table 14). Although this stretching mode is predicted to have high intensity, no experimental evidence could be found in the solid state rR spectrum. Nevertheless, if the corresponding <sup>18</sup>O labeled solution state spectrum is considered, an oxygen isotope sensitive signal at 504  $\text{cm}^{-1}$  is observed. Since both <sup>16</sup>O and <sup>18</sup>O labeled spectra are featuring a solvent signal at 546  $\text{cm}^{-1}$ , the coupled Cu-O stretch lies beneath this band in the <sup>16</sup>O labeled sample and only appears as weak shoulder at ca. 530  $\text{cm}^{-1}$  (see Figure 42). However, the second Cu-O stretch which is computationally predicted to lie in the region of 430  $\text{cm}^{-1}$  could not be identified in the solution state rR spectrum. One reason may be the presence of a broad solvent signal at 385  $\text{cm}^{-1}$ , superimposing with the weak Cu-O stretch. In summary, the experimental as well as the calculated Cu-O stretching frequencies shift to higher wavenumbers upon alkali metal binding, reflecting an increasing covalent character of the Cu-O bond. Since the electron density at the peroxide was observed to increase upon alkali metal binding, these findings are reasonable.

**Table 13.** Summary of experimental (solid state,  $\lambda_{\text{exc}} = 633 \text{ nm}$ ) and calculated geometry optimized Cu-O stretching frequencies.<sup>118</sup>

complex	exp. $\tilde{\nu}_{\text{Cu-O}}$ [ $\text{cm}^{-1}$ ]	calc. <sup>a</sup> $\tilde{\nu}_{\text{Cu-O}}$ [ $\text{cm}^{-1}$ ]	intensity [ $\text{km mol}^{-1}$ ]
<b>2</b>	415	464	44
<b>2+K<sup>+</sup></b>	455	488	18
<b>2+Na<sup>+</sup></b>	448	519	85
<b>2+Li<sup>+</sup></b>	430	424	19
	-	579 <sup>b</sup>	196

<sup>a</sup>frequency calculations were performed at the BP86-D<sub>3</sub>/TZ2P level of theory,<sup>148</sup> <sup>b</sup>the Cu-O mode is predicted to be coupled to a Li-O stretch.

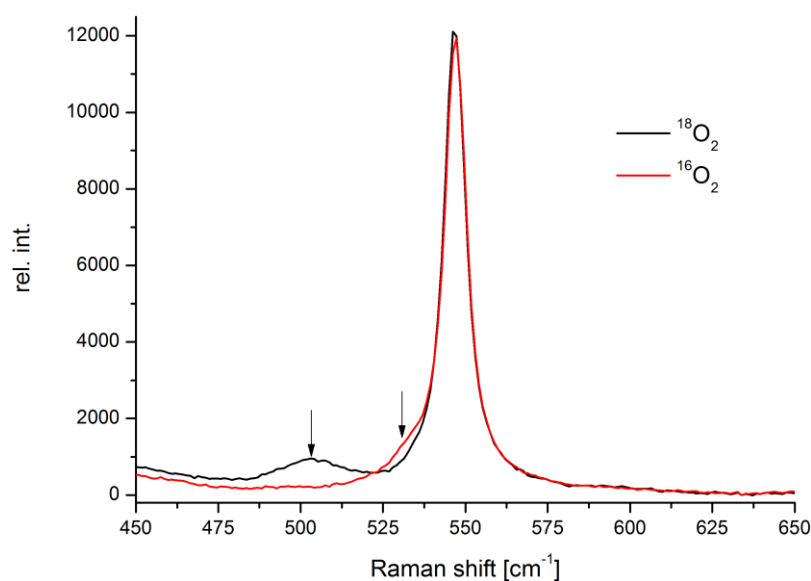


**Figure 42.** Solution state resonance Raman spectrum of **2+Li<sup>+</sup>** in EtCN at -30 °C in the range of 450 – 650  $\text{cm}^{-1}$  ( $c = 1 \times 10^{-2} \text{ M}$ ,  $\lambda_{\text{exc}} = 633 \text{ nm}$ ).

If the structural parameters such as O-O bond distance and average M-O bond length are compared to the data obtained from geometry optimization, these parameters are well described (see Table 14). However, by looking at the Cu-O-O-Cu torsion angles  $\phi$ , significant deviations between experimental and geometry optimized data are observed. While for **2** an experimental dihedral angle of 55.3° is determined, the corresponding geometry optimization predicts 62.4°. The calculated Cu-O-O-Cu torsion angle progressively increases from **2** to **2+Na<sup>+</sup>** and finally reaches 65.7° for **2+Li<sup>+</sup>** (see Table 14).

**Table 14.** Summary of selected structural parameters obtained from molecular structures and from corresponding fully optimized geometries (BP86 functional<sup>119,120</sup>, inclusion of Grimme's<sup>121</sup> dispersion energy (DFT-D<sub>3</sub>), TDZP basis set<sup>122, 118</sup>).

complex	$d$ (O-O) [Å]; exp./calc.	$d$ (M-O) <sup>a</sup> [Å]; exp./calc.	$\phi$ Cu-O-O-Cu [°]; exp./calc.
<b>2</b>	1.44/1.41	-	55.3/62.4
<b>2+K<sup>+</sup></b>	1.48/1.46	2.63/2.60	66.8/63.5
<b>2+Na<sup>+</sup></b>	1.50/1.48	2.30/2.24	65.2/64.7
<b>2+Li<sup>+</sup></b>	1.50/1.50	1.88/1.88	71.1/65.7

<sup>a</sup>The average of both M-O distances is shown.

The absolute differences between experimentally and computationally determined dihedral angles for **2** and **2+Li<sup>+</sup>** are 15.8° and 3.3°, respectively (see Table 14). This deviation consequently raises the question to which extent the Cu-O-O-Cu dihedral angle in the alkali metal adducts is induced by e.g. crystal packing rather than by the interaction of the cation with the peroxo moiety. Nevertheless, the DFT calculations predict an increasing dihedral angle from **2** to **2+Li<sup>+</sup>**, which is also observed experimentally. Since especially the Cu-O-O-Cu torsion angle affects the magnitude of overlap of copper magnetic and peroxide  $\pi^*$  orbitals, defining the antiferromagnetic contribution to the overall magnetic exchange coupling (see Section 6.1.5), a detailed comparison of experimentally and computationally determined singlet-triplet splitting is ambiguous.<sup>110</sup>

With this information in hand, the computationally predicted data for the magnetic ground state of the different <sup>6</sup>P complexes will be compared with the experimental results (see Table 15). It shall be noted that the experimentally determined absolute differences in magnetic exchange coupling in all complexes are minor. The complexes **2** and **2+K<sup>+</sup>** for instance are both antiferromagnetically coupled, but the singlet-triplet splitting only varies by 46 cm<sup>-1</sup>. The error within the DFT calculation for e.g. **2+K<sup>+</sup>** however lies in the region of 1000 cm<sup>-1</sup>. Consequently, the DFT calculations do not allow an adequate description of the correlation of Cu-O-O-Cu torsion angle and magnitude of antiferromagnetic coupling, and the computational results can only be compared relative to each other. The DFT calculations in general show good agreement with the experimental results concerning the small singlet-triplet splitting for the alkali metal adducts **2+M<sup>+</sup>** (see Table 15). For complex **2** on the other hand all applied XC functionals consistently predict a much larger splitting as observed experimentally. Indeed, the experimental value found for **2** is expected to be larger, based on to a Cu-O-O-Cu torsion angle of 55°. One reason for this small value may be the distortion of the coordination environment of the Cu<sup>II</sup> ions towards a more trigonal bipyramidal geometry compared to the alkali metal adducts (see Section 6.2.6 for details). Nevertheless, a computationally predicted singlet-triplet splitting of e.g. -546 cm<sup>-1</sup> (mPWxPc XC functional) is definitely too large in view of a calculated Cu-O-O-Cu dihedral angle of 62.4°. If this splitting is compared to that calculated for **2+K<sup>+</sup>**, where a geometry optimized torsion angle of 63.5°

was found, the singlet-splitting is five times larger although the torsion angle only changes by 1°. Since all different exchange (XC) functionals lead to similar results, the singlet-triplet splitting for **2** is systematically overrated. This discussion shows that a computational description of the correlation of Cu-O-O-Cu torsion angle and the magnitude of magnetic exchange coupling is difficult.

**Table 15.** Summary of experimentally and computationally determined spin state splitting for complexes **2** and **2+M<sup>+</sup>**.<sup>118</sup>

complex	$2J$ [cm <sup>-1</sup> ]			
	<b>2</b>	<b>2+K<sup>+</sup></b>	<b>2+Na<sup>+</sup></b>	<b>2+Li<sup>+</sup></b>
exp. data	-108	-154	-144	-80
XC functional				
S12g <sup>125</sup>	-402	-24	-38	49
mPWxPc <sup>149,150</sup>	-546	-98	-133	-70
PW86xPc <sup>150,151</sup>	-598	-119	-147	-17



## 6.2.8 Summary and Conclusion

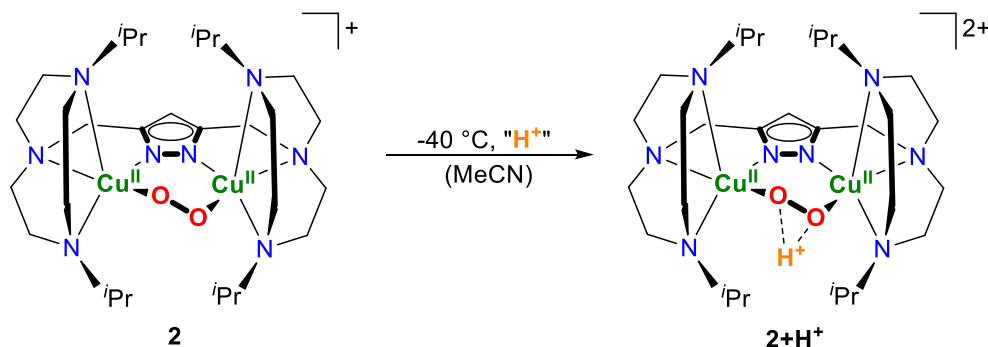
This section for the first time described the modification of the electronic structure of synthetic copper oxygen complexes. Starting from peroxide **2**, the different alkali metal adducts can be generated upon addition of the corresponding alkali triflate salts. The electronic structure of the copper oxygen core was observed to significantly change upon adduct formation in both solid and solution state. The alkali metal ions thereby affect the interaction of copper and oxygen atoms, giving rise to significant differences observed *via* e.g. UV/vis absorption spectroscopy. The magnetic exchange coupling of the Cu<sup>II</sup> ions was demonstrated to depend on the Cu-O-O-Cu torsion angle  $\phi$ , which is changing upon adduct formation. The magnitude of exchange interaction was furthermore observed to depend on the coordination geometry of the Cu<sup>II</sup> ions. While the adducts **2+M<sup>+</sup>** are featuring similar coordination geometry at the Cu<sup>II</sup> ions, the Cu<sup>II</sup> ions in **2** are coordinated in a more trigonal bipyramidal arrangement. However, the actual mechanism of action of how the alkali metal ions affect the Cu-O-O-Cu torsion angle is still unclear. DFT calculations in general support the experimental results and further underline the complexity of this interplay. While trends in electronic absorption and rR spectra could be simulated, absolute values of the experimentally observed singlet-triplet splitting cannot be reproduced reliably. However, the correlation of Cu-O-O-Cu dihedral angle and magnetic ground state could be shown for the adducts **2+M<sup>+</sup>**. These findings are essential towards a more detailed understanding of the actual mechanism of O<sub>2</sub> activation at type III active sites, where an *S*=1 intermediate Cu<sub>2</sub>/O<sub>2</sub> species is postulated to interconvert into the antiferromagnetically coupled <sup>5</sup>P binding mode.

A modification of the electronic structure of the Cu<sub>2</sub>/O<sub>2</sub> core at synthetic copper complexes by interaction with Lewis acidic metal ions has been unrepresented until to date. This work delivers valuable information of how electronic structure and thus reactivity may be tuned at other synthetic copper oxygen complexes. With respect to the mechanisms of action at natural copper sites, the influence of redox inert alkali metal ions has not been considered until today. However, this work shows that such interactions are also of considerable interest concerning natural copper sites. Thus, this chapter provides valuable information in understanding the mechanism of action at natural and synthetic copper active sites.

## 6.3 A Dinuclear Cupric Hydroperoxo Complex

### 6.3.1 Formation and pK<sub>a</sub> Determination

Complex **2** was observed to interact with different alkali metal ions and the influence of this interaction on the electronic structure of the copper oxygen core has been described (see Section 6.2). The extent of adduct formation of the Lewis basic peroxy moiety and Lewis acidic alkali metal ions was shown to increase from potassium to lithium as predicted by HSAB theory. In following the HSAB principle, this sequence has been completed by the H<sup>+</sup> cation (see Scheme 11).



**Scheme 11.** Schematic presentation of protonation of **2**; the molecular structure of **2+H<sup>+</sup>** is unknown until to date.

Complex **2** can be protonated by addition of 2,6-lutidinium triflate. Figure 43 shows the corresponding UV/vis titration experiment recorded at -40 °C in MeCN. Upon stepwise addition of substoichiometric amounts of acid complex **2** is converted into a new species, **2+H<sup>+</sup>**. An isosbestic point at 466 nm indicates a clean conversion, which is complete with 1.0 equivalent of acid being added (see Figure 43, right).

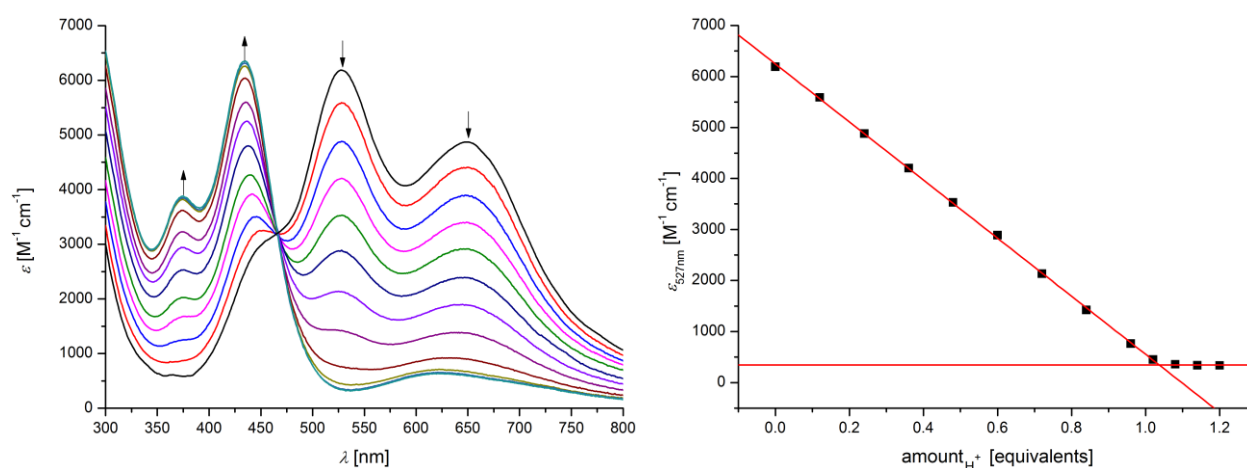


**Figure 43.** UV/vis titration of complex **2** with 2,6-lutidinium triflate (MeCN,  $T = -40\text{ }^\circ\text{C}$ ), an isosbestic point at 466 nm indicates a clean conversion; 2,6-lutidinium triflate was added in steps of 0.12 eq. (from 0 – 1.02 eq.) and in steps of 0.06 eq. (from 1.02 - 1.20 eq.).

The addition of an excess of 2,6-lutidinium triflate does not induce further spectral changes and thus no hydrogen peroxide is released as reported for other hydroperoxo complexes.<sup>69</sup> **2+H<sup>+</sup>** features two

intense maxima in absorbance at 374 nm ( $\epsilon = 3900 \text{ M}^{-1} \text{ cm}^{-1}$ ) and at 435 nm ( $\epsilon = 6000 \text{ M}^{-1} \text{ cm}^{-1}$ ) and a weak ligand field transition at ca. 620 nm ( $\epsilon = 600 \text{ M}^{-1} \text{ cm}^{-1}$ ). The bands at 435 and at 620 nm lie in the same region as those of already reported hydroperoxo systems, while the feature at 374 nm is exclusively observed for  $\mathbf{2}+\text{H}^+$ .<sup>47,69,74</sup> On the basis of the optical transitions as well as on the stoichiometry, the formation of a hydroperoxide is assumed.

Since only one equivalent of 2,6-lutidinium triflate is required to fully convert  $\mathbf{2}$  into  $\mathbf{2}+\text{H}^+$ , the affinity of the peroxide towards  $\text{H}^+$  is even higher than towards  $\text{Li}^+$  and consequently  $\mathbf{2}+\text{Li}^+$  should react to give  $\mathbf{2}+\text{H}^+$  upon addition of 2,6-lutidinium triflate. Figure 44 shows such an UV/vis titration experiment, where at first  $\mathbf{2}$  has been converted to  $\mathbf{2}+\text{Li}^+$  by adding in total 2.0 eq. of LiOTf in steps of 0.2 equivalents. Afterwards  $\mathbf{2}+\text{Li}^+$  was transformed into  $\mathbf{2}+\text{H}^+$  *via* addition of in total 1.4 eq. of 2,6-lutidinium triflate in steps of 0.2 equivalents. This experiment shows that the affinity of the peroxo moiety is higher towards  $\text{H}^+$ , which is in accordance with the HSAB principle.

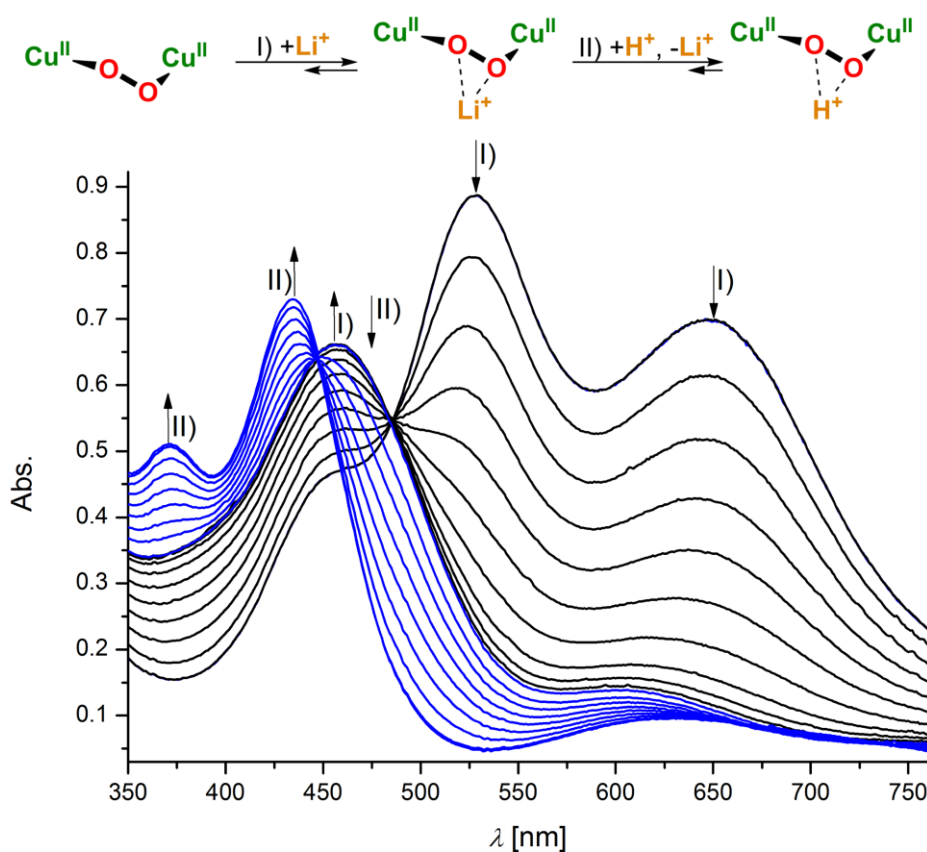
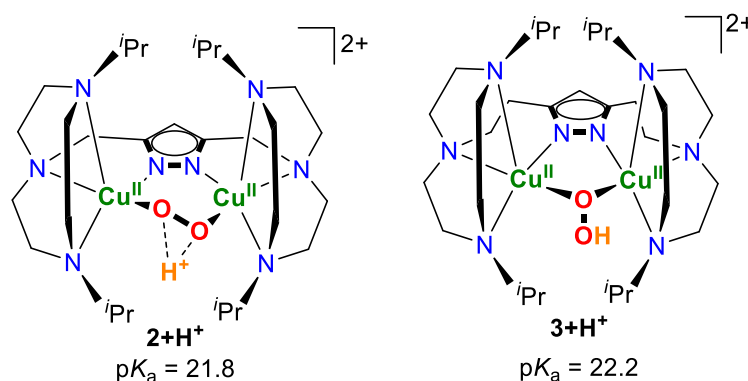


**Figure 44.** UV/vis titration experiment showing stepwise transformation of  $\mathbf{2}$  into  $\mathbf{2}+\text{Li}^+$  (black lines) (2.0 eq. of LiOTf were in total added, in steps of 0.2 eq.; isosbestic point at 486 nm), followed by stepwise transformation of  $\mathbf{2}+\text{Li}^+$  into  $\mathbf{2}+\text{H}^+$  (blue lines) (1.4 eq. of 2,6-lutidinium triflate have been in total added, in steps of 0.2 eq.; isosbestic point at 447 nm) (MeCN,  $T = -40 \text{ }^\circ\text{C}$ ).

Further analytical data, enabling a more detailed characterization of the presumed hydroperoxo motif, are lacking. Several solution state rR experiments have been performed at different complex concentrations in either MeCN or EtCN. However, no oxygen isotope sensitive feature has been observed independent of the applied laser excitation wavelength ( $\lambda_{\text{exc}} = 457$  or  $\lambda_{\text{exc}} = 633 \text{ nm}$ ). Although

various solvent combinations and diffusion/layering techniques have been applied, no crystalline material suitable for X-ray diffraction could be isolated. Next to acetone, MeCN and EtCN also other nitriles such as <sup>i</sup>PrCN, <sup>n</sup>BuCN and <sup>n</sup>PrCN have been unsuccessfully tested. This may also be due to the high sensitivity of this species in rapidly forming a stable decomposition product, which preferentially crystallizes at all tested crystallization conditions (this outcome will be discussed in Section 6.5.1). Even at -80 °C the formation of this undesired species has been observed over time, although the decomposition process was significantly slowed down.

Nevertheless, the UV/vis absorption spectrum of **2+H<sup>+</sup>** looks quite similar to that of the only to date structurally characterized dinuclear copper hydroperoxo complex, **3+H<sup>+</sup>** (denoted as **xv** in Section 3.3).<sup>47</sup> This species has been reversibly generated from the corresponding peroxo precursor **3** (see Section 5) by addition of one equivalent of 2,6-lutidinium triflate. A pK<sub>a</sub> value of 22.2 (MeCN, T = -20 °C) was determined *via* UV/vis back titration experiments of **3+H<sup>+</sup>** with 1,1,3,3-tetramethylguanidine (TMG).<sup>47</sup> However, complex **3+H<sup>+</sup>** is much more stable compared to other reported hydroperoxo complexes and could be isolated as single crystalline material at -30 °C.<sup>47,69,74</sup> The relatively high stability of **3+H<sup>+</sup>** compared to **2+H<sup>+</sup>** may be explained with the specific ligand design of complex **3+H<sup>+</sup>**, but this outcome will be discussed in Section 6.5.1. The similar optical spectra of both species as well as the stoichiometry support the formation of a hydroperoxide such as **2+H<sup>+</sup>**, although the molecular structure remains undefined.<sup>47</sup>



**Scheme 12.** Hydroperoxo complexes **2+H<sup>+</sup>** and **3+H<sup>+</sup>**; the molecular structure of **2+H<sup>+</sup>** is unknown.<sup>47</sup>

The protonation of complex **2** was furthermore reversible and a corresponding pK<sub>a</sub> value of 21.8 has been obtained (MeCN, T = -40 °C). In contrast to the pK<sub>a</sub> determination for **3+H<sup>+</sup>**,<sup>47</sup> the experiments with **2+H<sup>+</sup>** were more challenging due to the open cavity of the copper oxygen core in **2** and the resulting higher reactivity. Complex **2**, which is formed as conjugate base during the deprotonation of **2+H<sup>+</sup>**, was observed to form weak adducts with the protonated forms of the introduced bases, thus complicating the data interpretation. Finally, the pK<sub>a</sub> value of **2+H<sup>+</sup>** has been determined in titrating **2+H<sup>+</sup>** with complex **3**, where no side reactions were observed. The determination of the pK<sub>a</sub> value will be described chronologically in the following.

In order to determine a  $pK_a$  value of complex **2**, different bases such as **DBU** (DBU = 1,8-Diazabicyclo[5.4.0]undec-7-ene) and **TMG** have been added to a preformed solution of **2+H<sup>+</sup>** and the changes in absorbance were monitored *via* UV/vis absorption spectroscopy (see Figure 45). All measurements have been recorded in MeCN at -40 °C.

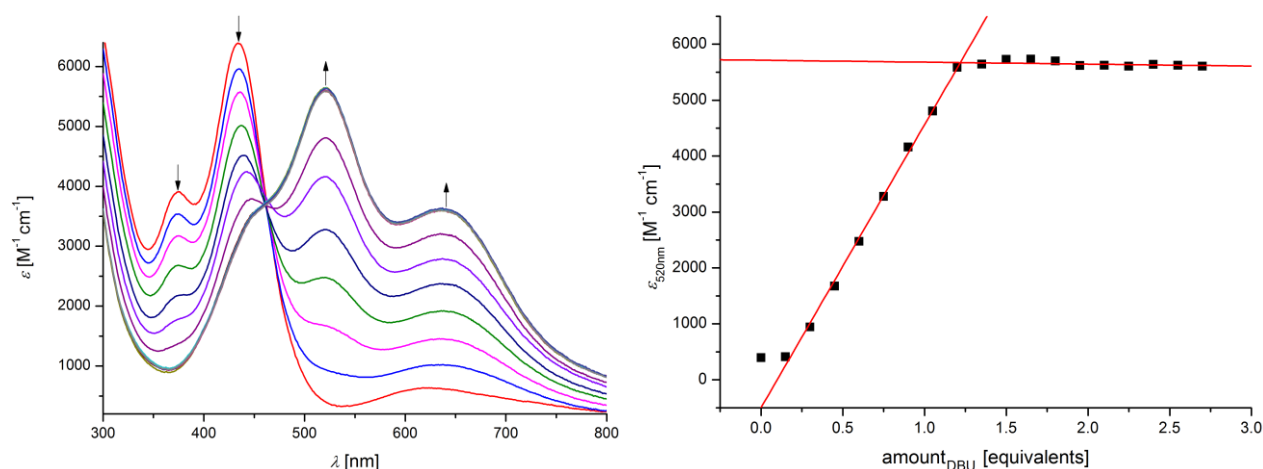
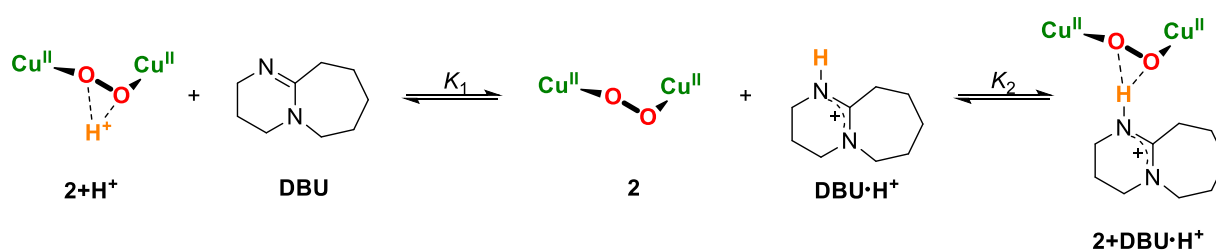


**Figure 45.** UV/vis titration of complex **2+H<sup>+</sup>** with 1,8-Diazabicyclo[5.4.0]undec-7-ene (DBU) in steps of 0.15 eq. (MeCN,  $T = -40$  °C). The first 0.2 eq. of DBU are required to neutralize the excess of 2,6-lutidinium triflate that originates from the previous protonation of complex **2** (see Figure 43).

When a solution of **DBU** ( $pK_a$  (MeCN) = 24.3,  $T = 25$  °C)<sup>152</sup> is titrated to a solution of **2+H<sup>+</sup>**, the hydroperoxide is continuously deprotonated. After the addition of 1.20 eq. of base no further changes in absorbance are observed. Since **2+H<sup>+</sup>** has been previously generated from complex **2** upon titration with overall 1.20 eq. of 2,6-lutidinium triflate, the first 0.20 eq. of base are required to neutralize the excess of acid. Since the titration is actually complete within the addition of 1.0 eq. of **DBU**, this base is much stronger than peroxy complex **2**. Thus, **DBU** cannot be used to determine the desired  $pK_a$  value because the equilibrium conditions are not suitable (see Section 7.2.1 for details).<sup>152,153,154</sup> However, another species than complex **2** is formed during deprotonation, featuring slightly different maxima in absorbance (see Figure 46, left). The new species has two main transitions at 521 nm and at 637 nm, while **2** shows two maxima in absorbance at 527 nm and 649 nm. In Section 6.2 complex **2** was described to interact with redox inert alkali metal ions in forming the corresponding alkali metal adduct, **2+M<sup>+</sup>**. During the titration of **2+H<sup>+</sup>** with **DBU**, depicted in Figure 45, the protonated species **DBU·H<sup>+</sup>** is formed. This species principally may act as hydrogen bond donor in forming a weak adduct with **2** (see Scheme 13). This possible adduct formation would explain the observed slight shifts in absorbance monitored during the titration of **2+H<sup>+</sup>** with **DBU**.



**Scheme 13.** Proposed equilibrium conditions, complicating an exact  $pK_a$  determination

In order to investigate the proposed adduct formation between complex **2** and  $\text{DBU}\cdot\text{H}^+$ , a solution of **2** has been titrated with  $\text{DBU}\cdot\text{H}^+$  at  $-40\text{ }^\circ\text{C}$  in MeCN (see Figure 46, left). Within stepwise addition of  $\text{DBU}\cdot\text{H}^+$  the initial maxima of **2** at 527 nm ( $\epsilon = 5300\text{ M}^{-1}\text{ cm}^{-1}$ ) and 649 nm ( $\epsilon = 4100\text{ M}^{-1}\text{ cm}^{-1}$ ) undergo a slight blue-shift and are simultaneously losing intensity, whereas the band at 640 nm is much more affected. The final product shows two bands at 521 nm ( $\epsilon = 5200\text{ M}^{-1}\text{ cm}^{-1}$ ) and at 639 nm ( $\epsilon = 3500\text{ M}^{-1}\text{ cm}^{-1}$ ). This trend has also been observed during the alkali metal adduct formation of **2** (see Section 6.2.1), whereas the titration of **2** with  $\text{DBU}\cdot\text{H}^+$  looks nearly identical to the UV/vis titration of **2** with  $\text{K}^+$  (see Figure 46, right). If  $\text{DBU}\cdot\text{H}^+$  is assumed to function as Lewis acid, a similar trend as observed during the titration of **2** with  $\text{K}^+$  is reasonable, since both cations are rather soft Lewis acids as predicted by HSAB principle.<sup>129</sup>

In summary, the titration of  $2+\text{H}^+$  results in the formation of a weak adduct of peroxo complex **2** and  $\text{DBU}\cdot\text{H}^+$ , which is denoted as  $2+\text{DBU}\cdot\text{H}^+$ . This example shows that a reliable  $pK_a$  determination regarding  $2+\text{H}^+$  is not possible by using DBU. On the one hand, the  $pK_a$  value of DBU is too large and consequently no suitable equilibrium conditions exist.<sup>152,153,154</sup> On the other hand, the protonated form  $\text{DBU}\cdot\text{H}^+$  and complex **2** are forming the weak adduct  $2+\text{DBU}\cdot\text{H}^+$ . This adduct formation is simultaneously affecting the pre-equilibrium which is used during the  $pK_a$  determination.

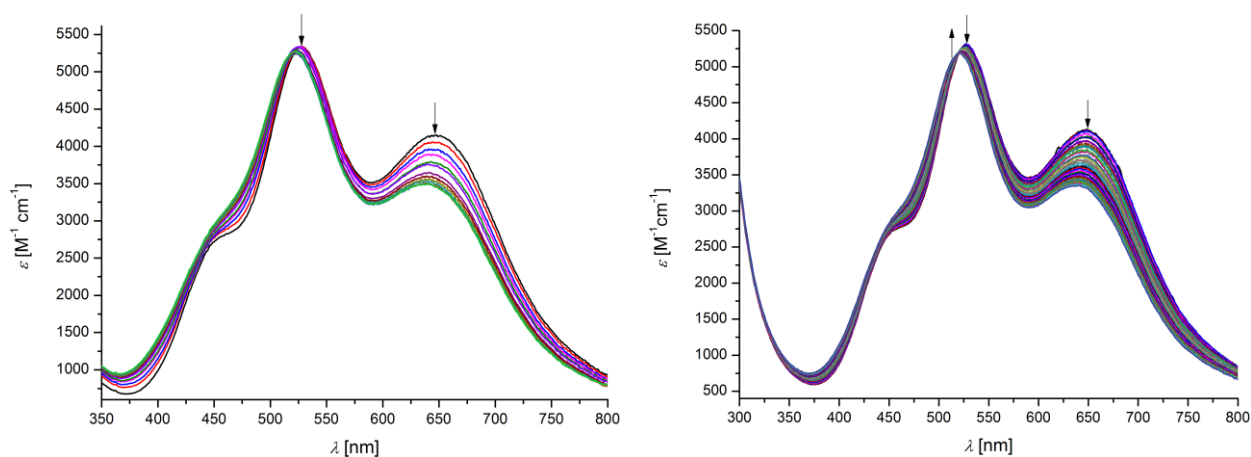


**Figure 46.** Left: UV/vis titration of complex **2** with  $\text{DBU}\cdot\text{H}^+$  in steps of 0.15 eq. and 2.1 eq. totally added (MeCN,  $T = -40\text{ }^\circ\text{C}$ ); right: UV/vis titration of **2** with KOTf in steps of 1.0 eq., with overall 48.0 eq. added (MeCN,  $T = -40\text{ }^\circ\text{C}$ ).

In another titration experiment, a solution of 1,1,3,3-tetramethylguanidine (**TMG**) has been added in steps of 0.15 eq. to a solution of **2** (see Figure 48). **TMG** is a weaker base than **DBU**, featuring a  $pK_a$

value of 23.3 (MeCN,  $T = 25\text{ }^{\circ}\text{C}$ ).<sup>155</sup> Upon stepwise addition of TMG to hydroperoxide  $2+\text{H}^+$ , complex **2** is directly formed. After the titration of 1.20 eq. of **TMG** no further changes in absorbance are observed. Since  $2+\text{H}^+$  has been generated from **2** and 1.20 eq. of 2,6-lutidinium triflate added prior to the deprotonation, the first 0.2 eq. of **TMG** are required to neutralize the excess of acid. Since the titration is actually complete within the addition of 1.0 eq. of **TMG**, this base is much stronger than peroxy complex **2**. However, the final spectrum shows an additional band at 449 nm and only 80% of complex **2** are regained. Interestingly, the same observation was made in a completely independent titration of  $2+\text{H}^+$  with the base (phenylimino)tripyrrolidinophosphorane (denoted as **PhNPPyr<sub>3</sub>**, see Figure 47) ( $\text{p}K_{\text{a}}$  (MeCN) = 22.3,  $T = 25\text{ }^{\circ}\text{C}$ )<sup>152</sup>. After the addition of 1.4 eq. of base no further spectral changes are observed, even when a huge excess of base was added (see Figure 49). Again only 80% of peroxy complex **2** have been recovered and an additional band at 449 nm is observed.

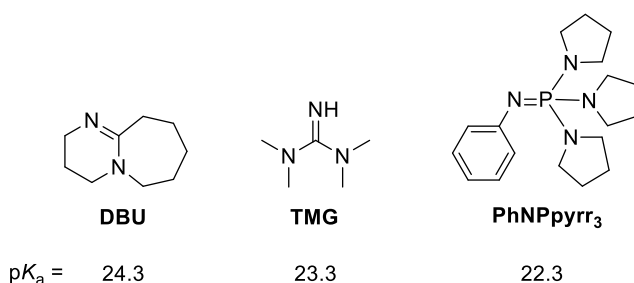


**Figure 47.** Different bases and corresponding  $\text{p}K_{\text{a}}$  values (MeCN,  $T = 25\text{ }^{\circ}\text{C}$ ).<sup>152,155</sup>

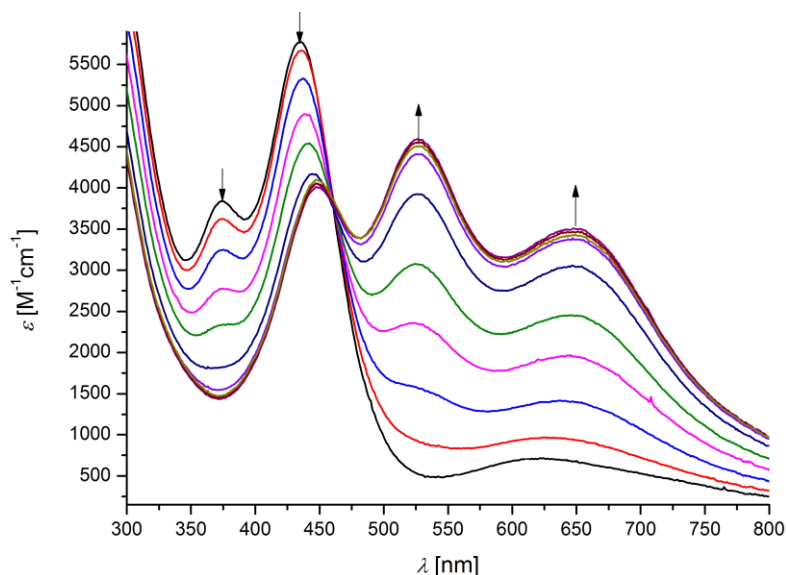


**Figure 48.** UV/vis titration of  $2+\text{H}^+$  with **TMG** in steps of 0.15 eq., no further changes in absorbance are observed after addition of 1.20 eq. (MeCN,  $T = -40\text{ }^{\circ}\text{C}$ ).

The origin of the band at 449 nm could not be determined. One explanation may be the formation of the same type of side product in both titrations. However, both bases have been purified before use *via*

distillation or by recrystallization in the case of **PhNPPyr**<sub>3</sub>. While for **TMG** a potential side product is formed during the titration, no side reaction occurs in using **DBU**, which has not been further purified prior to use. One possible side product may be superoxide **4**, which is formed from peroxy complex **2** *via* one-electron oxidation (see Section 6.4). However, neither **TMG** and its protonated form, nor **PhNPPyr**<sub>3</sub> and its protonated counterpart are known to function as oxidants or H-atom abstracting reagents, explaining the formation of a superoxide from **2** or **2+H**<sup>+</sup>, respectively. The solvent was not contaminated with impurities inducing the oxidation of **2**, since the same batch of solvent has been used for all titration experiments. Otherwise also the titration with **DBU** should show the corresponding side reaction.

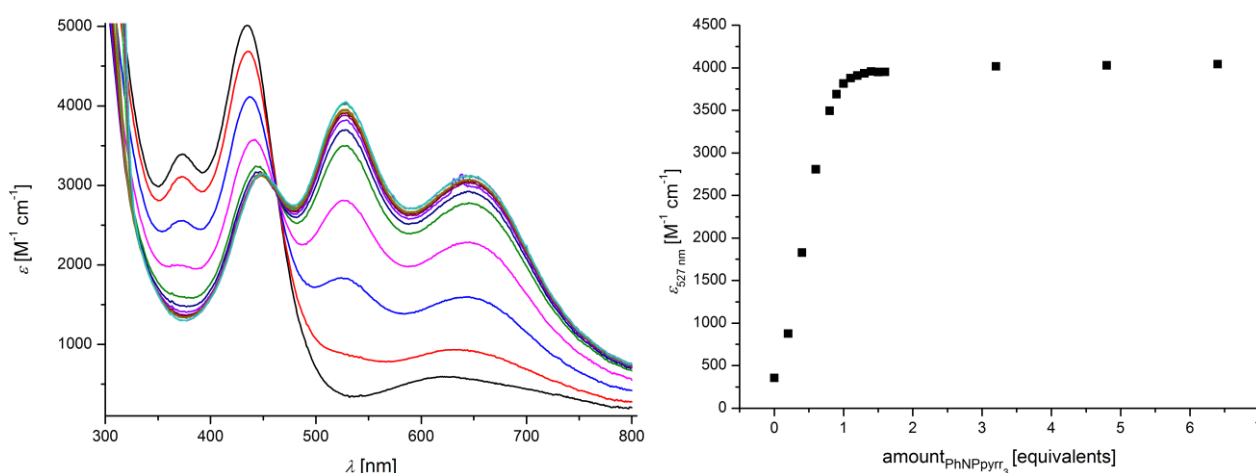


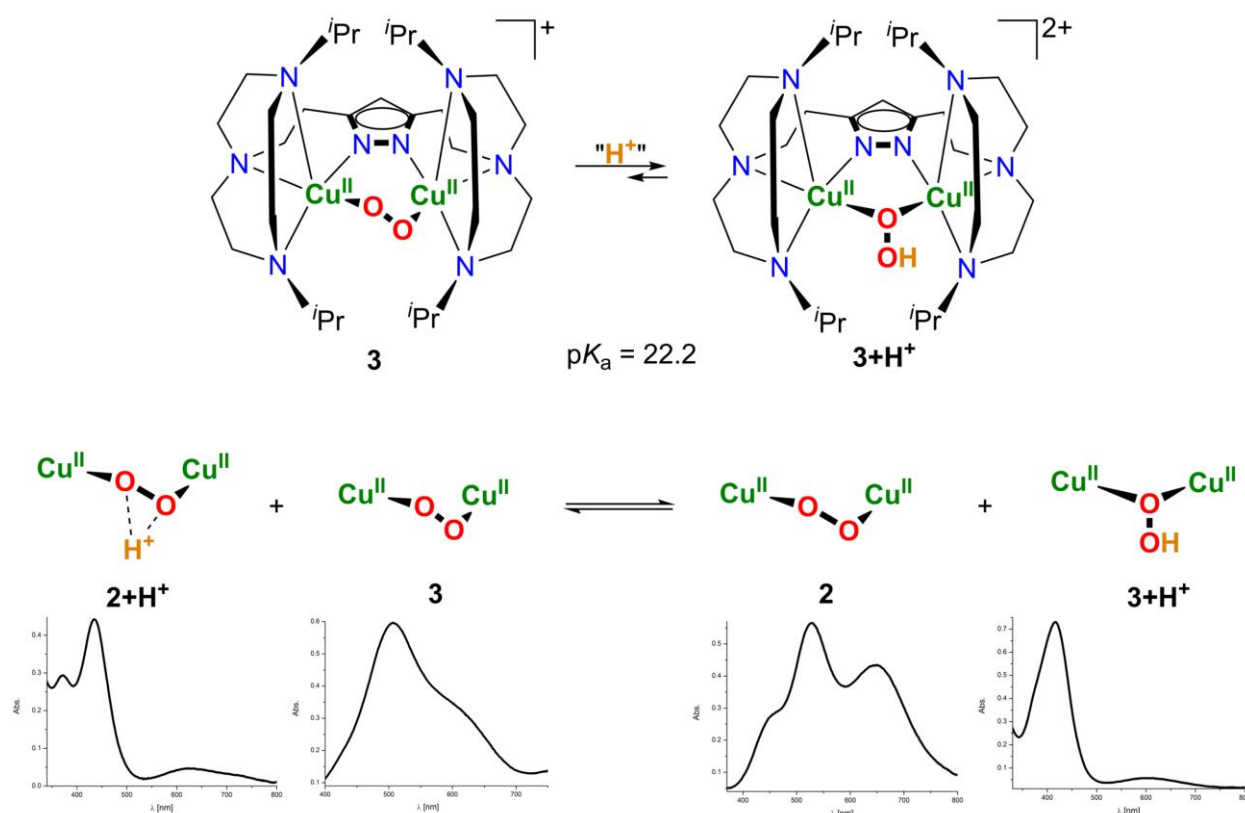
**Figure 49.** Titration of **2+H**<sup>+</sup> with **PhNPPyr**<sub>3</sub> in steps of 0.2 eq., no further changes in absorbance are observed after addition of 1.40 eq. of base (MeCN, *T* = -40 °C).

If the titration of **2+H**<sup>+</sup> with **DBU** is reconsidered, the protonated form of **DBU**, **DBU·H**<sup>+</sup>, was observed to form a weak adduct with peroxy complex **2**. However, such an adduct formation is not observed during the titration with **TMG** or **PhNPPyr**<sub>3</sub>, since the bands corresponding to complex **2** are not shifted as in the titration with **DBU**. Nevertheless, the protonated form of **TMG**, **TMG·H**<sup>+</sup>, should also interact with the peroxy moiety. The adduct formation must be even stronger, since **TMG·H**<sup>+</sup> is smaller and a stronger acid than **DBU·H**<sup>+</sup> and thus **TMG·H**<sup>+</sup> should bind with a higher affinity to complex **2**. Since this adduct formation is not observed, **TMG·H**<sup>+</sup> may interact with another species in solution. One possibility may be the interaction of **TMG·H**<sup>+</sup> with hydroperoxide **2+H**<sup>+</sup> in forming a new species which is even stable at an excess of base.

In summary none of the bases, depicted in Figure 47, enabled the determination of a *pK*<sub>a</sub> value for **2**. While in the case of **DBU** the *pK*<sub>a</sub> determination was not possible due to an adduct formation of **DBU·H**<sup>+</sup> and complex **2**, the titration with the bases **TMG** and **PhNPPyr**<sub>3</sub> involves either the formation of a side product or an interaction of the protonated forms of the bases with complex **2+H**<sup>+</sup>. However, with respect to the aforementioned adduct formation, a sterically more demanding base is required that additionally features a *pK*<sub>a</sub> value that suitable for establishing a proper equilibrium. For this purpose the



dinuclear peroxo complex **3** was used as a base (see Scheme 14). Compound **3** is structurally related to complex **2** and also forms a dinuclear hydroperoxo complex, for which a  $pK_a$  value of 22.2 (MeCN,  $T = -20\text{ }^\circ\text{C}$ ) has been determined (see Section 3.3 for details).<sup>47</sup> The  $pK_a$  value of **2** is assumed to be of similar magnitude as that of **3**, since both complexes are featuring a similar ligand design (see Section 5 for details).



**Scheme 14.** Top: structurally related peroxo complex **3** and corresponding hydroperoxo complex **3+H<sup>+</sup>** (denoted as compound **xv** in Section 3.3). Bottom: schematic representation of equilibrium between structurally related peroxo and hydroperoxo complexes, all of which are featuring characteristic UV/vis absorption spectra.<sup>34,47</sup>

Consequently, **2+H<sup>+</sup>** has been titrated with a solution of complex **3**, which was found to be more basic than its structural relative, **2** (see Figure 50). Besides **2** and **2+H<sup>+</sup>**, also the related complexes **3** and **3+H<sup>+</sup>** are featuring characteristic UV/vis absorption spectra. Thus, the in Scheme 14 depicted UV/vis titration experiment involves four individually colored species, which makes an accurate determination of the corresponding complex concentrations during the titration experiment challenging. Nevertheless, global analysis software packages such as SPECFIT/32 are capable of fitting such equilibria, but require highly accurate experimental data sets (see Section 7.2.1 for details). Figure 50 shows the titration of hydroperoxide **2+H<sup>+</sup>** with complex **3**. However, before the global analysis with SPECFIT/32 is explained, the UV/vis experiment will be described qualitatively first:

The titration starts from a solution of complex **2+H<sup>+</sup>**, featuring a main CT transition at 435 nm (see Figure 50). During the experiment complex **3** is added in steps of 0.2 equivalents. This species has a maximum in absorbance at 506 nm. Both complexes are transformed into the corresponding

deprotonated/protonated analogs, **2** and **3+H<sup>+</sup>** (see Scheme 14). **2** shows a main CT transition at 527 nm, while complex **3+H<sup>+</sup>** has a maximum in absorbance at 416 nm.

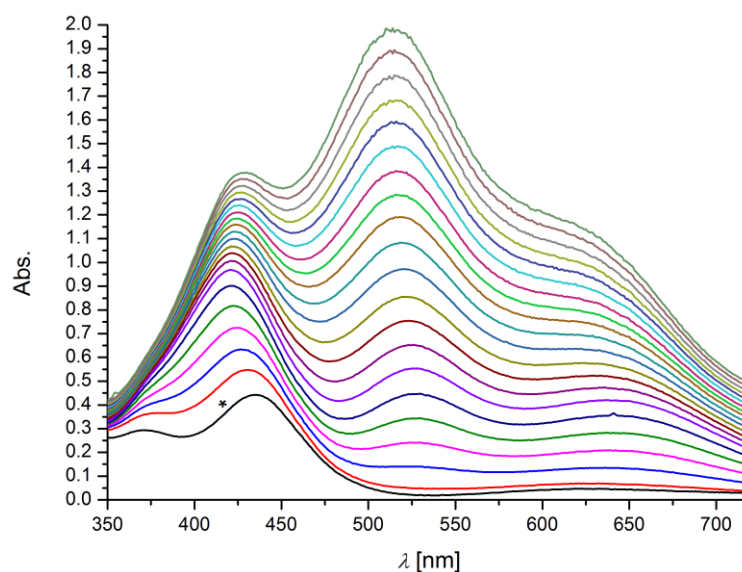


**Figure 50.** UV/vis titration of **2+H<sup>+</sup>** with **3**. Complex **3** was added in steps of 0.2 eq. (MeCN,  $T = -40\text{ }^{\circ}\text{C}$ ); the initial spectrum is marked with an asterisk.

With these different maxima in hand, the titration depicted in Figure 50, can be qualitatively interpreted. During the addition of substoichiometric amounts of **3** (0.2 eq., overall 4.0 eq. have been added), the initial maximum characteristic for **2+H<sup>+</sup>** at 435 nm is continuously shifting. After the addition of 1.0 eq. of base, this maximum is located at 421 nm (see Figure 51, left). During the titration of 1.0 – 1.8 eq. of base, the absorption maximum is no further shifting. However, in adding more excess of **3** (from 1.8 – 4.0 eq.), the aforementioned blue-shift is reversed and the maximum is finally found at 429 nm. To further understand this trend, the corresponding changes in intensity will be consulted (see Figure 51, right). If the absorbance at e.g.  $\lambda = 424\text{ nm}$  is considered, the intensity at this wavelength is observed to significantly change during the titration of the first 1.8 eq. of **3** (see red curve in Figure 51, right). Afterwards, the intensity equidistantly changes during the addition of another 2.2 eq. of **3**, as the linear regression in Figure 51, right illustrates. If a solution of any colored compound is titrated in equimolar steps into e.g. pure MeCN, the corresponding absorbance is also monitored to change linearly, since the compound concentration linearly increases. If this correlation is transferred to the titration of **2+H<sup>+</sup>** with **3**, the deprotonation of **2+H<sup>+</sup>** is almost completed after the addition of 1.8 eq. of **3**. Further addition of **3** consequently induces only equidistant changes in absorbance.

The same trend can be seen in Figure 51, left. During the titration of 1.0 eq. of **3**, the initial maximum at 435 nm is shifting to 421 nm. Complex **2+H<sup>+</sup>** is continuously deprotonated, in forming **3+H<sup>+</sup>** which has a maximum at 416 nm. From the titration of 1.0 – 1.8 eq. of **3**, the maximum is retained at 421 nm. At this stage, **2+H<sup>+</sup>** is further deprotonated but now also a significant amount of **3** is present in solution. It again shall be noted that **3** is featuring a maximum in absorbance at 506 nm. The interplay of gradually

lower formation of  $3+H^+$  and hence progressive enrichment of **3** causes the observed trend. Upon addition of 1.8 – 4.0 eq. of **3**, **3** is enriched in solution and thus the maximum at 421 nm progressively undergoes a red-shift. This evaluation is of course rather qualitative, but it clearly shows that this titration experiment can be analyzed with the help of professional software packages, such as SPECFIT/32.

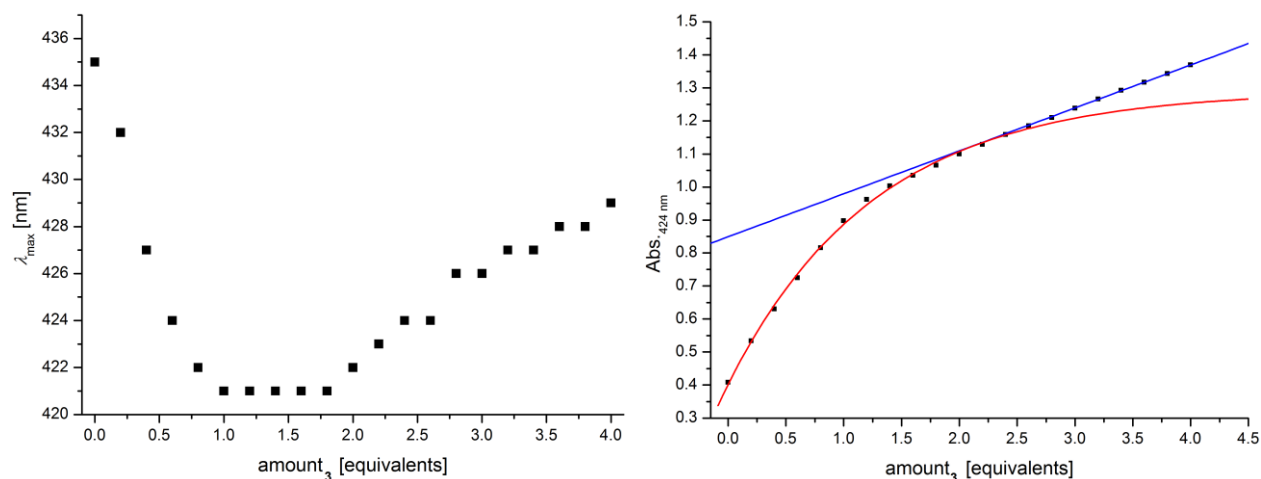


**Figure 51.** Left: changes of initial maximum corresponding to  $2+H^+$  during titration; right: changes in absorbance at 424 nm during titration.

In order to fit this equilibrium, SPECFIT/32 was used to determine the corresponding component concentrations during the titration experiment. The deprotonation of  $2+H^+$  yields the complexes **2** and  $3+H^+$  in equimolar concentrations, both featuring independent UV/vis absorption spectra. Due to limitations of the software package, these two individual species are expressed as one single species, **C** (see Figure 52). Consequently, **C** is featuring a combined UV/vis absorption spectrum (see Figure 54, black line.). In addition to component concentrations, the software furthermore calculates the individual UV/vis spectra of each component. If the corresponding fit is of adequate quality, the calculated UV/vis absorption spectra match with the real ones.

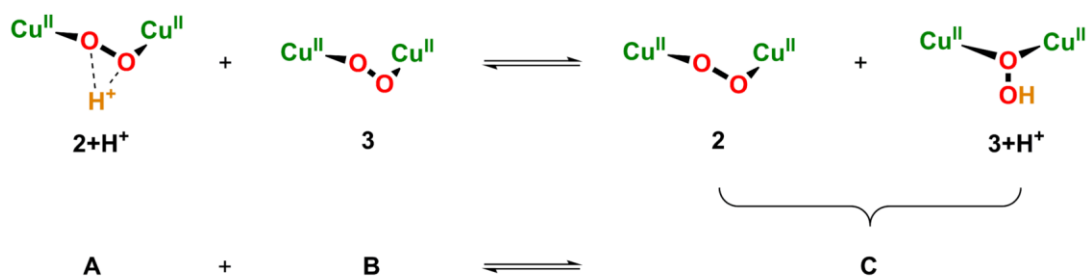


**Figure 52.** Equilibrium conditions used for determination of individual component concentration with SPECFIT/32.

Figure 53 shows the results of the fit of the aforementioned titration. After the addition of 2.0 eq. of base, more than 90% of  $2+H^+$  are already deprotonated and the concentration of **3** linearly increases

with subsequent titration (see Figure 53, right). This observation has also been made during the qualitative analysis of this experiment (see Figure 51, right).

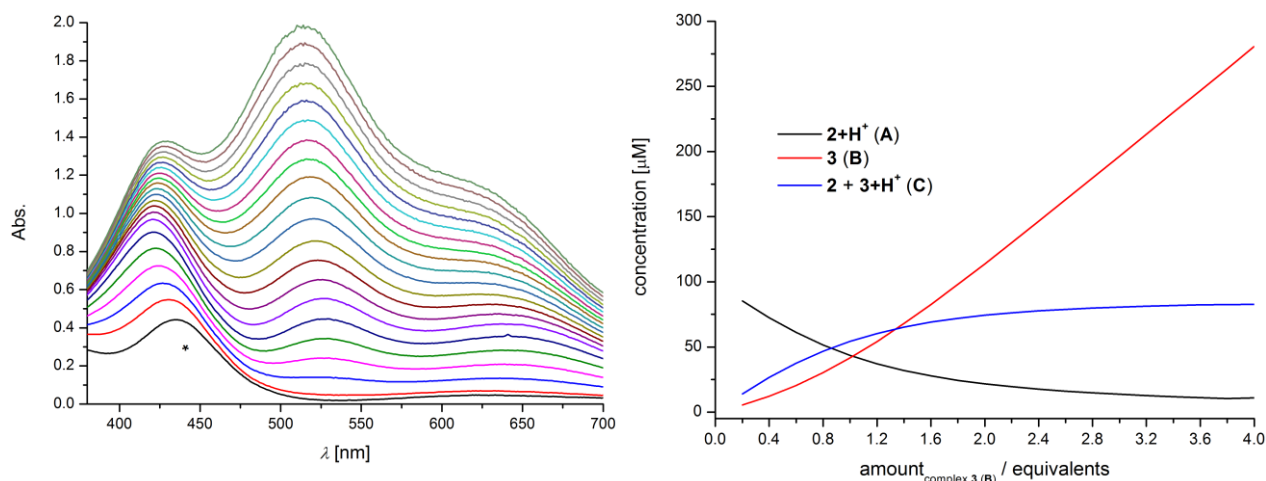


**Figure 53.** Left: UV/vis titration of  $2+H^+$  with **3**, added in steps of 0.2 eq. with 4.0 eq. finally added (MeCN,  $T = -40\text{ }^\circ\text{C}$ ); initial spectrum is marked with an asterisk. Right: change of component concentrations during titration derived from global analysis with the software package SPECFIT/32 (black:  $2+H^+$  (A); red: **3** (B); blue:  $2 + 3+H^+$  (C)).

Figure 54 shows a comparison of the calculated spectrum of compound **C** with an overlay of both experimental spectra of **2** and  $3+H^+$ . The simulated spectrum matches with the experimental data. Both simulated and experimental spectra show maxima in absorbance at 527 and 644 nm. The calculated maximum at 420 nm for complex **C** is only slightly shifted to 422 nm in the overlay of the corresponding experimental spectra. Even the small shoulder belonging to complex  $3+H^+$  at ca. 375 nm is present in the calculated spectrum. SPECFIT/32 further calculated the UV/vis absorption spectrum of complex **3**, which perfectly matches with the experimental one. From the comparison of calculated and experimentally obtained spectra a possible side reaction, as it is observed during the titration of  $2+H^+$  with e.g. TMG (see Figure 48), can be excluded. The formation of such a side product would significantly affect the corresponding UV/vis absorption spectrum and then the simulated spectra would drastically deviate from the overlay of the experimentally determined spectra of **2** and  $3+H^+$ .

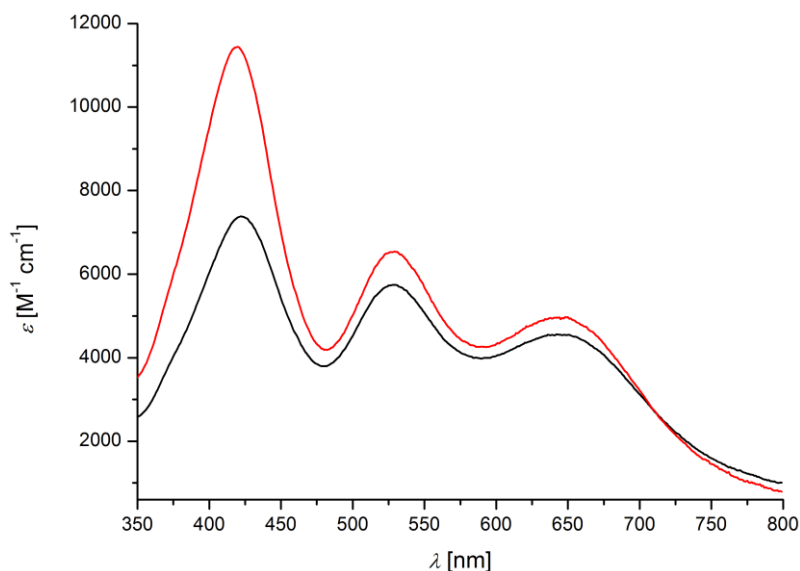


**Figure 54.** Red curve: spectrum corresponding to complex **C** simulated by SPECFIT/32. Black curve: overlay of individual spectra of products **3+H<sup>+</sup>** and **2**, defined as component **C** for fitting procedure with SPECFIT/32.

In summary, **3** was observed to be more basic than complex **2**. With the help of the global analysis software SPECFIT/32, the concentrations of all four colored species could be determined for the titration (see Figure 53, right). With the individual concentrations of all compounds in hand, the corresponding  $pK_a$  value for **2+H<sup>+</sup>** can be determined. The in Figure 52 depicted equilibrium can be described with equilibrium constant  $K_e$ :

$$12) \quad K_e = \frac{[2][3+H^+]}{[2+H^+][3]}$$

The relative basicity of the proton is defined as:<sup>152</sup>

$$13) \quad \Delta pK_a = pK_a(\mathbf{3} + \mathbf{H}^+) - pK_a(\mathbf{2} + \mathbf{H}^+) = \log \frac{[2][3+H^+]}{[2+H^+][3]}$$

$$14) \quad pK_a(\mathbf{2} + \mathbf{H}^+) = pK_a(\mathbf{3} + \mathbf{H}^+) - \log \frac{[2][3+H^+]}{[2+H^+][3]}$$

Since the complexes **2** and **3+H<sup>+</sup>** are formed in equimolar amounts, equation 14) can be simplified to:

$$15) \quad pK_a(\mathbf{2} + \mathbf{H}^+) = pK_a(\mathbf{3} + \mathbf{H}^+) - \log \frac{[3+H^+]^2}{[2+H^+][3]}; \quad \log \frac{[3+H^+]^2}{[2+H^+][3]} = \log(K_e)$$

Consequently, a plot of  $[3+H^+]^2/[2+H^+]$  versus  $[3]$  yields the equilibrium constant  $K_e$ , which can be used to calculate the relative  $pK_a$  value of complex **2+H<sup>+</sup>**.<sup>152</sup> The corresponding plot is shown in Figure 55.

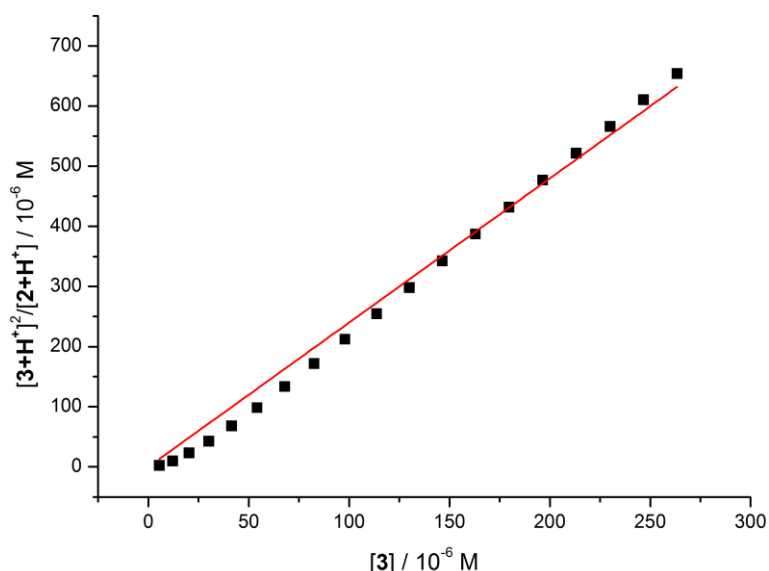


**Figure 55.** Plot of  $[3+H^+]^2/[2+H^+]$  versus  $[3]$  (fixed intersection with y-axis at  $y = 0$ ,  $R^2 = 0.996$ ). The concentrations are derived from global analysis of the titration experiment depicted in Figure 50. The slope gives equilibrium constant  $K_e$ , which is used to determine the  $pK_a$  value of  $2+H^+$ .

The linear fit of  $[3+H^+]^2/[2+H^+]$  versus  $[3]$  yields a  $K_e$  of  $2.40 \pm 0.03$  which leads to a value for  $pK_a(2+H^+)$  of 21.8. In order to support this results, complex **2** has been titrated with  $[HNEt_3]Cl$  which has a  $pK_a$  value of 18.8 (MeCN,  $T = 25^\circ C$ ). The corresponding UV/vis titration is depicted in Figure 56.

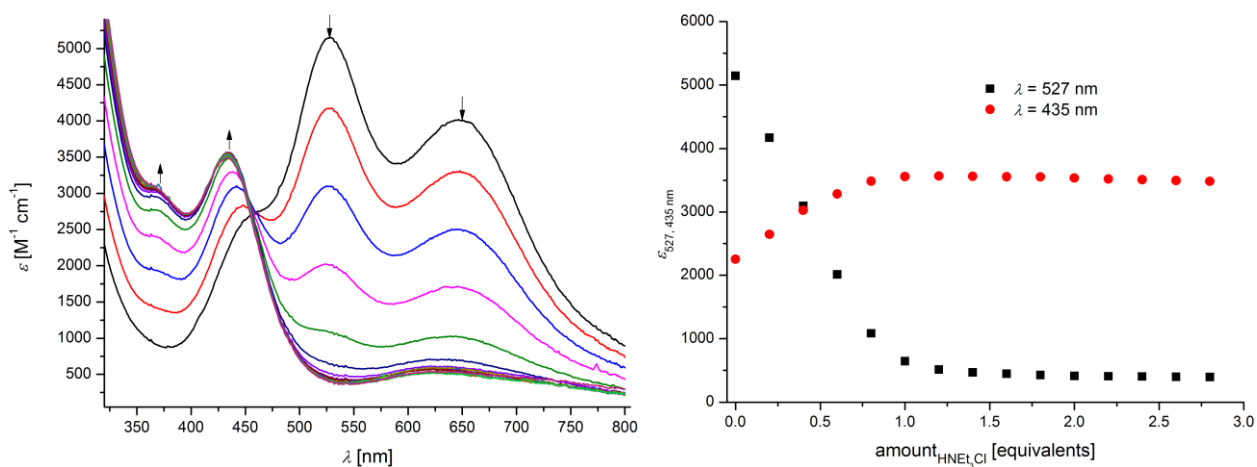


**Figure 56.** Titration of **2** with solution of  $[HNEt_3]Cl$  in steps of 0.2 eq., with finally 2.8 eq. added (MeCN,  $T = -40^\circ C$ ).

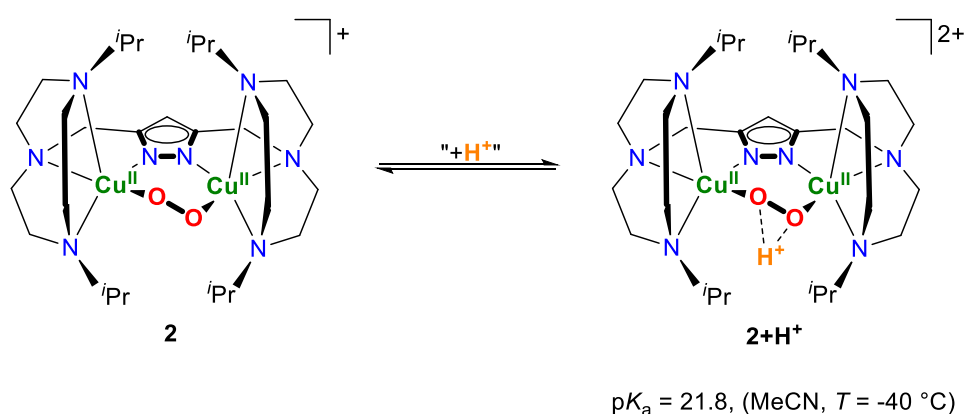
Upon stepwise addition of  $[HNEt_3]Cl$ , complex  $2+H^+$  is formed. After the titration of ca. 1.0 eq. of acid, no further changes in absorbance are observed (see Figure 56, right). However, the final UV/vis absorption spectrum of  $2+H^+$  is different from the corresponding spectrum of a titration of **2** with e.g. 2,6-lutidinium triflate (see Figure 43 for comparison). The main transitions of  $2+H^+$  are expected at significantly higher intensity ( $\epsilon = 5.0 - 6.0 \text{ mM}^{-1} \text{ cm}^{-1}$  instead of  $3.5 \text{ mM}^{-1} \text{ cm}^{-1}$ , see Figure 43). Furthermore, no clean isosbestic point is observed during the titration. This observation can be explained with a side reaction. Although  $[HNEt_3]Cl$  has been thoroughly dried prior to use, the acid was contaminated with traces of water. Complex  $2+H^+$  thereby easily forms the decomposition product **5** in

the presence of water (this topic is in detail discussed in Section 6.5.1). The decomposition of  $2+H^+$  in the presence of water further explains the decrease in intensity of the corresponding maximum at 435 nm upon addition of an excess of  $[HNEt_3]Cl$  (1.2 –2.8 eq., see Figure 56, right). With further titration of  $[HNEt_3]Cl$  even more traces of water are added, inducing the decomposition of  $2+H^+$ , as indicated by the decrease of the main CT band. Thus, the in Figure 56 depicted titration is affected by the decomposition of complex  $2+H^+$ , in consequently falsifying the pre-equilibrium. One further possibility may be the formation of an adduct of  $2+H^+$  and  $NEt_3$ . However, this titration shows that peroxo complex **2** is much more basic than  $NEt_3$ , since the titration of  $2+H^+$  with  $[HNEt_3]Cl$  is already completed after the addition of 1.0 eq. of acid.

In summary, the determination of the actual  $pK_a$  value for complex  $2+H^+$  is complicated due to adduct formation of complex **2** and the corresponding protonated bases. Furthermore, side reactions such as the formation of decomposition product **5** or of superoxide **4** may occur during the titration of  $2+H^+$  with **TMG** or **PhNPPyr<sub>3</sub>**. However, a titration of complex  $2+H^+$  with the structurally related complex **3** ( $pK_a = 22.2$ ) revealed that the peroxide in **3** is more basic than the peroxo moiety of complex **2**. On the basis of this UV/vis titration, a  $pK_a$  value for  $2+H^+$  of 21.8 has been determined. A titration of **2** with  $[HNEt_3]Cl$  ( $pK_a = 18.8$ ) has shown that **2** is more basic than the corresponding base  $NEt_3$ , although the titration is most likely compromised by the formation of a decomposition product. Thus, the magnitude of the  $pK_a$  value determined for  $2+H^+$  is correct.

### 6.3.2 Summary and Conclusion

This chapter demonstrated that peroxo complex **2** can be reversibly protonated in forming hydroperoxo species **2+H<sup>+</sup>** (see Scheme 15). The affinity of the peroxo moiety for H<sup>+</sup> is even higher than for Li<sup>+</sup> as demonstrated *via* a competition experiment, where **2+Li<sup>+</sup>** was quantitatively transformed into **2+H<sup>+</sup>**. A pK<sub>a</sub> value of 21.8 (MeCN, T = -40 °C) has been determined by UV/vis titration experiments of **2+H<sup>+</sup>** with the structurally related peroxo complex **3**. The pK<sub>a</sub> determination with other bases such as **DBU** or **TMG** was complicated due to adduct formation of complex **2** with the corresponding protonated bases, as well as due to side reactions.



**Scheme 15.** Protonation of peroxo complex **2** in forming hydroperoxide **2+H<sup>+</sup>**.

The desired molecular structure determination of the hydroperoxo complex **2+H<sup>+</sup>** has not been successful so far, although numerous crystallization conditions have been screened. One reason may be the pronounced instability of **2+H<sup>+</sup>** in forming a decomposition product that quantitatively crystallizes at all applied crystallization conditions. The decomposition of **2+H<sup>+</sup>** is assumed to be promoted by the species structure of the hydroperoxide, which will be in detail discussed in Section 6.5.



## 6.4 A Dinuclear Cupric Superoxo Complex

Dicopper peroxo complex **2** was found to interact with different alkali metal ions that affect the electronic structure of this *cis*-peroxo species (see Section 6.2). These findings raise the question, if such weak interactions also play a role in natural metal oxygen intermediates, and further investigations may help to selectively control spin states, redox potentials and thus the reactivity of synthetic copper oxygen species.<sup>147</sup> The role of  $\text{Ca}^{2+}$  in the oxygen evolving complex for instance is still under debate and is discussed to have an essential effect during the formation and release of dioxygen.<sup>102,156,157</sup> NAM and co-workers recently published a mononuclear iron peroxo complex that interacts with different redox inert metal ions such as  $\text{Ca}^{2+}$  and  $\text{Sc}^{3+}$  (see Figure 57).<sup>102</sup> Whereas the peroxo- $\text{Ca}^{2+}$  adduct can be oxidized with the release of dioxygen, the peroxo- $\text{Sc}^{3+}$  adduct cannot be oxidized with  $\text{O}_2$ -release. Since the  $\text{Sc}^{3+}$  ion is much more Lewis acidic than the  $\text{Ca}^{2+}$  ion, the following oxidation of the peroxo moiety is shifted towards higher potential in the  $\text{Sc}^{3+}$ -adduct and is not observed under the applied conditions.<sup>102,158</sup> This work shows that the electronic structure of - in that case - iron peroxo complexes can be modified by introducing different redox inert metal ions. Consequently, the alkali metal adducts of dicopper peroxo complex **2**, discussed in this thesis, have been studied in the same context. The following section will introduce superoxo complex **4**, which can be selectively generated from peroxo complex **2**. The spectroscopic features as well as selected substrate reactivity of this species will be presented. Finally, the electrochemical properties of the alkali metal adducts will be discussed. The interaction of Lewis acidic alkali metal ions with peroxo complex **2** indeed was observed to affect the redox potential of the corresponding oxidation to complex **4** and provides insight into the possible role of redox inert metal ions in modulating reactivity at natural copper active sites.

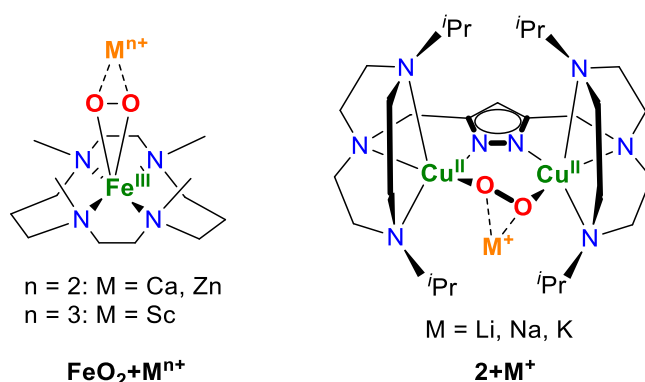
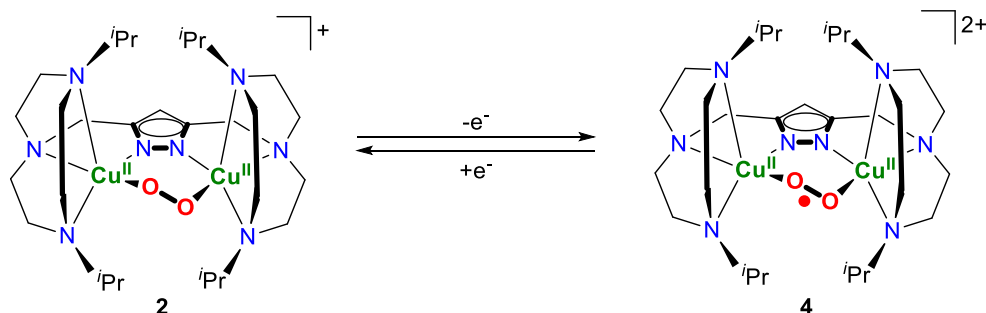


**Figure 57.** Schematic representation of interaction of mononuclear iron(III) peroxo complex (not structurally characterized) and of dinuclear copper(II) peroxo complex with redox inert metal ions.<sup>102</sup>

### 6.4.1 Electrochemical and Chemical Generation

At first, electrochemical studies (for experimental details see Section 7.5) have been performed on complex **2**, finally revealing the generation of a dicopper superoxo species, which is denoted as complex **4** (see Scheme 16).



**Scheme 16.** Electrochemically reversible generation of dicopper superoxo complex **4**.

The corresponding cyclic voltammogram (see Figure 58) shows two oxidation events of which the first oxidation at  $E_{1/2} = -0.58$  V (vs. Fc/Fc<sup>+</sup>, MeCN,  $T = 0$  °C) is reversible (see Figure 59, right). The second oxidation at  $E_{pa} = 0.59$  V is not reversible and is assigned to the release of molecular dioxygen (this outcome will be discussed later).

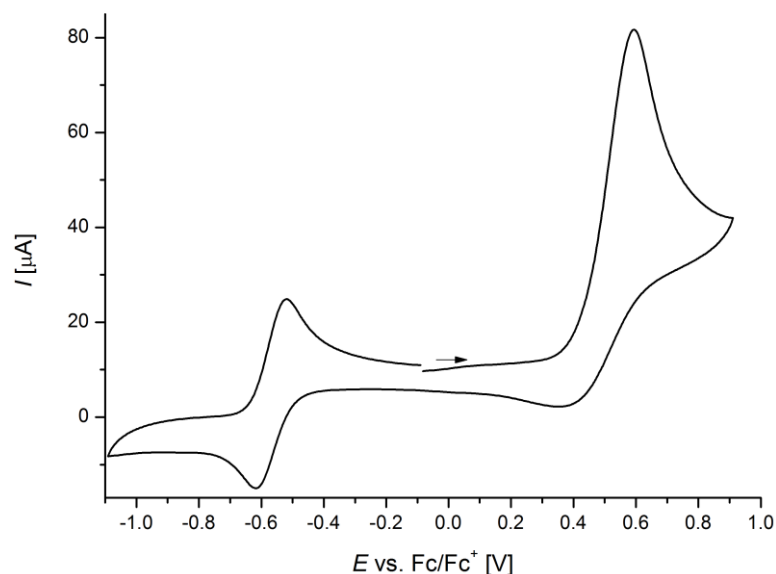


**Figure 58.** Cyclic voltammogram spectrum of 2.8 mM solution of **2** at 100 mV/s scan rate (0.1 M solution of NBu<sub>4</sub>PF<sub>6</sub> as supporting electrolyte,  $T = 0$  °C).

In order to get further insight into the oxidation event at  $E_{1/2} = -0.58$  V, complex **2** has also been oxidized chemically and the formation of a new species was followed *via* UV/vis absorption spectroscopy (see Figure 60). Therefore, a solution of AgSbF<sub>6</sub> ( $E^0 = 0.04$  V vs. Fc/Fc<sup>+</sup>, MeCN,  $T = 25$  °C)<sup>159</sup> was added stepwise in substoichiometric amounts to a solution of preformed peroxo complex **2** at -40 °C. The titration was complete with the addition of approximately 1.0 eq. of oxidant, showing that **2**

is oxidized by one electron. An isosbestic point at 485 nm indicates a clean conversion. The new species was found to be stable event at 0 °C and has a half-life time of ca. 8 h at 20 °C. A rR spectrum of this compound was recorded in solution at 22 °C and shows one oxygen isotope sensitive feature at 1073 cm<sup>-1</sup> ( $\Delta(^{16}\text{O}-^{18}\text{O}) = 60 \text{ cm}^{-1}$ ), which is at typical energy for a superoxide O-O stretching vibration (see Figure 60, right).<sup>82,76</sup>

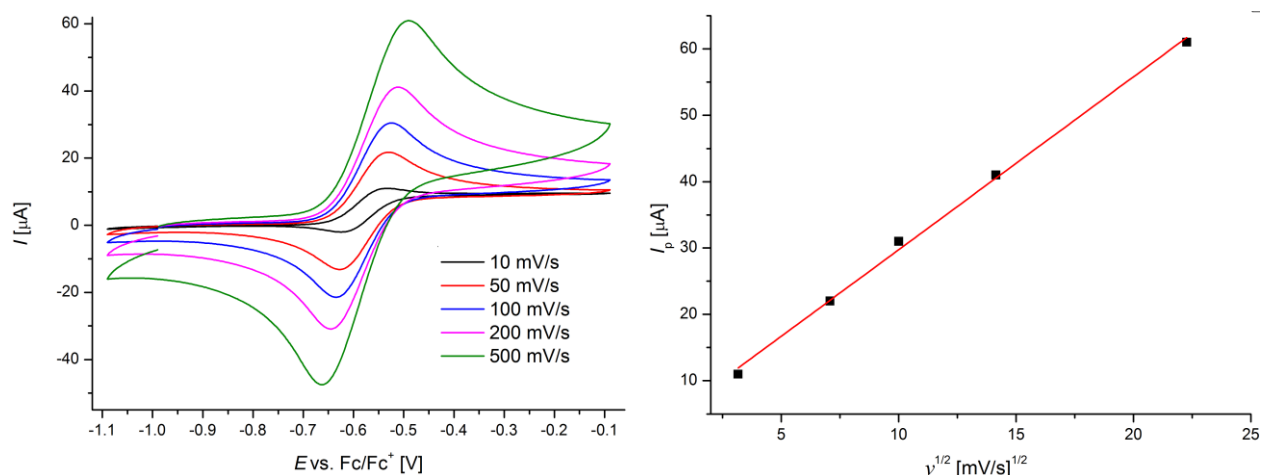


**Figure 59.** Left: Cyclic voltammograms of 3.0 mM solution of complex **2** at different scan rates (0.1 M solution of  $\text{NBu}_4\text{PF}_6$  as supporting electrolyte,  $T = 0 \text{ }^\circ\text{C}$ ); right: plot of anodic peak current  $I_p$  versus square root of scan rate;  $R^2 = 0.997$ .

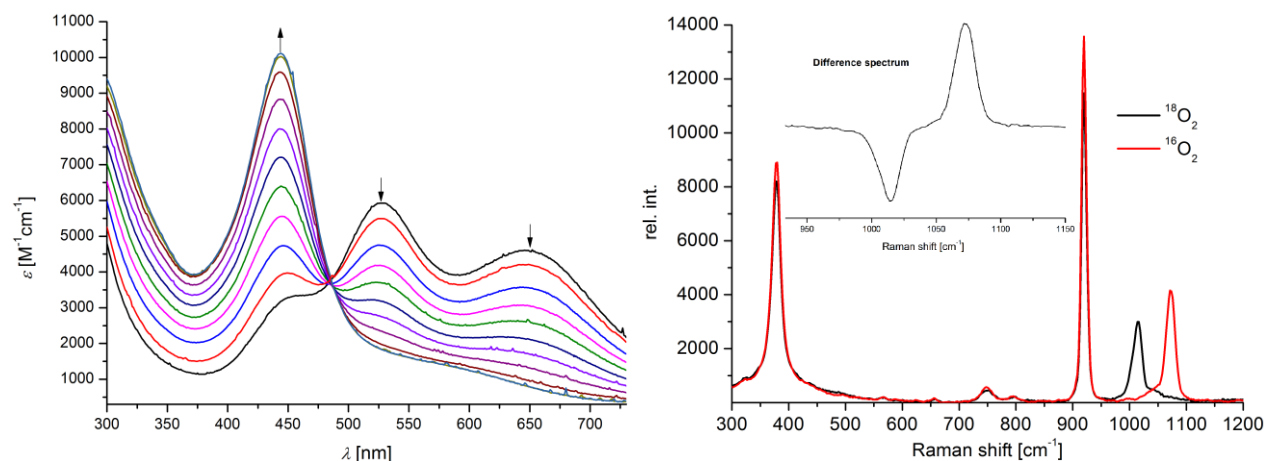
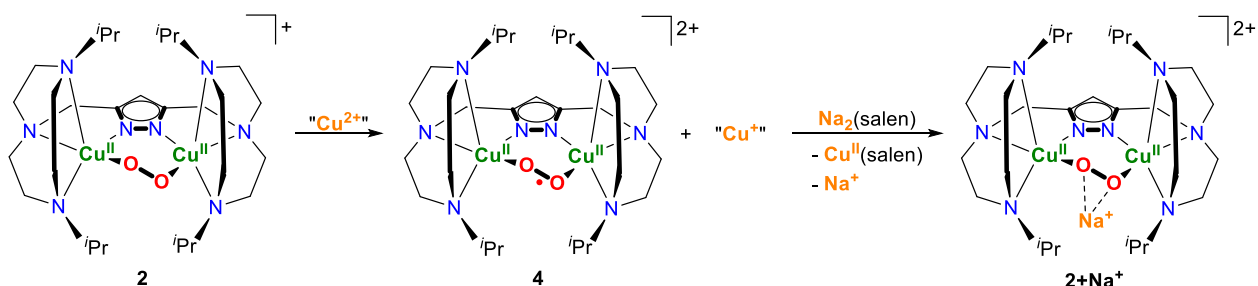


**Figure 60.** Left: Generation of superoxo complex **4** by addition of substoichiometric amounts of  $\text{AgSbF}_6$  to complex **2** in steps of 0.11 eq. with finally 1.10 eq. added; After the addition of 0.99 eq. of oxidant, no further change in absorbance was observed; (MeCN)  $T = -40 \text{ }^\circ\text{C}$ , isosbestic point at 485 nm; right: rR spectrum of 1.4 mM solution of **4** with laser excitation at 457 nm (MeCN,  $T = 22 \text{ }^\circ\text{C}$ ).

Besides  $\text{AgSbF}_6$  as chemical oxidant, also  $\text{Cu}(\text{OTf})_2$  and  $[(\text{Pr}_3\text{TACN})\text{Cu}(\text{CH}_3\text{CN})_2][(\text{SbF}_6)_2]$ <sup>160</sup> have been used during the UV/vis titration experiments. The resulting spectra, corresponding to cupric superoxide **4**, are identical and show that the electronic absorption spectra of **4** are independent from the introduced oxidant. The chemical oxidation of complex **2** was furthermore demonstrated to be

reversible. For that purpose, complex **2** has been oxidized with  $\text{Cu}(\text{OTf})_2$  and subsequently a solution of the disodium salt of *N,N'*-bis(salicylidene)ethylenediamine (**Na<sub>2</sub>salen**) was added. The addition of **Na<sub>2</sub>salen** immediately induced the reduction of **4** in forming sodium adduct **2+Na<sup>+</sup>** and **Cu<sup>I</sup>(salen)** (see Scheme 17 and Figure 61). The back reactions driving force is the formation of **Cu<sup>I</sup>(salen)** that is preferably formed under these conditions ( $E^\circ(\text{Cu}^{\text{I}}/\text{Cu}^{\text{II}}) = -1.66 \text{ V vs. Fc/Fc}^+$ , MeCN,  $T = 25 \text{ }^\circ\text{C}$ ).<sup>161</sup> The one electron that is needed to reduce **4** back to the peroxo level is delivered from the  $\text{Cu}^{\text{I}}$  cation that in return is oxidized into  $\text{Cu}^{\text{II}}$  in forming the corresponding **Cu<sup>II</sup>(salen)**-complex.



**Scheme 17.** Schematic representation of chemically reversible generation of complex **4** in using the  $\text{Cu}^{\text{II}}/\text{Cu}^{\text{I}}$  redox couple.

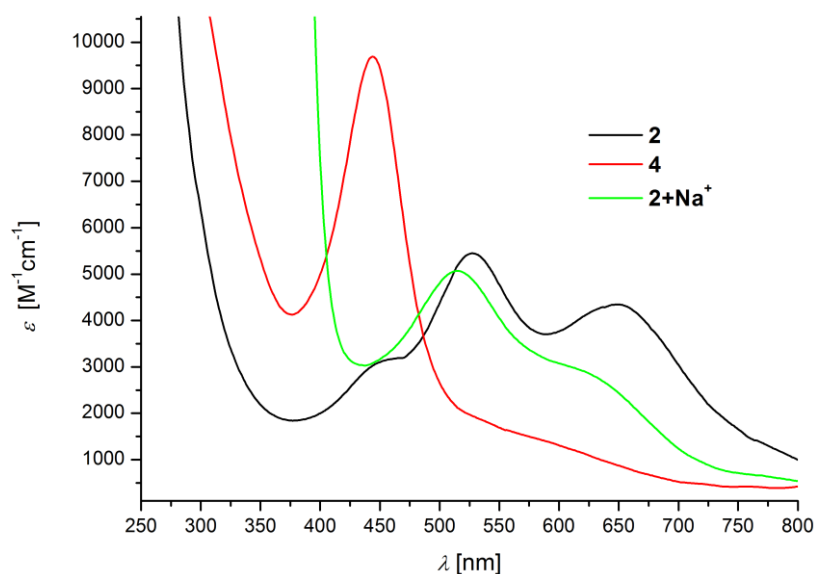


**Figure 61.** Electronic absorption spectra of precursor **2**, superoxo complex **4** (after addition of 1.1 eq. of  $\text{Cu}(\text{OTf})_2$  to complex **2**) and of **2+Na<sup>+</sup>** after the addition of 5.0 eq. of  $\text{Na}_2(\text{salen})$ .

In order to combine the aforementioned electrochemical oxidation of complex **2** with UV/vis absorption spectroscopy, the redox chemistry of complex **2** was also investigated by spectro-electrochemistry. Figure 62 shows the oxidation of **2** (for details see Section 7.6) *via* controlled potential electrolysis at  $-0.2 \text{ V vs. Fc/Fc}^+$ , MeCN,  $T = -15 \text{ }^\circ\text{C}$ ) for 20 minutes. The measurement shows the progressive formation of complex **4**, featuring the same maximum in absorbance as during a chemical generation from precursor **2**. The isosbestic point at 486 nm matches with that determined during the UV/vis titration experiment. Since complex **2** is oxidized electrochemically, the in Figure 62

depicted electronic absorption spectra exclusively correspond to the species **2** and **4**. Consequently, the nature of the UV/vis absorption spectrum shown in Figure 60 is not affected by the introduced oxidant, AgSbF<sub>6</sub> or by colloidal silver particles.

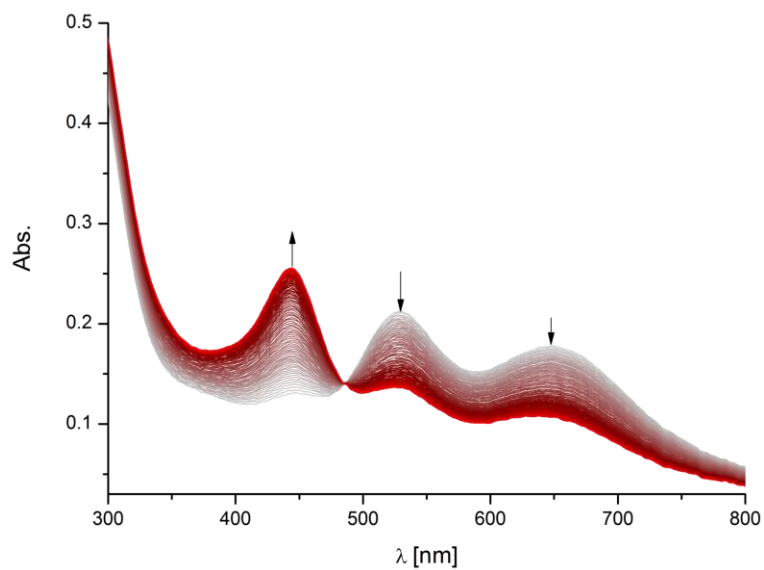


**Figure 62.** Spectro-electrochemistry of 600  $\mu\text{M}$  solution of **2** in MeCN at  $-15\text{ }^\circ\text{C}$ . Complex **2** is oxidized to superoxo species **4** (see Figure 60 for comparison) *via* controlled potential electrolysis at  $-0.2\text{ V}$  versus  $\text{Fc}/\text{Fc}^+$  for 20 minutes. After 20 minutes, no significant changes in the UV/vis spectrum can be observed; isosbestic point at 486 nm.

## 6.4.2 First Solid State Structure of a Dinuclear Copper(II) Superoxo Complex

Next to a detailed spectroscopic characterization of this cupric superoxo complex, also a solid state structure could be determined (see Figure 63). Crystalline material was obtained *via* Et<sub>2</sub>O diffusion into a concentrated solution of complex **4** in MeCN at -36 °C, with [(<sup>i</sup>Pr<sub>3</sub>TACN)Cu(CH<sub>3</sub>CN)<sub>2</sub>][SbF<sub>6</sub>]<sub>2</sub> used as oxidant. Next to this unusual oxidant also AgSbF<sub>6</sub> and AgBF<sub>4</sub> have been used, but no crystalline material was isolated.

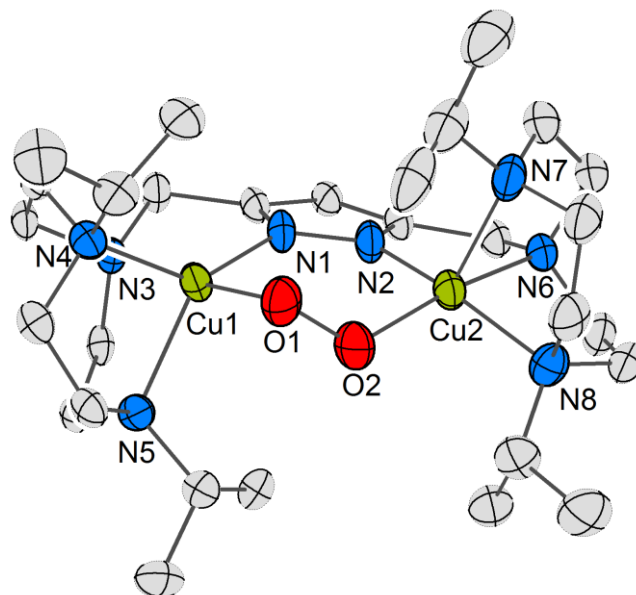


**Figure 63.** Molecular structure of **4** with thermal displacement ellipsoids given at 30% probability. Hydrogen atoms, counterion SbF<sub>6</sub><sup>-</sup>, and additional solvent molecules are omitted for clarity; for selected bond lengths and angles see Section 7.7.

The solid state structure represents the first structural evidence of a dinuclear copper superoxo complex. The superoxo moiety shows the same *cis*-geometry of the copper oxygen core as observed for peroxo complex **2**. However, the O-O bond length was found to decrease from 1.44 Å in **2** to 1.33 Å in **4**, which reflects the one-electron oxidation to occur at the peroxide with strengthening of the O-O bond. The Cu-O-O-Cu torsion angle in **4** was determined to 75.4° and is significantly larger than in complex **2** ( $\phi = 55.3^\circ$ ). The Cu...Cu distance was determined to 3.82 Å. The Cu-pyrazolate bond lengths are substantially shorter (Cu1-N1 = 1.90 Å, Cu2-N2 = 1.89 Å) than those of the Cu<sup>II</sup> ions to the TACN side arm nitrogen donor atoms (2.07-2.16 Å). The coordination environment of one of the two Cu<sup>II</sup> ions is nearly ideal square pyramidal ( $\tau(\text{Cu}2) = 0.08$ ) in contrast to that of the second Cu<sup>II</sup> ions ( $\tau(\text{Cu}1) = 0.63$ ), indicating a distorted trigonal bipyramidal coordination environment. The different coordination geometries at the Cu<sup>II</sup> ions as well as the Cu-O-O-Cu torsion angle of 75° may affect the overlap of copper- and oxygen-centered orbitals, but this outcome is discussed in Section 6.4.3.

### 6.4.3 DFT Calculations

Preliminary DFT calculations have been performed based on the crystallographic data of complex **4**, using the ORCA software package.<sup>162</sup> Spin unrestricted structure optimizations were conducted using the BP86 functional in combination with a def2-TZVP basis set.<sup>163,164</sup> The influence of solvent (MeCN) was considered using the COSMO method.<sup>165,166</sup> A comparison of calculated and experimental structural parameters is listed in Table 16.

**Table 16.** Selected distances and angles of experimental and calculated structures of **4**.

	$d$ (O-O) [Å]	$d$ (Cu-Cu) [Å]	$\phi$ (Cu-O-O-Cu) [°]
exp.: [L <sup>1</sup> Cu <sub>2</sub> ( $\mu$ -O <sub>2</sub> )] ( $S = 0.5$ )	1.33	3.82	75.4
calc.: [L <sup>1</sup> Cu <sub>2</sub> ( $\mu$ -O <sub>2</sub> )] ( $S = 0.5$ )	1.32	3.81	65.6
calc.: [L <sup>1</sup> Cu <sub>2</sub> ( $\mu$ -O <sub>2</sub> )] ( $S = 0.5$ ), MeCN	1.33	3.80	66.2
calc.: [L <sup>1</sup> Cu <sub>2</sub> ( $\mu$ -O <sub>2</sub> )] ( $S = 1.5$ )	1.32	3.89	32.2

The calculations for the doublet ground state revealed no significant differences irrespective of solvent influences being included or not (see Table 16, third and fourth line). The calculated distances match with those determined experimentally. Only the predicted Cu-O-O-Cu torsion angles deviate by approximately 10° from the experimental value. However, if the calculated parameters of the corresponding quartet ground state are considered (Table 16, line five), a Cu-O-O-Cu dihedral angle of 32° is predicted, which significantly deviates from the experimental value of 75°. Additionally, the calculated Cu-Cu distance is not supported by the experimentally determined parameters.

In order to verify the magnetic ground state of complex **4**, spin unrestricted single point calculations have been performed using a B3LYP functional and a def2-TZVP basis set (RIJCOSX approximation in combination with auxiliary def2-TZVP/J basis set; D3 dispersion correction with zero damping).<sup>167</sup> The calculations predict a quartet ground state. The  $S = 0.5$  state was calculated to be 4.6 kcal mol<sup>-1</sup> higher in energy. This outcome however is contrary to the aforementioned geometry optimization, favoring a doublet ground state.

To gain insight into the magnitude of magnetic coupling between the copper atoms and superoxide, spin unrestricted broken symmetry calculations have been performed (functional: B3LYP, def2-TZVP basis set, RIJCOSX approximation in combination with auxiliary def2-TZVP/J basis set). The calculations started from a quartet state of which the spin of the unpaired electron of e.g. Cu1 has been flipped, resulting in an overall doublet state. The magnetic coupling between Cu1 and the superoxide then was investigated. This procedure was as well applied on Cu2. The corresponding magnetic orbitals are depicted in Figure 64.

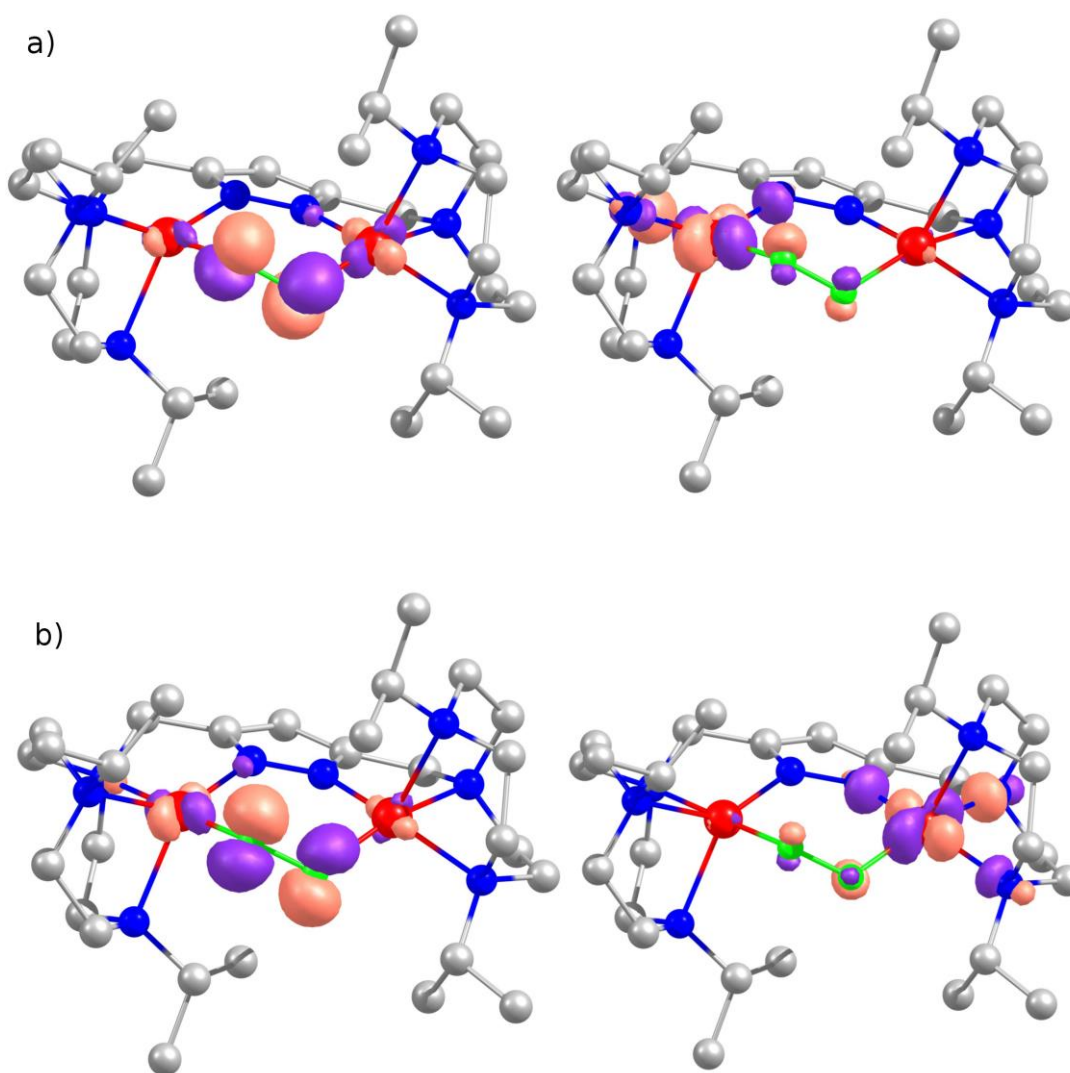


**Figure 64.** Corresponding magnetic orbitals of broken symmetry calculations after flipping the spin of a): Cu1 (left: orbital 178 $\alpha$ , right: orbital 178 $\beta$ ); and after flipping the spin of b): Cu2 (left: orbital 178 $\alpha$ , right: orbital 178 $\beta$ ).

The magnetic coupling between Cu and oxygen atoms is a function of overlap of the magnetic orbitals.<sup>111</sup> The magnetic coupling constant  $J$  has been calculated according to equation 16):

$$16) \quad J = \frac{E_{HS} - E_{BS}}{\langle S_{orb}^2 \rangle_{HS} - \langle S_{orb}^2 \rangle_{BS}}$$

$S_{orb}$  represents the overlap of the involved magnetic orbitals.<sup>168</sup>  $S_{orb} = 0$  corresponds to no overlap (full overlap is observed for  $S_{orb} = 1$ ) and thus no magnetic coupling would be observed. The overlap of the magnetic orbital pairs was calculated to be 0.45 (O1Cu1) and 0.40 (O2Cu2), resulting in magnetic coupling constants of  $J(O1Cu1) = -480 \text{ cm}^{-1}$  and  $J(O2Cu2) = -475 \text{ cm}^{-1}$ , respectively. This outcome demonstrates that copper and oxygen atoms in **4** magnetically interact, but show significant lower magnetic coupling than other literature known dinuclear superoxo complexes, featuring a doublet ground state (see ref.<sup>90</sup>  $J(O1Cu1) = -1066 \text{ cm}^{-1}$ ;  $J(O2Cu2) = -1057 \text{ cm}^{-1}$ ). Figure 65 shows the calculated spin density after flipping the spin of Cu1 and Cu2, respectively. A significant amount of spin density is observed on the copper and oxygen atoms.



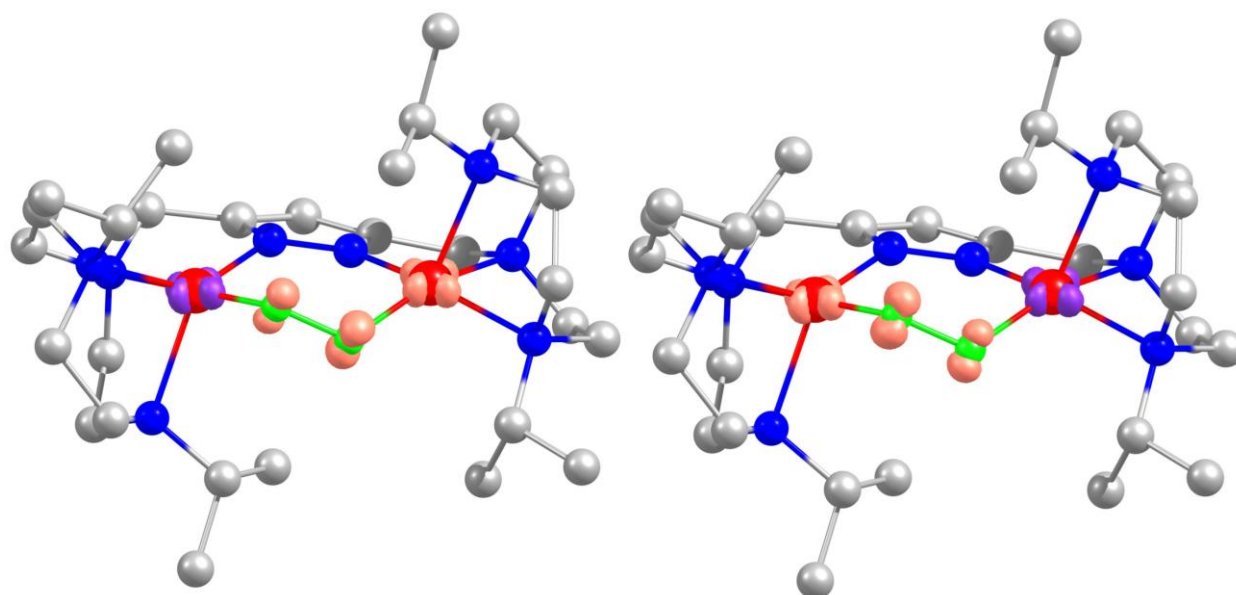
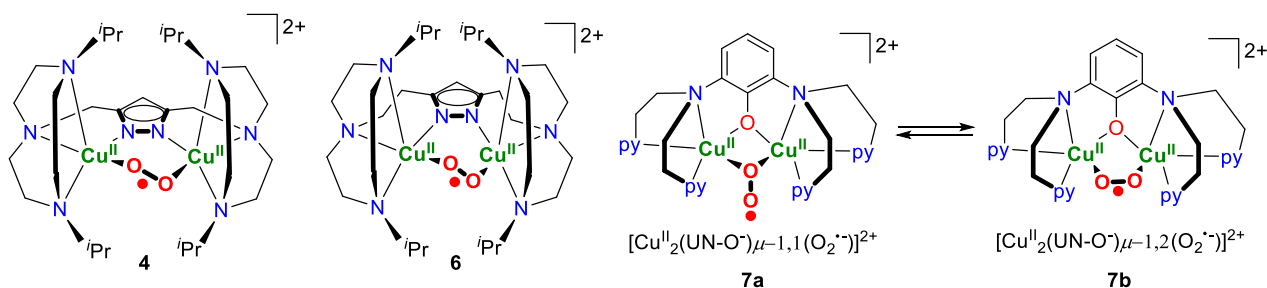


**Figure 65.** Corresponding spin density after flipping the spin of Cu1 (left) and Cu2 (right); Mulliken spin population left: Cu1 = -0.51, Cu2 = 0.54, O1 = 0.37, O2 = 0.55; right: Cu1 = 0.53, Cu2 = -0.51, O1 = 0.59, O2 = 0.39.

In summary, the structural parameters obtained from fully optimized geometries favor a doublet ground state, while spin unrestricted single point calculations predict a quartet state to be lowest in energy. Spin unrestricted broken symmetry calculations show the magnitude of magnetic coupling in complex **4** to be relatively weak due to small overlap of copper- and oxygen-centered orbitals, thus supporting the assumed quartet ground state. The weak magnetic coupling between copper and oxygen atoms may be induced by the Cu-O-O-Cu torsion of 75° angle as well as by the more trigonal bipyramidal coordination geometry of one of the Cu<sup>II</sup> ions (see Section 6.4.2).

## 6.4.4 EPR Spectroscopy and SQUID Magnetometry

In order to verify the spin ground state of superoxo complex **4**, EPR spectroscopy of frozen MeCN solution state samples was performed. Several independent spectra have been recorded, of which one sample was prepared from crystalline material of complex **4**, while other samples were obtained from reacting complex **2** with  $\text{AgSbF}_6$  in situ (see Section 7.8 for experimental details). All experiments independently show the same signal pattern. In Section 6.4.1, complex **4** was demonstrated to be selectively synthesized from precursor **2** and various oxidants. No side reactions were observed and **4** is stable for several hours even at 0 °C. Thus, the corresponding EPR samples are assumed to exclusively contain complex **4**. However, before the results for superoxide **4** are presented, the EPR spectra of the literature known dinuclear superoxo complexes **6**, **7a** and **7b** will be discussed (see Scheme 18).<sup>77,90</sup> It should be however noted that no structural information exist for any of these complexes.



**Scheme 18.** Discussed dinuclear superoxo complexes, all of which are showing different EPR spectra due to a specific geometry of the corresponding copper oxygen cores (UN-OH = 2-(bis(2-(pyridin-2-yl)ethyl)amino)-6-((bis(2-(pyridin-2-yl)ethyl)amino)-methyl)phenol).<sup>77,90</sup> Only complex **4** is structurally characterized.

The complexes **6** and **7a** exhibit significant structural differences, which are reflected by the corresponding EPR spectra.<sup>77,90</sup> In complex **7a**, the superoxide shows a  $\mu$ -1,1 binding mode.<sup>77</sup> **7a** has been proposed to be in a fast equilibrium with complex **7b**, where the copper oxygen core is featuring a *cis*-geometry ( $\mu$ -1,2  $\text{O}_2^-$  binding mode).<sup>77</sup> Irrespective of the superoxide binding motif, a doublet ground state was predicted for both complexes by DFT calculations.<sup>77</sup> In complex **6** on the other hand, only a  $\mu$ -1,2 binding mode is observed.<sup>90</sup> DFT calculations also predict a doublet ground state.<sup>90</sup> The two completely different superoxide binding modes in **6** and **7a** are giving rise to characteristic EPR spectra.<sup>77,90</sup> In complex **7a** the two  $\text{Cu}^{\text{II}}$  ions are strongly antiferromagnetically coupled *via* the bridging oxygen atom, resulting in one unpaired electron located on the superoxide.<sup>77</sup> The corresponding EPR spectrum shows one characteristic nearly isotropic signal, featuring a *g*-value of approximately 2.0, which is typical for an organic radical.<sup>77</sup> However, since **7a** is in equilibrium with **7b**, the corresponding EPR spectrum is a mixture of both species and additionally shows some fine structure, which could not be resolved.<sup>77</sup> No coupling to copper atoms is assumed to take place.<sup>77</sup> Consequently, both species are featuring the same spin ground state with the unpaired electron located on the superoxide. However,

the authors did not specify the actual ratio of the complexes **7a** and **7b** in solution and thus the interpretation of the EPR spectrum is only qualitative. If for instance **7a** represents the main species, complex **7b** only marginally contributes to the mixed EPR spectrum. The unpaired electron in **7b** could then also be located on a Cu<sup>II</sup> ion and the corresponding total EPR spectrum would still show a roughly isotropic signal at  $g \approx 2$  with no significant contribution of a Cu<sup>II</sup> signal. The experimentally observed but only poorly resolved postulated fine structure then would correspond to complex **7b**, with the unpaired electron being located on a Cu<sup>II</sup> ion.

The spectrum of compound **6** on the other hand shows a typical axial signal pattern of a copper(II) complex.<sup>90</sup> DFT calculations predict a doublet ground state for complex **6**.<sup>90</sup> In contrast to **7a**, the unpaired electron is located on a Cu<sup>II</sup> ion.<sup>90</sup> The strong antiferromagnetic coupling of the superoxide to one of the Cu<sup>II</sup> ions can be rationalized by the computationally predicted Cu-O-O-Cu torsion angle of approximately 103° in **6**. Due to this arrangement, each of the superoxide  $\pi^*$  orbitals is interacting with only one of the Cu<sup>II</sup> ions. No superexchange of the copper-centered unpaired electrons *via* the superoxide bridge is possible, as observed for complex **7a**.<sup>77</sup> Nevertheless also this interpretation is only qualitative, since no structural evidence for the proposed  $\mu$ -1,2 binding mode is available and the Cu-O-O-Cu torsion angle of 103° is only predicted by DFT calculations. However, comparison of complexes **6** and **7a** shows that structural differences in the superoxide binding mode can be visualized by EPR spectroscopy.

With this knowledge in hand, the structural properties of superoxo complex **4** will be reconsidered. The molecular structure of **4** revealed a  $\mu$ -1,2 binding mode, which is also assumed for the complexes **6** and **7b**. In contrast to compound **6**, a Cu-O-O-Cu torsion angle of 75° is observed in complex **4**, providing a possible superexchange pathway for antiferromagnetic coupling of the Cu<sup>II</sup> ions *via* the superoxide bridge. However, DFT calculations predict a  $S = 1.5$  ground state in ruling out an effective superexchange of the Cu<sup>II</sup> ions *via* the superoxide (see also Section 6.4.3). Nevertheless, the calculated Cu-O-O-Cu dihedral angle for the quartet ground state ( $\phi_{\text{calc.}}^{S=1.5} = 32^\circ$ ) significantly deviates for the experimentally observed torsion angle, whereas the computationally predicted parameters of the corresponding doublet ground state ( $\phi_{\text{calc.}}^{S=0.5} = 66^\circ$ ) are similar to the structural values. In summary, the computationally predicted  $S = 1.5$  ground state is counterintuitive, since the associated computationally predicted Cu-O-O-Cu torsion angle of 32° would provide a superexchange pathway *via* the superoxo moiety. The Cu<sup>II</sup> ions would then be antiferromagnetically coupled, resulting in an overall doublet ground state. However, the magnitude of magnetic exchange interactions of the two copper atoms *via* the superoxide bridge is furthermore affected by the geometry at the Cu<sup>II</sup> ions.<sup>145</sup> The corresponding molecular structure of **4** revealed a square pyramidal coordination geometry of one Cu<sup>II</sup> ion ( $\tau(\text{Cu}2) = 0.08$ )), whereas the second Cu<sup>II</sup> ion is coordinated in a trigonal bipyramidal fashion ( $\tau(\text{Cu}1) = 0.63$ ).

These large differences indeed may affect the superexchange pathway *via* the superoxide bridge due to significantly different coordination geometries of the two Cu<sup>II</sup> ions.

In order to verify the actual magnetic ground state of complex **4** experimentally, SQUID magnetic measurements were carried out with solution state samples (for experimental details see Section 7.3). Until to date not enough crystalline material of complex **4** could be grown and thus only solution state data are available for this species. Figure 66 shows one representative example of a 16 mM solution of **4**. The molar magnetization  $M_m$  of complex **4** is thereby described as:<sup>169</sup>

$$17) \quad M_m = N_A g \mu_B S B_S(x); \quad x = \frac{g \mu_B B}{kT}$$

For large values of  $x$ , the Brillouin-function  $B_S(x)$  becomes 1 and equation 17) simplifies to:<sup>169</sup>

$$18) \quad M_m = N_A g \mu_B S$$

Consequently, the total spin  $S$  of the system can be determined *via* a plot of  $M_m/N_A g \mu_B$  versus  $\mu_B B/kT$ . The saturation of the curve, depicted in Figure 66, corresponds to the total spin of complex **4**, which was determined to  $S = 0.5$  ( $T = 2$  K).

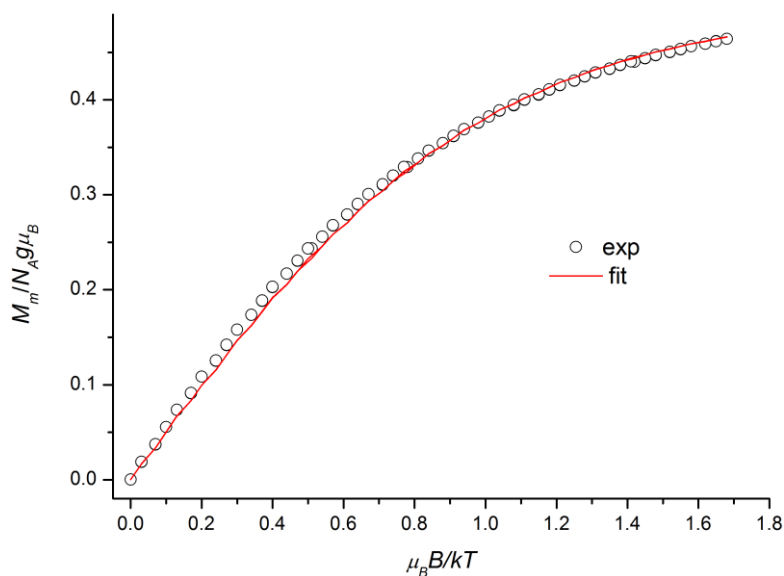


**Figure 66.** Plot of  $M_m/N_A g \mu_B$  versus  $\mu_B B/kT$ ; from the saturation the spin ground state is determined to  $S = 0.5$  ( $T = 2$  K,  $B = 5$  T,  $g = 2.00$  (fixed)).

With the actual spin ground state of superoxide **4** in hand, the corresponding EPR spectrum can be interpreted. Figure 67 shows an axial Cu<sup>II</sup> X-band EPR spectrum of a frozen MeCN solution of complex **4** recorded at 161 K. The spectrum was simulated as  $S = 0.5$  system with the software package easyspin, reproducing the experimental data ( $g$ -strains were applied).<sup>117</sup> Three  $g$ -values of  $g_x = 2.01$ ,  $g_y = 2.06$ ,  $g_z = 2.23$  were simulated ( $a_1 = 10$  G,  $a_2 = 70$  G,  $a_3 = 225$  G). In comparison to the X-band EPR spectrum of complex **6**, significant line broadening is observed. Since the sample was prepared in a glove box with  $<0.1$  ppm O<sub>2</sub>, line broadening due to a contamination with O<sub>2</sub> can be excluded. One further possibility may be the presence of a second superoxo species as observed for the complexes **7a** and **7b**, featuring a slightly different electronic structure. However, the simulated  $g$ -values of **4** and **6** are nearly identical

(6:  $g_x = 2.02$ ,  $g_y = 2.05$ ,  $g_z = 2.22$ ;  $a_1 = 10$  G,  $a_2 = 30$  G,  $a_3 = 165$  G), pointing at similar geometries of the copper oxygen cores in both complexes.

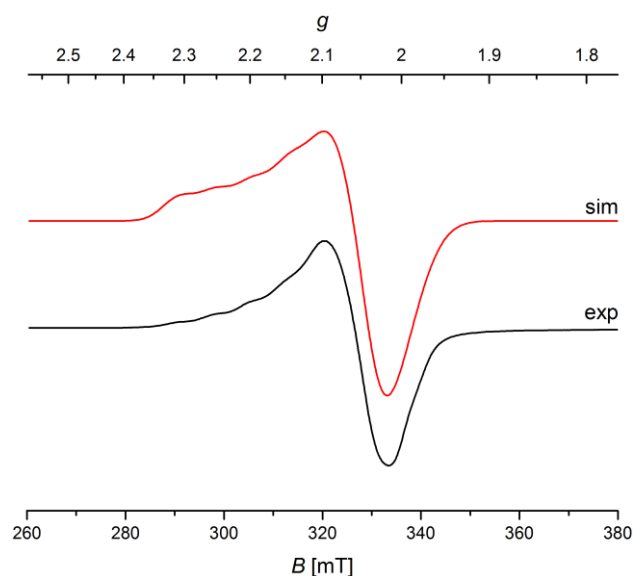


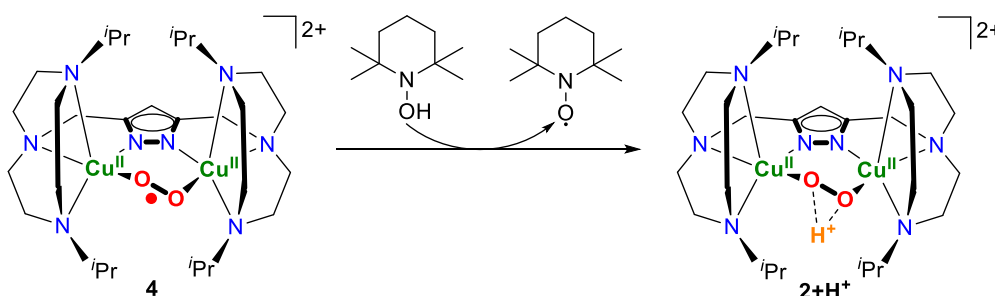
**Figure 67.** X-band EPR spectrum (black line) and corresponding simulation<sup>117</sup> (red line) of 0.01 M frozen solution of **4** in MeCN recorded at 161 K.

In summary, the magnetic properties of complex **4** were investigated. While preliminary DFT calculations do not allow any definite assignment of the magnetic ground state, SQUID magnetometric measurements in solution revealed a doublet ground state. With respect to EPR spectroscopy, the unpaired electron may be located on one of the two  $\text{Cu}^{\text{II}}$  ions while the other  $\text{Cu}^{\text{II}}$  ion antiferromagnetically couples with the superoxide. However, these findings are not supported by the DFT calculations. With respect to the molecular structure of complex **4**, the coordination environment of one of the  $\text{Cu}^{\text{II}}$  ions is more square pyramidal while the coordination environment of the other  $\text{Cu}^{\text{II}}$  ion is significantly distorted towards a trigonal bipyramidal geometry. With respect to an effective antiferromagnetic coupling of superoxide and  $\text{Cu}^{\text{II}}$  ion, the more square pyramidal coordination environment of one of the  $\text{Cu}^{\text{II}}$  ions corresponds to a good overlap of copper- and oxygen-centered orbitals, while a distortion towards a more trigonal bipyramidal environment diminishes such an interaction. However, only solution state magnetic data are available which cannot be directly related to the structural parameters, and thus magnetic data obtained from solid state samples of **4** are of considerable future interest.

## 6.4.5 Substrate Reactivity

The to date limited number of cupric superoxo complexes, of which only a few mononuclear examples are structurally characterized,<sup>76,84</sup> has been mainly tested towards phenolic O-H bond cleavage reactions.<sup>170,79,146</sup> The working groups of ITOH<sup>87</sup> and KARLIN<sup>78</sup> recently reported mononuclear copper superoxo complexes that mediate also benzylic C-H bond oxygenation, providing mechanistic insight into the biological processes of peptidylglycine  $\alpha$ -hydroxylating monooxygenase (PHM) and of dopamine  $\beta$ -monooxygenase (D $\beta$ M), which have been proposed to involve reactive copper oxygen species during substrate conversion.<sup>87,171,43</sup>

Since complex **4** represents the first structurally characterized dinuclear cupric superoxo complex, its reactivity has been tested towards various O-H and C-H bond substrates. Substrate reactivity was monitored by UV/vis absorption spectroscopy in the temperature range from 0 to -40 °C in MeCN. Complex **4** is unreactive towards various C-H substrates, such as 1,4-Cyclohexadiene, 9,10-Dihydroanthracene and Thioxanthene. Also O-H substrates such as the phenol derivatives 2,4-*tert*-butylphenol and 4-(dimethylamino)phenol have been tested without observing any reactivity. However, when TEMPO-H is used as substrate (BDFE = 66.5 kcal mol<sup>-1</sup>, BDE = 69.6 kcal mol<sup>-1</sup> in MeCN)<sup>172,173</sup> kinetic data could be obtained (for experimental details see Section 7.12). Complex **4** thereby cleanly reacts with TEMPO-H in forming hydroperoxide **2+H<sup>+</sup>** (see Scheme 19).



**Scheme 19.** Reaction of **4** with TEMPO-H in forming hydroperoxide **2+H<sup>+</sup>**.

Before the kinetic data of this reaction will be discussed in detail, a thermodynamic square scheme for the transformation of **4** into **2+H<sup>+</sup>** will be introduced (see Scheme 20).<sup>174</sup> Since the thermodynamic parameters for the reaction of **2+H<sup>+</sup>** to **2** as well as for the oxidation of **2** into superoxide **4** are available (see Step1 and Step2 in Scheme 20), the strength of the O-H bond in **2+H<sup>+</sup>** can be calculated according to Hess' Law.<sup>174</sup> The corresponding bond dissociation free energy (BDFE) can be derived as follows:<sup>174</sup>

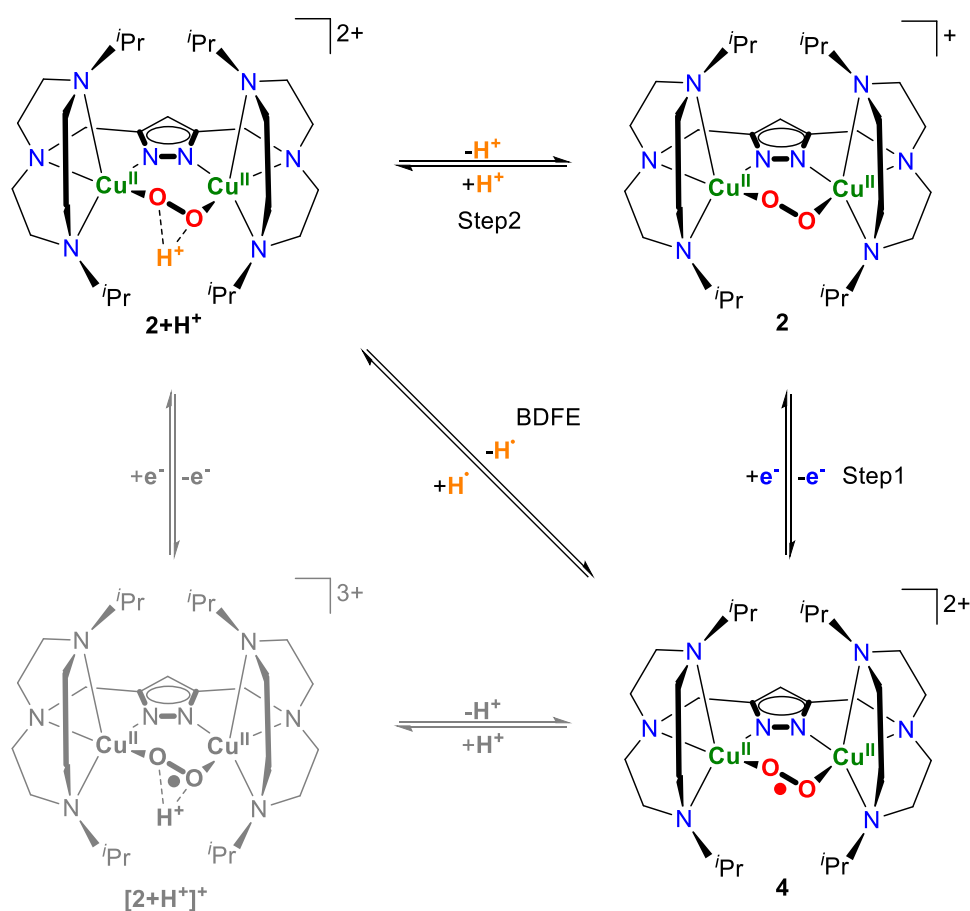
$$19) \quad \text{BDFE}_{\text{sol}}(\text{OOH}) = 1.37\text{p}K_{\text{a}}(T = 25 \text{ }^{\circ}\text{C}) + 23.06E^0 + C_{G,\text{sol}}$$

Where  $C_{G,\text{sol}}$  includes the free energy of formation of H<sup>•</sup>, the free energy for solvation of H<sup>•</sup> and the nature of the used reference electrode.<sup>174</sup> However, the pK<sub>a</sub> of **2+H<sup>+</sup>** has been determined at -40 °C,

which will be used instead of the  $pK_a$  value at  $T = 25\text{ }^\circ\text{C}$ . Furthermore,  $E_{1/2}$  is assumed to be a good approximation of  $E_0$  and thus equation 19) is changed to:<sup>174</sup>

$$20) \quad \text{BDFE}_{\text{sol}}(\text{OOH}) = 1.37pK_a(T = -40\text{ }^\circ\text{C}) + 23.06E_{1/2} + C_{G,\text{sol}} = 71.4 \pm 0.3 \text{ kcal mol}^{-1}$$

With  $pK_a(\mathbf{2}+\mathbf{H}^+) = 21.8$  (MeCN,  $T = -40\text{ }^\circ\text{C}$ ),  $E_{1/2} = -0.58\text{ V}$  (versus  $\text{Fc}/\text{Fc}^+$ , MeCN,  $T = 0\text{ }^\circ\text{C}$ ) and  $C_{G,\text{sol}} = 54.9 \text{ kcal mol}^{-1}$  (MeCN,  $T = 25\text{ }^\circ\text{C}$ )<sup>174</sup>, a BDFE of  $71.4 \pm 0.3 \text{ kcal mol}^{-1}$  could be determined. In order to substantiate this calculation, different reagents were tested to bracket the relevant BDFE range. Since complex **4** cleanly reacts with TEMPO-H (BDFE =  $66.5 \text{ kcal mol}^{-1}$ )<sup>174</sup>, but does not react with 4-(Dimethylamino)phenol (BDFE =  $72.4 \text{ kcal mol}^{-1}$ )<sup>175</sup>, the BDFE must fall within the mentioned limits. Thus, the calculated BDFE of  $71.4 \text{ kcal mol}^{-1}$  for complex  $\mathbf{2}+\mathbf{H}^+$  is in good agreement with the observed chemical behavior (see Table 17 for BDFEs of all studied substrates).



**Scheme 20.** Thermodynamic square scheme for reaction of **4** to  $\mathbf{2}+\mathbf{H}^+$ . No experimental evidence for  $[\mathbf{2}+\mathbf{H}^+]^+$  could be found.<sup>174</sup>

Nevertheless, the reaction of **4** to  $\mathbf{2}+\mathbf{H}^+$  could occur *via* one concerted kinetic step (concerted proton-electron transfer (CPET) or H-atom transfer (HAT)) or *via* two sequential steps such as electron transfer (ET) in forming complex **2**, followed by subsequent proton transfer (PT) (see Scheme 20). Since a hydrogen atom is transferred to the superoxide during the concerted process, this reaction is denoted as HAT rather than CPET. A two-step reaction starting with the protonation of **4** in forming an oxidized

hydroperoxide (denoted as  $[2+H^+]^+$  in Scheme 20) followed by successive reduction is ruled out. A corresponding control experiment showed that **4** cannot be protonated with e.g. 2,6-lutidinium triflate. In order to verify if the H-atom transfer from TEMPO-H on superoxo complex **4** occurs *via* one concerted step or by two sequential steps starting with ET on superoxide **4**, the thermodynamic parameters for both possible mechanisms will be compared. Since **4** readily reacts with TEMPO-H,  $\Delta G_{\text{HAT}}^0$  can be derived as follows:<sup>174</sup>

$$21) \quad \Delta G_{\text{HAT}}^0 = \text{BDFE}(\text{TEMPO-H}) - \text{BDFE}(\mathbf{2} + \mathbf{H}^+) = -4.9 \pm 0.3 \text{ kcal mol}^{-1}$$

The free energy for the ET (**4** → **2**) can be calculated according to:<sup>174</sup>

$$22) \quad \Delta G_{\text{ET}}^0 = -zF\Delta E^0 = -(23.06 \text{ kcal mol}^{-1} \text{ V}^{-1})\Delta E^0 = 29.7 \pm 0.2 \text{ kcal mol}^{-1}$$

, where  $R$  represents the gas constant and  $F$  the Faraday constant;  $E^0(\text{TEMPO-H}/\text{TEMPO-H}^+) = 0.71 \text{ V}$ .<sup>176</sup>

The free energy for the ET is rather high and thus two steps initiated by an ET are unlikely. However, a more detailed discussion is provided later, when the free energy for the ET will be compared to the actual activation energy of this reaction obtained from kinetic studies.

**Table 17.** Substrates tested during substrate reactivity with **4**.

substrate	BDFE	reaction <sup>c</sup>
2,4-Di- <i>tert</i> -butylphenol	78.9 <sup>a,175</sup>	no
9,10-Dihydroanthracene	75.0 <sup>174</sup>	no
Thioxanthene	73.7 <sup>b,90</sup>	no
1,4-Cyclohexadiene	72.9 <sup>b,174</sup>	no
4-(Dimethylamino)phenol	72.3 <sup>a,175</sup>	no
TEMPO-H	66.5 <sup>174</sup>	yes

<sup>a</sup>BDFEs have been calculated from corresponding BDEs according to:  $\text{BDFE}_{\text{sol}}(\text{O-H}) = \text{BDE}_{\text{sol}}(\text{O-H}) - (C_{\text{H},\text{sol}} - C_{\text{G},\text{sol}})$ ;  $C_{\text{H},\text{sol}} = 59.4 \text{ kcal mol}^{-1}$ ,  $C_{\text{G},\text{sol}} = 54.9 \text{ kcal mol}^{-1}$ .<sup>174</sup> <sup>b</sup>BDFEs were calculated from gas phase BDFEs according to:  $\text{BDFE}_{\text{sol}}(\text{X-H}) = \text{BDFE}_{\text{gas}}(\text{XH}) + \Delta G_{\text{sol}}^0(\text{H}^+) + \Delta G_{\text{sol}}^0(\text{X}^-) - \Delta G_{\text{sol}}^0(\text{XH})$ ; the free energies of XH and X<sup>-</sup> were assumed to be of same dimension ( $\Delta G_{\text{sol}}^0(\text{X}^-) - \Delta G_{\text{sol}}^0(\text{XH}) = 0$ ) and thus  $\text{BDFE}_{\text{sol}}(\text{X-H}) = \text{BDFE}_{\text{gas}}(\text{XH}) + \Delta G_{\text{sol}}^0(\text{H}^+)$ .<sup>174</sup> <sup>c</sup> $T = -40 \text{ }^\circ\text{C}$ , MeCN.

With the BDFE of complex  $\mathbf{2+H}^+$  in hand, the reaction of **4** with TEMPO-H will be reconsidered. If TEMPO-H is added to the preformed superoxo complex (generated from complex **2** and  $\text{AgSbF}_6$ ), the complex rapidly forms complex  $\mathbf{2+H}^+$  (see Figure 68 and Figure 69). Isosbestic points at 290, 362 and 380 nm indicate a clean conversion.



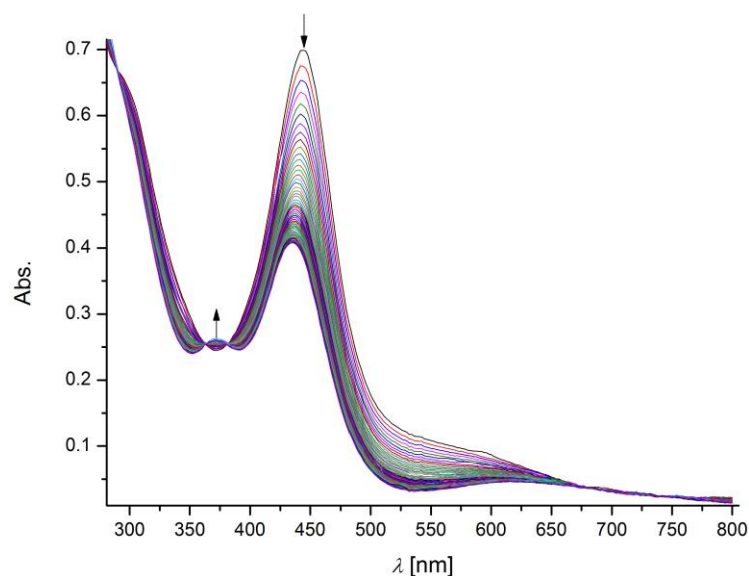


**Figure 68.** Reaction of complex **4** with 1.5 eq. of TEMPO-H; (MeCN,  $T = -40\text{ }^{\circ}\text{C}$ ); isosbestic points at 290, 362 and 380 nm.

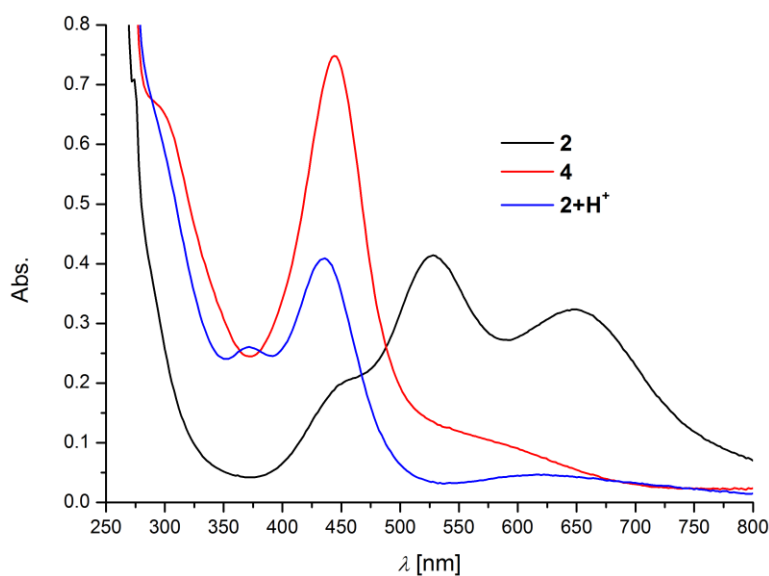


**Figure 69.** UV/vis spectra of complex **4** (red line), its precursor **2** (black line) and the product after addition of 1.5 eq. of TEMPO-H (blue line).

The conversion of **4** into  $\mathbf{2+H}^+$  is not only clean but also quantitative, as control experiments prove. To that end, a solution of precursor **2** was reacted with a solution of 2,6-lutidinium triflate in MeCN in forming  $\mathbf{2+H}^+$  (see Section 6.3 for details concerning protonation of **2**), which is used as reference spectrum (Figure 70, black line). Then, equimolar solutions of precursor **2** were oxidized into cupric superoxo complex **4** and subsequently 3.0 eq. (Figure 70, red line) and in another experiment 18.0 eq. (Figure 70, blue line) of TEMPO-H were added. The dilution of the precursor concentration during the addition of oxidant and substrate was minimal.

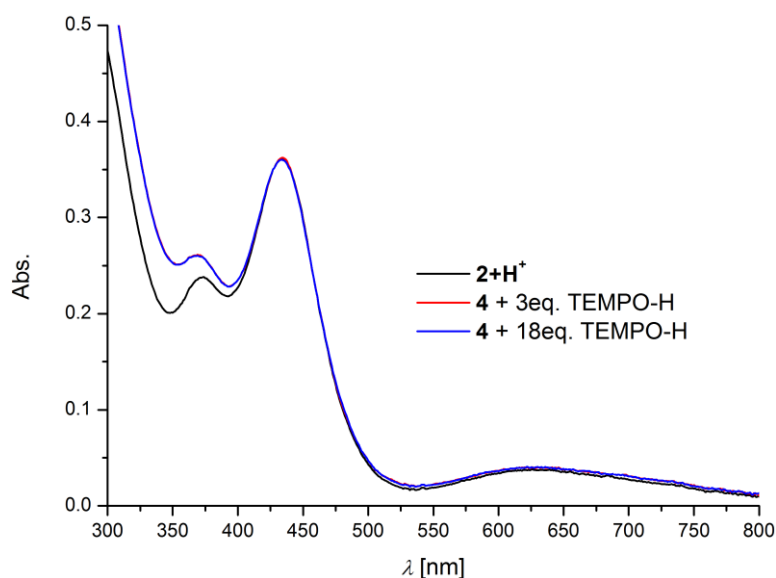


**Figure 70.** UV/vis absorption spectra of  $2+H^+$  generated from titration of **2** with 2,6-lutidinium triflate (black line) and of the product of the reaction of **4** with different excess of TEMPO-H (red and blue line). The concentration of precursor **2** was  $74 \mu\text{M}$  in all three experiments, showing that **4** quantitatively reacts with TEMPO-H under exclusion of side reactions.

Both product UV/vis absorption spectra are identical and match with the reference spectrum of  $2+H^+$ . The maximum at 372 nm of both product spectra is slightly more intense and blue-shifted compared to that of the reference, which is due to the presence of TEMPO radical after the reaction. The TEMPO radical has an absorption maximum in the near UV region that adds to the maximum of  $2+H^+$  and induces the observed blue-shift of the band at 372 nm.

From previous experiments (see Section 6.3 for details), complex  $2+H^+$  is known to be reversibly formed from **2** and 2,6-lutidinium triflate. Consequently,  $2+H^+$  has also been deprotonated under the aforementioned substrate reactivity conditions. Figure 71 shows the corresponding UV/vis absorption spectrum after addition of 2.0 eq. of DBU to the product of the reaction of **4** with TEMPO-H,  $2+H^+$ . The spectrum is identical to the electronic absorption spectrum of the “usual” deprotonation of  $2+H^+$  with DBU (see Section 6.3), highlighting the overall clean conversion of e.g. **4** into  $2+H^+$ . It should be noted that peroxo complex **2** forms a weak adduct with the protonated form of DBU. Thus, the in Figure 71 depicted electronic absorption spectra are slightly varying (see Section 6.3 for details).

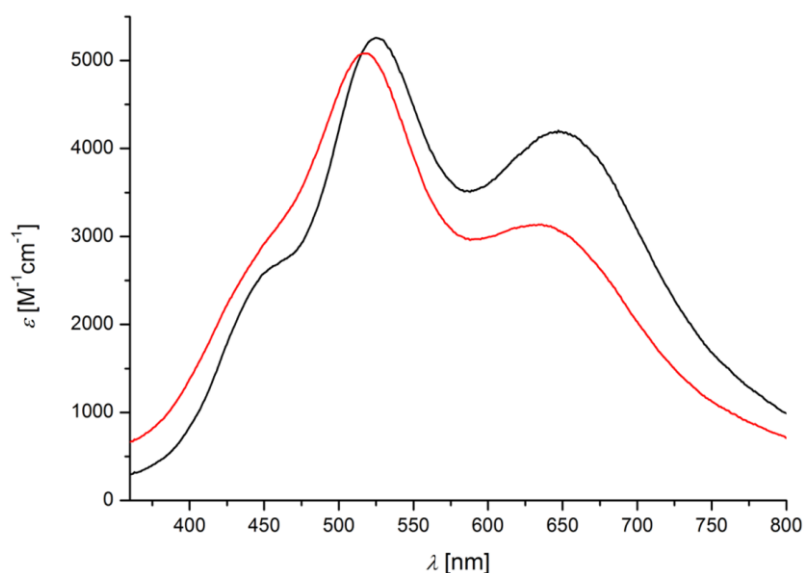


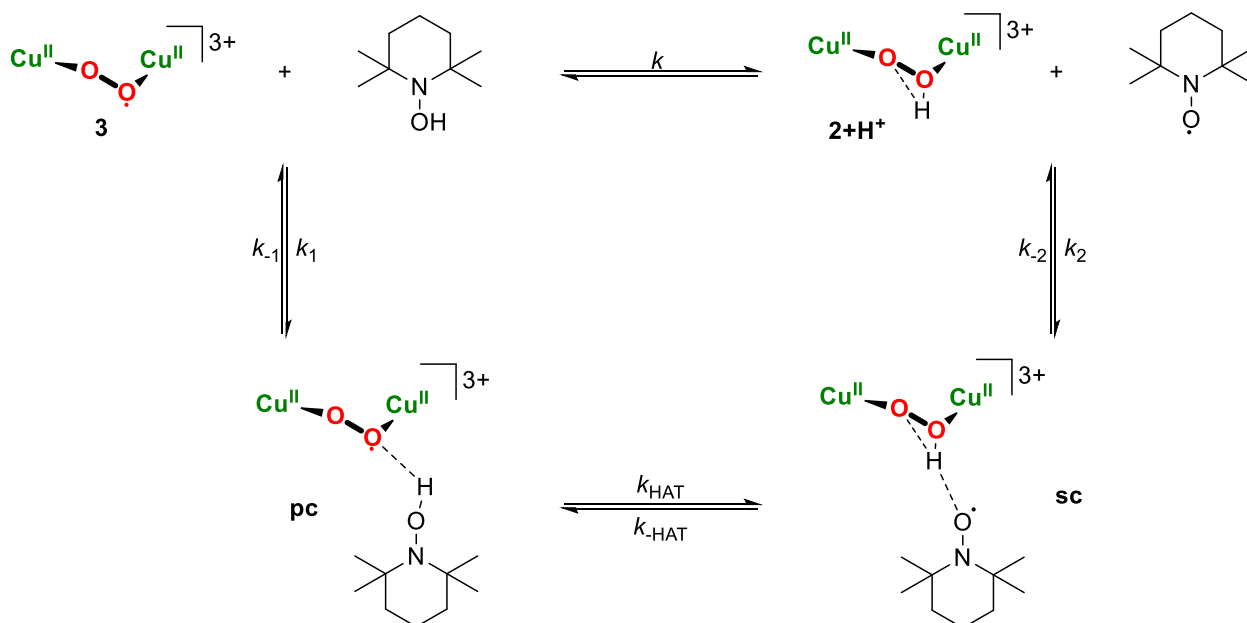
**Figure 71.** Electronic absorption spectra of complex **2** before its oxidation to complex **4** (black line) and after the reaction of **4** with TEMPO-H to **2+H<sup>+</sup>**, which then has been deprotonated with DBU (red line).

Upon reaction of **4** with TEMPO-H, one proton and one electron are transferred from the substrate on the superoxide. In theory different mechanisms can be proposed for this type of reaction.<sup>177</sup> The most common reaction is the hydrogen atom transfer (HAT), where a proton and an electron are simultaneously transferred in one kinetic step.<sup>177</sup> The classical HAT mechanism starts with an organic radical that abstracts the hydrogen atom from the corresponding substrate, whereas transition metal complexes, acting as the H-atom acceptor, usually contain high valent metal centers.<sup>177,178</sup> During this mechanism the metal center accepts the electron, while the proton is taken up by a basic ligand. Consequently, this reaction is better described as proton coupled electron transfer (PCET). The PCET usually proceeds *via* one concerted kinetic step and therefore is denoted as concerted proton-electron transfer (CPET).<sup>177,178</sup> However, both mechanisms start with the formation of a so called precursor complex (**pc**) followed by e.g. subsequent HAT in forming a so-called successor complex (**sc**) that dissociates into the reaction products (see Scheme 21). The formation of the **pc** is mainly defined by the extent of steric interaction between the two reactants and can be the limiting step in HAT reactions, if the steric demand of one of the reactants is too high.<sup>177,179,180</sup> The rate of the successive HAT is then determined by the magnitude of the reaction barrier,  $\Delta G^\ddagger$ , which can be described by Marcus Theory.<sup>177</sup> The adiabatic form of the Marcus equation (see equation 23)) contains the reaction free energy  $\Delta G^0$  as well as the reorganization energy  $\lambda$ , which is the energy that is required to reorganize the system from initial to final product coordinates.<sup>181,182,177</sup>

$$23) \quad \Delta G^\ddagger = \frac{(\Delta G^0 + \lambda)^2}{4\lambda}$$

The higher the reorganization energy is, *i.e.* the more pronounced the structural changes between complex **4** and **2+H<sup>+</sup>**, the larger the reaction barrier will be and the more unlikely the HAT will occur.

Since the actual molecular structure of  $2+H^+$  is unknown, no further conclusion concerning the reorganization energy for the reaction of **4** to  $2+H^+$  can be made.



**Scheme 21.** Schematic product formation *via* HAT from **pc**.<sup>177</sup>

The formation of  $2+H^+$  from superoxide **4** and TEMPO-H formally occurs *via* the transfer of a hydrogen atom on the superoxide and the reaction is assumed to follow the HAT mechanism (this outcome will be discussed later). With respect to the formation of the corresponding **pc**, the molecular structure of **4** will be reconsidered. The solid state structure of complex **4** is similar to that of peroxo complex **2**, where the peroxo unit is known to interact with different Lewis acids such as  $Li^+$ . Even the protonated form of DBU,  $DBU \cdot H^+$ , was observed to form a weak adduct with **2** (see Section 6.3). The space-filling models of **2** and of **4** are depicted in Figure 72 and demonstrate that an easy access to the superoxo core for potential O-H substrates such as TEMPO-H is possible (this outcome will be discussed later). Consequently, the formation of the **pc** should easily occur in enabling subsequent HAT.

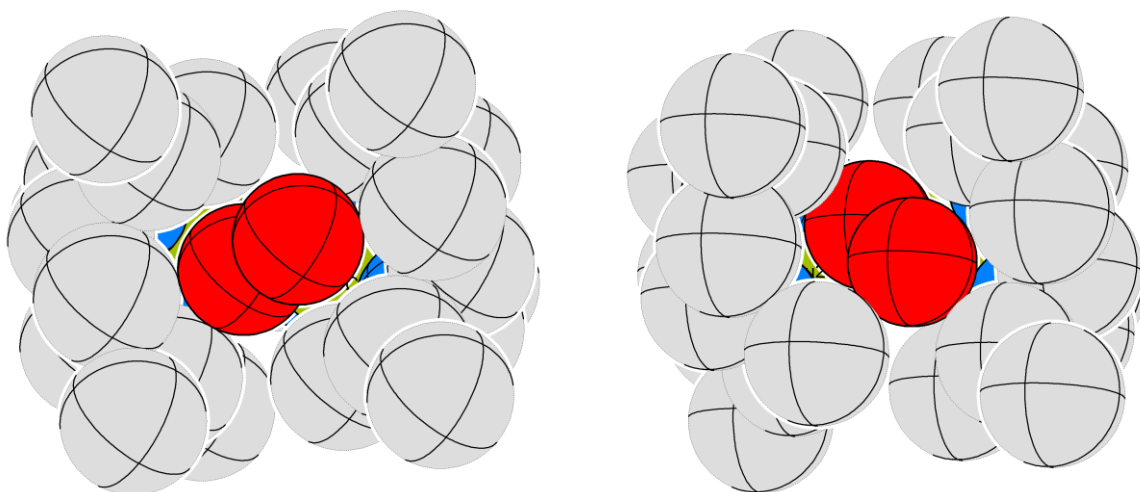


**Figure 72.** Space-filling models of peroxo complex **2** (left) and of superoxo complex **4** (right).

By monitoring the reaction of complex **4** with TEMPO-H *via* UV/vis absorption spectroscopy, only a global rate constant can be determined (denoted as  $k$  in Scheme 21) that will be defined by the rate determining step. The global rate expression for the formation of  $\mathbf{2+H^+}$  from **4** and TEMPO-H is defined as:

$$24) \quad v = \frac{d[\mathbf{2+H^+}]}{dt} = k[\mathbf{4}]^a[\text{TEMPO-H}]^b$$

Since the reaction of **4** and TEMPO-H occurs quantitatively and cleanly, the concentrations of **4** and of TEMPO-H can be determined at any time during the reaction and kinetic data have been obtained by monitoring the reaction progress at  $\lambda = 550 \text{ nm}$  over the whole course of the transformation (see Figure 73).<sup>183,184</sup>

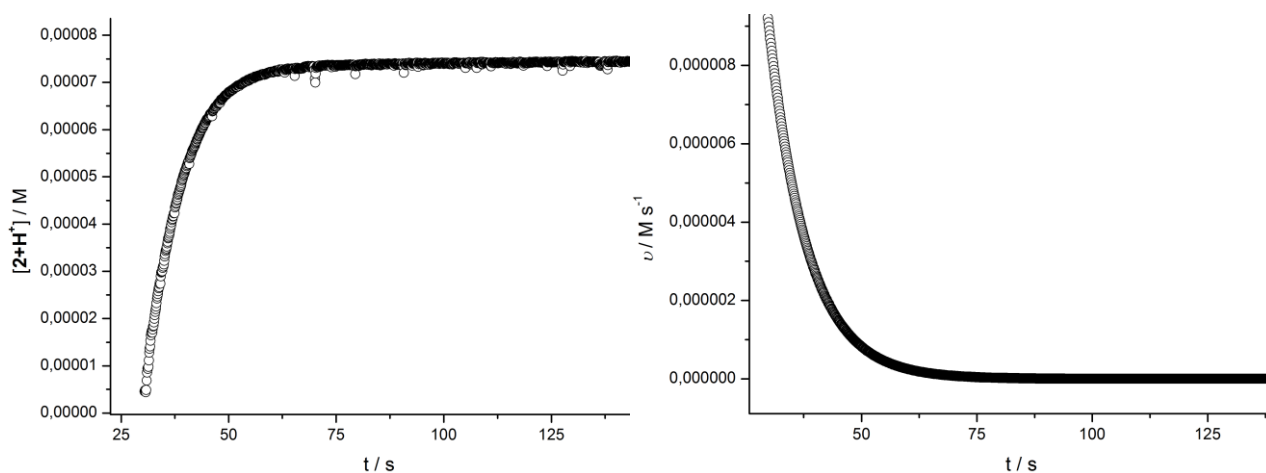


**Figure 73.** Left: formation of reaction product  $\mathbf{2+H^+}$  versus time at 1.28 mM excess of TEMPO-H ( $c(\mathbf{2+H^+}) = 70 \mu\text{M}$ ); (right) calculated reaction rate for product formation versus time.

The kinetic data have been obtained under substrate excess conditions (0.8 - 2.0 mM) at  $-40 \text{ }^\circ\text{C}$ . For linear regression methods, data have been used between 20 and 80% of complex conversion.<sup>185</sup> The

overall rate was found to be first order in [4] (see Figure 74, right) and of first order in [TEMPO-H] (see Figure 74, left). The overall second order rate constant was determined at four different substrate excess conditions (see Figure 75 and Table 18), all showing similar values for  $k$ . An average rate constant of  $k_{av} = 93 \text{ M}^{-1} \text{ s}^{-1}$  ( $T = -40 \text{ }^\circ\text{C}$ , substrate excess = 0.8 – 2.0 mM) could be determined, which will be used in the following discussion. At lower substrate excess conditions (0.07 mM, 0.15 mM) the overall rate constant was found to be of more complex order and no further investigations have been pursued.

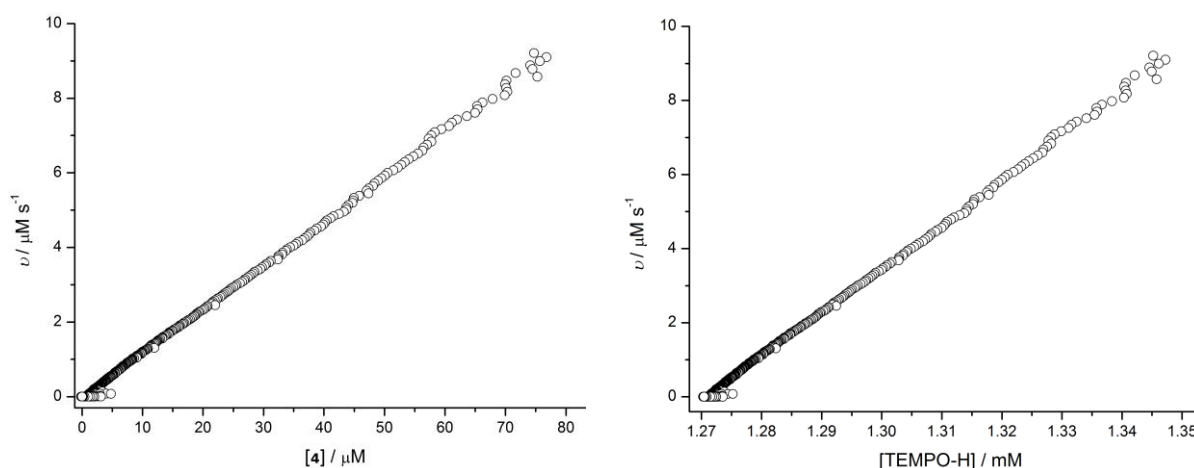


**Figure 74.** Left: Plot of reaction rate versus [4] at 1.28 mM excess of substrate. The reaction exhibits first order kinetics in the concentration of TEMPO-H; Right: Plot of reaction rate versus [TEMPO-H] at 1.28 mM excess of substrate. The reaction exhibits first order kinetics in the concentration of 4.

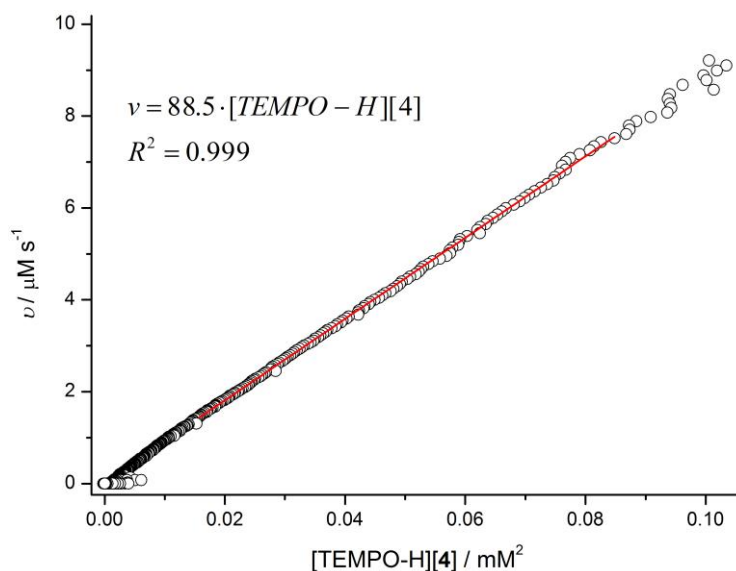
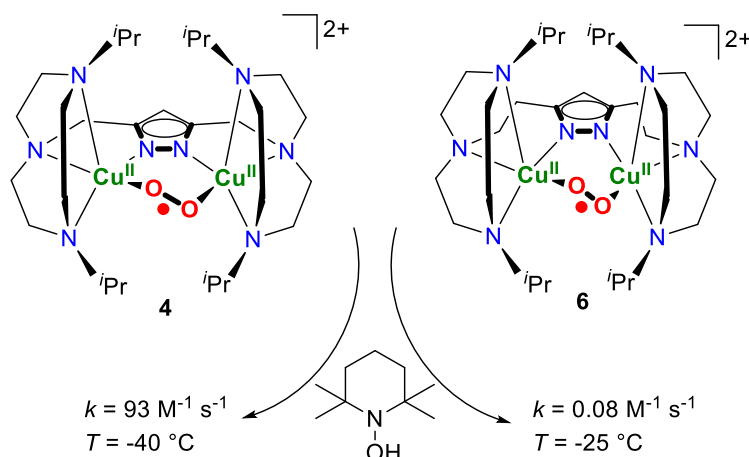


**Figure 75.** Linear fit (data were used between 20 – 80% of complex conversion)<sup>185</sup> of reaction rate  $v$  versus [4]·[TEMPO-H] at 1.28 mM excess of substrate. The slope represents the overall second order rate constant (MeCN,  $T = -40^\circ\text{C}$ ).

**Table 18.** Second order rate constants determined for **4** at different TEMPO-H excess conditions (MeCN,  $T = -40\text{ }^{\circ}\text{C}$ ); an average second order rate constant of  $k_{\text{av}} = 93\text{ M}^{-1}\text{ s}^{-1}$  was determined.

substrate excess [mM]	$k$ [ $\text{M}^{-1}\text{ s}^{-1}$ ]
0.82	95.6
1.16	95.5
1.28	88.5
2.04	94.9

Interestingly,  $k_{\text{av}}$  is much larger compared to the second order rate constants determined for other mononuclear and dinuclear superoxo complexes, also performing O-H bond cleavage with TEMPO-H.<sup>186,90</sup> The however not crystallographically characterized dinuclear superoxo complex **6** (see Scheme 22) for instance shows a corresponding second order rate constant of  $0.08\text{ M}^{-1}\text{ s}^{-1}$  ( $T = -25\text{ }^{\circ}\text{C}$ ), which is three orders of magnitude smaller than  $k_{\text{av}}(\mathbf{4})$ .<sup>90</sup> One explanation for the comparably large rate constant may be an easy access to the superoxo core. The corresponding space-filling model for **4** was discussed previously (see Figure 72).



**Scheme 22.** Substrate reactivity of complexes **4** and **6** with TEMPO-H and corresponding second order rate constants.

To gain deeper insight into the reaction mechanism, kinetic isotope labeling studies with TEMPO-D have been performed at  $-40\text{ }^{\circ}\text{C}$ . A kinetic isotope effect (KIE) of 3.5 has been determined, suggesting the HAT to be the rate determining step of the reaction. Thermodynamic data concerning the transition state of this reaction have been determined *via* an Eyring plot<sup>183</sup> (see Figure 76,  $\Delta H^{\ddagger} = 16.0 \pm 0.8\text{ kJ mol}^{-1}$ ;  $\Delta S^{\ddagger} = -137 \pm 3\text{ J mol}^{-1}\text{ K}^{-1}$ ;  $\Delta G^{\ddagger} = 47.9 \pm 0.7\text{ kJ mol}^{-1}$  ( $T = 233\text{ K}$ )). The negative transition state entropy of  $\Delta S^{\ddagger} = -137\text{ J mol}^{-1}\text{ K}^{-1}$  points at an associative mechanism being part of the transition state that may be the HAT from the substrate on the cupric superoxo complex.

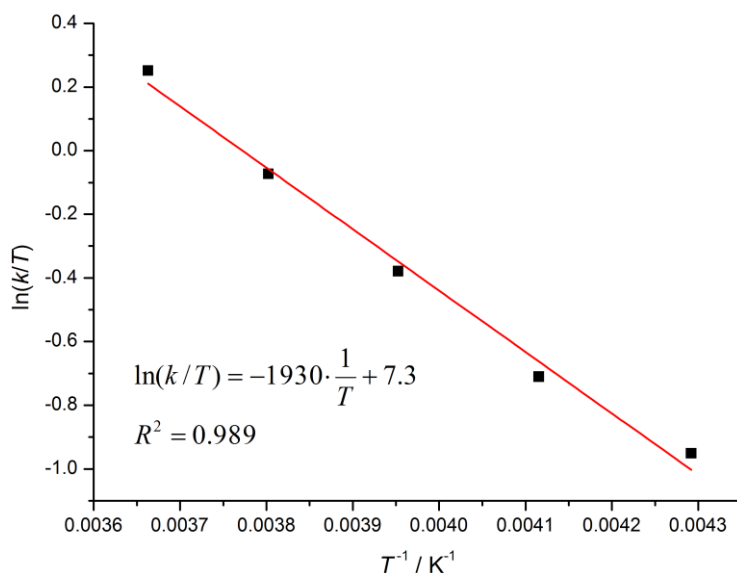


**Figure 76.** Eyring plot correlating rate constant  $k$  and temperature  $T$ .

The activation energy of  $\Delta G^\ddagger = 47.9 \text{ kJ mol}^{-1}$  ( $T = 233 \text{ K}$ ) is considerably smaller compared to that determined for the reaction of the structurally related complex **6** with TEMPO-H ( $\Delta G^\ddagger = 63.9 \text{ kJ mol}^{-1}$ ,  $T = 233 \text{ K}$ ).<sup>90</sup> These findings are in agreement with a significantly smaller second order rate constant determined during reactivity studies of **6** with TEMPO-H.<sup>90</sup>

With the thermodynamic data of the corresponding transition state in hand, the previously discussed possible mechanisms will be reconsidered. The transfer of proton and electron from TEMPO-H on complex **4** may occur *via* one concerted step (HAT) or *via* two isolated steps (ET followed by PT). The corresponding free energy of the ET has been previously calculated to  $\Delta G_{\text{ET}}^0 = 29.7 \text{ kcal mol}^{-1}$ . Since the activation free energy for the observed reaction has been determined to  $\Delta G^\ddagger = 13.8 \text{ kcal mol}^{-1}$  ( $T = 298 \text{ K}$ ), the stepwise pathway can be excluded ( $\Delta G_{\text{ET}}^0$  is much larger than the free activation energy). Consequently, the H-atom transfer most likely occurs *via* one concerted step.

Since **4** quantitatively reacts with TEMPO-H in forming hydroperoxide **2+H<sup>+</sup>**, this reaction should furthermore be reversible. Consequently, the 2,4,6-tri-*tert*-butyl-phenoxy radical,  ${}^t\text{Bu}_3\text{PhO}\cdot$  (BDFE ( ${}^t\text{Bu}_3\text{PhOH}$ ) =  $77.1 \text{ kcal mol}^{-1}$ , MeCN)<sup>187</sup> was added stepwise in substoichiometric amounts to a solution of **2+H<sup>+</sup>**, which has been freshly generated from compound **2** and 2,6-lutidinium triflate (see Section 6.3 for details). The reaction was monitored by UV/vis absorption spectroscopy at  $-40 \text{ }^\circ\text{C}$  (see Figure 77). The initial absorption maxima of **2+H<sup>+</sup>** were found to decrease, simultaneously forming the corresponding superoxo complex, **4**. After the addition of in total 1.02 equivalents of the radical, no further changes in absorbance are observed (see Figure 78, right). Next to complex **4**, also minor parts of unreacted radical are present, giving rise to the absorption bands at ca. 380 and 410 nm. However,  ${}^t\text{Bu}_3\text{PhO}\cdot$  as well as  ${}^t\text{Bu}_3\text{PhOH}$  are non-absorbing in the region of 450 nm and thus the maximum in intensity at 445 nm exclusively originates from complex **4**. This fact can also be seen in Figure 78, right since the intensity of the maximum of **4** is not changing upon addition of excess of radical.



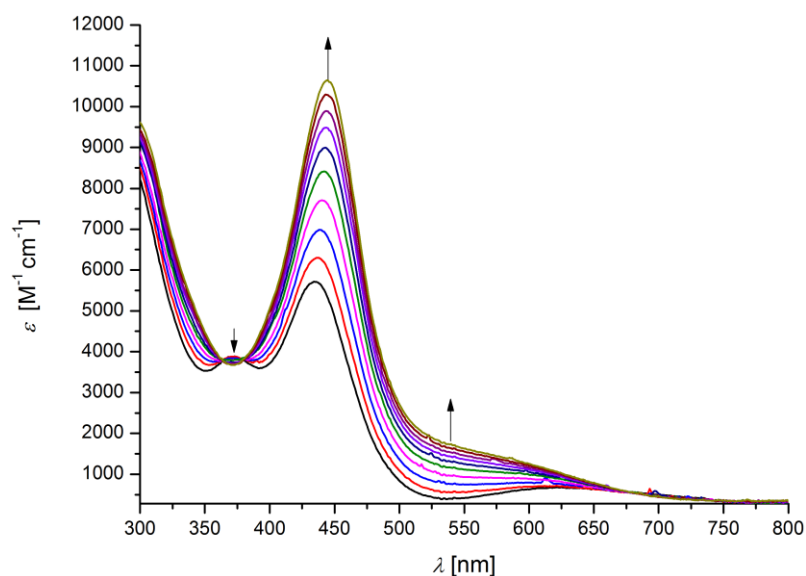


**Figure 77.** UV/vis titration of  $2+\text{H}^+$  with  ${}^t\text{Bu}_3\text{PhO}\cdot$ , forming superoxo complex **4**.  ${}^t\text{Bu}_3\text{PhO}\cdot$  was added stepwise in different concentrations. At first the radical was titrated in steps of 0.15 eq. (from 0 - 0.6 eq.), followed by steps of 0.075 eq. (from 0.6 - 1.05 eq.). Isosbestic points at 363 nm and 380 nm indicate a clean conversion (MeCN,  $T = -40\text{ }^\circ\text{C}$ ).

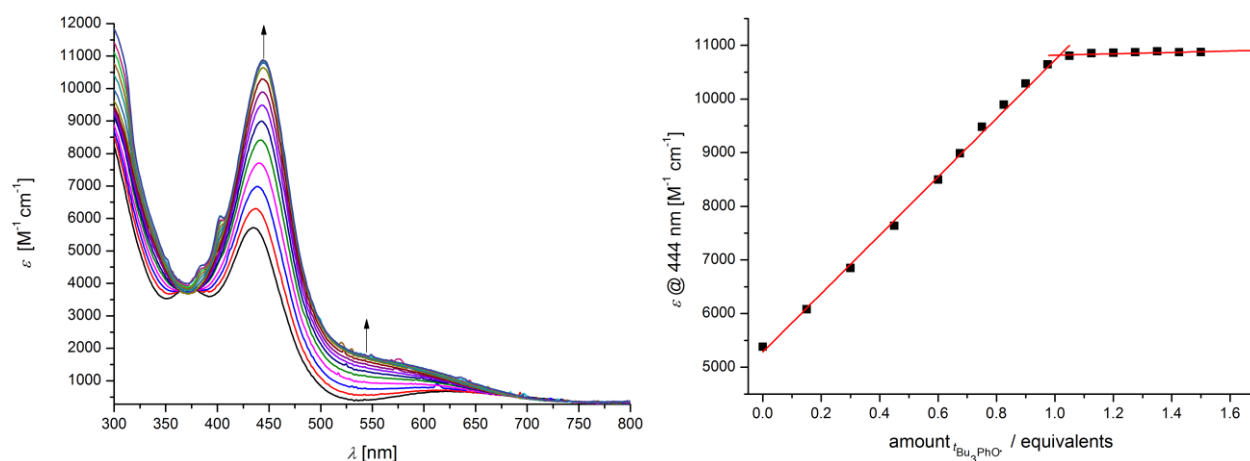


**Figure 78.** Left: UV/vis titration of  $2+\text{H}^+$  with  ${}^t\text{Bu}_3\text{PhO}\cdot$ .  ${}^t\text{Bu}_3\text{PhO}\cdot$  was added stepwise in different concentrations. At first the radical was titrated in steps of 0.15 eq. (from 0 - 0.6 eq.), followed by steps of 0.075 eq. (from 0.6 - 1.5 eq.). Right: plot of extinction coefficient at  $\lambda_{\text{max}} = 444\text{ nm}$  versus added amount of  ${}^t\text{Bu}_3\text{PhO}\cdot$ ; the titration is completed after addition of 1.02 eq. of radical (MeCN,  $T = -40\text{ }^\circ\text{C}$ ).

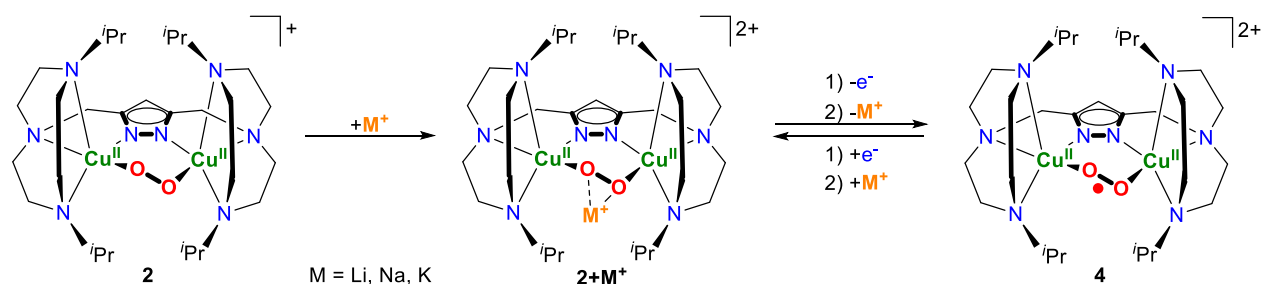
With this background in hand, one further possibility to quantify the completeness of the titration will be introduced, which will become essential in Section 6.5.1. For this purpose, the UV/vis absorption spectrum of product **4** will be compared with the corresponding spectrum of peroxy complex **2**, from which  $2+\text{H}^+$  has been generated prior to the reaction with  ${}^t\text{Bu}_3\text{PhO}\cdot$ .

Superoxide **4** can also be quantitatively generated from complex **2**, no side reactions are observed (see Section 6.3 for details). If the molar extinction coefficients of the maximum of **4** at 445 nm and of the maximum of **2** at 527 nm are compared, the absorption maximum of complex **4** is observed to be more intense by a factor of ca. 2.0. The same ratio is observed for the above-mentioned titration of  $2+\text{H}^+$  with

${}^t\text{Bu}_3\text{PhO}\cdot$ , where complex **4** is formed (**2+H<sup>+</sup>** has been generated from **2** previously, see Section 6.3 for preparation). Consequently, **2+H<sup>+</sup>** is quantitatively transformed into compound **4** upon addition of  ${}^t\text{Bu}_3\text{PhO}\cdot$ . Although this evaluation is quite trivial, this method will become essential in Section 6.5.1.

## 6.4.6 Modulation of the Redox Potential *via* Interaction with Alkali Metal Ions

Complex **2** can be reversibly oxidized in forming superoxo complex **4**. This species represents the first fully characterized dinuclear superoxo moiety, which has been in detail introduced in Sections 6.4.1 - 6.4.5. With this background in hand, the electrochemical properties of the alkali metal adducts of **2** have been investigated (see Scheme 23).



**Scheme 23.** Schematic representation of electrochemical oxidation of alkali metal adducts into superoxo complex **4**.

The alkali metal adducts **2+M<sup>+</sup>** were generated from complex **2** and the corresponding alkali metal triflate salt. This equilibrium is described by an association constant,  $K_a$ . The different binding constants have been determined *via* UV/vis titration experiments (see Section 6.2). While **2+Li<sup>+</sup>** is almost quantitatively formed within the addition of approximately 5 eq. of LiOTf, more than 50 eq. of KOTf are required for a nearly complete transformation of **2** into **2+K<sup>+</sup>**. Since the electrochemical properties of exclusively the alkali metal adducts should be investigated, a huge excess of the corresponding alkali metal triflate salts has been used during the experiments (Li<sup>+</sup>: excess = 19 eq.; Na<sup>+</sup>: excess = 39 eq.; K<sup>+</sup>: excess = 119 eq.). Figure 79 shows a comparison of the cyclic voltammograms of **2** and **2+Li<sup>+</sup>**, recorded at 0 °C in MeCN.

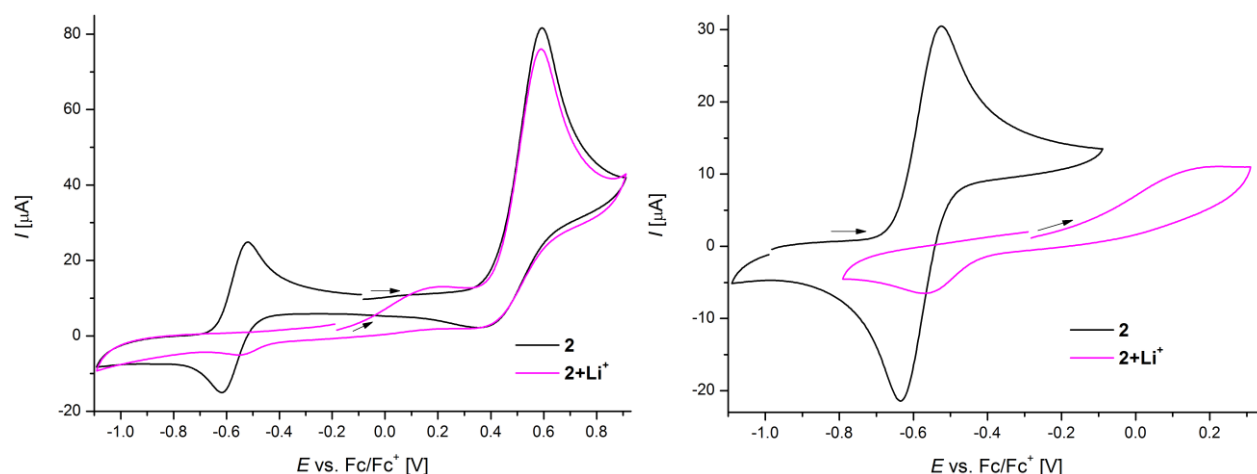


**Figure 79.** Cyclic voltammograms of **2** ( $c = 2.8$  mM) and of **2+Li<sup>+</sup>** ( $c = 2.7$  mM; excess of Li<sup>+</sup>: 51.3 mM) recorded at 100 mV/s scan rate ( $T = 0$  °C, MeCN, 0.1 M solution of NBu<sub>4</sub>PF<sub>6</sub> as supporting electrolyte).

Both spectra show the same irreversible oxidation event at  $E_{pa,2} = 0.59$  V, while the first oxidation at  $E_{pa,1}$  is shifted from  $-0.52$  V in **2** to  $0.23$  V in **2+Li<sup>+</sup>**. The corresponding reduction for **2** at  $E_{pc} = -0.63$  V is

only slightly shifted for  $2+Li^+$  ( $E_{pc} = -0.58$  V). Since the oxidation of **2** to superoxide **4** occurs at the peroxy unit, this trend can be qualitatively explained. In  $2+Li^+$ , the  $Li^+$  ion is assumed to abstract electron density from the peroxide, as indicated by the short Li-O distances obtained from the molecular structure (see Section 6.2.3). Thus, the corresponding oxidation is shifted to higher potential in  $2+Li^+$  in finally leaving complex **4** and a  $Li^+$  cation at the electrode. A subsequent reduction of **4** back to the peroxy level occurs at nearly same potential ( $E_{pc,1}(2+Li^+) = -0.58$  V) as observed in the absence of  $Li^+$  ( $E_{pc,1}(2) = -0.63$  V, see Table 19). This may be due to no significant interaction of the  $Li^+$  cation and superoxy moiety **4**. Indeed, a UV/vis titration of **4** with up to 100 eq. of LiOTf revealed no changes in absorbance and thus **4** is not interacting with  $Li^+$  as observed for complex **2** (see Section 6.2). Figure 80 shows a summary of the cyclic voltammograms of **2** and the alkali metal adducts.

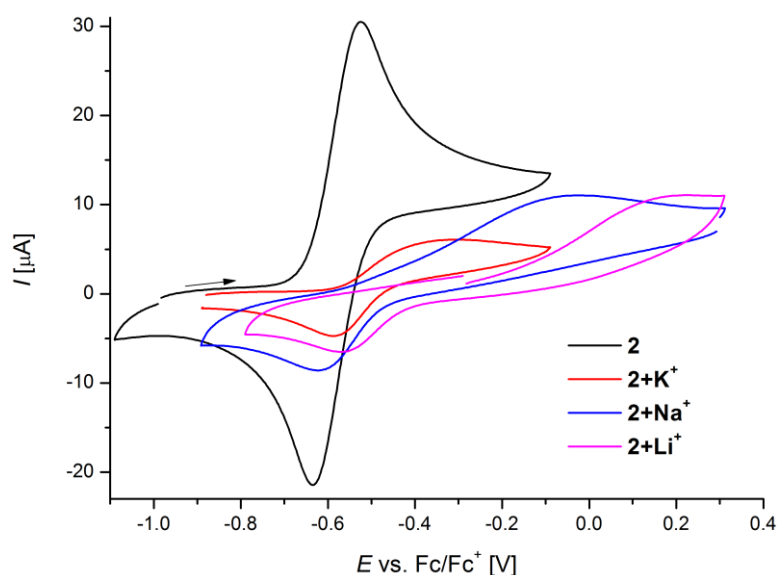


**Figure 80.** Cyclic voltammograms of complexes **2** and  $2+M^+$  at 100 mV/s scan rate. Complex concentration: **2**: 3.02 mM;  $2+K^+$ : 2.67 mM (excess of  $K^+$ : 318 mM);  $2+Na^+$ : 2.26 mM (excess of  $Na^+$ : 88.1 mM);  $2+Li^+$ : 2.69 mM (excess of  $Li^+$ : 51.3 mM) ( $T = 0$  °C, 0.1 M solution of  $NBu_4PF_6$  as supporting electrolyte). The anodic peak potential shifts towards higher potential in the presence of  $M^+$ . The total shift increases from  $2+K^+$  to  $2+Li^+$  and reflects the in Section 6.2 demonstrated strength of Lewis acid and Lewis base interaction.

The anodic peak potential of the first oxidation event of **2** at -0.52 V shifts to higher potential upon formation of the corresponding alkali metal adducts (see also Table 19). The absolute shift in potential clearly is a function of Lewis acidity of the coordinating alkali metal ion. A quantitative determination of the Lewis acidity of metal ions, however, is difficult.<sup>188</sup> The Lewis acidity of a metal ion generally depends on the ratio of charge and ion radius.<sup>158</sup> If the single positively charged alkali metal ions are considered, the Lewis acidity decreases from  $Li^+$  to  $K^+$  since the ionic radii increase in the same direction. Figure 81, left shows a plot of  $E_{pa,1}$  versus the reciprocal ion radius of the alkali metal ions. The observed correlation of peak potential and reciprocal ion radii shows that the anodic peak potential of the first oxidation event linearly depends on the Lewis acidity of the coordinating cation. Another possibility is a plot of  $E_{pa,1}$  versus the relative Lewis acidity (see Figure 81, right). The relative Lewis

acidity of the cations  $\text{Li}^+$  and  $\text{Na}^+$  was taken from the literature where it has been determined *via* EPR spectroscopy in comparing the binding energies of different metal ions with  $\text{O}_2^-$  evaluated from deviation of the  $g_{zz}$  value from the free spin value.<sup>158,188</sup> Again a linear correlation can be found, confirming the linear correlation of anodic peak potential and Lewis acidity of the coordinating alkali metal ion.

**Table 19.** Anodic peak potentials of first and of second oxidation of **2** and of alkali metal adducts **2+M<sup>+</sup>** versus  $\text{Fc}/\text{Fc}^+$ .

complex	$E_{\text{pa},1}$ [V]	$E_{\text{pc},1}$ [V]	$E_{\text{pa},2}$ [V]
<b>2</b>	-0.52	-0.63	0.59
<b>2+K<sup>+</sup></b>	-0.45	-0.57	0.61
<b>2+Na<sup>+</sup></b>	-0.07	-0.63	0.64
<b>2+Li<sup>+</sup></b>	0.23	-0.58	0.61

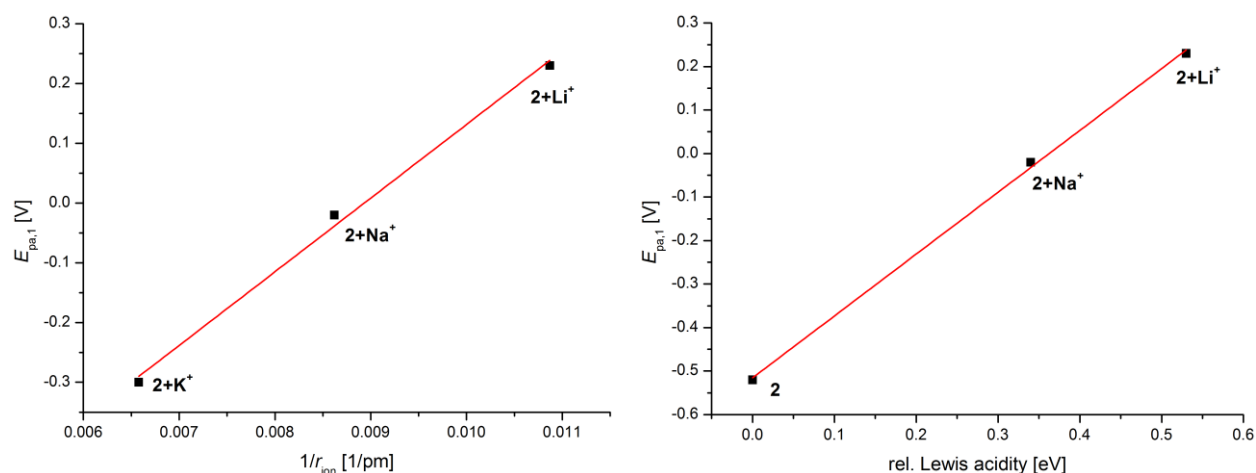


**Figure 81.** Left: Plot of anodic peak potential of first oxidation versus reciprocal ion radii of the alkali metal ions.<sup>189</sup> Right: Plot of anodic peak potential of first oxidation versus relative Lewis acidity of the alkali metal ions  $\text{Na}^+$  and  $\text{Li}^+$ . The values are taken from literature, no value for  $\text{K}^+$  has been found.<sup>158,188</sup> Relative Lewis acidity has been determined *via* EPR spectroscopy in comparing the binding energies of alkali metal ions with  $\text{O}_2^-$  evaluated from deviation of  $g_{zz}$  value from the free spin value.<sup>158,188</sup>

However, the observed trend is only qualitative, since especially the electrolyte concentration significantly varies in all four experiments. For **2+Li<sup>+</sup>** 20 eq. of LiOTf have been added, while for **2+K<sup>+</sup>** more than 100 eq. of KOTf were used. Additionally, background decay of especially **2+K<sup>+</sup>** was observed during the measurement, which is most likely due to minor impurities of KOTf. Nevertheless, the redox potential of the first oxidation event is observed to increase upon alkali metal binding. The same trend has been observed for the aforementioned mononuclear iron peroxo complex (see Section 6.4). However, the interaction of the iron peroxo core with the different redox inert metal ions is only predicted on the basis of DFT calculations, while the adduct formation of the alkali metal ions with complex **2** has also been confirmed spectroscopically. Thus, complex **2** represents the first reported

example, where the electronic structure of the metal oxygen core can be selectively modified by interaction with redox inert metal ions. Since especially  $\text{Na}^+$  and  $\text{K}^+$  are ubiquitous abundant, the function of these alkali metal ions in controlling reactivity in natural copper sites has to be investigated. The second oxidation event at ca. 0.6 V is not significantly affected by the presence of the different alkali metal ions (see Table 19). This oxidation may either correspond to the liberation of molecular dioxygen or to an oxidation of the ligand framework or of the  $\text{Cu}^{\text{II}}$  ions. If the cyclic voltammogram of complex **5** is considered (see Section 6.5), no oxidation event is observed at this potential. **5** thereby consist of the same ligand, with the peroxide being replaced by a water and a hydroxide molecule. An oxidation of the ligand framework or of the  $\text{Cu}^{\text{II}}$  ions should therefore not significantly deviate in potential from e.g. **2** and thus the oxidation event at 0.6 V may include the peroxide/superoxide bridge. Since the anodic peak potential for the oxidation of the peroxy moiety into the corresponding superoxo complex was observed to increase with the addition of LiOTf ( $E_{\text{pa},1} = 0.23$  V), a chemical oxidation of  $\mathbf{2+Li}^+$  via  $\text{Ag}^+$  should not be possible ( $E^0 = 0.04$  V vs.  $\text{Fc}/\text{Fc}^+$  (MeCN))<sup>159</sup>. Figure 82 shows a UV/vis experiment where 1.6 eq. of  $\text{AgSbF}_6$  were added to a solution of  $\mathbf{2+Li}^+$  ( $\mathbf{2+Li}^+$  has been previously synthesized from **2** and ca. 14 eq. of LiOTf).

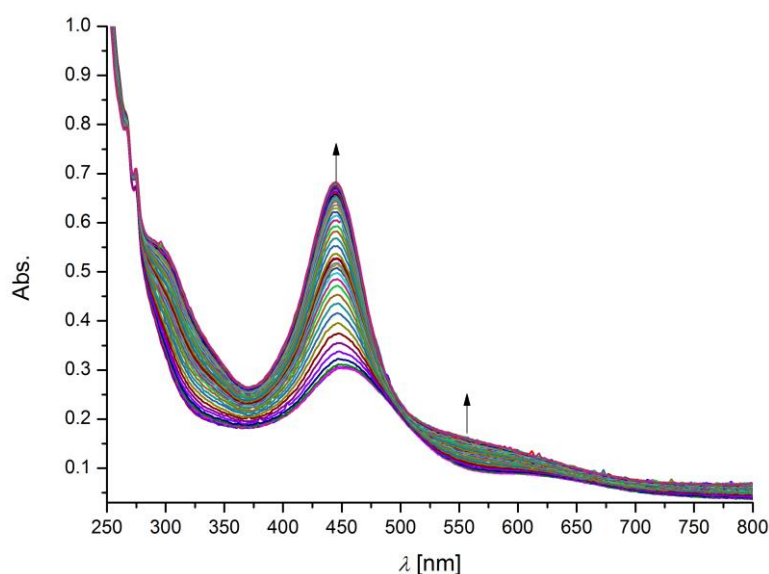


**Figure 82.** Reaction of 60  $\mu\text{M}$  solution of  $\mathbf{2+Li}^+$  with  $\text{AgSbF}_6$  (1.6 eq.) in forming superoxide **4** over ca. 30 min (MeCN,  $T = -40$  °C).  $\mathbf{2+Li}^+$  has been previously generated from complex **2** and ca. 14 eq. of LiOTf.

However, the formation of **4** was observed over a period of 30 min. If this reaction is compared to the oxidation of **2** with  $\text{AgSbF}_6$ , superoxide **4** is formed much slower (the oxidation of **2** into **4** with  $\text{AgSbF}_6$  is completed after few minutes). One explanation for the formation of **4** from complex  $\mathbf{2+Li}^+$  may be the equilibrium between  $\mathbf{2+Li}^+$  and peroxy complex **2**. Although **2** binds the lithium ion with a high affinity ( $K_b = 6.9 \times 10^5$ , see Section 6.2.1), still a minor amount of **2** is present in solution, which then is oxidized into complex **4**. With respect to mass balance, **2** is subsequently formed from  $\mathbf{2+Li}^+$  and finally  $\mathbf{2+Li}^+$  is quantitatively oxidized to superoxide **4**.

### 6.4.7 Summary and Conclusion

This chapter for the first time described the synthesis of a dinuclear copper(II) superoxo complex which could be characterized also crystallographically.

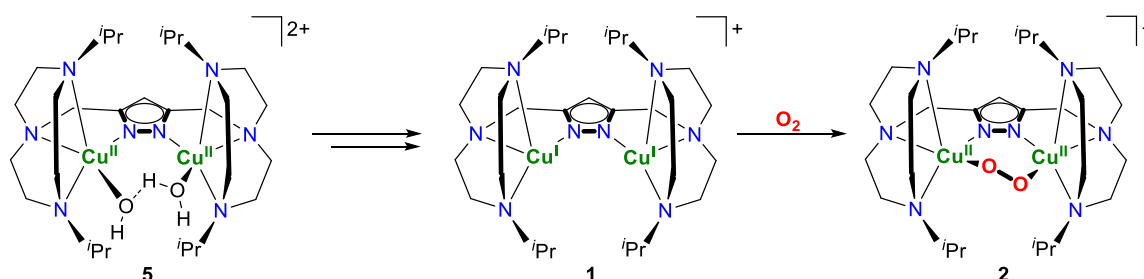
Superoxide **4** can be generated from peroxo complex **2** both chemically as well as electrochemically, whereas both transformations are reversible. Since complex **2** represents the first ever reported example of a dicopper(II) peroxo complex, where the electronic structure of the Cu<sub>2</sub>/O<sub>2</sub> core can be selectively modified by interaction with redox inert alkali metal ions (see Section 6.2), also the properties with respect to an oxidation to complex **4** were studied. The redox potential of the corresponding oxidation was thereby observed to increase upon alkali metal binding, whereas the total shift in redox potential significantly increases from **2+K<sup>+</sup>** to **2+Li<sup>+</sup>**. Since especially Na<sup>+</sup> and K<sup>+</sup> are ubiquitarily available, the function of these alkali metal ions in controlling reactivity in natural copper sites has to be investigated.

Preliminary DFT calculations were performed on the molecular structure of **4**, predicting a relatively weak magnetic coupling of Cu<sup>II</sup> ions and superoxide due to a diminished overlap of copper- and oxygen-centered orbitals. However, the DFT calculations allow no absolutely clear assignment of the magnetic ground state. Nevertheless, with the help of solution state SQUID magnetometry, a *S* = 0.5 ground state could be determined. The corresponding EPR spectrum shows an axial Cu<sup>II</sup> line shape and thus the unpaired electron is located to a significant extent on one of the two Cu<sup>II</sup> ions.

Finally, kinetic investigations with complex **4** and TEMPO-H as substrate have been performed, revealing the selective formation of hydroperoxide **2+H<sup>+</sup>** in a concerted HAT process. A corresponding thermodynamic square scheme was developed and a BDFE of 71.4 kcal mol<sup>-1</sup> could be determined for complex **2+H<sup>+</sup>**. The second order rate constant determined for the reaction with TEMPO-H was found to be three orders of magnitude larger compared to that obtained for the structurally related superoxo complex **6**.<sup>90</sup> One explanation for these vast differences may be the open binding pocket of complex **4**, enabling an easy access for potential substrates. With respect to future complex design for efficient substrate reactivity, this example shows that even small changes of the ligand scaffold strongly affect electronic and structural properties of reactive oxygen intermediates.

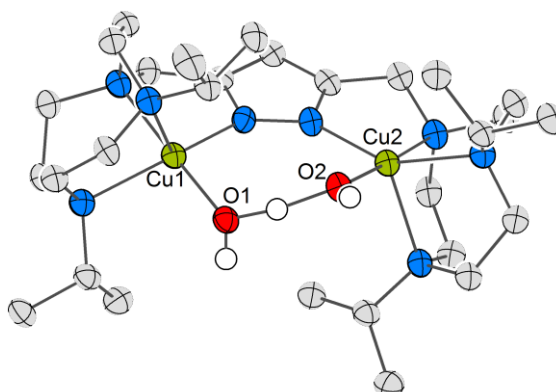
## 6.5 A Decomposition Product – Recycling and Formation

The aforementioned copper oxygen complexes **2**, **2+M<sup>+</sup>** and **4** all decompose at temperatures above -25 °C with exception of **2+H<sup>+</sup>**, which is only stable at temperatures below -80 °C. This species is furthermore highly sensitive towards traces of water, but this finding is discussed in Section 6.5.1. No matter which of these compounds is considered, all are forming the same decomposition product over time, which is denoted as complex **5**. Until to date this species has been discarded when formed which is rather unsatisfactory, since ligand **HL<sup>1</sup>** is generated in a multi-step synthesis under a high consumption of resources (see Section 7.13). With respect to “green chemistry” a possible “recycling” of **5** *via* e.g. generating the dinuclear copper(I) complex **1**, which again can be selectively reacted into the corresponding dioxygen complexes, is of high interest (see Scheme 24).<sup>190,191</sup> The following section will thus focus on the selective recycling of complex **5** and will further introduce Section 6.6, dealing with electrolytic water oxidation starting from compound **5**.



**Scheme 24.** Targeted recycling of hydroxo complex **5**.

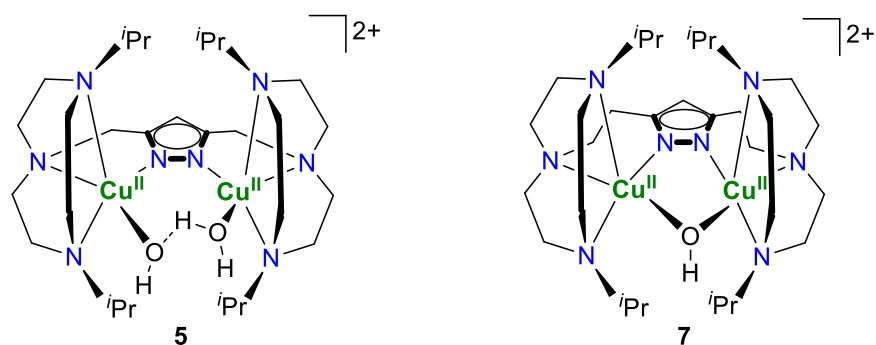
Figure 83 shows the molecular structure of hydroxo complex **5**, which has already been isolated in previous work.<sup>32,99</sup> The Cu<sup>II</sup> ions are coordinated in a distorted trigonal bipyramidal geometry ( $\tau(\text{Cu}1) = 0.44$ ;  $\tau(\text{Cu}2) = 0.45$ ) by four nitrogen donor atoms and by one additional oxygen atom of one water or of one hydroxide ligand, respectively.



**Figure 83.** Solid state structure of complex **5** with thermal displacement ellipsoids given at 30% probability. Hydrogen atoms (except those of the H<sub>3</sub>O<sub>2</sub> bridge), counterion ClO<sub>4</sub><sup>-</sup>, and additional solvent molecules are omitted for clarity; for selected bond lengths and angles see Section 7.7.

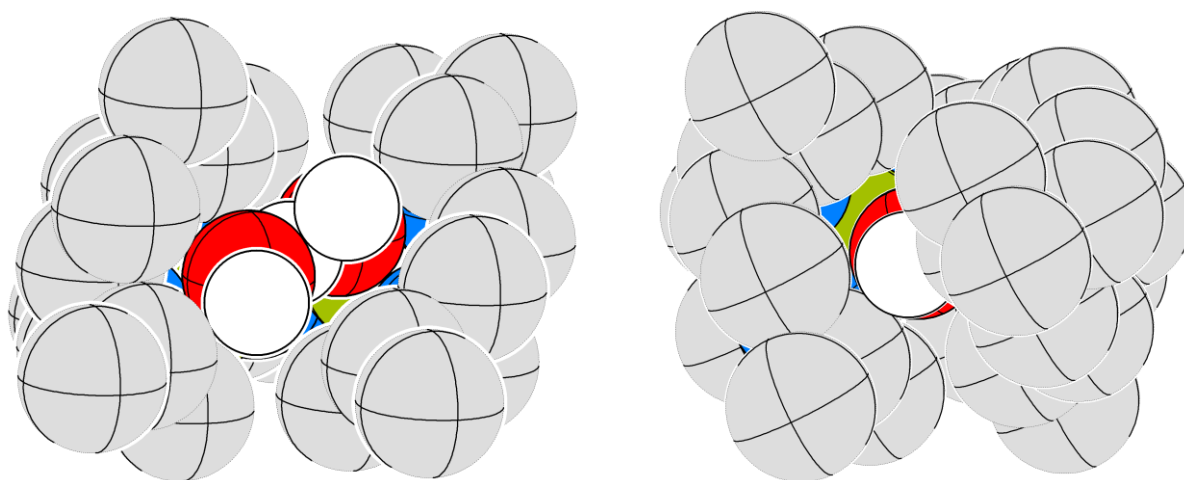


The two  $\text{Cu}^{\text{II}}$  ions are bridged by a hydroxide and an additional water molecule (denoted as  $\text{H}_3\text{O}_2$  bridge). The observed  $\text{H}_3\text{O}_2$  bridge is facilitated by the given design of ligand  $\text{HL}^1$ , inducing a constrained Cu-Cu separation ( $d(\text{Cu}-\text{Cu}) = 4.38 \text{ \AA}$ ) which is too large for a monoatomic bridging unit such as a hydroxide.<sup>32</sup> Consequently, the hydroxide is not solely bridging the two  $\text{Cu}^{\text{II}}$  ions in **5**. A genuine hydroxide bridge is indeed observed for complex **7** (see Figure 84).<sup>34</sup> This species is the decomposition product of peroxo moiety **3**, which is structurally related to complex **2** (see Section 5).<sup>34</sup>



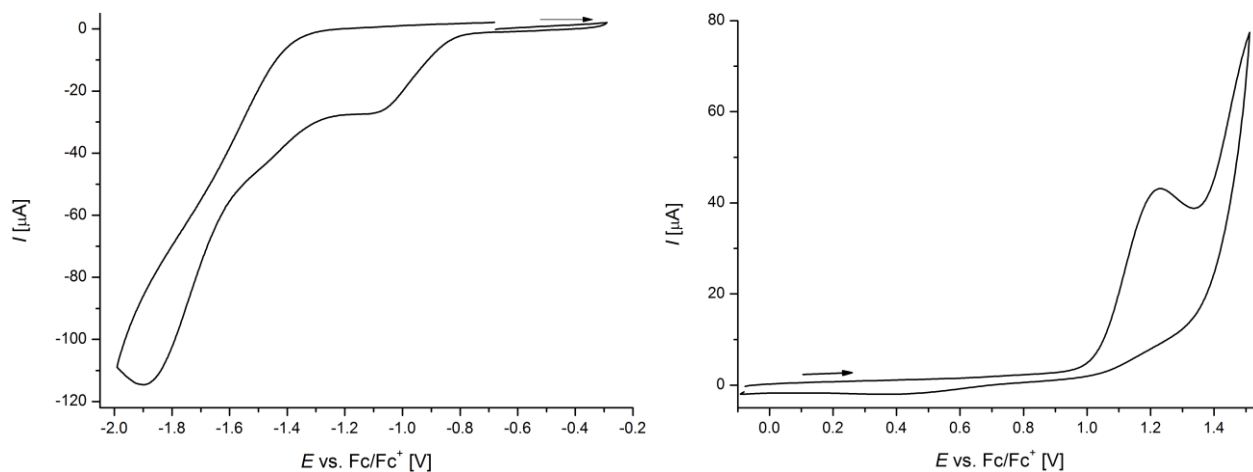
**Figure 84.** Schematic representation of hydroxo complexes **5** and **7**. Complex **7** is the decomposition product of peroxo compound **3**.<sup>34</sup>

The  $\text{Cu}\cdots\text{Cu}$  distance in **7** was determined to  $3.41 \text{ \AA}$  which is significantly shorter than the metal-metal separation in **5**, enabling the hydroxide to bridge the two metal centers.<sup>34</sup> This example again demonstrates the concept of intentional ligand design (see Section 5), to selectively determine geometry and consequently also reactivity of the corresponding metal site. While this section will demonstrate *i.a.* the selective transformation of **5** into the corresponding hydroperoxo and superoxo complexes **2+H<sup>+</sup>** and **4**, complex **7** does not exhibit such chemistry.<sup>192</sup> This effect is most likely due to a better accessibility of the binding pocket in complex **5**, as can be seen by comparing the space-filling models of both complexes (see Figure 85).



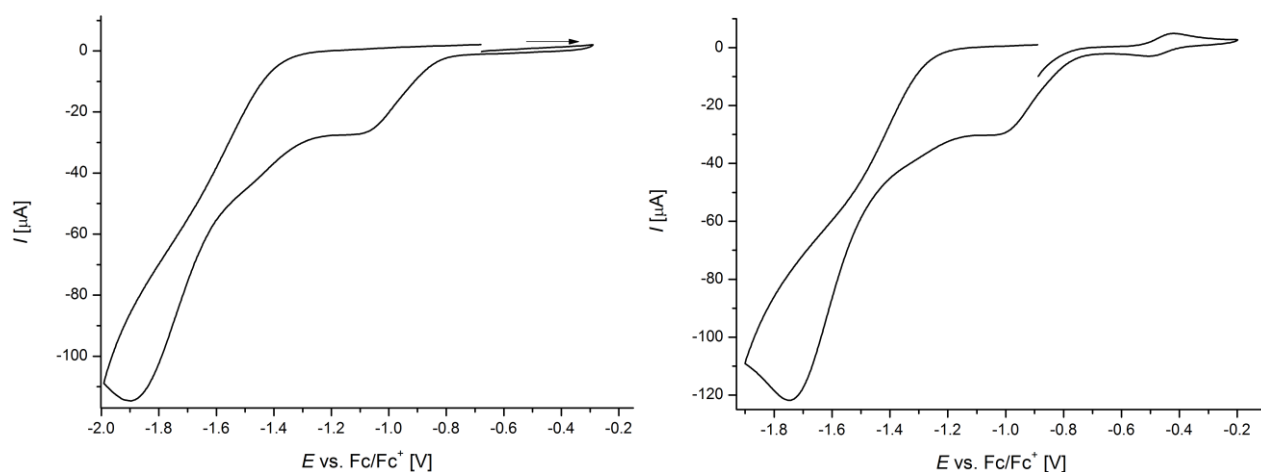
**Figure 85.** Space-filling models of hydroxo complexes **5** (left) and **7** (right).<sup>34</sup>

First studies focused on the electrochemical recycling of complex **5**. Figure 86 shows selected cyclic voltammograms of **5** recorded under inert conditions at 100 mV/s scan rate. Mainly three irreversible waves at  $E_{pc,2} = -1.9$  V,  $E_{pc,1} = -1.1$  V and  $E_{pa,1} = 1.2$  V are observed. With respect to a possible recycling of complex **5** the reductive wave at  $E_{pc,1} = -1.1$  V is of considerable interest. Its origin may be a reduction of the ligand or a reduction of one or of both  $Cu^{II}$  ions.



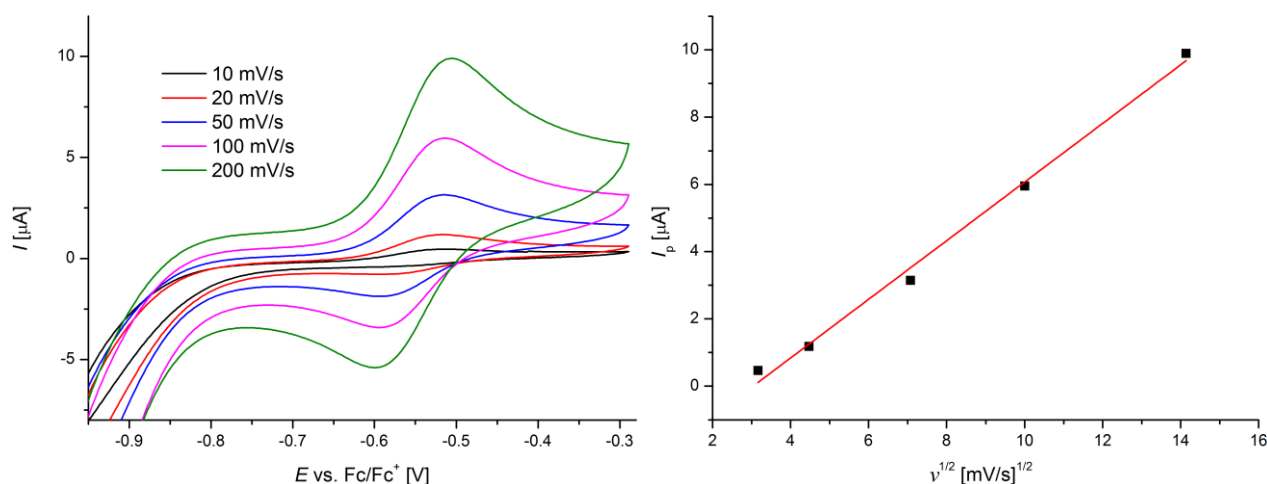
**Figure 86.** Cyclic voltammograms of complex **5** recorded under inert conditions at 100 mV/s scan rate (MeCN,  $c = 2.6$  mM,  $T = 23$  °C); left: scan from -0.7 V to -2.0 V; right: scan from -0.1 V to 1.5 V;

If the reduction event at ca.  $E_{pc,1} = -1.1$  V corresponds to the formation of dinuclear copper(I) complex **1** (see Scheme 23), this species should mainly remain located at the electrode within the scanning process and subsequently form peroxy complex **2** in the presence of molecular dioxygen. Consequently, dry dioxygen has been added to the CV cell and the experiment was repeated. Figure 87 shows two scans starting from -0.6 V (Figure 87, left) and from -0.9 V (Figure 87, right). The left spectrum looks similar to the experiment shown in Figure 86, which has been recorded under argon atmosphere. The right spectrum on the other hand starts from a potential of -0.9 V and shows a reversible wave at  $E_{1/2} = -0.56$  V (vs.  $Fc/Fc^+$ , MeCN,  $T = 23$  °C). Subsequent experiments (see Figure 88 and Figure 89) confirmed this wave to correspond to the reversible oxidation of peroxy complex **2**. Consequently, the irreversible wave in the cyclic voltammogram of complex **5** at approximately  $E_{pc,1} = -1.1$  V can be assigned to the formation of dinuclear copper(I) complex **1**. In the presence of molecular dioxygen, **1** reacts at the electrode to form complex **2**. If the reductive scan starts from -0.6 V (see Figure 87, left), complex **1** is not present at the electrode and the corresponding cyclic voltammogram looks as that of complex **5** recorded under inert conditions.



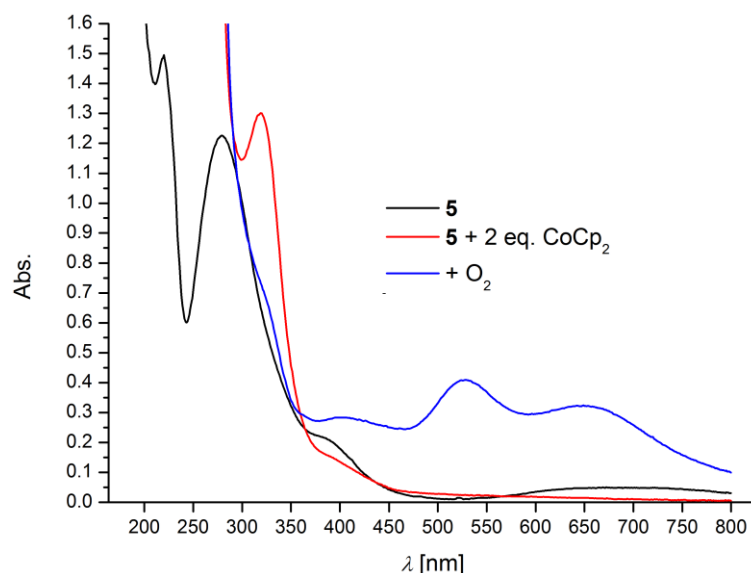
**Figure 87.** Cyclic voltammograms of complex **5** in the presence of dry dioxygen at 100 mV/s scan rate (MeCN,  $c = 2.6$  mM,  $T = 23$  °C); left: scan from -0.6 V to -2.0 V; right: scan from -0.9 V to -2.0 V.

Figure 88 shows the cyclic voltammograms of a 2.6 mM solution of complex **5** recorded from -1.0 V to -0.3 V at different scan rates. Since dioxygen is present in solution, the formed copper(I) complex readily reacts to complex **2** which is then reversibly oxidized to superoxo compound **4** ( $E_{1/2} = -0.56$  V (vs.  $\text{Fc}/\text{Fc}^+$ , MeCN,  $T = 23$  °C)). The reversible wave looks similar to that of a freshly prepared solution of complex **2** recorded at 0 °C ( $E_{1/2} = -0.58$  V (vs.  $\text{Fc}/\text{Fc}^+$ , MeCN); see Section 6.4.1, Figure 59 for details). The slight difference in potential is most likely due to different reaction conditions.



**Figure 88.** Left: cyclic voltammograms of complex **5** under an atmosphere of dry dioxygen and argon at different scan rates from -1.0 V to -0.3 V (MeCN,  $c = 2.6$  mM,  $T = 23$  °C); right: plot of anodic current versus square root of scan rate;  $R^2 = 0.993$ .

These experiments show that complex **5** can be electrochemically recycled to form complex **1**, which then can be selectively transformed into peroxo complex **2**. The recycling of **5** can also be achieved chemically by using a reductant of suitable redox potential. Figure 89 shows the reaction of **5** with 2.2 eq. of  $\text{CoCp}_2$ , which has a redox potential of -1.34 V (vs.  $\text{Fc}/\text{Fc}^+$ , MeCN,  $T = 25$  °C).<sup>193</sup>



**Figure 89.** Black line: UV/vis absorption spectrum of 99  $\mu\text{M}$  solution complex **5** (MeCN,  $T = -40\text{ }^\circ\text{C}$ ); red line: electronic absorption spectrum of complex **5** after the addition of 2.2 eq. of  $\text{CoCp}_2$ ; blue line: UV/vis spectrum after addition of dioxygen to mixture of complex **5** and  $\text{CoCp}_2$ .

The initial solution of complex **5** shows two maxima in absorbance at ca. 280 nm and at ca. 700 nm plus an additional weak shoulder at ca. 390 nm. The broad band at ca. 700 nm can be most likely attributed to a ligand field transition which vanishes upon addition of the reductant,  $\text{CoCp}_2$  (Figure 89, red line). Since the two  $\text{Cu}^{\text{I}}$  ions of the fully reduced complex have a  $d^{10}$  configuration no d-d transition is possible, explaining the absence of an absorption band in the region of 700 nm upon addition of the reductant. The intense band at ca. 320 nm as well as the shoulder at ca. 400 nm are attributed to the oxidized form of  $\text{CoCp}_2$ ,  $\text{CoCp}_2^+$ .<sup>194,195</sup> With subsequent addition of an excess of dry dioxygen, peroxy complex **2** is immediately formed (Figure 89, blue line). The spectrum shows the typical absorption pattern corresponding to  $^{\text{C}}\text{P}$  species **2**. The absorption bands of  $\text{CoCp}_2^+$  at 320 nm and at 400 nm additionally almost disappeared which may be explained by a decay of this species under the existing conditions.

This method enables the selective chemical recycling of decomposition product **5**. Peroxy complex **2** can afterwards be selectively reacted to the corresponding alkali metal adducts as well as to superoxy complex **4** or to the hydroperoxide  $\mathbf{2+H}^+$  (see Sections 6.2 – 6.4 for details). However, with respect to “green chemistry” an electrochemical recycling of **5** should be preferred, since a chemical transformation requires stoichiometric amounts of reductant.

Complex **5** can be furthermore directly transformed into hydroperoxide  $\mathbf{2+H}^+$  (see Figure 90). For this purpose a solution of hydrogen peroxide (35% in  $\text{H}_2\text{O}$ ) has been added to a solution of complex **5** (MeCN,  $T = 1\text{ }^\circ\text{C}$ ). The initial bands of  $\text{H}_2\text{O}_2$  bridged complex **5** immediately vanished by forming the corresponding hydroperoxy complex  $\mathbf{2+H}^+$ . However, the formation of  $\mathbf{2+H}^+$  was only observed for a few seconds since this compound rapidly decomposes at such high temperatures and in the presence of an excess of water. Indeed, complex  $\mathbf{2+H}^+$  is known to be very sensitive towards traces of water and

rapidly decomposes at temperatures above  $-40\text{ }^{\circ}\text{C}$  (see Sections 6.3). From previous work (see Section 6.4 for details) complex  $\mathbf{2}+\text{H}^+$  is known to be selectively transformed into superoxo complex  $\mathbf{4}$  *via* H-atom abstraction. The corresponding superoxide is much more stable towards traces of water and elevated temperatures. Thus, the reaction has been repeated with subsequent addition a solution of 2,4,6-tri-*tert*-butyl-phenoxy radical (referred to as  ${}^t\text{Bu}_3\text{PhO}\cdot$ ) to a solution of  $\mathbf{5}$  and hydrogen peroxide (see Figure 90).

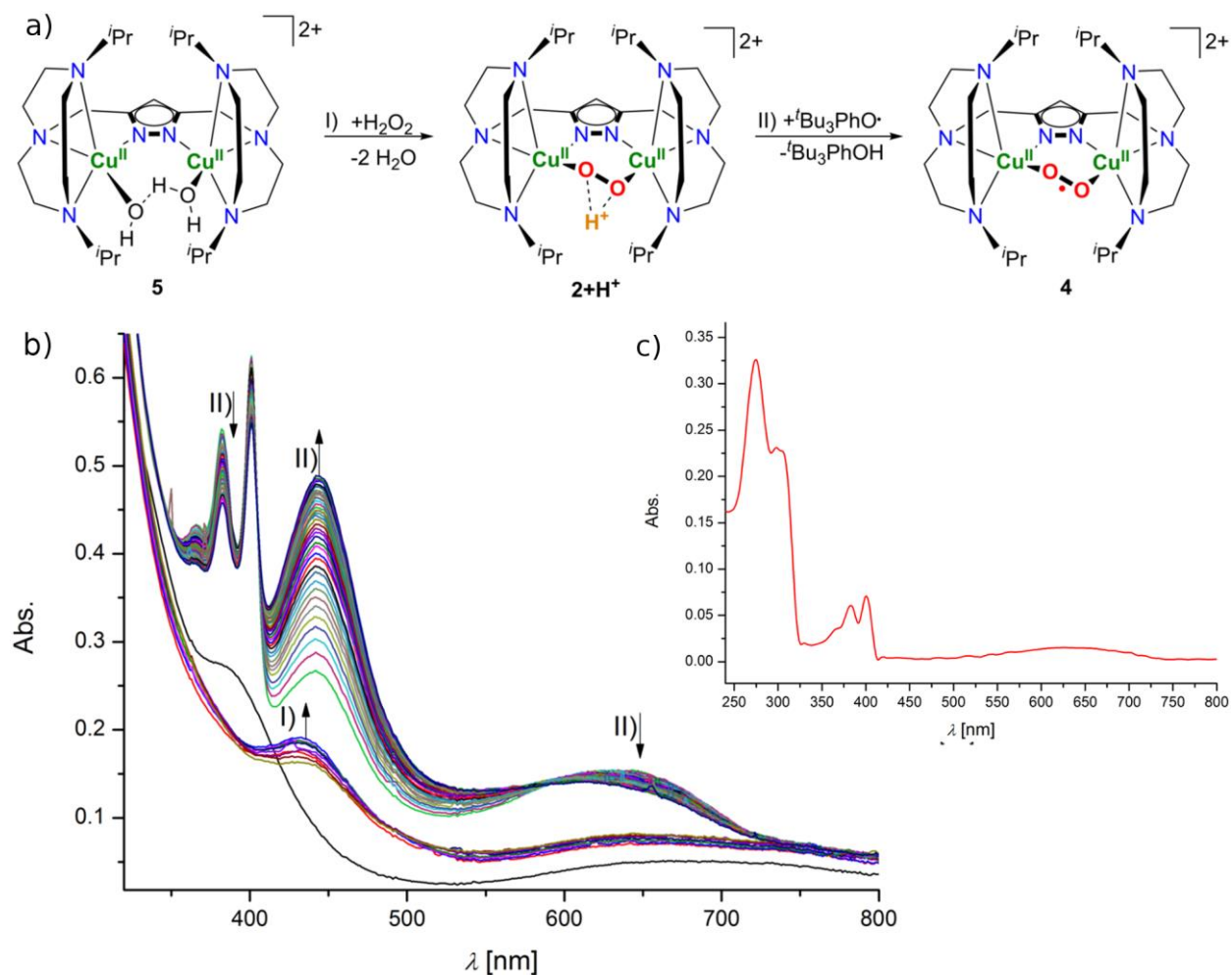


**Figure 90.** a): Schematic representation of reaction of  $\mathbf{5}$  to the corresponding hydroperoxo/superoxo complexes  $\mathbf{2}+\text{H}^+$ / $\mathbf{4}$ ; b): reaction of  $130\text{ }\mu\text{M}$  solution of hydroxo complex  $\mathbf{5}$  (black line) with I): 1.1 eq. of  $\text{H}_2\text{O}_2$  in forming compound  $\mathbf{2}+\text{H}^+$  and II): 5.0 eq. of radical  ${}^t\text{Bu}_3\text{PhO}$  in forming superoxo species  $\mathbf{4}$  (MeCN,  $T = 1\text{ }^{\circ}\text{C}$ ); c): UV/vis absorption spectrum of  $30\text{ }\mu\text{M}$  solution of radical  ${}^t\text{Bu}_3\text{PhO}$  (MeCN,  $T = 1\text{ }^{\circ}\text{C}$ ).

Within addition of 1.1 eq. of aqueous  $\text{H}_2\text{O}_2$  to a solution of complex  $\mathbf{5}$ , hydroperoxo complex  $\mathbf{2}+\text{H}^+$  directly starts to form (see Figure 90, b)). Subsequently, a solution of  ${}^t\text{Bu}_3\text{PhO}\cdot$  has been added (5.0 eq.) and the formation of superoxo complex  $\mathbf{4}$  was observed over ca. 5 min, after which time complex  $\mathbf{4}$  started to decompose. This experiment demonstrates that the decomposition product  $\mathbf{5}$  can be chemically recycled by forming the complexes  $\mathbf{2}+\text{H}^+$  and  $\mathbf{4}$ . This reaction was also possible at room temperature, although the complexes  $\mathbf{2}+\text{H}^+$  and  $\mathbf{4}$  were observed to rapidly decompose under these conditions.

In another experiment a solution of  ${}^t\text{Bu}_3\text{PhO}\cdot$  has been at first added to a solution of complex **5**, followed by addition of different excess of hydrogen peroxide (see Figure 91). When the radical is added to decomposition product **5**, no reaction is observed (Figure 91, red line) until aqueous  $\text{H}_2\text{O}_2$  is injected, immediately initiating the formation of superoxide **4** (see Figure 91, blue line). However, when 2.0 eq. of  $\text{H}_2\text{O}_2$  are used instead of 1.1 eq., much less **4** is formed. An excess of  $\text{H}_2\text{O}_2$  seems to promote the decay of complex **4**. This may be due to the excess of hydrogen peroxide, initiating further side reactions or due to the excess of water accelerating the decay of complex **4**. After complete decomposition, the solution has been again analyzed by means of UV/vis absorption spectroscopy. Next to complex **5** a colorless precipitate has been observed, which could not be identified.

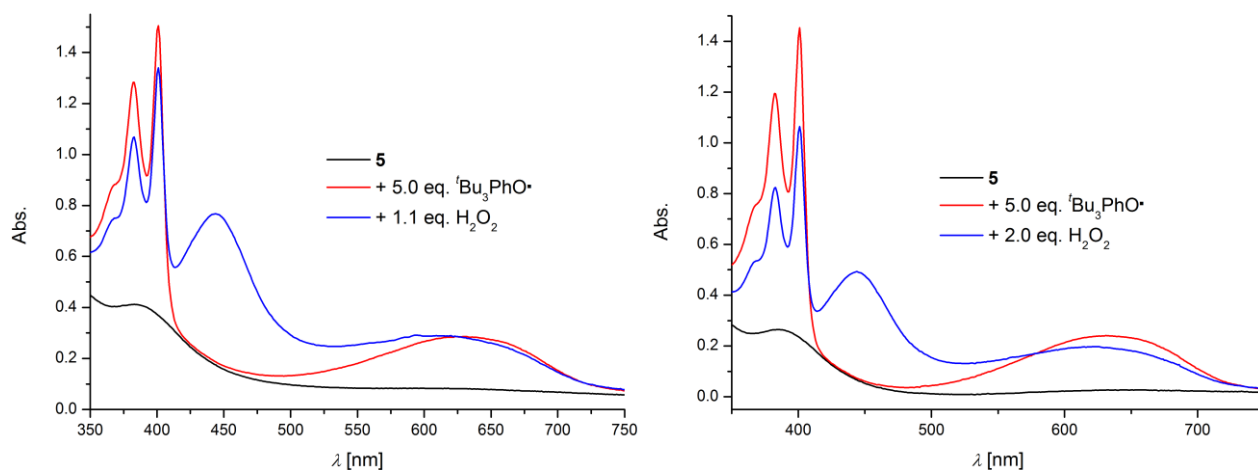
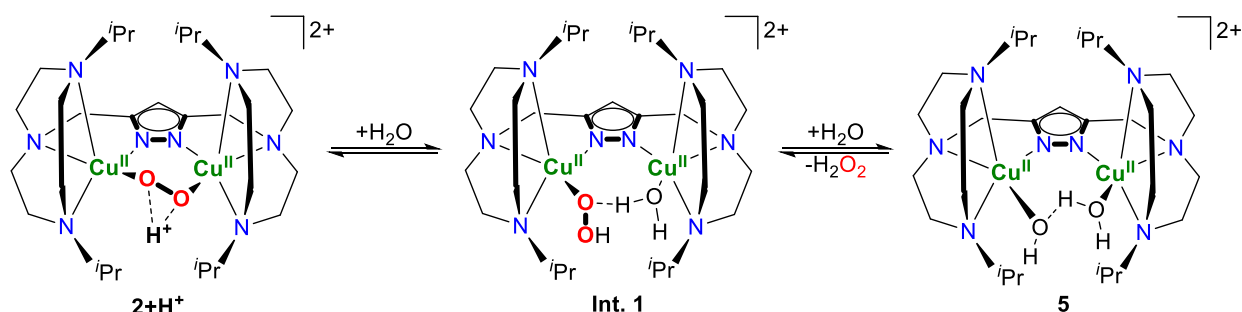


**Figure 91.** Reaction of 86  $\mu\text{M}$  solution of complex **5** and  ${}^t\text{Bu}_3\text{PhO}\cdot$  with different excess of hydrogen peroxide.

### 6.5.1 Formation of **5** from Hydroperoxo Complex **2+H<sup>+</sup>**

The previous section described in detail the recycling of complex **5**, which is similarly formed during the decomposition of the reactive species **2**, **2+M<sup>+</sup>**, **2+H<sup>+</sup>** and **4**. However, the complexes **2**, **2+M<sup>+</sup>** and **4** are much more stable with respect to the formation of the H<sub>3</sub>O<sub>2</sub> bridged decomposition product than hydroperoxide **2+H<sup>+</sup>** (see Sections 6.1 – 6.4). Thus, the formation of **5** from **2+H<sup>+</sup>** may occur *via* a different mechanism, which is potentially promoted by the special geometry of the copper oxygen core in **2+H<sup>+</sup>**. The following section will present a possible mechanism for the decay of complex **2+H<sup>+</sup>**, explaining conclusively the high instability of this species.

Complex **5** was shown to partially react to hydroperoxo complex **2+H<sup>+</sup>** upon addition of aqueous hydrogen peroxide (see Section 6.5) and thus H<sub>2</sub>O<sub>2</sub> may on the other hand be released during the decomposition of **2+H<sup>+</sup>** (see Scheme 25). The H<sub>3</sub>O<sub>2</sub> bridge in complex **5** suggests that H<sub>2</sub>O may also be mechanistically involved in the decomposition of complex **2+H<sup>+</sup>**. Indeed, **2+H<sup>+</sup>** was observed to be sensitive towards water, which will be discussed later. However, the actual molecular structure of the copper oxygen core of **2+H<sup>+</sup>** is still ambiguous and thus the following discussion is only of tentative character. The assumed  $\mu$ -1,2 HO<sub>2</sub><sup>-</sup> binding mode in **2+H<sup>+</sup>** is rather unlikely in such as an additional water molecule may be involved in the actual complex. The additional water molecule may connect the hydroperoxide bound end-on to one of the copper ions with the second copper atom (see Scheme 25, **Int. 1**). However, for both **2+H<sup>+</sup>** and **Int. 1** no structural evidence is available and thus the following discussion will deal with **2+H<sup>+</sup>** rather than **Int. 1**.



**Scheme 25.** Possible mechanism of the decay of complex **2+H<sup>+</sup>**; the actual structure of **2+H<sup>+</sup>** is unclear and may conform with that of **Int. 1**.

The mechanistic considerations are based on different UV/vis experiments of which selected examples will be presented in the following. First of all, another experiment will be reconsidered which has been introduced previously. In Section 6.4.5, the quantitative transformation of **2+H<sup>+</sup>** into superoxide **4** upon addition of the H-atom abstracting reagent <sup>t</sup>Bu<sub>3</sub>PhO<sup>-</sup> was demonstrated. **2+H<sup>+</sup>** thereby was synthesized from complex **2** and 2,6-lutidinium triflate. Peroxide **2** can be furthermore directly transformed into superoxide **4** *via* addition of various oxidants such as AgSbF<sub>6</sub> and Cu(OTf)<sub>2</sub> (see Section 6.4.1). Regardless of the different syntheses, all UV/vis absorption spectra of the final product **4** show the

same maxima in absorbance with similar intensity. The intensity of the main CT transition of **4** ( $\lambda_{\max} = 445 \text{ nm}$ ,  $\epsilon = 10 - 11 \text{ mM}^{-1} \text{ cm}^{-1}$ ) is around two times higher than the maximum of **2** ( $\lambda_{\max} = 527 \text{ nm}$ ,  $\epsilon = 5.1 - 6.0 \text{ mM}^{-1} \text{ cm}^{-1}$ ). A similar ratio is observed by comparing the maxima of **4** and **2+H<sup>+</sup>** (see Table 20).

**Table 20.** Selected absorption maxima and corresponding intensities of relevant copper oxygen complexes.

complex	$\lambda_{\max}$ [nm]	$\epsilon$ [ $\text{mM}^{-1} \text{ cm}^{-1}$ ]
<b>4</b>	445	10 - 11
<b>2</b>	527	5.1 - 6.0
<b>2+H<sup>+</sup></b>	435	5.1 - 6.2

With this knowledge in hand, the primarily mentioned sensitivity of **2+H<sup>+</sup>** towards H<sub>2</sub>O will be reconsidered. Figure 92 shows two independent titration experiments of precursor complex **2** with 2,6-lutidinium triflate (MeCN,  $T = -40 \text{ }^\circ\text{C}$ ). The first experiment (Figure 92, left) was performed in MeCN, containing 3.5 ppm of water (determined *via* Karl-Fischer titration). The spectrum illustrates the already described formation of **2+H<sup>+</sup>** (see Section 6.3) which is completed after an addition of ca. 1.0 eq. of 2,6-lutidinium triflate. The final absorption spectrum shows two maxima in absorbance at 372 nm and 435 nm ( $\epsilon = 3.7$  and  $6.2 \text{ mM}^{-1} \text{ cm}^{-1}$ ).

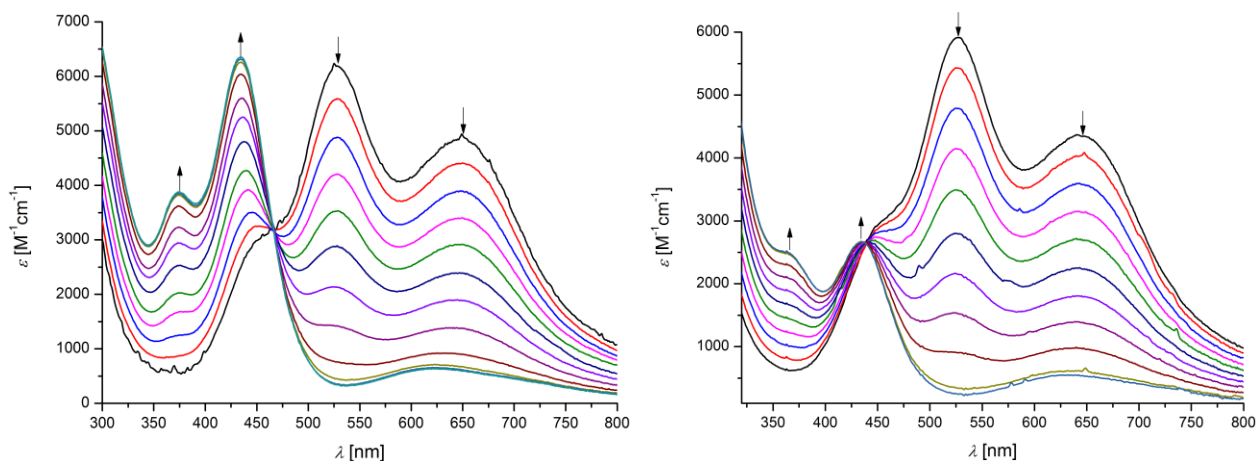


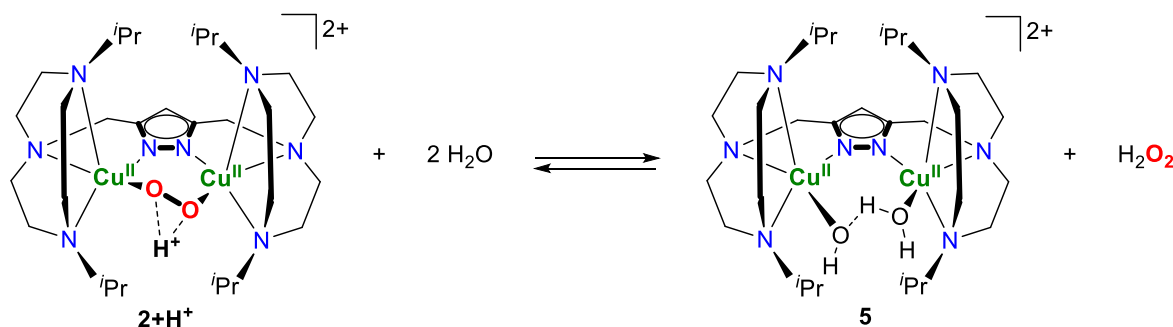
**Figure 92.** UV/vis spectra of the titration of **2** with 2,6-lutidinium triflate in MeCN, containing different amount of water (left: 3.5 ppm; right: 15.6 ppm) (MeCN,  $T = -40 \text{ }^\circ\text{C}$ ); the water content of the solvent was determined *via* Karl-Fischer titration.

The second titration was carried out in another batch of MeCN, containing 15.6 ppm of water. The titration was also finished after the addition of ca. 1.0 eq. of 2,6-lutidinium triflate. However, **2+H<sup>+</sup>** is not cleanly formed under these conditions (see Figure 92, right). The final spectrum features a maximum in absorbance at 435 nm ( $\epsilon = 2.6 \text{ mM}^{-1} \text{ cm}^{-1}$ ) and a shoulder at 364 nm ( $\epsilon = \text{ca. } 2.5 \text{ mM}^{-1} \text{ cm}^{-1}$ ). In contrast to the first titration (see Figure 92, left), however, hydroperoxide **2+H<sup>+</sup>** was only formed in 40% yield in the second experiment. Since both titrations have been performed under same conditions except of a different content of H<sub>2</sub>O in the solvent, the total concentration of water seems to influence the outcome. One explanation for this trend may be the formation of a weak adduct of complex **2+H<sup>+</sup>**



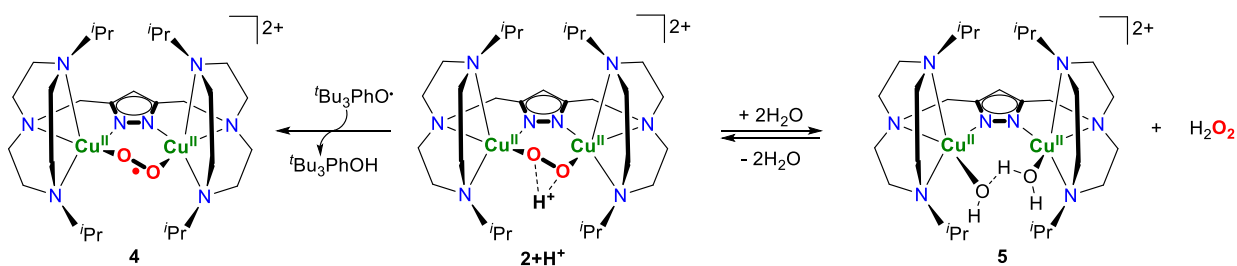
and water, which is formed to a greater extent during the second titration. Nevertheless, such an adduct formation should induce structural and thus electronic changes of the copper oxygen core, as observed during e.g. the alkali metal adduct formation of complex **2** described in Section 6.2. Consequently, the absorption maxima of the adduct of **2+H<sup>+</sup>** and water would shift in energy and the final spectra of both titration experiments should vary considerably. Since the main CT transition of **2+H<sup>+</sup>** is found at  $\lambda = 435$  nm in both experiments, an adduct formation between **2+H<sup>+</sup>** and H<sub>2</sub>O is rather unlikely and will be neglected in the following discussion.

One further possibility may be the decomposition of **2+H<sup>+</sup>** in the presence of H<sub>2</sub>O in forming complex **5** (see Scheme 26). The UV/vis absorption spectrum of **5** is thereby showing two main CT transitions at 278 nm ( $\epsilon = 9700$  M<sup>-1</sup>cm<sup>-1</sup>) and at 390 nm ( $\epsilon = 4600$  M<sup>-1</sup>cm<sup>-1</sup>) and a ligand field transition at ca. 690 nm ( $\epsilon = 800$  M<sup>-1</sup>cm<sup>-1</sup>). If the second titration is reconsidered (see Figure 92, right), the partial formation of decomposition product **5** may explain the shift of the shoulder of **2+H<sup>+</sup>** from 372 nm to 364 nm, since complex **5** is featuring an intense band at 278 nm. Indeed, hydroxide **5** was demonstrated to react to **2+H<sup>+</sup>** in the presence of hydrogen peroxide in Section 6.5. A corresponding formation of **5** from **2+H<sup>+</sup>** by liberation of e.g. H<sub>2</sub>O<sub>2</sub> is thus principally possible. With respect to the in Figure 92 depicted UV/vis experiments, the possible formation of **5** clearly depends on the concentration of H<sub>2</sub>O in the solvent. Consequently, H<sub>2</sub>O must be involved in the actual mechanism of decomposition. One possible mechanism may be a water-mediated liberation of H<sub>2</sub>O<sub>2</sub> in forming decomposition product **5**. The possible equilibrium of **2+H<sup>+</sup>**, H<sub>2</sub>O, **5** and hydrogen peroxide is depicted in Scheme 26.



**Scheme 26.** Proposed equilibrium between complexes **2+H<sup>+</sup>** and **5**.

Since **2+H<sup>+</sup>** is known to quantitatively react with the <sup>t</sup>Bu<sub>3</sub>PhO· radical forming complex **4** (see Section 6.4.5), this reaction was used to probe the in Scheme 26 proposed equilibrium between **2+H<sup>+</sup>** and hydroxide **5**. A successive addition of <sup>t</sup>Bu<sub>3</sub>PhO· to complex **2+H<sup>+</sup>** will immediately induce the generation of superoxide **4** from hydroperoxide **2+H<sup>+</sup>**. Consequently, **2+H<sup>+</sup>** is gradually formed from **5** and hydrogen peroxide (see Scheme 27). The addition of <sup>t</sup>Bu<sub>3</sub>PhO· should therefore quantitatively produce complex **4** from the proposed mixture of **2+H<sup>+</sup>** and **5** (see Scheme 27).



**Scheme 27.** Proposed equilibrium between complexes  $2+\text{H}^+$  and **5** and reaction of  $2+\text{H}^+$  with  ${}^t\text{Bu}_3\text{PhO}\cdot$  in forming superoxide **4**.

Figure 93 shows the titration of the assumed mixture of the complexes  $2+\text{H}^+$  and **5** with  ${}^t\text{Bu}_3\text{PhO}\cdot$  depicted in Figure 92, right. Upon addition of substoichiometric amounts of  ${}^t\text{Bu}_3\text{PhO}\cdot$  (titration in steps of 0.065 eq., with overall 1.235 eq. added), complex **4** is gradually generated. After the addition of 1.235 eq. of radical, no further changes in absorbance are observed.

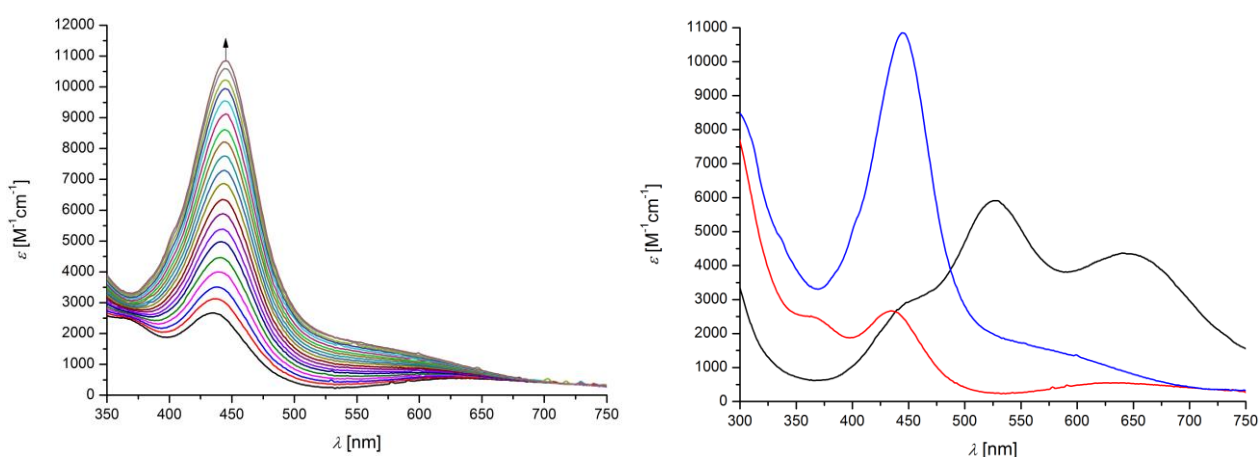


**Figure 93.** Left: UV/vis titration of mixture of  $2+\text{H}^+$  and **5** with  ${}^t\text{Bu}_3\text{PhO}\cdot$  in steps of 0.065 equivalents. The mixture of  $2+\text{H}^+$  and **5** has been previously generated from complex **2** and 2,6-lutidinium triflate (with the solvent containing 15.6 ppm of water,  $T = -40\text{ }^\circ\text{C}$  (see Figure 92, right for corresponding titration)). After addition of in total 1.235 eq. of radical, no further changes in absorbance are observed. Right: UV/vis absorption spectra of precursor **2** (black line); of mixture of complexes  $2+\text{H}^+$  and **5**, synthesized from precursor **2** and 2,6-lutidinium triflate (red line); and of superoxide **4**, generated from titration of the mixture with  ${}^t\text{Bu}_3\text{PhO}\cdot$ . With respect to the intensities of the maxima of complexes **2** and **4**, the mixture of  $2+\text{H}^+$  and **5** has been transformed quantitatively into superoxide **4** (see Table 20).

When comparing the intensities of the maxima in absorbance of superoxide **4** and of precursor **2**, a ratio of ca. 2:1 is observed. With respect to peroxide **2**, complex **4** has thus been quantitatively synthesized from the mixture of  $2+\text{H}^+$  and **5** (see Table 20). This experiment shows that complex  $2+\text{H}^+$  may be in equilibrium with hydroxide **5**. The stepwise generation of **4** induces the formation of  $2+\text{H}^+$  from **5** in the presence of  $\text{H}_2\text{O}_2$ . If on the other hand  ${}^t\text{Bu}_3\text{PhO}\cdot$  is added to a solution exclusively containing complex **5**, no reaction is observed, neither in the presence of dioxygen and/or water. This experiment shows that most likely hydrogen peroxide is reversibly released during the decomposition of complex  $2+\text{H}^+$ . In another experiment, complex  $2+\text{H}^+$  has been freshly generated from **2** and 2,6-lutidinium triflate (see Figure 94, left). The water content of the solvent was determined to ca.

4 ppm. Afterwards, H<sub>2</sub>O was added stepwise (H<sub>2</sub>O was dissolved in MeCN, approximately 2 eq. of water were added per addition) to complex **2+H**<sup>+</sup> and the changes in absorbance were monitored (see Figure 94, right). Upon stepwise addition of H<sub>2</sub>O, the initial maxima of **2+H**<sup>+</sup> at 435 nm and 372 nm rapidly decreased. Between each addition, an equilibration time of several minutes was given, where no further significant changes in absorbance were observed, until another 2 eq. of H<sub>2</sub>O were added. While the maximum at 435 nm is not shifting during the experiment, the weaker band at 372 nm is slightly blue-shifted to a final value of 365 nm. This trend has already been observed (see Figure 92, right). Consequently, the experiment shown in Figure 94 represents a combination of the two previously discussed titrations (see Figure 92). At first, **2+H**<sup>+</sup> is generated under “dry” conditions and the spectrum depicted in Figure 94, left is observed, which is identical to that shown in Figure 92, left. Then, H<sub>2</sub>O is successively added and **2+H**<sup>+</sup> is partially transformed into complex **5**, which corresponds to the experiment depicted in Figure 92, right. Subsequent addition of <sup>t</sup>Bu<sub>3</sub>PhO· to the mixture of **2+H**<sup>+</sup> and **5** leads to a quantitative formation of superoxide **4** from **2+H**<sup>+</sup> and **5**, as already demonstrated previously. In summary, the ratio of **2+H**<sup>+</sup> and **5** clearly depends on the concentration of H<sub>2</sub>O in the corresponding solvent. In the presence of H<sub>2</sub>O<sub>2</sub>, however, addition of the <sup>t</sup>Bu<sub>3</sub>PhO· radical induces quantitative formation of **4**. Consequently, the gradual formation of **5** from **2+H**<sup>+</sup> and water is reversible. Most likely, hydrogen peroxide is released during the decomposition of **2+H**<sup>+</sup>.

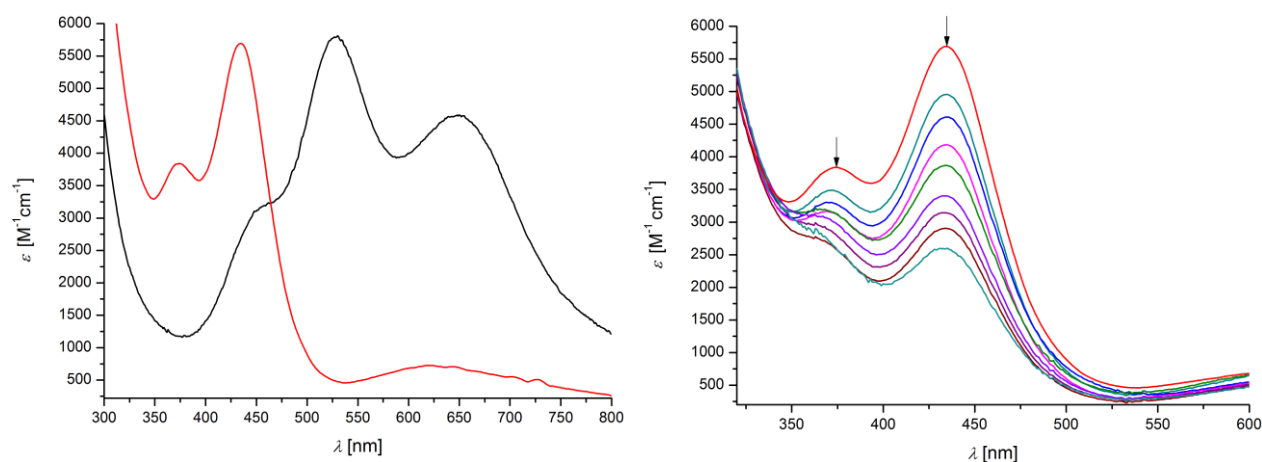
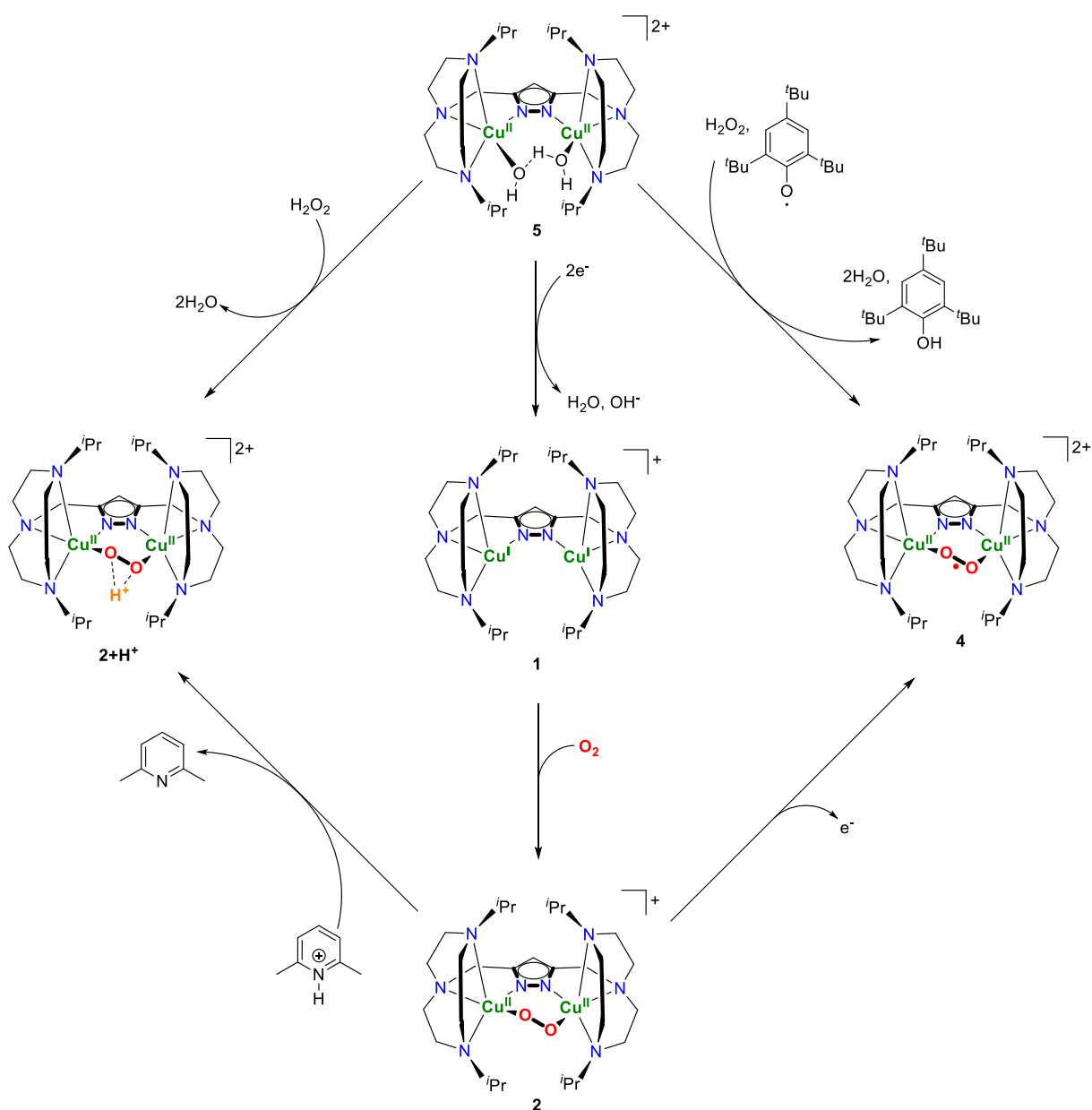


**Figure 94.** Left: UV/vis spectra of precursor **2** (black line) and of **2+H**<sup>+</sup> (red line). Right: UV/vis titration of **2+H**<sup>+</sup> with H<sub>2</sub>O in steps of ca. 2 eq. (mixture of H<sub>2</sub>O and MeCN, *T* = -40 °C); a formation of hydroxide **5** is observed upon addition of H<sub>2</sub>O.

Complex **2+H**<sup>+</sup> was demonstrated to easily form hydroxide **5**. Due to the equilibrium between these two species always small amounts of **5** are present in solution, since it is de facto not possible to work under absolutely water free conditions. The equilibrium between **2+H**<sup>+</sup> and **5** may thereby be one essential reason, why so far no molecular structure of **2+H**<sup>+</sup> could be determined. Since hydroxide **5** preferably crystallizes under all so far tested crystallization conditions, this species is permanently formed from **2+H**<sup>+</sup>. Finally, complex **5** quantitatively crystallized although this species was only present in small amounts in solution.

## 6.5.2 Summary and Conclusion

This section exclusively focused on the recycling of decomposition product **5**, which can be selectively reduced to give complex **1** both chemically and electrochemically. Complex **1** has been subsequently treated with dioxygen to form peroxy complex **2**, which can be furthermore transformed to the corresponding superoxo or hydroperoxy species (see Scheme 28). Complex **5** has also been directly transformed into complex **2+H<sup>+</sup>** by using hydrogen peroxide. Subsequent treatment with <sup>t</sup>Bu<sub>3</sub>PhO<sup>•</sup> further enables the synthesis of superoxo complex **4**. Thus, by starting from decomposition product **5** the complexes **2**, **2+H<sup>+</sup>** and **4** can be selectively recovered.



**Scheme 28.** Synthesis of oxygen complexes **2**, **2+H<sup>+</sup>** and **4** starting from decomposition product **5**.

Hydroxo complexes such as **5** and **7** are usually formed during the decomposition of synthetic dicopper oxygen complexes and have been discarded until to date. This approach is rather unsatisfactory since the ligand systems **HL**<sup>1</sup> and **HL**<sup>2</sup> as well as the corresponding copper(I) complexes are generated in a time consuming multi-step synthesis under a high consumption of resources.<sup>32,34</sup> With respect to potential substrate conversion performed by reactive copper oxygen species such as the complexes **2**, **2+H**<sup>+</sup> or **4**, complex **5** will be unavoidably formed as decomposition product over time. Until today the mechanistic understanding of substrate conversion performed by reactive oxygen complexes is intensively focused, while the development of sustainable systems of the type of **2**, **2+H**<sup>+</sup> or **4** is unrepresented. A specific recycling of **5** to the corresponding copper oxygen complexes is thus of considerable interest, since the efficiency of possible substrate conversion promoted by such reactive oxygen species could be increased drastically. This work therefore presents unique approaches of how biomimetic copper oxygen complexes could become efficient catalysts.

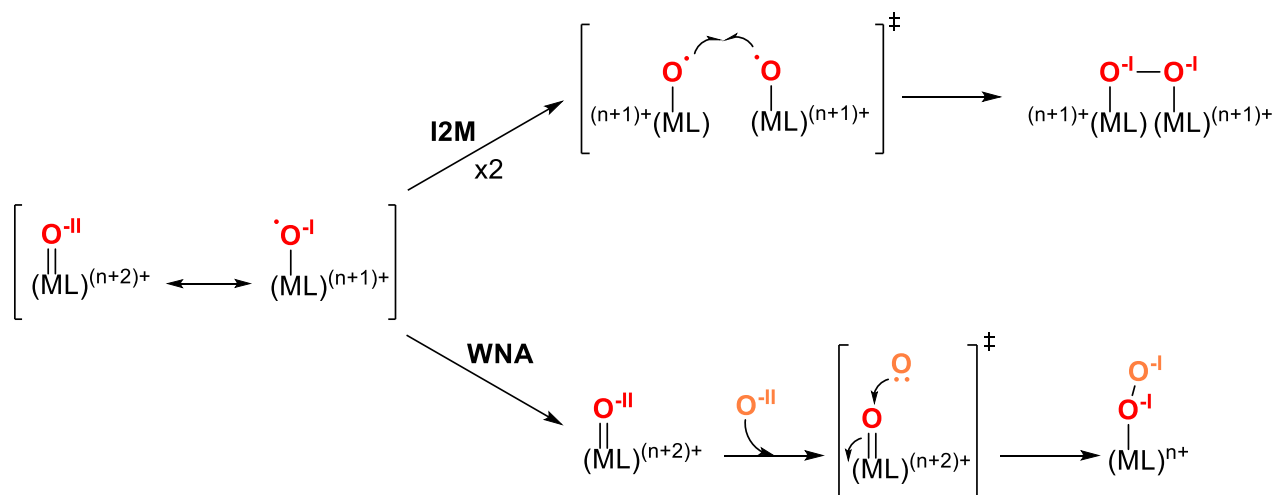
However, only complex **5** can be chemically recycled, while **7** is inert towards this kind of chemistry. The structural differences of these quite similar complexes were discussed and provide important information for the synthesis of other copper complexes. With respect to a chemical recycling, the access of the substrate binding pocket of the corresponding copper complex is of major relevance. While the copper site in **7** is less accessible due to the specific ligand design, **5** features an open binding pocket which most likely is the main reason for the possible chemical recycling.

With respect to “green chemistry”, especially the electrochemical generation of **1** may be of future interest, since no chemical reagent is required for this transformation. This observation suggests further investigations towards a possible application of complex **5** or of structurally related systems for electro-catalytic substrate conversion.

Next to a selective recycling of complex **5**, this chapter further investigated the low stability of hydroperoxide **2+H**<sup>+</sup>. UV/vis spectroscopic studies revealed a water-dependent equilibrium between **2+H**<sup>+</sup> and **5**. Hydroperoxide **2+H**<sup>+</sup> was thereby observed to be sensitive towards traces of water and most likely, hydrogen peroxide is released during the decomposition of **2+H**<sup>+</sup> under aqueous conditions. However, the mechanistic details of especially the transformation of complex **5** into hydroperoxide **2+H**<sup>+</sup> are not clear until to date and require further investigations. A molecular structure of **2+H**<sup>+</sup> is thus of considerable interest, although a successful crystallization of this species is challenging due to the equilibrium with **5**, which preferably crystallizes under all tested conditions.

## 6.6 Electrocatalytic Water Oxidation

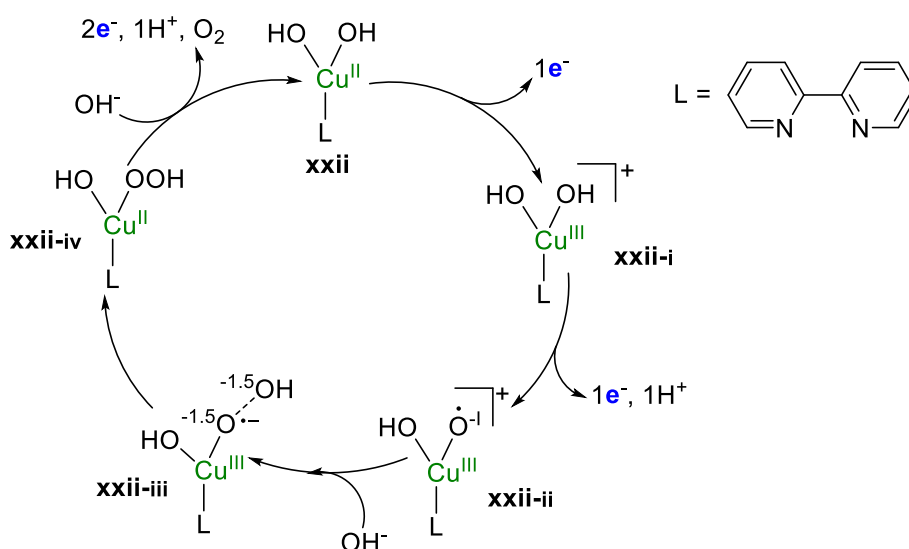
Electrocatalytic water oxidation has become a topic of intensive studies within the last decade, since a sustainable production of clean energy is one of the main scientific challenges of this century.<sup>196,197,198</sup> The pioneering investigations are thereby inspired by Photosystem II, where water is split into protons, O<sub>2</sub> and electrons ( $2\text{H}_2\text{O} \rightarrow \text{O}_2 + 4\text{H}^+ + 4\text{e}^-$ ).<sup>199</sup> The actual oxidation of water occurs at the oxygen evolving complex (OEC), where four manganese and one calcium atom are held together by bridging oxo and hydroxo ligands in a cubic structure.<sup>196</sup> The specific mimicking of this unique reactivity implies a significant mechanistic challenge, since water is split in protons and electrons in breaking four O-H bonds under subsequent O-O bond formation.<sup>199,200</sup> Since a high thermodynamic potential of 1.23 V (vs NHE at pH 0.0) is required for this process, oxidatively robust ligand systems have to be developed that additionally enable the synthesis of water soluble metal complexes.<sup>200</sup> The most intensively studied synthetic metal sites are based on ruthenium (Ru) and iridium (Ir), whereas earth abundant first row transition metals such as iron and copper are recently gaining increasing interest.<sup>196</sup> In contrast to Ru and Ir the first row transition metals are attractive because of their low costs.<sup>201</sup> Additionally, iron and copper are promising candidates for artificial water oxidation due to a wide scope of biomimetic oxygen complexes (see Sections 2 and 3).<sup>201,44,202</sup> However, the actual mechanism of action at synthetic model complexes is still under debate, whereas mainly two different mechanisms have been proposed (see Scheme 29).<sup>203</sup>



**Scheme 29.** Schematic representation of I2M and WNA mechanisms.<sup>203</sup>

The water nucleophilic attack (WNA) mechanism involves the nucleophilic attack of one external water molecule on a high valent metal oxo compound, forming a metal peroxo intermediate.<sup>196,203</sup> The metal oxidation state is thereby reduced by two units. The I2M mechanism on the other hand describes the coupling of two formal oxyl radicals.<sup>203</sup> The oxidation state of the metal centers is not changed during this process. However, both mechanisms involve high valent metal oxo compounds (the I2M

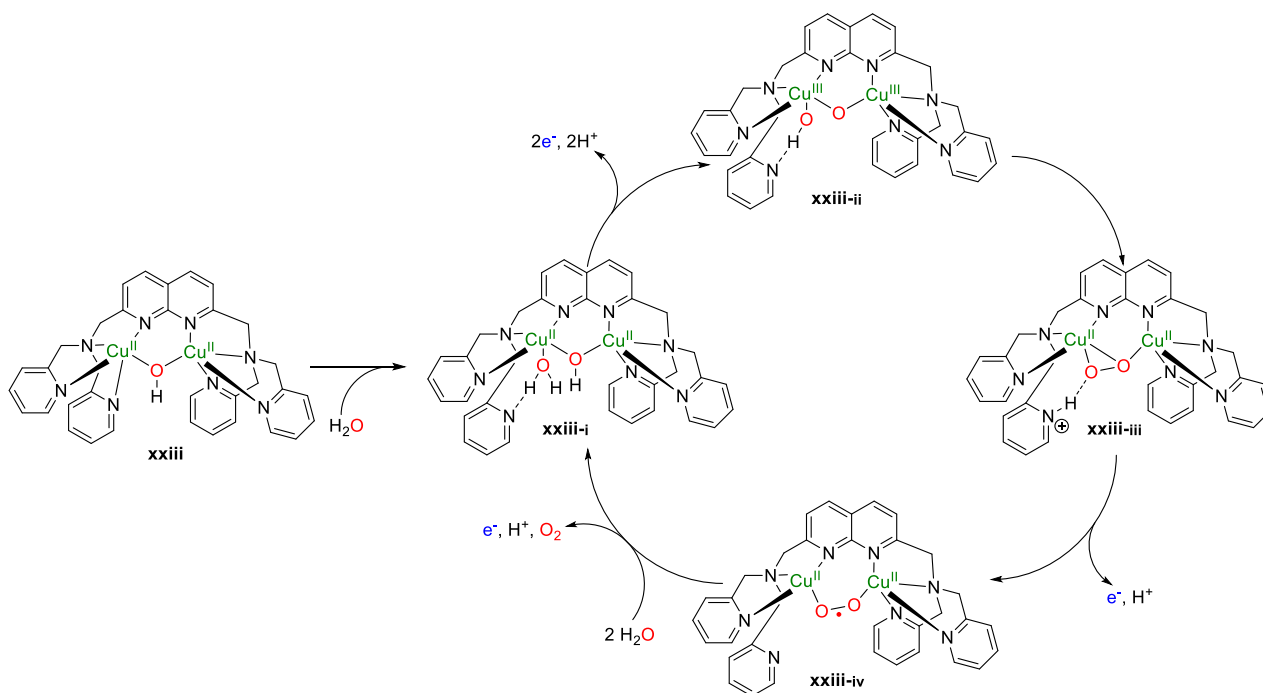
mechanism describes two metal oxo species that hold radical character) which is the reason for a usually short lifetime of the catalyst due to self-oxidation of the ligand framework.<sup>196</sup> Thus, the synthesis of oxidatively robust ligand systems is one fundamental requirement in water oxidation catalysis.<sup>204</sup> Most of the Ru and Ir based water oxidation catalysts were found to follow one of these two aforementioned pathways.<sup>196</sup> Nevertheless the mechanism of action of first row transition metal complexes is mostly unknown. Recently, a third mechanism has been proposed for mononuclear copper and ruthenium complexes, which is referred to as single electron transfer water nucleophilic attack (SET-WNA).<sup>203</sup> The SET-WNA is a combination of WNA and I2M since it most likely proceeds either from a metal oxo or from the corresponding metal oxyl moiety.<sup>203</sup> In the SET-WNA mechanisms the external oxygen atom does not transfer two electrons in one concerted step as during the WNA attack.<sup>203</sup> Instead, two single electron transfers are observed. The first SET involves a (O...OH)<sup>-</sup> fragment, where both oxygen atoms are featuring a formal oxidation state of -1.5 (see Scheme 30, intermediate **xxii-iii**).<sup>203</sup> The second SET occurs in forming a hydroperoxo complex (see Scheme 30, intermediate **xxii-vi**), from which dioxygen is finally released.<sup>203</sup> Thus, the SET-WNA mechanism requires the formation of a stable (O...OH)<sup>-</sup> intermediate.<sup>203</sup> This mechanism shows that water oxidation especially at early transition metal complexes may occur without the formation of high valent metal oxo species. With this knowledge in hand, new early transition metal complexes may be designed, enabling water oxidation at lower overpotential.<sup>203</sup> Consequently, the lifetime of the corresponding catalyst may be increased due to less favored self-oxidation of the ligand.



**Scheme 30.** Postulated catalytic cycle for SET-WNA attack mechanism.<sup>203</sup>

Recently, a dinuclear copper complex has been published that performs water oxidation at neutral aqueous conditions.<sup>205</sup> The postulated mechanism involves an intramolecular O-O bond formation by avoiding high valent Cu(IV) oxo sites (see Scheme 31).<sup>205</sup> The actual catalyst is assumed to consist of a water and an additional hydroxide molecule, the latter bridging the two Cu(II) atoms (see Scheme 31,

**xxiii-i).**<sup>205</sup> At first, two protons and two electrons are released in two independent steps from the water and hydroxide ligands. The corresponding intermediate **xxiii-ii** is featuring two Cu(III) ions, most likely being bridged by an oxo moiety. Subsequently, an oxo bridge and an additional hydroxo ligand are forming the O-O bond whereat a pyridyl donor site serves as proton acceptor (Scheme 31, **xxiii-iii**).<sup>205</sup> The resulting peroxy species then is oxidized by one electron to the corresponding superoxo complex, **xxiii-iv**. Finally, molecular dioxygen is released and the catalyst is retained.<sup>205</sup> However, this mechanism is exclusively based on DFT calculations and none of the postulated intermediates has been isolated or spectroscopically characterized.



**Scheme 31.** Postulated water oxidation mechanism for dinuclear complex  $[\text{Cu}(\text{BPMAN})(\mu\text{-OH})]^{3+}$  BPMAN = 2,7-[bis(2-pyridylmethyl)aminomethyl]-1,8-naphthyridine.<sup>205</sup>

In summary, different mechanisms for water oxidation at mid and late transition metal complexes are postulated, which are mainly supported by DFT calculations. In this thesis complex **5** has been introduced, which can be selectively transformed into the reactive  $\text{Cu}_2/\text{O}_2$  species **2**,  $\mathbf{2}+\text{H}^+$  and **4** at ambient conditions (see Section 6.5). With respect to the mechanism depicted in Scheme 31, all of these  $\text{Cu}_2/\text{O}_2$  species are potential intermediates during water oxidation at dinuclear copper complexes. Thus, **5** is a valuable candidate for studying electrolytic water oxidation. The following section will focus on electrolytic water oxidation starting from complex **5** and will further introduce Section 6.6.2, dealing with a computational consideration of this topic.



### 6.6.1 Towards Electrocatalytic Water Oxidation

The formation of complex **5** during decomposition of e.g. peroxy complex **2** and hydroperoxy complex **2+H<sup>+</sup>** has been described in previous sections. However, for electrocatalytic water oxidation complex **5** has been synthesized directly from ligand **HL<sup>1</sup>** and Cu(ClO<sub>4</sub>)<sub>2</sub> (see Section 7.13.6 for instructions). Single crystalline material was obtained *via* Et<sub>2</sub>O diffusion into concentrated solutions of CHCl<sub>3</sub>/MeCN. Elemental analysis revealed the presence of complex **5** in high purity. An ESI mass spectrum was recorded and exclusively shows complex **5** as product (see Section 7.13.6).

In order to investigate the properties of **5** towards electrolytic water oxidation, the water solubility of this species has been tested at first. Figure 95 shows the UV/vis absorption spectrum of **5** recorded at 22 °C (MeCN, *c* = 99 μM). Two absorption maxima at 281 nm and 690 nm and a shoulder at 386 nm are observed. When 100 μL of demineralized water were added, the shoulder at 390 nm vanished and the maximum at 281 shifted to 278 nm (see Figure 95, blue line).

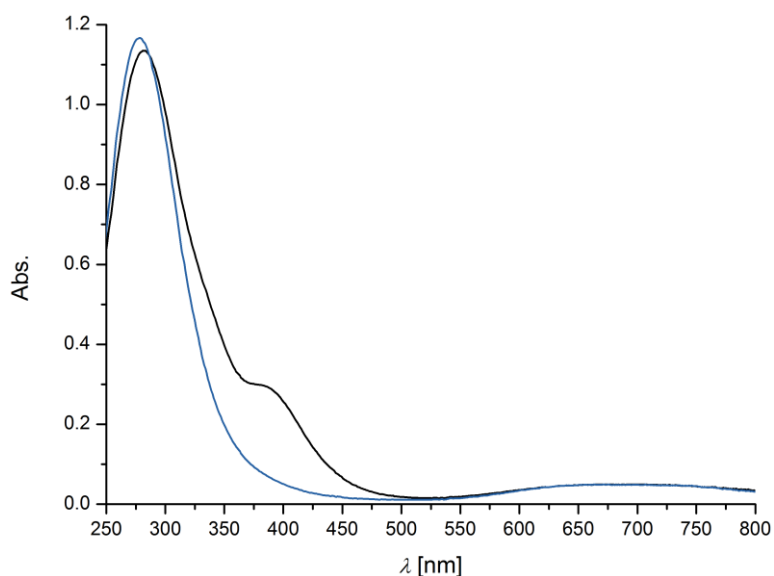


**Figure 95.** UV/vis absorption spectra of **5** dissolved in MeCN (black line) and after addition of 100 μL of demineralized water (blue line) (*T* = 22 °C). No further spectral changes were observed during addition of more water.

Further addition of water induced neither spectral changes, nor precipitation of **5** was observed. If on the other hand a solution of **5** in MeCN (*V* = 20 μL, *c* = 0.01 M) is added to 2.5 mL of demineralized water (pH 6.5), the same electronic absorption spectrum is monitored, which does not change during storage at RT over month. However, complex **5** is only water soluble in the presence of MeCN, although the overall amount of organic solvent can be small. With respect to electrolytic water oxidation, **5** needs to be stable in e.g. phosphate buffer, since the pH value must be hold constant especially during long term electrolysis. For this purpose, a solution of **5** in MeCN was mixed with water (pH 13, 0.1 M ionic strength phosphate buffer) and the corresponding electronic absorption spectrum was recorded. The spectrum looks similar to that recorded at pH 6.5, with the main CT transition located at 275 nm (see Figure 96, left). The same solution was recorded after two weeks of storage at RT, showing no

differences in absorption. Thus, complex **5** is stable under these conditions, while the mononuclear copper-bipyridine system capable of electrolytic water oxidation established by MAYER<sup>201</sup> was observed to decompose at pH 12.5 (0.1 M NaOAc,  $T = 22\text{ }^{\circ}\text{C}$ ) within 24 h.<sup>206</sup> Since the electronic absorption spectrum of complex **5** recorded in phosphate buffer looks exactly like the spectrum recorded in demineralized water, phosphate is not interacting with the copper core by e.g. binding to the metal centers. Additionally, the  $\text{H}_3\text{O}_2$ -bridge is not deprotonated at e.g. pH 13, which would significantly change the electronic absorption spectrum. However, in order to further study a possible deprotonation of the bound water molecule at basic conditions, complex **5** has been analyzed *via* UV/vis absorption spectroscopy from pH 8 – pH 13 (see Figure 96). Indeed, all electronic absorption spectra show the same maxima in absorbance from pH 8 to pH 13 ( $T = 23\text{ }^{\circ}\text{C}$ , 0.1 M phosphate buffer). Consequently, the nature of the  $\text{H}_3\text{O}_2$  bridge is not changed in that pH range, since any protonation or deprotonation equilibria would induce significant spectral changes. However, spectral changes were observed at lower pH. When a 1 mM solution of complex **5** was adjusted to e.g. pH 4 (100  $\mu\text{M}$  solution of  $\text{H}_2\text{SO}_4$ ) two new bands at 380 nm and 450 nm are observed which may be due to a protonation of the hydroxide. Since the here presented water oxidation will not take place at such low pH, no further investigations were carried out.

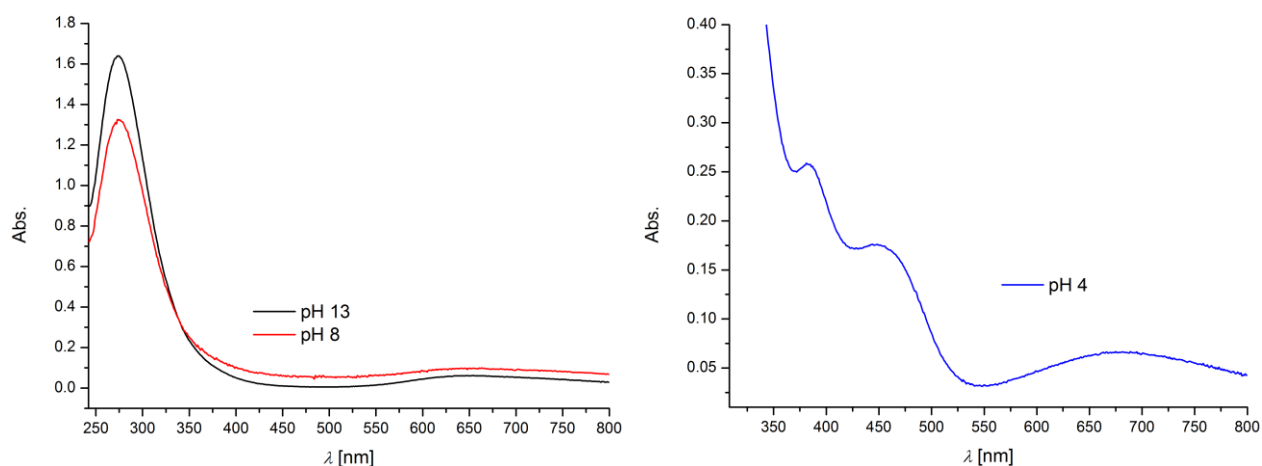


**Figure 96.** Electronic absorption spectra of ca. 1 mM solution of complex **5** at different pH (pH 8, pH13: 0.1 M phosphate buffer; pH 4: 100  $\mu\text{M}$  solution of  $\text{H}_2\text{SO}_4$ ).

With this background in hand, first electrochemical studies were performed at different pH (for experimental details see Section 7.5). Figure 97 shows two cyclic voltammograms of complex **5** recorded at pH 10 and pH 13 in 0.1 M ionic strength phosphate buffer ( $V$  (electrolyte) = 2.5 mL,  $V$  (MeCN) = 20  $\mu\text{L}$ ). While the cyclic voltammogram at pH 10 is almost identical to the corresponding blank measurement (see Figure 97, blue and purple lines), the spectrum recorded at pH 13 looks significantly different. In contrast to the blank measurement, a large irreversible oxidative wave is observed starting at approximately 1.0 V (vs. normal hydrogen electrode (NHE)). This behavior has also been reported for other copper complexes.<sup>196,201</sup> The mononuclear copper-bipyridine system developed

by MAYER for instance shows similar cyclic voltammograms starting from pH 11, while at pH 10 no such oxidative waves are observed.<sup>201</sup> The cyclic voltammogram of **5** recorded at pH 13 (see Figure 96) can still be reproduced from the same solution, which has been stored for several months at ambient conditions. Furthermore, successive scanning for more than 30 times did not change the original cyclic voltammogram.

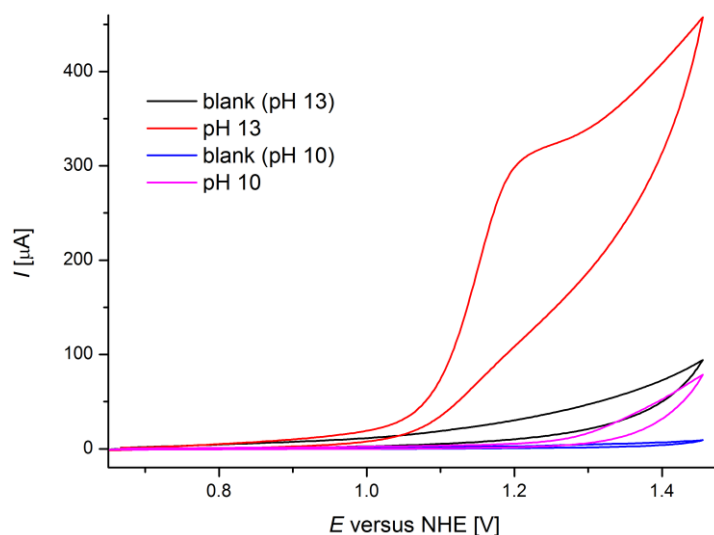


**Figure 97.** Cyclic voltammograms of 1.0 mM solution of complex **5** at different pH (0.1 M ionic strength phosphate buffer,  $T = 22\text{ }^{\circ}\text{C}$ , 100 mV/s scan rate). The corresponding blank spectra were recorded under the same conditions.

Irrespective of a potential water oxidation, these experiments confirm the high stability of **5** which has been already demonstrated *via* UV/vis absorption spectroscopy. With respect to possible water oxidation, the electrochemical properties of complex **5** were investigated in detail from pH 11 to pH 13 (see Figure 98).

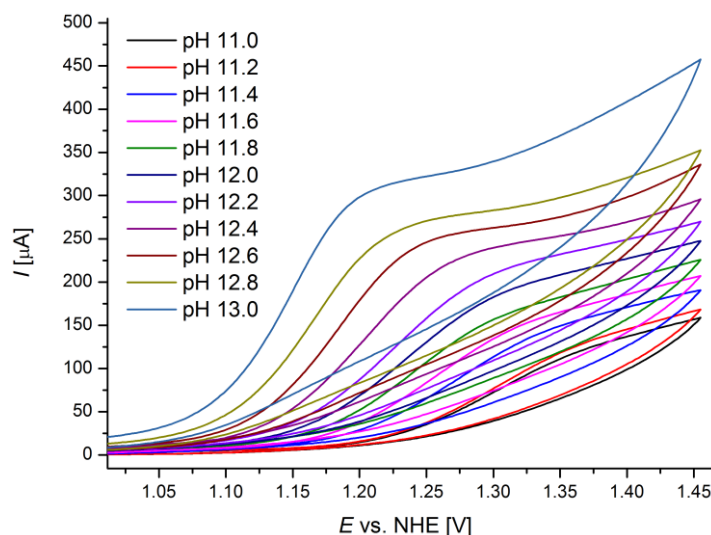


**Figure 98.** Cyclic voltammograms of 1.0 mM solution of complex **5** at different pH (0.1 M ionic strength phosphate buffer,  $T = 22\text{ }^{\circ}\text{C}$ , 100 mV/s scan rate); a solution of **5** in 20  $\mu\text{L}$  of MeCN was mixed with 2.0 mL of electrolyte for each measurement.

While the oxidation event is only slightly observed at pH 11, the current of this wave significantly increases from pH 11 to pH 13. Additionally, the oxidative wave is shifting to lower potential with increasing pH. Figure 99 shows a plot of pH versus the corresponding potential of the oxidation event.

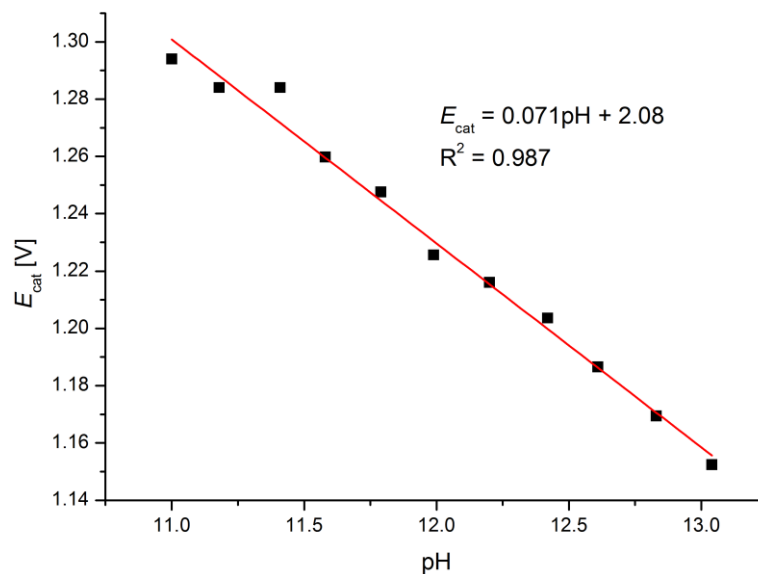


**Figure 99.** Investigated pH dependence of possible water oxidation with **5**; the first inflection point of the catalytic wave is used for determination of  $E_{\text{cat}}$ .

Since no clear maximum of the oxidative wave is observed, the first inflection point of the oxidation event was determined for each pH value (determination from 2<sup>nd</sup> derivative of plot of current vs. potential). The corresponding potential linearly changes with pH (slope = 71 mV) and clearly illustrates the pH dependence of this process. Consequently, further investigations towards electrolytic water oxidation were conducted. Figure 100 shows a plot of different complex concentrations versus the corresponding current at  $E = 1.3$  V (vs. NHE).

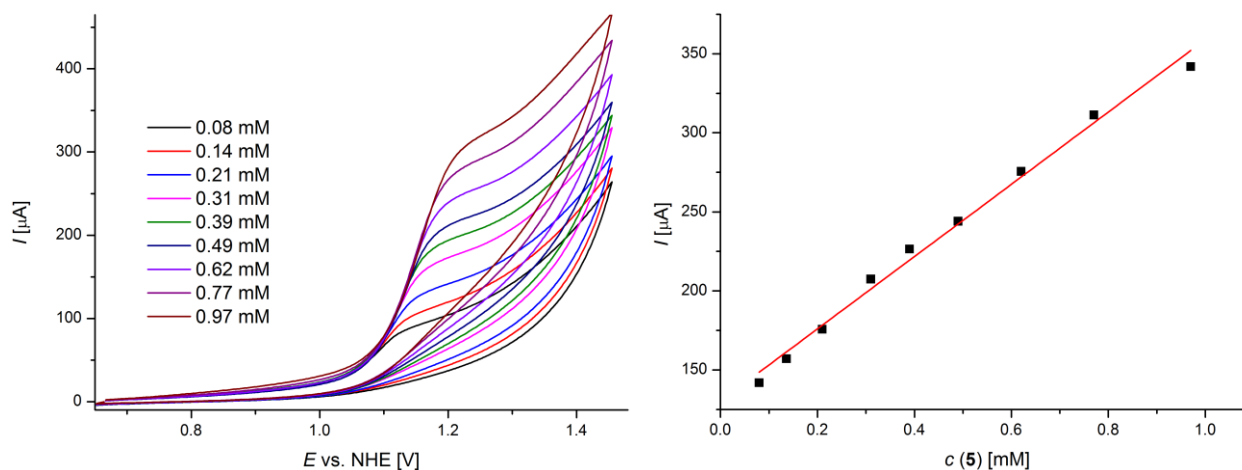


**Figure 100.** Left: cyclic voltammograms of **5** at pH 13 at different complex concentrations (0.1 M ionic strength phosphate buffer,  $T = 22$  °C, 100 mV/s scan rate); right: plot of catalytic current at 1.3 V versus complex concentration ( $R^2 = 0.996$ ).

The current was observed to linearly increase with complex concentration. This behavior has also been observed for other copper complexes and shows that the formation of solid material on the electrode such as copper oxides is rather unlikely.<sup>200,207</sup> However, one further possibility may be a complete dissociation of complex **5** in 0.1 M phosphate buffer, by liberating Cu<sup>II</sup> ions performing the actual water oxidation. Thus, the electrochemical properties of a 2 mM solution of Cu(ClO<sub>4</sub>)<sub>2</sub> were monitored under the same experiment conditions, which are applied for complex **5**. A comparison of the cyclic voltammograms of a 1 mM solution of **5** and a 2 mM solution of Cu(ClO<sub>4</sub>)<sub>2</sub> is depicted in Figure 101. The cyclic voltammogram of the 2 mM solution of Cu(ClO<sub>4</sub>)<sub>2</sub> shows no oxidation event and thus the oxidation event observed for **5** is not induced by free Cu<sup>II</sup> ions. However, one further possibility may be the deposition of e.g. copper oxides on the working electrode over time. Consequently, the oxidative wave would not correspond to homogeneous water oxidation but rather be induced by copper oxides, deposited on the electrode. This effect has often been observed for other copper or cobalt complexes.<sup>196,208</sup>

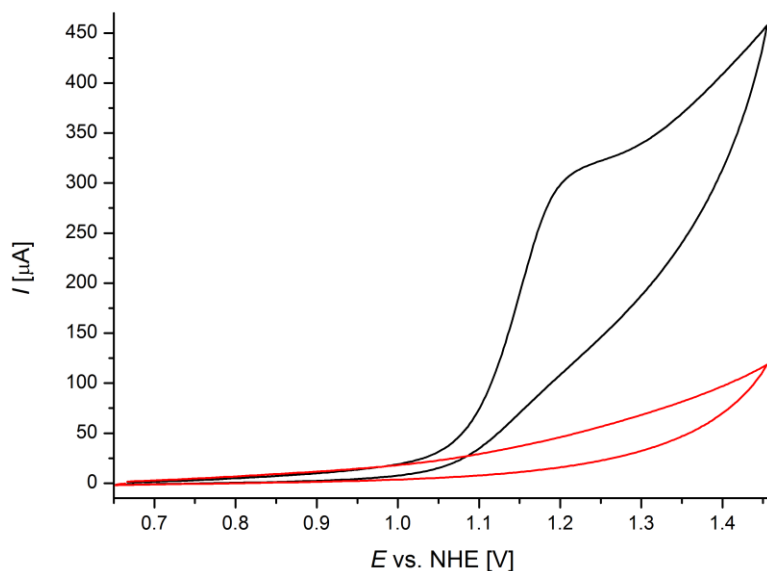


**Figure 101.** Cyclic voltammograms of 1.0 mM solution of **5** (black line) and of 2.0 mM solution of Cu(ClO<sub>4</sub>)<sub>2</sub> at pH 13 (0.1 M ionic strength phosphate buffer,  $T = 22\text{ }^{\circ}\text{C}$ , 100 mV/s scan rate); during the experiment with Cu(ClO<sub>4</sub>)<sub>2</sub>, precipitation of bluish material was observed which most likely corresponds to copper hydroxide.

In order to investigate a possible deposition of solid material on the glassy carbon (GC) working electrode, controlled potential coulometry was performed with a 1 mM solution of complex **5** ( $E = 1.15\text{ V vs. NHE}$ ,  $t = 4\text{ h}$ , pH 13, 0.1 M ionic strength phosphate buffer,  $T = 22\text{ }^{\circ}\text{C}$ ). The GC working electrode (GC disc,  $A = 0.07\text{ cm}^2$ ) was afterwards scanned in blank electrolyte. The cyclic voltammogram looks nearly identical to that of the GC working electrode recorded after electrolysis in pure electrolyte (see Figure 102). Since both cyclic voltammograms look similar, no catalytically active material is deposited on the electrode during long term electrolysis with complex **5** under the aforementioned conditions.<sup>201</sup> Nevertheless, long term electrolysis at higher potential ( $E = 1.25\text{ V vs. NHE}$ ,  $t = 4\text{ h}$ ) with a

1 mM solution of complex **5** revealed the deposition of solid material on the GC working electrode which goes in hand with a decomposition of **5**. Since the GC disc working electrode only provides a small electrode surface, which would lead to even longer reaction times in order to produce a significant amount of molecular dioxygen, the experimental setup was changed for further investigations. Consequently, no further investigations concerning the decomposition of complex **5** during long term electrolysis at the GC disc were performed were conducted at this stage.

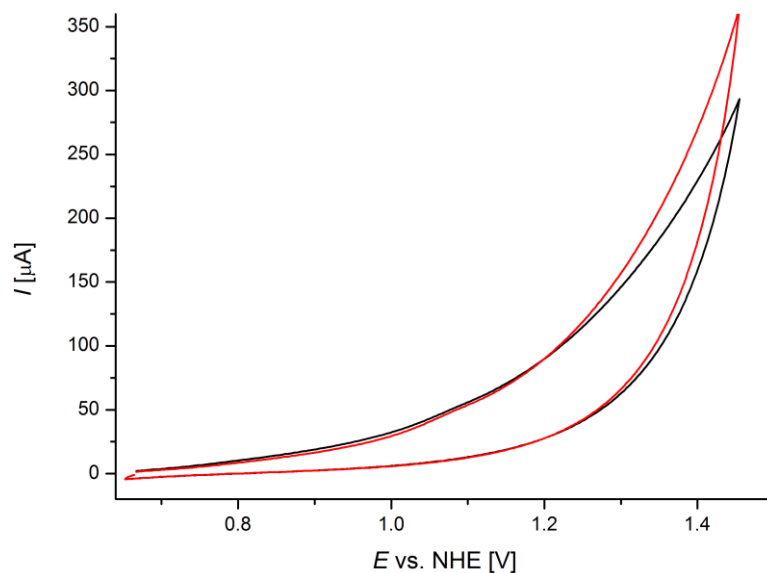


**Figure 102.** Cyclic voltammograms of GC working electrode (disc,  $A = 0.07 \text{ cm}^2$ ) after 4 h of controlled potential coulometry in blank electrolyte (black line,  $E = 1.354 \text{ V vs. NHE}$ , pH 13, 0.1 M ionic strength phosphate buffer,  $T = 22 \text{ }^\circ\text{C}$ ) and after 4 h of controlled potential coulometry with **5** (red line). No deposition of copper oxides is observed.

Instead, the GC disc was replaced by a GC rod of 0.7 cm diameter, providing a much larger electrode surface quantified by the actual contact area with electrolyte (rod:  $A = 0.4 - 0.6 \text{ cm}^2$ ; disc:  $A = 0.07 \text{ cm}^2$ ). In order to further study the assumed water oxidation performed by complex **5**, the  $\text{O}_2$  evolution during controlled potential coulometry was investigated. Formation of molecular dioxygen was therefore quantified *via* gas chromatography coupled to a thermal conductivity detector (GC-TCD, see Section 7.5.2 for details), for which a calibration curve has been determined (see Figure 103).<sup>209</sup>

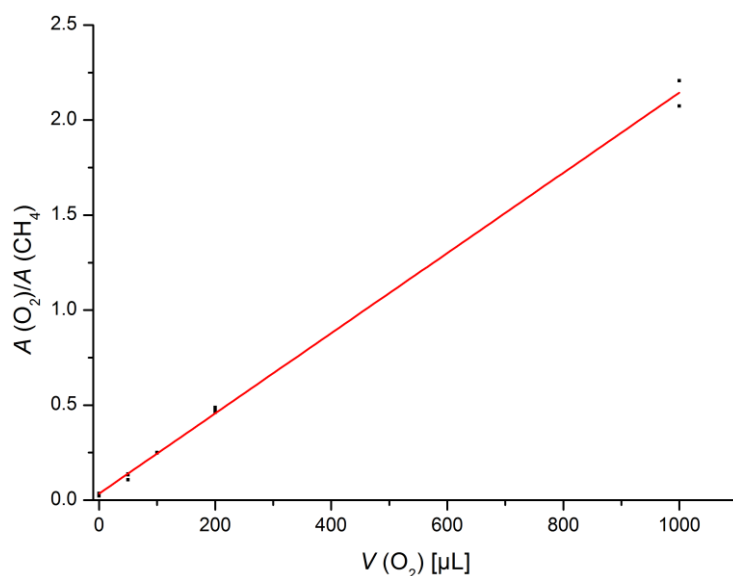


**Figure 103.** Calibration curve for quantification of O<sub>2</sub> evolution *via* GC-TCD;  $R^2 = 0.998$ .<sup>209</sup>

For this purpose, the amount of molecular dioxygen in the cell has been quantified relative to a constant amount of methane, which was added as internal standard. With this calibration curve in hand the amount of molecular dioxygen formed during the electrolysis can be calculated.

Figure 104, left shows one selected example of a controlled potential coulometry experiment of a 0.5 mM solution of complex **5** at pH 13 (0.1 M ionic strength phosphate buffer,  $E = 1.45$  V vs. NHE,  $T = 22$  °C,  $t = 20$  min). A rinse test of the working electrode after the coulometry was negative and thus deposition of copper oxides on the electrode can be excluded (see Figure 104, right). The cyclic voltammograms of the complex solution as well as the corresponding UV/vis absorption spectra (see Figure 104, right) before and after the electrolysis are identical. Consequently, complex **5** is still intact after the electrolysis with no decay being observed. Additionally, the pH value of the solution decreased from 13.04 to 12.92 over the 20 min of electrolysis, indicating the formation of H<sup>+</sup> ions during the experiment. With respect to the blank measurement, a total charge of 5.3 C was transported. With respect to potential water oxidation performed by complex **5**, this corresponds to a turn over number (TON) of ca. 3.4. It should be noted that this value has limited meaning since it relates to the total number of molecules of **5** in solution while only catalyst molecules close to the electrode surface mediate the reaction.

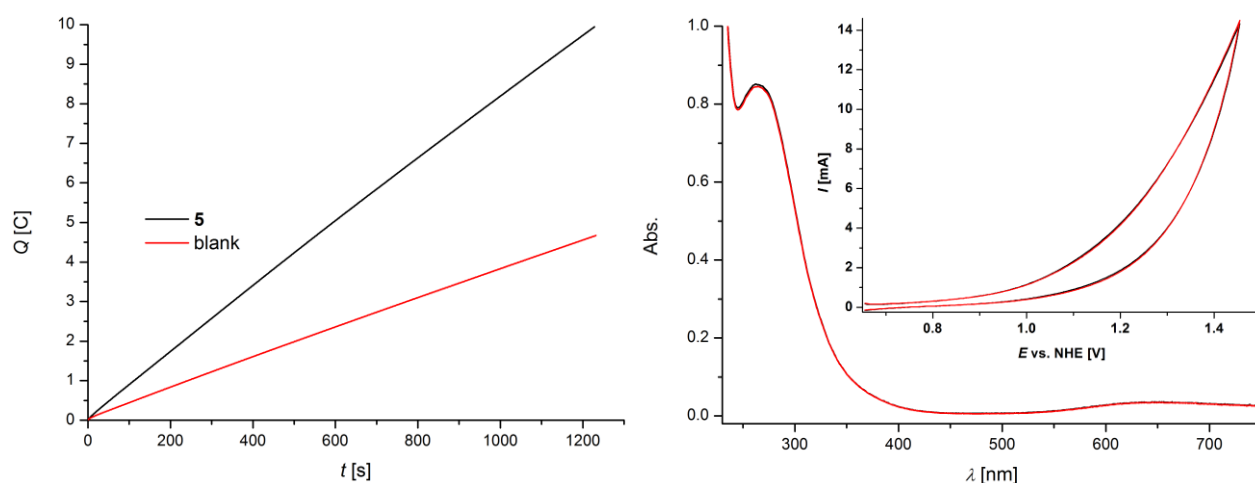


**Figure 104.** Left: Controlled potential coulometry with 0.5 mM solution of complex **5** (pH 13, 0.1 M ionic strength phosphate buffer,  $T = 22\text{ }^{\circ}\text{C}$ ,  $E = 1.45\text{ V vs. NHE}$ ); right: UV/vis absorption spectra before (black line) and after (red line) coulometry and rinse test of GC working electrode before (black line) and after the experiment (red line).

From analysis of the gas phase, the formation of molecular dioxygen could be confirmed. After background correction, the formation of  $79\text{ }\mu\text{L}$  of molecular dioxygen was calculated, corresponding to a Faraday-efficiency of 24%. In another experiment performed under the same conditions but with different batches of complex and electrolyte,  $\text{O}_2$  production could be reproduced although the determined Faraday-efficiency was even lower ( $V(\text{O}_2) = 50\text{ }\mu\text{L}$ , Faraday-efficiency = 15%). Since the cyclic voltammograms of the complex solution as well as the corresponding electronic absorption spectra are identical before and after the coulometry, **5** is still intact after the measurement. The solution has furthermore been tested for hydrogen peroxide with a solution of potassium iodide and starch but this test was negative. Nevertheless, no experimental evidence explaining the low Faraday-efficiency could be found. The literature known bipyridine system investigated by MAYER on the other hand shows a Faraday-efficiency of 35 – 45% at GC working electrode, which is significantly higher.<sup>201</sup> One possible explanation for the low Faraday-efficiency may be a reaction of a reactive oxygen intermediate with e.g. traces of MeCN, which are necessary to dissolve complex **5** in the electrolyte. Consequently, a solution of **5** was titrated with MeCN and the corresponding cyclic voltammograms were recorded (see Figure 105). The observed catalytic current indeed is increasing with increasing concentration of MeCN and thus the organic solvent may act as substrate which would explain the observed low Faraday-efficiency. However, traces of MeCN are absolutely necessary to dissolve complex **5** in the electrolyte. With respect to a better Faraday-efficiency, further investigations towards this possible off-cycle reaction and a replacement of MeCN by an inert solvent need to be carried out. Additionally, investigations towards electrolytic water oxidation at lower potential than the applied  $1.45\text{ V vs. NHE}$  have to be performed. First experiments point at  $\text{O}_2$  evolution also at  $1.35\text{ V vs. NHE}$  while at  $1.25\text{ V vs. NHE}$  no  $\text{O}_2$  production could be detected.



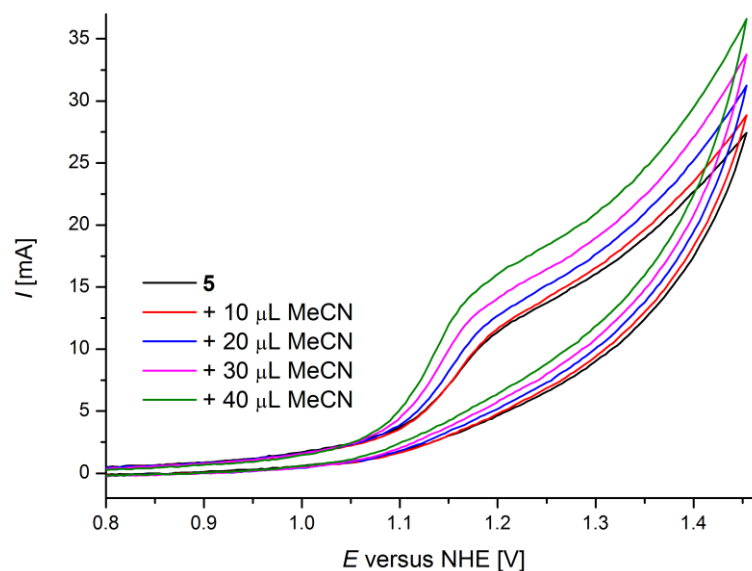


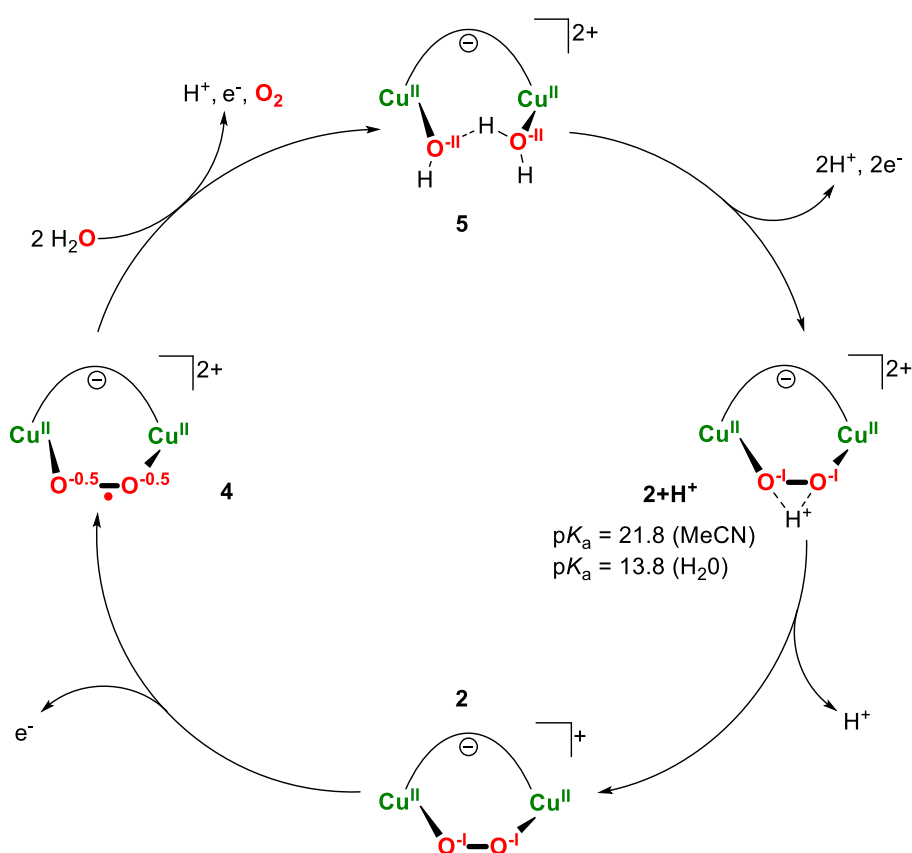
**Figure 105.** Titration of 0.5 mM solution of complex **5** (prepared from 8 mL of 0.1 M ionic strength phosphate buffer and 40  $\mu\text{L}$ )

In summary, the properties of complex **5** towards electrolytic water oxidation from pH 11 to pH 13 were investigated. Hydroxide **5** was found to be stable in phosphate buffer, with no decay being observed over months even at pH 13. Controlled potential coulometry at  $E = 1.45$  V (vs. NHE) revealed the formation of molecular dioxygen with a Faraday-efficiency of 15 - 24%. One reason for the low Faraday-efficiency may be an off-cycle reaction of traces of MeCN with reactive oxygen intermediates, and thus further investigations need to be carried out. However, no decomposition of **5** was observed during controlled potential coulometry and the deposition of solid material on the electrode could be excluded. These findings make complex **5** a potential candidate for further investigations for electrolytic water oxidation although MeCN needs to be replaced by an inert solvent prior to continuing studies.

Since complex **5** was demonstrated to react to hydroperoxide  $\mathbf{2}+\mathbf{H}^+$  in the previous section, the formation of this species during water oxidation is possible. The corresponding water oxidation mechanism thus may proceed *via* the intermediates  $\mathbf{2}+\mathbf{H}^+$ , **2** and **4** by avoiding the formation of high valent  $\text{Cu}^{\text{IV}}$  oxo species, as proposed for other synthetic copper sites.<sup>196</sup> Complex **5** consequently may deliver important information for the targeted synthesis of dinuclear copper water oxidation catalysts and an understanding of the mechanism of action of this process is of considerable interest.

## 6.6.2 DFT Calculations

The previous section in detail discussed electrolytic water oxidation starting from hydroxo complex **5**. Since **5** can be chemically transformed into the reactive  $\text{Cu}_2/\text{O}_2$  species  $\mathbf{2}+\text{H}^+$ , **2** and **4** (see Section 6.5), these complexes may also be involved in the actual mechanism of water oxidation. The formation of peroxy and superoxy species during electrolytic water oxidation with a dinuclear copper complex has indeed been proposed based on DFT calculations by ZHANG and co-workers (see Section 6.6, Scheme 31), although no spectroscopic evidences were found.<sup>205</sup> However, such proposed intermediates could be isolated and fully characterized in this work (see Sections 6 and 6.4). By starting from complex **5**, in principal two electrons and two protons need to be released to form hydroperoxy complex  $\mathbf{2}+\text{H}^+$  (see Scheme 32).

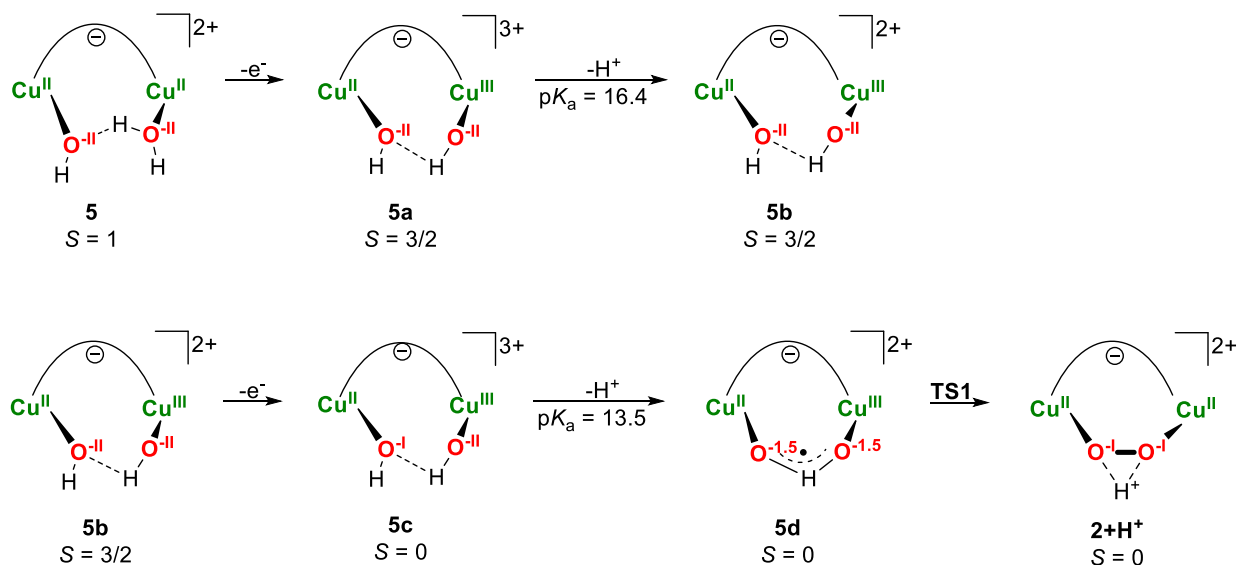


**Scheme 32.** Possible mechanism of water oxidation involving the oxygen intermediates  $\mathbf{2}+\text{H}^+$ , **2** and **4**.

Since the water oxidation is performed at pH 13,  $\mathbf{2}+\text{H}^+$  will immediately deprotonate by forming peroxide **2** which can be easily oxidized to superoxide **4** (see Section 6.4.1). Finally, molecular dioxygen and one further electron are released and **5** is recovered (see Scheme 32). In order to get insight into the actual mechanism, DFT calculations were performed by Roy.<sup>210</sup> First preliminary results of these calculations indeed predict a mechanism that involves the complexes  $\mathbf{2}+\text{H}^+$ , **2** and **4**. At first one electron and one proton are released in two steps from precursor **5**, then giving rise to intermediate **5b**, where one  $\text{Cu}^{\text{II}}$  ion is oxidized to the +III oxidation state (see Scheme 33). Afterwards a second sequence

of coupled electron and proton transfer is predicted, forming intermediate **5d**. Intermediate **5d** then is converted *via* transition state **TS1** into **2+H<sup>+</sup>** (see Figure 106).

Interestingly, the abstraction of two protons and two electrons from **5** does not proceed *via* high valent copper(IV) oxo species as predicted for other first row transition metal complexes.<sup>196</sup> Instead, one electron is delivered from a copper bound hydroxide by forming a hydroxyl radical (see Scheme 33, intermediated **5c**).



**Scheme 33.** Proposed intermediates for electrochemical formation of hydroperoxide **2+H<sup>+</sup>** from precursor **5**.

However, these are only preliminary results. After the O-O bond formation, both oxygen atoms feature a -I oxidation state. Consequently, in going from **5** to **2+H<sup>+</sup>**, the first two protons and electrons of the water oxidation process result from the copper bound hydroxide and water molecule.

After the formation of hydroperoxide **2+H<sup>+</sup>**, complex **2** is formed under release of one proton (see Scheme 34). The corresponding pK<sub>a</sub> value of **2+H<sup>+</sup>** could not be calculated until to date but is known from experiments from MeCN solution (see Section 6.3.1). The corresponding peroxide is then subsequently oxidized to superoxide **4** which finally reacts to complex **5** under release of molecular dioxygen and one additional electron. The final release of molecular dioxygen thereby most likely occurs *via* a second transition state, which however could not be calculated until to date.

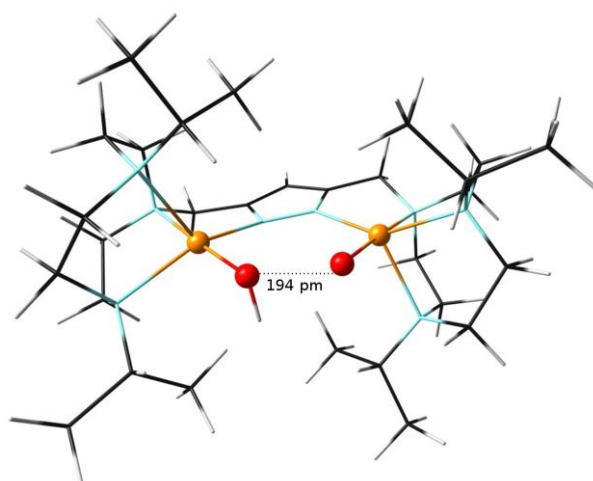
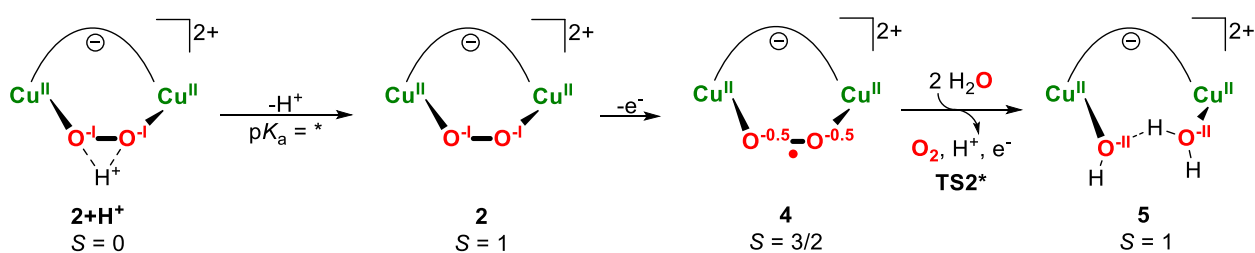


**Figure 106.** calculated O-O bond formation via **TS1**.

However, the mechanistic findings for the formation of hydroperoxide **2+H<sup>+</sup>** from **5** are similar to the SET-WNA mechanism, recently published by LLOBET and MASERAS (see Section 6.6, Scheme 30).<sup>203</sup> The major difference between both scenarios is the formation of the (O<sup>••</sup>OH)<sup>-</sup> fragment (intermediate **5d** in Scheme 33 and intermediate **xxii-iii** in Scheme 30). Whereas **xxii-iii** is formed *via* WNA from an external hydroxide molecule on an oxyl radical, this transformation starts from intermediate **5c** for the mechanism proposed here. **5c** contains a hydroxyl radical, which reacts with the neighboring hydroxide under release of one proton.<sup>203</sup> This sequence is promoted by the specific design of complex **5**, enabling the coordination of two OH moieties in close proximity to the copper atoms, whereas the mononuclear complexes studied by LLOBET and MASERAS require an external hydroxide molecule for this transformation.<sup>203</sup>



**Scheme 34.** Computationally predicted transformation of **2+H<sup>+</sup>** into **5**; missing information is marked with an asterisk.

### 6.6.3 Summary and Conclusion

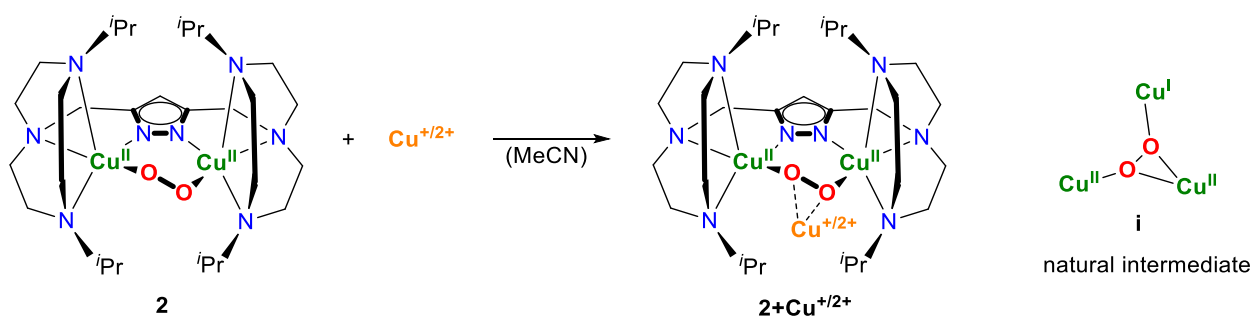
The properties of hydroxide **5** towards electrocatalytic water oxidation were investigated. Upon applying a potential of 1.45 V vs. NHE the formation of molecular dioxygen could be shown with the help of GC-TCD measurements although the observed Faraday-efficiency is rather low. One reason for the low Faraday-efficiency might be an off-cycle reaction with traces of MeCN which is necessary to dissolve complex **5** in the electrolyte. Thus, further investigations towards replacement of MeCN by an inert solvent need to be conducted.

However, a deposition of copper oxides on the GC rod during controlled potential coulometry was not observed. No decay of **5** was monitored during controlled potential coulometry, as proven by electronic absorption spectroscopy and cyclic voltammetry. Thus, complex **5** is a potential candidate for homogeneous water oxidation, although MeCN needs to be replaced by an inert solvent prior to further studies.

Since **5** can be chemically transformed into the reactive oxygen intermediates **2+H<sup>+</sup>**, **2** and **4** (see Section 6.5), the water oxidation is assumed to also proceed *via* these intermediates. Preliminary computational studies indeed predict the formation of these species. Thus, this work presents the first synthetic copper catalyst, where likely intermediates of the water oxidation process could be isolated. A more detailed computational investigation of this mechanism is in progress, which may enable the development of more efficient first row transition metal complexes for water oxidation catalysis.

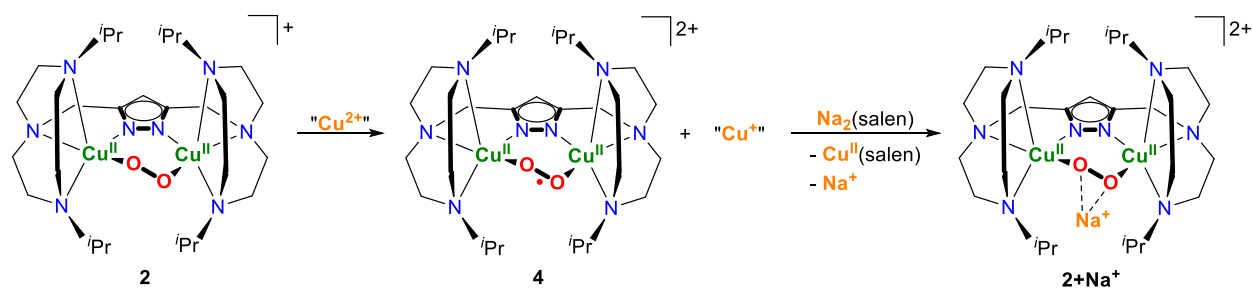
## 6.7 Towards a Synthetic Type IV Copper Active Site

Since peroxo complex **2** features a constrained binding pocket that enables the interaction of the peroxide with e.g. redox inert alkali metal ions (see Section 6.2), this sequence has been further extended by the Cu<sup>I</sup>/Cu<sup>II</sup> redox couple. The corresponding trinuclear copper peroxo motif would be a synthetic model complex for the biologically relevant intermediate **i**, which is believed to be of relevance in the mechanism of action of type IV active sites (see Section 2.3 and Scheme 35). Until to date, no model complex for this biologically relevant intermediate could be isolated. A possible adduct formation of peroxo complex **2** with Cu<sup>I</sup> or Cu<sup>II</sup> ions is thus of considerably interest. For this purpose the interaction of **2** with different copper(I/II) complexes was monitored *via* UV/vis absorption spectroscopy.



**Scheme 35.** Desired generation of synthetic trinuclear copper peroxo complex from precursor **2** and different copper(I/II) sources and proposed natural intermediate, **i**.<sup>33,40</sup>

Since the Cu<sup>I</sup> ion is only a weak and soft Lewis acid, the interaction of the dicopper peroxo core at first has been studied with different copper(II) complexes. However, peroxide **2** has a low redox potential, easily forming superoxide **4** ( $E_{1/2} = -0.58$  V (vs. Fc/Fc<sup>+</sup>, MeCN,  $T = 0$  °C)). If for instance one equivalent of Cu(OTf)<sub>2</sub> is added to complex **2**, the quantitative formation of superoxide **4** is immediately observed, with the Cu<sup>II</sup> source serving as one-electron oxidant (see Section 6.4.1 for details). The same reaction was furthermore observed with other copper(II) complexes such as [Cu<sup>II</sup>(*N*-Me<sub>4</sub>Cyclam)](ClO<sub>4</sub>)<sub>2</sub> or [Cu<sup>II</sup>(*i*Pr<sub>3</sub>TACN)(CH<sub>3</sub>CN)<sub>2</sub>][SbF<sub>6</sub>]<sub>2</sub>. However, the formation of superoxide **4** can be reversed. For this purpose a solution of the disodium salt of *N,N'*-bis(salicylidene)ethylenediamine (Na<sub>2</sub>(salen)) has been subsequently added to superoxide **4**, which was quantitatively reduced back to the peroxo level. Complex **2** thereby forms the structurally related sodium adduct, **2+Na<sup>+</sup>** (see Scheme 36 and Section 6.4.1 for further details). Next to the alkali metal adduct **2+Na<sup>+</sup>**, Cu<sup>II</sup>(salen) was formed during this reaction which can be explained with the low redox potential of the Cu<sup>I</sup>/Cu<sup>II</sup> redox couple in Cu<sup>II</sup>(salen) ( $E^\circ(\text{Cu}^I/\text{Cu}^{II}) = -1.66$  V (vs. Fc/Fc<sup>+</sup>, MeCN,  $T = 25$  °C)).<sup>161</sup> The one electron needed to reduce **4** back to the peroxo level is delivered from the free Cu<sup>+</sup> cation that in return is oxidized to Cu<sup>2+</sup> in forming the corresponding Cu<sup>II</sup>(salen) complex.



**Scheme 36.** Schematic representation of chemically reversible generation of complex **4** in using the Cu<sup>II</sup>/Cu<sup>I</sup> redox couple.

Consequently, a solution of Cu<sup>II</sup>(salen) was added in substoichiometric amounts to peroxo complex **2** (in steps of 0.3 eq.), since no redox chemistry is expected. Indeed, no formation of superoxide **4** was detected (see Figure 107, left). The increase in intensity of the initial maxima of complex **2** at 527 nm and 648 nm and of the shoulder at 460 nm is due to the purple color of Cu<sup>II</sup>(salen), which is successively added during the titration (see Figure 107, right). Thus, an adduct formation of peroxo complex **2** and Cu<sup>II</sup>(salen) was not observed, which most likely is due to the high steric demand of the neutral Cu<sup>II</sup>(salen) complex. The solubility of Cu<sup>II</sup>(salen) in e.g. MeCN or acetone is furthermore rather low, hence crystallization attempts were also not successful.

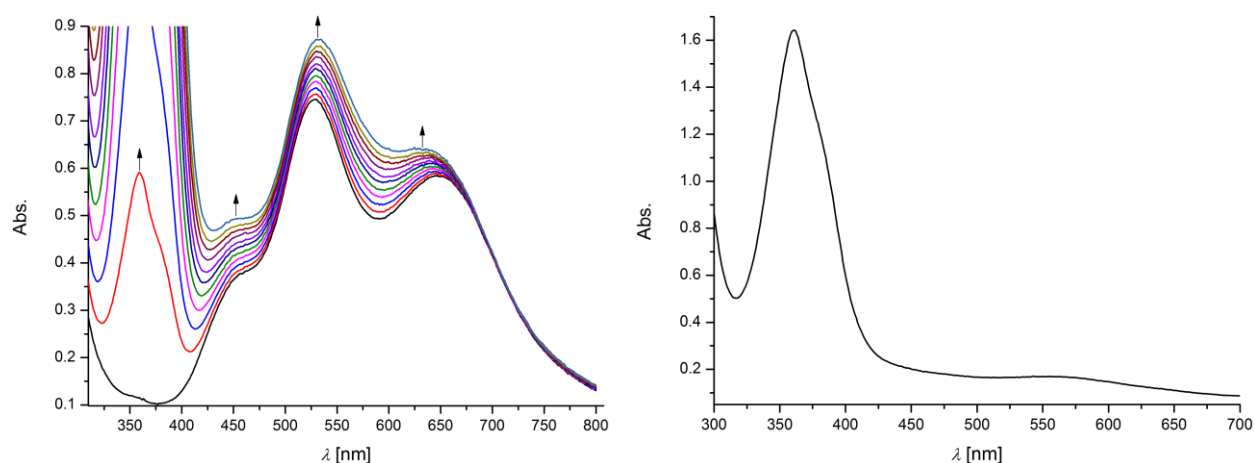
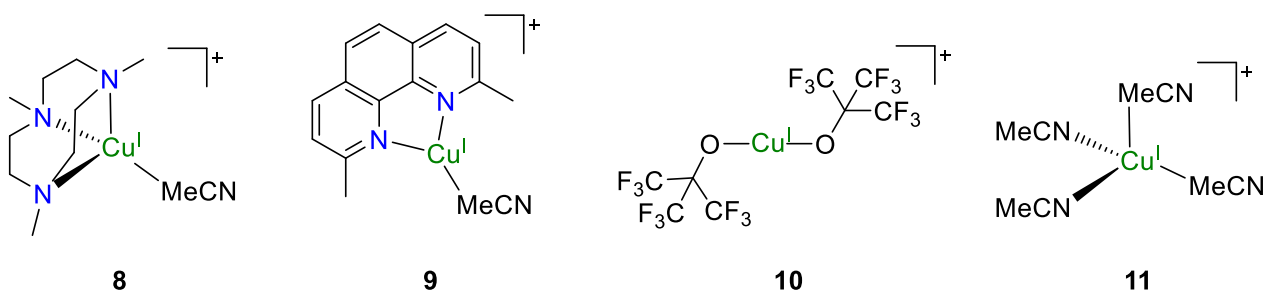


**Figure 107.** Left: UV/vis titration of complex **2** with Cu<sup>II</sup>(salen) in steps of 0.3 eq. (overall 3.0 eq. were added). Right: UV/vis absorption spectrum of 130 μM solution of Cu<sup>II</sup>(salen) (MeCN, *T* = -40 °C).

If on the other hand copper(I) complexes are used as potential Lewis acids, the corresponding solution of peroxo complex **2** and Cu<sup>I</sup> source has to be absolutely free of molecular dioxygen, since the copper(I) complexes themselves react with dioxygen in forming reactive copper oxygen intermediates. Although various copper(I) complexes were tested (see Scheme 37), no adduct formation was observed. Figure 108 shows the UV/vis titration of complex **2** with [Cu<sup>I</sup>(Me<sub>3</sub>TACN)(CH<sub>3</sub>CN)][BPh<sub>4</sub>] in steps of 1.0 equivalents. Overall 20 eq. of **8** have been added, but no changes in absorbance were observed. The minor decrease in intensity is due to gradual dilution during the titration. Although no adduct formation is observed for complex **8**, various crystallization attempts in different solvent combinations were

performed since the corresponding alkali metal adduct of **2**,  $2+K^+$  can be crystallized in 90% yield from only 1.5 eq. of KOTf, although more than 50 equivalents of KOTf are necessary to almost quantitatively generate  $2+K^+$  from its precursor **2** in solution (see Section 6.2.1). Thus solutions of complex **2** and approximately 2.0 eq. of **8** in MeCN, EtCN or acetone were stored at  $-26\text{ }^\circ\text{C}$  for Et<sub>2</sub>O diffusion. However, the decomposition of the initially purple solutions was observed within a few days.



**Scheme 37.** Summary of tested Cu(I) complexes. <sup>211,160,212</sup>

Next to the titration with **8**, the corresponding measurement with compound **9** also showed no interaction of the peroxy moiety with the copper(I) complex and will not be further discussed here. In another experiment, a solution of complex **11** in MeCN was added to complex **2**. Although the steric demand of the MeCN molecules in **11** is much lower compared to the TACN derivative in **8**, no adduct formation was observed neither.

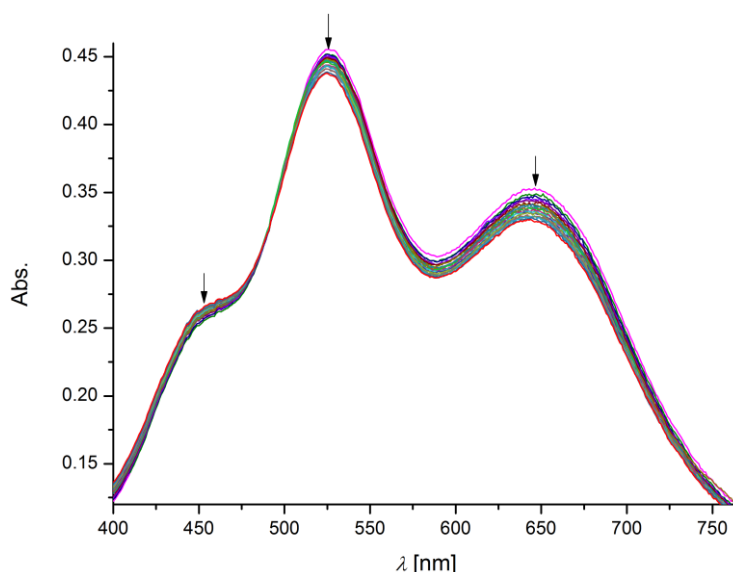


**Figure 108.** UV/vis titration of peroxide **2** with complex **8** in steps of 1.0 eq. (overall 20 eq. were added). The initial maxima of **2** are not shifting, but slightly lose intensity due to gradual dilution.

If on the other hand compound **10** is added to a solution of complex **2**, the rapid decay of **2** is observed. Most likely **10** abstracts the peroxide from **2** in forming a reactive oxygen species that subsequently decays under the present conditions. However, since no adduct formation was observed, this reaction was not further studied.

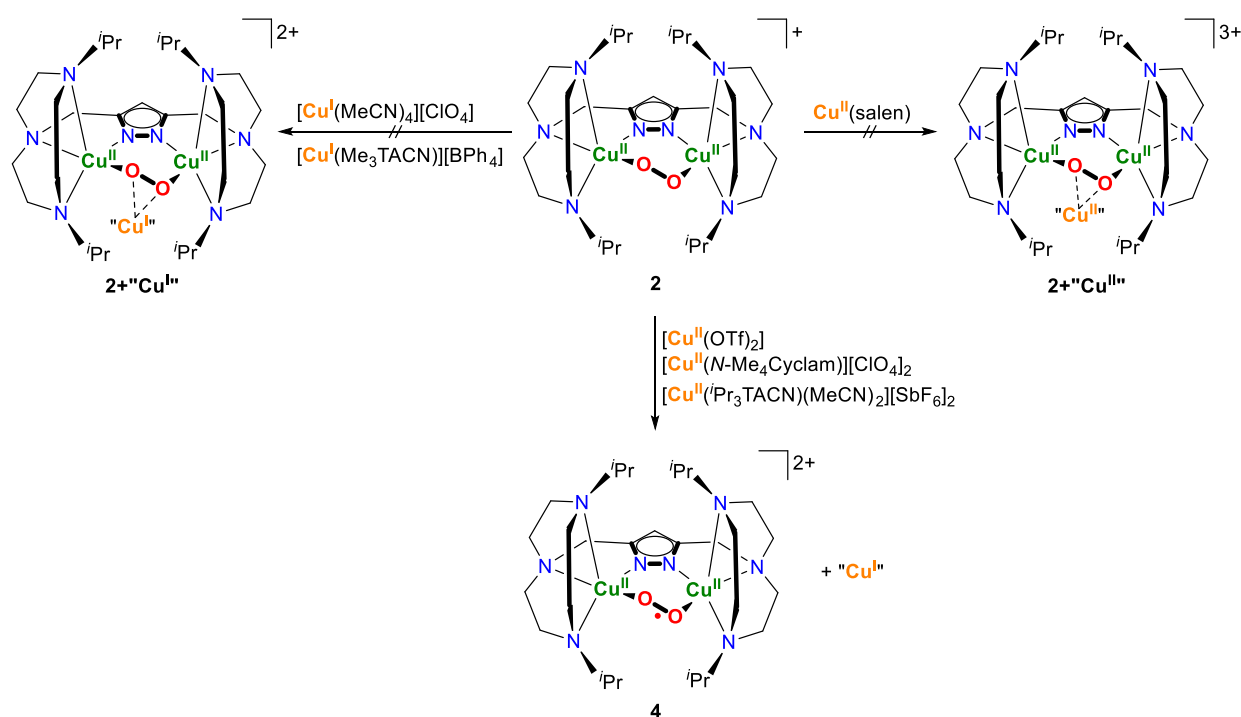


## 6.7.1 Summary and Conclusion

In summary, the synthesis of a trinuclear copper peroxy complex so far has not been possible by using the Cu<sup>I</sup> ion as Lewis acid, since the low redox potential of complex **2** leads to a formation of superoxide **4** with the Cu<sup>2+</sup> ion functioning as one-electron oxidant (see Scheme 38). Only if Cu<sup>II</sup>(salen) is used as potential Lewis acid, no redox chemistry is observed. Nevertheless, Cu<sup>II</sup>(salen) is not interacting with the peroxy moiety, most likely due to steric reasons in combination with the neutral charge of the complex. Crystallization attempts with Cu<sup>II</sup>(salen) were not successful.

Whereas the addition of copper(II) complexes induces the oxidation of peroxide **2**, the copper(I) complexes **8** and **9** do not interact with the peroxy moiety due to a low Lewis acidity of the Cu<sup>+</sup> ion in combination with a high steric demand of the surrounding ligand framework. However, also the addition of compound **11** did not lead to the formation of a corresponding adduct and thus no trinuclear copper oxygen complex could be synthesized, neither with copper(I) nor copper(II) complexes acting as potential Lewis acids.

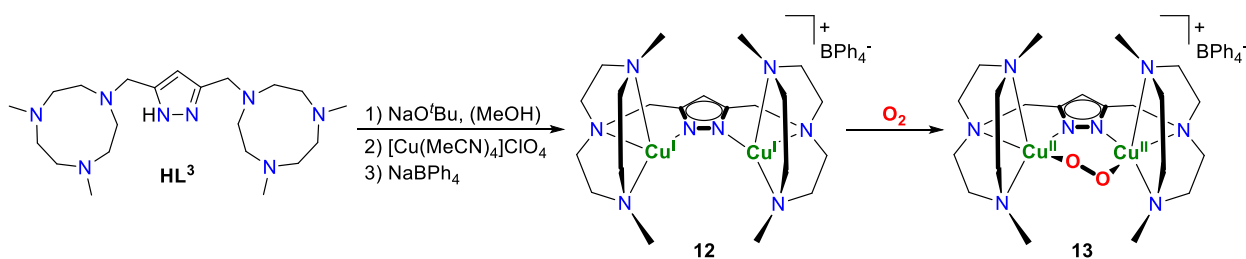
One possibility may be the synthesis of a new copper peroxy complex, featuring a similar but even more accessible binding pocket. Such a potential complex may enable the interaction of the peroxy moiety with sterically more demanding Lewis acids such as [Cu<sup>I</sup>(Me<sub>3</sub>TACN)(CH<sub>3</sub>CN)][BPh<sub>4</sub>] and will be introduced in Section 6.8.



**Scheme 38.** Summary of studied adduct formation of peroxo complex **2** with copper(I) and copper(II) complexes.

## 6.8 A Novel Dicopper(II)-Peroxo Adduct – First Results

The spectroscopic properties of peroxo complex **2** and the corresponding alkali metal ions **2+M<sup>+</sup>** have been discussed in detail in the previous sections. Neither complex **2** nor the alkali metal adduct **2+Na<sup>+</sup>** thereby show any significant substrate reactivity.<sup>31,32</sup> Also superoxide **4** is rather stable and only shows substrate reactivity with TEMPO-H, featuring a weak O-H bond (BDFE = 66.5 kcal mol<sup>-1</sup>, see Section 6.4.5 for details). However, the specific geometry of the copper oxygen core enables the interaction of this <sup>C</sup>P unit with alkali metal ions such as Li<sup>+</sup>, which modifies e.g. the redox potential of the copper oxygen core (see Section 6.4.6). With respect to possible substrate conversion performed by such peroxo complexes, a specific control of redox potential means controlling reactivity and thus is of high interest. Since the unique geometry of the copper oxygen core in complex **2** is induced by the specific ligand design, this concept is adapted for future complexes. One possibility in tuning the reactivity of complex **2** may be the substitution of the <sup>i</sup>Pr-groups of the ligand framework by CH<sub>3</sub>-groups (see Scheme 39). The corresponding ligand **HL<sup>3</sup>** was already applied in previous work for dinuclear iron complexes.<sup>213</sup> However, the ligand synthesis has been slightly modified (see Section 7.13.7 for details).



**Scheme 39.** Synthesis of new <sup>C</sup>P complex for possible substrate reactivity.

As already discussed in Section 5, the basis for dioxygen chemistry with dinuclear copper(I) complexes such as **1** and **12** is the availability of clean starting material. Thus, major efforts have been made in isolating crystalline material of dicopper(I) complex **12**. Complex **12** therefore has been synthesized by adapting protocols developed for complex **1** (see Section 7.13.8). However, no crystalline material could be obtained, even though multiple crystallization conditions were applied. Even while standing in a glove box with <0.1 ppm O<sub>2</sub>, the initially colorless solutions of **12** were observed to turn brown within a few days. The origin of this decomposition reaction could not be verified. Finally, amorphous material of complex **12** could be isolated after two days of Et<sub>2</sub>O diffusion into a saturated solution of **12**, dissolved in a mixture of acetone/Et<sub>2</sub>O. According to <sup>1</sup>H-NMR spectroscopy, the amorphous material still contained ca. 15% of impurities.

Although no clean material of complex **12** is available, primarily investigations toward possible dioxygen chemistry were made. Figure 109 shows the UV/vis absorption spectrum of the corresponding peroxo complex **13**, which has been generated from **12** and an excess of molecular dioxygen at -40 °C. Two main maxima in absorbance at 513 nm and 615 nm can be observed, which are blue-shifted compared

to the maxima of the structurally related peroxy complex **2** (see Section 6.1.1 for details). However, the desired peroxy complex **13** was observed to rapidly decay in forming a new species, which is denoted as complex **14** (see Figure 110).

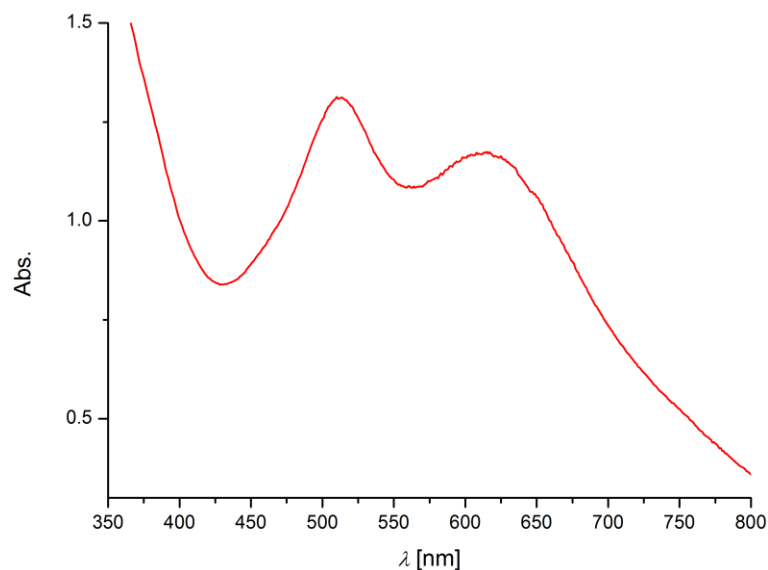


**Figure 109.** UV/vis absorption spectrum of proposed peroxy species **13** (MeCN,  $T = -40\text{ }^{\circ}\text{C}$ ). Since precursor **12** contains impurities, the actual concentration of peroxy complex **13** is unclear.

In order to isolate the decomposition product of peroxy complex **13**, precursor **12** has been oxidized with dry dioxygen at  $-40\text{ }^{\circ}\text{C}$ . Then the solution was stored at  $-26\text{ }^{\circ}\text{C}$ , and it turned green overnight. Finally, complex **14** has been crystallized *via* Et<sub>2</sub>O diffusion into a concentrated solution of the products in acetone at ambient conditions. The molecular structure of **14** shows two Cu<sup>II</sup> ions which are bridged by a formate anion (see Figure 110).

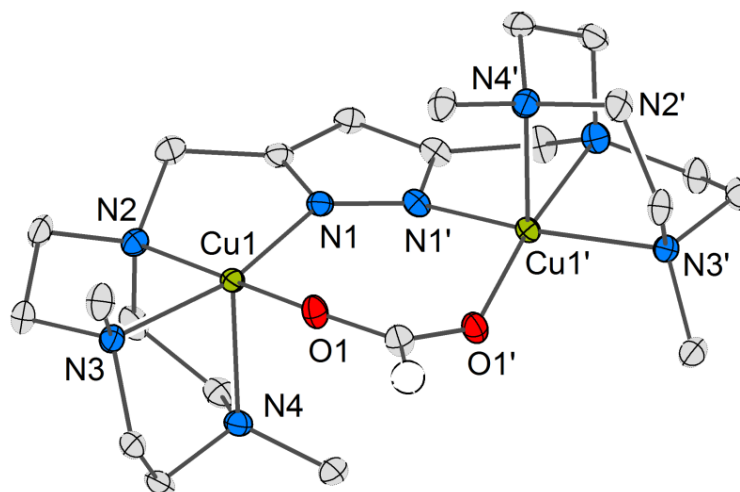


**Figure 110.** Molecular structure of **14** with thermal displacement ellipsoids given at 30% probability. Hydrogen atoms and counterions are omitted for clarity; for selected bond lengths and angles see Section 7.7.

The Cu $\cdots$ Cu distance was determined to 4.13 Å. Both Cu<sup>II</sup> ions are coordinated in an almost ideal square pyramidal geometry ( $\tau(\text{Cu1}, \text{Cu1}') = 0.15$ ) by four nitrogen donor atoms of TACN side arms and a

bridging pyrazole unit and by one oxygen donor atom of the formate anion. The copper-pyrazolate bond distances are significantly shorter ( $\text{Cu1-N1} = \text{Cu1'-N1}' = 1.945(3) \text{ \AA}$ ) than those of the copper ions to the TACN side arm nitrogen donor atoms ( $2.06 - 2.21 \text{ \AA}$ ). The formate ion is assumed to originate from residual MeOH solvent of the previous synthesis of the copper(I) precursor, which may have reacted with the corresponding peroxy complex, **13**. The corresponding UV/vis absorption spectrum of the decomposition product **14** is depicted in Figure 111. Two main transitions at 373 nm and 612 nm can be observed while the latter most likely can be assigned to a d-d transition.

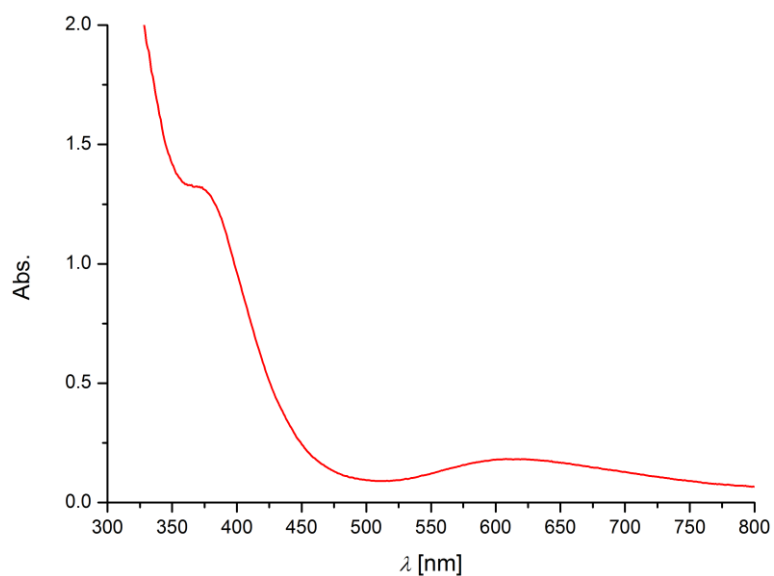


**Figure 111.** UV/vis absorption spectrum of decomposition product **14** (MeCN,  $T = 22 \text{ }^\circ\text{C}$ ).

### 6.8.1 Interaction with Alkali Metal Ions

In analogy to the interaction of peroxy complex **2** with alkali metal ions (see Section 6.2), a possible interaction of complex **13** with e.g.  $\text{Li}^+$  has been studied. However, no clean starting material of precursor **12** was available (see previous section) and thus the following results are rather qualitative. If a solution of LiOTf is added in substoichiometric amounts (ca. 1.0 eq. finally added in steps of ca. 0.05 eq., an accurate determination of stoichiometry is difficult, since precursor **12** contains ca. 15% of impurities) to complex **13** at  $-40\text{ }^\circ\text{C}$ , the initial maxima in absorbance of complex **13** were observed to continuously decrease (see Figure 112, left). A new species is simultaneously formed, showing two maxima in absorbance at ca. 380 nm and 617 nm. However, no adduct formation is observed, since the newly formed species was identified as decomposition product **14** or a related dicopper(II) complex (see Figure 112, right). Consequently, the addition of  $\text{Li}^+$  induced the decomposition of peroxy complex **13**. Since complex **13** is assumed to feature a similar geometry of the  $\text{Cu}_2/\text{O}_2$  core than complex **2**,  $\text{Li}^+$  most likely binds to the peroxide in inducing significant structural and electronic changes of the  $\text{Cu}_2/\text{O}_2$  core, which then rapidly decomposes. As mentioned before, this discussion is rather qualitative but the titration with LiOTf indicates that peroxy complex **13** is less stable than complex **2**. With respect to substrate reactivity, peroxy complex **13** may be a promising candidate. Nevertheless, for substrate reactivity with complex **13** pure starting material of complex **12** is required and thus the synthesis of clean precursor is a basic prerequisite.

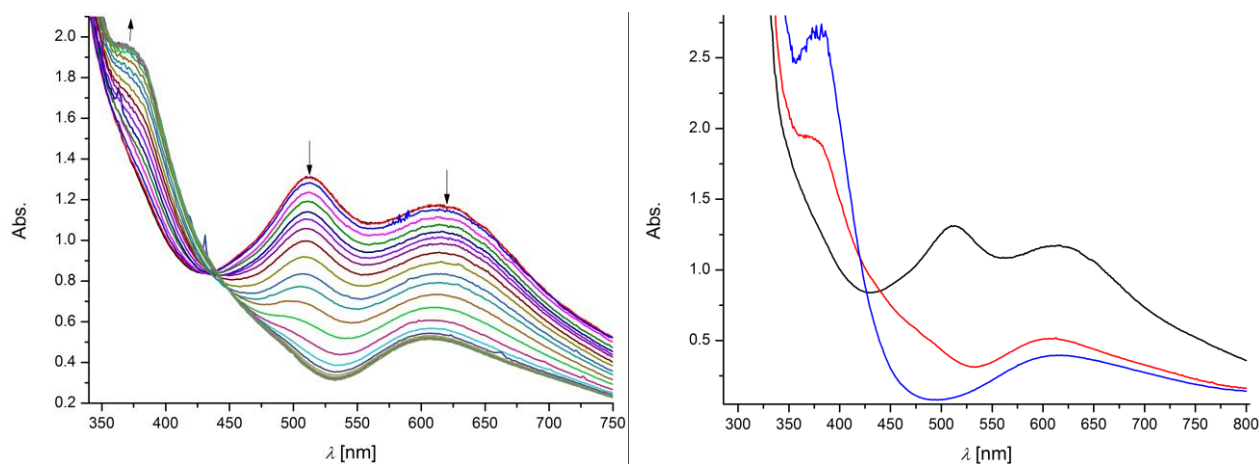


**Figure 112.** Left: Titration of complex **13** with LiOTf in steps of ca. 0.05 eq., with overall ca. 1.0 eq. of titrant being added (MeCN,  $T = -40\text{ }^\circ\text{C}$ ). The formation of decomposition product **14** is observed. Right: UV/vis absorption spectra of complex **13** (black line), after the titration with  $\text{Li}^+$  (red line) and final spectrum observed after 1 h (blue line). The final spectrum thereby is attributed to a decomposition product, such as **14**.

## 6.8.2 Summary and Conclusion

The synthesis of dicopper(I) complex **12** was presented in this section. Complex **12** is structurally related to complex **1** (see Section 6.1), with the *i*Pr groups of the TACN side arms being replaced by CH<sub>3</sub> units. The corresponding peroxo complex **13** is assumed to show enhanced substrate reactivity compared to its structural analog, **2**, since the Cu<sub>2</sub>/O<sub>2</sub> core is less shielded by the CH<sub>3</sub> groups. However, no clean material of **12** could be isolated. Nevertheless, first experiments showed that **12** reacts with molecular dioxygen in forming peroxo complex **13**.

A possible interaction of this copper peroxo site with Li<sup>+</sup> has been studied, revealing accelerated decomposition of the peroxo complex upon addition of the redox inert alkali metal ion. Since the corresponding alkali metal adducts of the structurally related peroxo complex **2** were all observed to be more stable than the free peroxo complex, the addition of Li<sup>+</sup> to complex **13** is assumed to induce significant structural changes of the Cu<sub>2</sub>/O<sub>2</sub> core, promoting a subsequent decomposition. With respect to desired substrate reactivity starting from complex **13**, a tunable stability of the peroxide may be of future interest. However, the main future goal is the isolation of clean starting material of complex **12**, enabling the synthesis of pure peroxo complex for further reactivity studies.

## 7 EXPERIMENTAL SECTION

---

### 7.1 General Synthetic Methods and Materials

Air sensitive reactions were carried out under an atmosphere of purified argon 5.0 or dinitrogen 5.0 using standard Schlenk or glove box (M. BRAUN, LabMaster) techniques. All solvents were dried with standard methods<sup>214</sup>, degassed and furthermore freeze pump degassed for minimum three times. Reactions in the glove box were carried out with <0.1 ppm O<sub>2</sub> and H<sub>2</sub>O. Used dioxygen gas was dried over P<sub>2</sub>O<sub>5</sub>. All used chemicals were purchased from standard suppliers (SIGMA ALDRICH, VWR, ABCR, DEUTERO, ACROS and MERCK) and not furthermore purified.

### 7.2 UV/vis Spectroscopy

UV/vis experiments in solution were recorded in quartz cuvettes on an AGILENT Cary 60 or on an AGILENT Cary 8454, which are equipped with an UNISOKU cryostat (CoolSpek) for low temperature measurements, connected with a magnetic stirrer. Stock solutions of oxygen isotope sensitive compounds were freshly prepared in a glove box with <0.1 ppm O<sub>2</sub> and H<sub>2</sub>O and transferred into glass cuvettes, which were sealed with a rubber septum. Usual concentrations of the studied complexes were 50 – 170 μM. Dioxygen chemistry was monitored at -40 °C with an excess of dry dioxygen being injected through the rubber septum *via* a gas-tight syringe. Excess of dioxygen was removed by bubbling dry argon 5.0 through the cuvette for minimum 15 minutes, at which no decay of the preformed oxygen-species was detected. Titration experiments were monitored at -40 °C by adding the titrant in substoichiometric amounts to the oxygenated species *via* a HAMILTON syringe. The corresponding stock solutions were freshly prepared in a glove box with <0.1 ppm O<sub>2</sub> and H<sub>2</sub>O.

UV/vis experiments in the solid state were performed on an AGILENT Cary 5000 UV/vis-NIR in a PRAYING MANTIS™ high vacuum sample cell. The samples were prepared inside a glove box with <0.1 ppm O<sub>2</sub> and H<sub>2</sub>O by mixing crystalline material of the corresponding compounds with dry KBr.

#### 7.2.1 pK<sub>a</sub> Determination *via* UV/vis Titration Experiments

The relative pK<sub>a</sub> value of compound **2+H**<sup>+</sup> was determined *via* UV/vis titration experiments by adding an appropriate base stepwise in substoichiometric amounts to a solution of **2+H**<sup>+</sup>, which subsequently reacted to peroxo complex **2** (see Scheme 40). Since **2+H**<sup>+</sup> and **2** are featuring characteristic electronic absorption spectra, the concentration of both species can be determined during the experiment. For this purpose, the software package SPECFIT/32 was used.



**Scheme 40.** Equilibrium used to determine the relative  $pK_a$  value of  $2 + \text{H}^+$ .

The in Scheme 40 depicted chemical equilibrium can be described with equilibrium constant  $K_e$  (see equation 25)). By assuming equal activity coefficients of all components, the relative basicity of the transferred proton is defined as:<sup>152</sup>

$$26) \quad \Delta pK_a = pK_a(\text{B} + \text{H}^+) - pK_a(2 + \text{H}^+) = \log \frac{[2][\text{B} + \text{H}^+]}{[2 + \text{H}^+][\text{B}]}$$

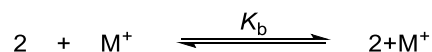
Since  $2$  and  $\text{B} + \text{H}^+$  are formed in equimolar amounts, equation 26) can be simplified to:

$$27) \quad pK_a(2 + \text{H}^+) = pK_a(\text{B} + \text{H}^+) - \log \frac{[2]^2}{[2 + \text{H}^+][\text{B}]}; \quad \log \frac{[2]^2}{[2 + \text{H}^+][\text{B}]} = \log(K_e)$$

Consequently, a plot of  $[2]^2/[2 + \text{H}^+]$  versus  $[\text{B}]$  yields the equilibrium constant  $K_e$ , which can be used to calculate the relative  $pK_a$  value of complex  $2 + \text{H}^+$ .<sup>152</sup> However, the  $pK_a$  value of  $2 + \text{H}^+$  can only be determined roughly, since species of different ionic strength are involved.<sup>152</sup> Furthermore, the  $pK_a$  value of  $\text{B} + \text{H}^+$  has been determined likewise as in the abovementioned procedure, but at 25 °C. The titration of  $2 + \text{H}^+$  was performed at -40 °C due to thermal instability of the copper oxygen complexes. Since the  $pK_a$  value of  $\text{B} + \text{H}^+$  has been determined at 25 °C, the titration of  $2 + \text{H}^+$  should have been carried out at the same temperature, to enable comparable conditions.

## 7.2.2 Determination of Association Constants *via* UV/vis Titration Experiments

The association constants of the different alkali metal adducts (see Section 6.2.1) were calculated with the THORDARSON program<sup>128</sup> running under Matlab®. The software package assumes the formation of a 1:1 host-guest complex of peroxo moiety and Lewis acid:



The equilibrium is described by an association constant, in which  $2$  represents the host (H) that forms together with the alkali metal ion (G) a host-guest complex (HG):<sup>128</sup>

$$28) \quad K_b = \frac{[\text{HG}]c^0}{[\text{H}][\text{G}]}; \quad c^0 = 1 \frac{\text{mol}}{\text{L}}$$

If the concentration of HG is known, the remaining concentrations of H and of G can be determined as follows:<sup>128</sup>

$$29) \quad [\text{H}] = [\text{H}]_0 - [\text{HG}]$$

$$30) \quad [\text{G}] = [\text{G}]_0 - [\text{HG}]$$

If both equations are inserted into the mass balance, which then is expressed for [HG], equation 31) can be derived:<sup>128</sup>

$$31) \quad [\text{HG}] = \frac{1}{2} \left( [\text{G}]_0 + [\text{H}]_0 + \frac{1}{K_b} \right) - \left( \left( [\text{G}]_0 + [\text{H}]_0 + \frac{1}{K_b} \right)^2 + 4[\text{H}]_0[\text{G}]_0 \right)^{\frac{1}{2}}$$



Since the concentration of HG complex is not known in this UV/vis titration experiment, its formation is assumed to correlate with a decrease of absorbance ( $\Delta Y$ ) of the bands belonging to the host. The physical change  $Y$  can be described as the aggregate of the individual components as a function of concentration.<sup>128</sup>

$$32) \quad Y = y_H[H] + Y_G[G] + Y_{HG}[HG]$$

The guest in this experiment is non-absorbing and  $Y$  refers to absolute concentrations, and thus  $\Delta Y$  can be described as follows:<sup>128</sup>

$$33) \quad \Delta Y = Y_{\Delta HG}([HG])$$

The equations 31) and 33) will be used to fit the changes of absorbance at selected wavelength during a titration experiment from two known ( $[G]_0$  and  $[H]_0$ ) and two unknown ( $K_b$  and  $Y_{\Delta HG}$ ) parameters. The parameters  $K_b$  and  $Y_{\Delta HG}$  are obtained by non-linear regression, at which the association constant is of final interest. The software Matlab® for instance, uses an algorithm to calculate the unknown parameters in varying  $K_b$  and  $Y_{\Delta HG}$ , until a good fit is obtained between equation 31) and the experimentally derived data.<sup>128</sup>

### 7.3 Magnetic Measurements

Temperature dependent susceptibility measurements were performed on a QUANTUM DESIGN MPMS XL-5 SQUID magnetometer (5 T magnet). The samples were filled in a gelatin capsule and after the measurement the data was corrected for the magnetic contribution of the capsule. Solution state samples of **4** were prepared at a Schlenk line from precursor **2** and the oxidant  $\text{AgBF}_4$ . The sample was freeze pump degassed for 10 times to remove excess  $\text{O}_2$  and filtered over a WHATMAN glass microfiber filter (minimum 8 layers) to remove the formed silver particles. The sample finally was encapsulated in a NMR tube.

The simulation of the magnetic data was carried out with the program JulX<sup>215</sup> by applying a fitting procedure to the spin Hamiltonian for isotropic exchange coupling and Zeeman splitting.

$$34) \quad \hat{H} = -2J\hat{S}_1\hat{S}_2 + g\mu_B\vec{B}(\vec{S}_1 + \vec{S}_2)$$

Paramagnetic impurities (PI) and temperature independent paramagnetism (TIP) were included according to:

$$35) \quad \chi_{\text{calc}} = (1 - \text{PI}) \cdot \chi + \text{PI} \cdot \chi_{\text{mono}} + \text{TIP}$$

### 7.4 Resonance Raman Spectroscopy

Resonance Raman (rR) spectra were recorded with a HORIBA Scientific LabRAM HR 800 spectrometer with an open-electrode CCD detector and a confocal pinhole with user controlled variable

aperture, in combination with a free space optical microscope. For excitation a He:Ne-laser ( $\lambda_{\text{exc}} = 633 \text{ nm}$ ) or a diode-laser ( $\lambda_{\text{exc}} = 457 \text{ nm}$ ) were used. A Kryovac KONTI-Cryostat-Mikro cell cooled with liquid  $\text{N}_2$  was applied in solution state measurements at low temperatures. Measurements of solid material were performed under air, at which the sample was mounted on a glass slid. Selected data have been treated with the software LabSpec 5.

## 7.5 Electrochemistry

### 7.5.1 Cyclic voltammetry

Cyclic voltammetry measurements of sensitive oxygen complexes such as **2** and **2+M<sup>+</sup>** were carried out by using a METROHM Autolab potentiostat under inert conditions in a one-compartment gastight cell at  $0 \text{ }^\circ\text{C}$ . Stock solutions were prepared freshly in MeCN ( $0.1 \text{ M } ^n\text{Bu}_4\text{NPF}_6$ ) in a glove box with  $<0.1 \text{ ppm O}_2$  and  $\text{H}_2\text{O}$ . Compound **2** was generated from precursor **1** at  $-40 \text{ }^\circ\text{C}$  inside a Schlenk tube and the resulting solution was degassed with argon (for minimum 15 min) to remove excess  $\text{O}_2$  and transferred into the cell. Glassy carbon working electrode and platinum counter electrode were polished with  $0.1 \text{ }\mu\text{m}$  aluminum paste and rinsed with water and acetone prior to use. The Ag/AgNO<sub>3</sub> reference electrode (MeCN,  $0.01 \text{ M AgNO}_3$ ,  $0.1 \text{ M } ^n\text{Bu}_4\text{NPF}_6$ ) was prepared freshly and calibrated on the Fc/Fc<sup>+</sup> redox couple after each measurement.

With respect to water oxidation, cyclic voltammetry measurements have been performed at ambient conditions by using the aforementioned experimental setup. The Hg/HgSO<sub>4</sub> reference electrode was calibrated on the Fc/Fc<sup>+</sup> redox couple. Buffer solutions of  $0.1 \text{ M}$  ionic strength have been prepared according to literature known procedures.<sup>216</sup>

### 7.5.2 Controlled Potential Coulometry

Controlled potential coulometry was performed by using a GAMRY Instruments Reference 600<sup>+</sup> potentiostat. A glassy carbon rod of  $7 \text{ mm}$  diameter (length =  $9 \text{ cm}$ ) was used in combination with a Pt spiral counter electrode.  $\text{O}_2$  evolution was quantified with a thermal conductivity detector. A calibration curve was determined previously.<sup>209</sup> For this purpose, the amount of molecular dioxygen in the gastight cell has been quantified relative to a constant amount of methane, which was added as internal standard. The ratio of the signals of dioxygen and methane was observed to linearly correlate with different  $\text{O}_2$  concentrations.

## 7.6 Spectro-Electrochemistry

Spectro-electrochemical measurements were recorded with a METROHM Autolab GTSTAT101 connected with an AVANTES AvaSpec 2048×14 UV/vis-spectrometer, using a Ag/Ag<sup>+</sup> (MeCN,  $0.01 \text{ M}$

AgNO<sub>3</sub>, 0.1 M <sup>n</sup>Bu<sub>4</sub>NPF<sub>6</sub>) reference electrode, glassy-carbon counter electrode and a Pt-net working electrode in a spectro-electrochemistry cuvette (optical pathway = 0.1 cm). All measurements were performed in a glove box (M. BRAUN, LabMaster) with <0.1 ppm O<sub>2</sub> and <0.1 ppm H<sub>2</sub>O. Spectro-electrochemical studies of complex **2** were conducted with single crystalline material that was dissolved in MeCN before the measurement and immediately cooled down to -15 °C inside the spectro-electro cuvette.

## 7.7 X-Ray Diffraction

X-ray data were collected on a STOE IPDS II diffractometer, equipped with a graphite monochromator (Mo-K $\alpha$  radiation,  $\lambda$  = 0.71073 Å) by scanning at ca. 130 K. The structures were solved with SHELXT<sup>217</sup> or SHELXS and refined on  $F^2$  with the software package SHELXL-2014 in using all reflections.<sup>218</sup> All non-hydrogen atoms were refined anisotropically. SAME, SADI and ISOR restraints and EADP constraints were applied. Face-indexed absorption corrections were performed numerically with the program X-RED.<sup>219</sup>

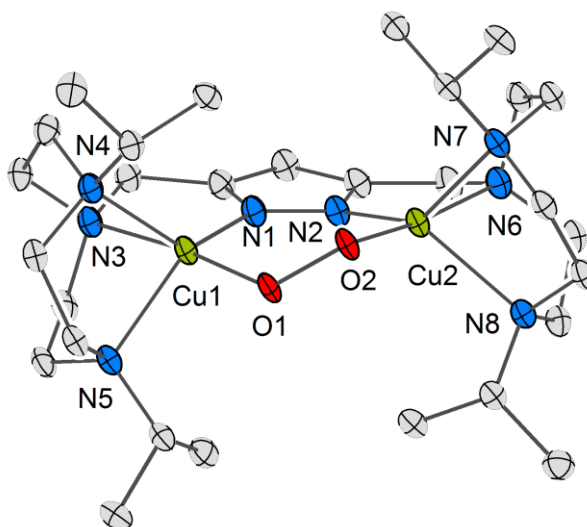


**Figure 113.** Molecular structure of **2** (thermal displacement ellipsoids given at 30% probability). Hydrogen atoms, counterion BPh<sub>4</sub><sup>-</sup> and additional solvent molecules are omitted for clarity. Selected bond lengths [Å] and angles [°]: Cu1-Cu2 3.7413(5), O1-O2 1.4412(17), Cu1-O1 1.8900(13), Cu1-N1 1.8987(17), Cu1-N3 2.1737(16), Cu1-N5 2.1771(17), Cu1-N4 2.2615(18), Cu2-O2 1.8971(14), Cu2-N2 1.9046(16), Cu2-N7 2.1341(16), Cu2-N6 2.2014(17), Cu2-N8 2.2493(17); O1-Cu1-N1 100.40(6), O1-Cu1-N3 173.60(7), N1-Cu1-N3 80.03(7), O1-Cu1-N5 91.98(6), N1-Cu1-N5 135.90(7), N3-Cu1-N5 83.44(6), O1-Cu1-N4 104.05(6), N1-Cu1-N4 132.95(7), N3-Cu1-N4 79.88(6), N5-Cu1-N4 82.80(6), O2-Cu2-N2, 100.76(6), O2-Cu2-N7, 92.41(6), N2-Cu2-N7, 137.68(7), O2-Cu2-N6, 173.80(7), N2-Cu2-N6 79.64(7), N7-Cu2-N6 83.33(6), O2-Cu2-N8 104.59(6), N2-Cu2-N8 129.83(7), N7-Cu2-N8 83.69(6), N6-Cu2-N8 79.486, O2-O1-Cu1 121.23(10), O1-O2-Cu2 122.09(10).

**Table 21.** Crystal data and refinement details for **2**.

Compound	<b>2</b>
Empirical formula	$C_{53}H_{77}BCu_2N_8O_2$ $C_{5.5}H_{13}O_{1.5}$
Formula weight [g/mol]	1099.27
Temperature [K]	133(2)
Wavelength MoK $\alpha$ [Å]	0.71073
Crystal system	Triclinic
Space group	<i>P</i> -1
Unit cell dimensions	$a = 13.5497(5)$ Å; $\alpha = 64.231(3)^\circ$ $b = 16.2465(6)$ Å; $\beta = 88.701(3)^\circ$ $c = 165666(6)$ Å; $\gamma = 65.676(3)^\circ$
Volume [Å <sup>3</sup> ]	2937.8(2)
Z	2
Density (calculated) [mg/m <sup>3</sup> ]	1.243
Absorption coefficient [mm <sup>-1</sup> ]	0.774
F(000) [mm <sup>-1</sup> ]	1176
Crystal size [mm <sup>3</sup> ]	0.500 x 0.500 x 0.480
Theta range for data collection	1.390 to 26.865°
Index ranges	-17 ≤ h ≤ 17, -20 ≤ k ≤ 20, -20 ≤ l ≤ 20
Reflections collected	42453
Independent reflections	12459 [R(int) = 0.0413]
Completeness to theta = 25.242°	100.0 %
Absorption correction	Numerical
Max. and min. transmission	0.7779 and 0.7155
Refinement method	Full-matrix least-squares on F <sup>2</sup>
Data / restraints / parameters	12459 / 102 / 764
Goodness-of-fit on F <sup>2</sup>	1.035
Final R indices [I > 2σ(I)]	R1 = 0.0370, wR2 = 0.0983
R indices (all data)	R1 = 0.0464, wR2 = 0.1024
Extinction coefficient	n/a
Largest diff. peak and hole	0.468 and -0.531 e.Å <sup>-3</sup>

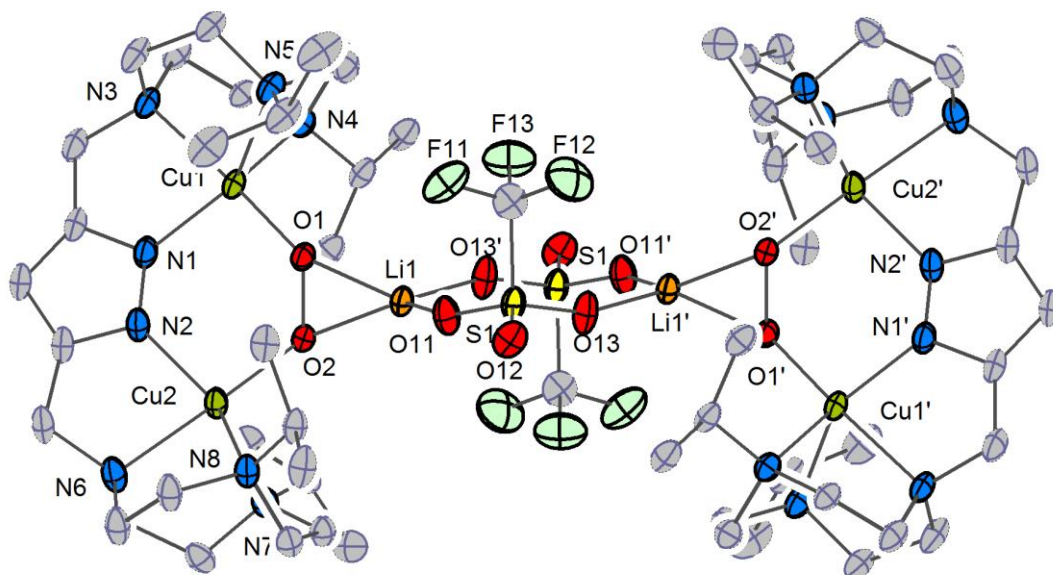


**Figure 114.** Solid state structure of  $2+Li^+$ . Thermal displacement ellipsoids given at 30% probability. The Hydrogen atoms and the counterion  $BPh_4^-$  are omitted for clarity. Only one of the crystallographically independent molecules is shown (the second one shows a disorder of the  $O_2$  moiety). Symmetry transformation used to generate equivalent atoms: #1  $-x+1, -y+1, -z+1$ . Selected bond lengths [ $\text{\AA}$ ] and bond angles [ $^\circ$ ]: Cu1-Cu2 3.8562(9), O1-O2 1.497(3), Cu1-O1 1.902(2), Cu1-N1 1.915(3), Cu1-N3 2.123(2), Cu1-N4 2.175(3), Cu1-N5 2.211(3), Cu2-O2 1.917(2), Cu2-N2 1.927(3), Cu2-N6 2.143(3), Cu2-N7 2.173(3), Cu2-N8 2.220(3), Li1-O1 1.868(5), Li1-O2 1.893(5), O1-Cu1-N1, 95.63(10), O1-Cu1-N3 170.39(9), N1-Cu1-N3 81.15(11), O1-Cu1-N4 105.66(9), N1-Cu1-N4 136.37(11), N3-Cu1-N4 82.59(10), O1-Cu1-N5 93.08(9), N1-Cu1-N5 133.32(11), N3-Cu1-N5 82.79(10), N4-Cu1-N5 83.76(10), O2-Cu2-N2 96.16(10), O2-Cu2-N6 169.91(10), N2-Cu2-N6 80.57(11), O2-Cu2-N7 92.67(9), N2-Cu2-N7 137.64(11), N6-Cu2-N7 83.61(11), O2-Cu2-N8 107.25(9), N2-Cu2-N8 131.65(10), N6-Cu2-N8 81.73(10), N7-Cu2-N8 83.79(10), O1-Li1-O2 46.91(14), O2-O1-Cu1 118.91(14), O1-O2-Cu2 118.39(13).

**Table 22.** Crystal data and refinement details for  $2+Li^+$ .

Compound	$2+Li^+$
Empirical formula	$C_{108}H_{154}B_2Cu_4F_6Li_2N_{16}O_{10}S_2$
Formula weight [g/mol]	2304.24
Temperature [K]	133(2)
Wavelength MoK $\alpha$ [ $\text{\AA}$ ]	0.71073
Crystal system	Monoclinic
Space group	$P 2_1/c$
Unit cell dimensions	$a = 33.1189(5) \text{ \AA}; \alpha = 90^\circ$ $b = 33.1189(5) \text{ \AA}; \beta = 95.5650(10)^\circ$ $c = 20.9993(4) \text{ \AA}; \gamma = 90^\circ$
Volume [ $\text{\AA}^3$ ]	12841.5(4)
Z	4
Density (calculated) [ $\text{mg/m}^3$ ]	1.192
Absorption coefficient [ $\text{mm}^{-1}$ ]	0.750
F(000) [ $\text{mm}^{-1}$ ]	4848

Crystal size [mm <sup>3</sup> ]	0.500 x 0.500 x 0.280
Theta range for data collection	1.230 to 25.647°
Index ranges	-19<=h<=22, -40<=k<=40, -25<=l<=25
Reflections collected	131775
Independent reflections	24202 [R(int) = 0.0739]
Completeness to theta = 25.242°	100.0 %
Absorption correction	Numerical
Max. and min. transmission	0.8011 and 0.6172
Refinement method	Full-matrix least-squares on F <sup>2</sup>
Data / restraints / parameters	24200 / 0 / 1386
Goodness-of-fit on F <sup>2</sup>	1.025
Final R indices [I>2sigma(I)]	R1 = 0.0524, wR2 = 0.1233
R indices (all data)	R1 = 0.0715, wR2 = 0.1316
Extinction coefficient	n/a
Largest diff. peak and hole	0.896 and -0.637 e.Å <sup>-3</sup>

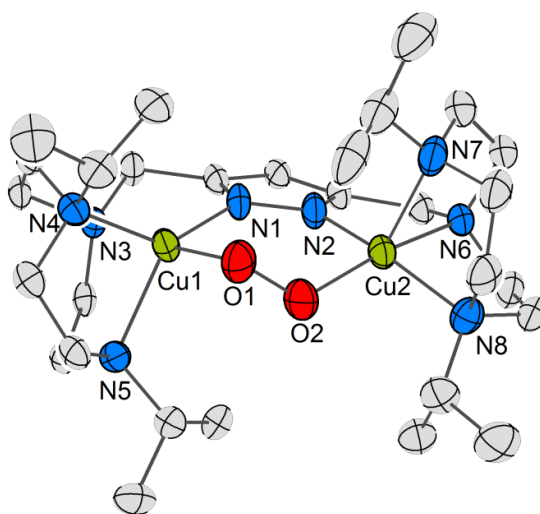


**Figure 115.** Molecular structure of **4**. Thermal displacement ellipsoids given at 30% probability. The Hydrogen atoms, the counterions BPh<sub>4</sub><sup>-</sup> and SbF<sub>6</sub><sup>-</sup> are omitted for clarity. Selected bond lengths [Å] and bond angles [°]: Cu1-Cu2 3.816, Cu1-N1 1.898(5), Cu1-O1 1.924(5), Cu1-N3 2.068(4), Cu1-N4 2.112(5), Cu1-N5 2.160(5), Cu2-N2 1.889(5), Cu2-O2 1.940(5), Cu2-N8 2.044(6), Cu2-N6 2.090(5), Cu2-N7 2.242(6), O1-O2 1.329(7); N1-Cu1-O1 93.4(2), N1-Cu1-N3 82.47(19), O1-Cu1-N3 175.8(2), N1-Cu1-N4 138.2(2), O1-Cu1-N4 98.3(2), N3-Cu1-N4 84.15(18), N1-Cu1-N5 130.8(2), O1-Cu1-N5 97.8(2), N3-Cu1-N5 85.67(18), N4-Cu1-N5 87.18(18), N2-Cu2-O2 92.9(2), N2-Cu2-N8 160.9(2), O2-Cu2-N8 95.2(2), N2-Cu2-N6 81.3(2), O2-Cu2-N6 165.7(2), N8-Cu2-N6 86.7(2), N2-Cu2-N7 108.2(2), O2-Cu2-N7 110.4(2), N8-Cu2-N7 85.1(2), N6-Cu2-N7 83.9(2).

**Table 23.** Crystal data and refinement details for **4**.

Compound	<b>4</b>
Empirical formula	C <sub>53</sub> H <sub>77</sub> BCu <sub>2</sub> F <sub>6</sub> N <sub>8</sub> O <sub>2</sub> Sb
Formula weight [g/mol]	1231.86
Temperature [K]	133(2)
Wavelength MoK $\alpha$ [Å]	0.71073
Crystal system	Triclinic
Space group	<i>P</i> -1
Unit cell dimensions	$a = 14.4712(4)$ Å; $\alpha = 99.776(2)^\circ$ $b = 21.3029(6)$ Å; $\beta = 94.380(2)^\circ$ $c = 21.9065(7)$ Å; $\gamma = 90.158(2)^\circ$
Volume [Å <sup>3</sup> ]	6635.0(3)
Z	4
Density (calculated) [mg/m <sup>3</sup> ]	1.233
Absorption coefficient [mm <sup>-1</sup> ]	1.096
F(000) [mm <sup>-1</sup> ]	2540
Crystal size [mm <sup>3</sup> ]	0.500 x 0.410 x 0.320
Theta range for data collection	1.411 to 25.722°
Index ranges	-17 ≤ h ≤ 17, -25 ≤ k ≤ 25, -25 ≤ l ≤ 26
Reflections collected	87543
Independent reflections	25003 [R(int) = 0.0537]
Completeness to theta = 25.242°	99.9 %
Absorption correction	Numerical
Max. and min. transmission	0.7446 and 0.6346
Refinement method	Full-matrix least-squares on F <sup>2</sup>
Data / restraints / parameters	25003 / 820 / 1501
Goodness-of-fit on F <sup>2</sup>	1.034
Final R indices [I > 2σ(I)]	R1 = 0.0863, wR2 = 0.2364
R indices (all data)	R1 = 0.1137, wR2 = 0.2566
Extinction coefficient	n/a
Largest diff. peak and hole	1.814 and -1.721 e.Å <sup>-3</sup>

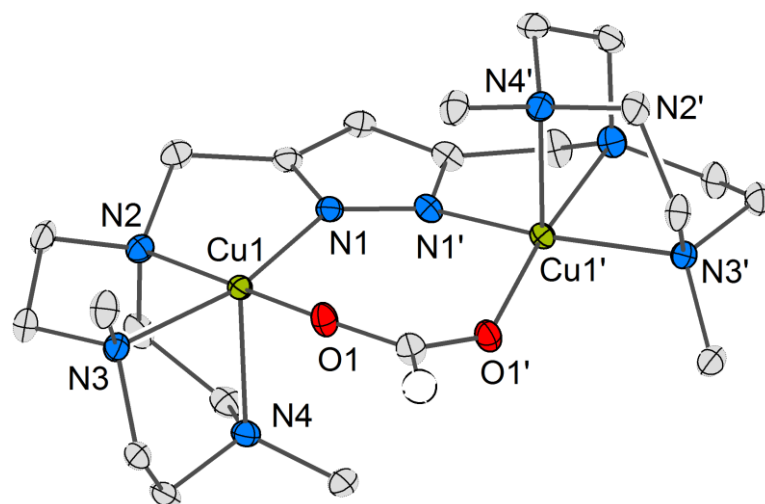


**Figure 116.** Molecular structure of **8**. Thermal displacement ellipsoids given at 30% probability. The Hydrogen atoms and counterions  $\text{ClO}_4^-$  are omitted for clarity. Symmetry transformation used to generate equivalent atoms: #1  $-x+1, -y+2, z+0$ . Selected bond lengths [Å] and bond angles [°]: Cu1-N1 1.945(3), Cu1-O1 1.976(2), Cu1-N3 2.061(3), Cu1-N2 2.063(3), Cu1-N4 2.208(2), N1-C2 1.346(4), N1-N1 1.347(5); N1-Cu1-O1 102.02(11), N1-Cu1-N3 164.58(11), O1-Cu1-N3 91.43(10), N1-Cu1-N2 81.99(11), O1-Cu1-N2 173.66(10), N3-Cu1-N2 83.99(11), N1-Cu1-N4 101.66(11), O1-Cu1-N4 98.33(11), N3-Cu1-N4 83.56(10), N2-Cu1-N4 5.54(11).

**Table 24.** Crystal data and refinement details for **8**.

Compound	<b>8</b>
Empirical formula	$\text{C}_{22}\text{H}_{42}\text{Cl}_2\text{Cu}_2\text{N}_8\text{O}_{10}$
Formula weight [g/mol]	776.61
Temperature [K]	133(2)
Wavelength MoK $\alpha$ [Å]	0.71073
Crystal system	Tetragonal
Space group	$I4_1cd$
Unit cell dimensions	$a = 15.5316(4)$ Å; $\alpha = 90^\circ$ $b = 15.5316(4)$ Å; $\beta = 90^\circ$ $c = 25.3786(7)$ Å; $\gamma = 90^\circ$
Volume [Å <sup>3</sup> ]	6122.1(4)
Z	8
Density (calculated) [mg/m <sup>3</sup> ]	1.685
Absorption coefficient [mm <sup>-1</sup> ]	1.630
F(000) [mm <sup>-1</sup> ]	3216
Crystal size [mm <sup>3</sup> ]	0.500 x 0.160 x 0.140
Theta range for data collection	2,453 to 26.769°
Index ranges	$-19 \leq h \leq 19, -19 \leq k \leq 19, -28 \leq l \leq 32$
Reflections collected	34178



Independent reflections	3143 [R(int) = 0.0311]
Completeness to theta = 25.242°	99.9 %
Absorption correction	Numerical
Max. and min. transmission	0.8117 and 0.6841
Refinement method	Full-matrix least-squares on F <sup>2</sup>
Data / restraints / parameters	3143 / 61/ 248
Goodness-of-fit on F <sup>2</sup>	1.025
Final R indices [I>2sigma(I)]	R1 = 0.0227, wR2 = 0.0489
R indices (all data)	R1 = 0.0254, wR2 = 0.0496
Extinction coefficient	n/a
Largest diff. peak and hole	0.259 and -0.188 e.Å <sup>-3</sup>

## 7.8 EPR Spectroscopy

All samples have been prepared freshly in a glove box with <0.1 ppm O<sub>2</sub> and H<sub>2</sub>O. Complex **2** has been generated at a Schlenk line, where dioxygen was added at -40 °C. The sample was afterwards freeze pump degassed for minimum three times. Superoxo complex **4** was generated from a solution of precursor **2** and AgSbF<sub>6</sub>. The brown solution was afterwards filtered through a WHATMAN glass microfiber filter (minimum 10 layers) to remove the formed silver particles.

EPR spectra at approximately 140 K have been recorded on a BRUKER E500 ELESYS X-band machine, equipped with a standard cavity (ER4102ST, 9.5 GHz). The temperature was controlled by using an OXFORD helium flow cryostat (ESP810) in addition with an OXFORD temperature controller (ITC-4). Measurements at helium temperature were performed on a BRUKER ELESYS E500 T X-band spectrometer. All spectra have been simulated with the software package easyspin<sup>117</sup>, running under Matlab®.

## 7.9 NMR Spectroscopy

NMR spectra were recorded on a BRUKER DRX 500 and on a BRUKER Avance 300 at 298 K. Chemical shifts ( $\delta$ ) are given in ppm and related to residual proton or carbon signals of the solvent ((CD<sub>3</sub>)<sub>2</sub>CO,  $\delta$ H = 2.05, 2.84,  $\delta$ C = 29.84, 206.26). Coupling constants are given in Hertz [Hz]. Abbreviations for observed signal multiplicities are: s = singlet, d = doublet, sep = septet, m = multiplet and br = broad. Spectra were interpreted with the software MestReNova NMR (version 8.0.0-10524; Co. MESTRELAB).

## 7.10 IR Spectroscopy

IR data of oxygen sensitive species were collected in a glove box (Co. M. BRAUN) on an AGILENT Cary 630 FTIR with Diamond ATR attachment. Oscillation frequencies are reported in wave numbers [ $\text{cm}^{-1}$ ]. Intensities are specified with: very weak = vw, weak = w, medium = m, strong = s and very strong = vs.

## 7.11 Elemental Analysis

Elemental analyses were carried out in a vario EL III (Co. ELEMENTAR). Oxygen sensitive species were sealed inside a glove box with  $<0.1$  ppm  $\text{O}_2$  and  $\text{H}_2\text{O}$  in an aluminum capsule.

## 7.12 Substrate Reactivity

Screening for substrate reactivity of complex **4** was carried out in MeCN in the temperature range of  $0\text{ }^\circ\text{C}$  to  $-40\text{ }^\circ\text{C}$  by monitoring the spectral changes *via* UV/vis absorption spectroscopy. Kinetic data have been treated *via* Reaction Progress Kinetic Analysis (RPKA).<sup>184</sup>

At first, a solution of complex **1** has been oxidized with molecular dioxygen at  $-40\text{ }^\circ\text{C}$ . Then the excess of dioxygen has been removed in bubbling dry argon through the solution for minimum 15 min. No spectral changes were observed. Subsequently, **2** was oxidized with  $\text{AgSbF}_6$  in yielding complex **4**. Then the corresponding substrate was added *via* a HAMILTON syringe and the spectral changes were collected. Substrate reactivity with TEMPO-H has also been performed in using  $[\text{Cu}(\text{Pr}_3\text{TACN})(\text{MeCN})_2][(\text{SbF}_6)_2]$  as oxidant for the previous synthesis of **4**, but no different reactivity was observed.

## 7.13 Syntheses

Ligand **HL**<sup>1</sup> was synthesized according to a modified previously reported route<sup>31</sup>, by reacting 1,4-diisopropyl-1,4,7-triazacyclononane<sup>220</sup> with 1*H*-pyrazole-3,5-dicarbonyl dichloride<sup>221</sup> followed by reduction of the product with LiAlH<sub>4</sub>. The oxidant [Cu(<sup>i</sup>Pr<sub>3</sub>TACN)(MeCN)<sub>2</sub>][(SbF<sub>6</sub>)<sub>2</sub>]<sup>160</sup>, the Phosphonium base<sup>222,223</sup> PhNPPyr<sub>3</sub>, as well as the mononuclear Copper complexes Cu(salen)<sup>161,224</sup>, [Cu(cyclam)][(ClO<sub>4</sub>)<sub>2</sub>]<sup>225</sup> and [Cu(cyclen)][(ClO<sub>4</sub>)<sub>2</sub>]<sup>225</sup> were synthesized according to literature known procedures.

### 7.13.1 [L<sup>1</sup>Cu<sub>2</sub>]BPh<sub>4</sub> (**1**)

Complex **1** has been synthesized according to a previously reported route.<sup>10</sup> To a solution of **HL**<sup>1</sup> (197 mg, 380 μmol, 1.00 eq.) and NaO<sup>t</sup>Bu (55.0 mg, 570 μmol, 1.50 eq.) in MeOH (1 mL), a solution of [Cu(MeCN)<sub>4</sub>]ClO<sub>4</sub> (249 mg, 760 μmol, 2.00 eq.) in MeOH (3 mL) was added in one portion and the resulting yellow solution was stirred for 2 h at room temperature. Then a solution of NaBPh<sub>4</sub> (195 mg, 570 μmol, 1.50 eq.) in MeOH (1 mL) was added. Immediately white solid formed that was stirred for 30 min, filtered off, washed with MeOH (1 mL), dried *in vacuo* and dissolved in acetone (0.5 mL). The slightly green solution was left for Et<sub>2</sub>O diffusion at room temperature. After 3 d, green oil was separated from a now colorless solution. The colorless solution was taken for a second run of Et<sub>2</sub>O diffusion, of which colorless crystals were obtained within a few days (168 mg, 174 μmol, 46%).

<sup>1</sup>H-NMR (500 MHz, (CD<sub>3</sub>)<sub>2</sub>CO): δ (ppm) = 7.36-7.32 (m, 8H, *o*-BPh<sub>4</sub>), 6.94-6.91 (m, 8H, *m*-BPh<sub>4</sub>), 6.79-6.76 (m, 4H, *p*-BPh<sub>4</sub>), 5.72 (s, 1H, <sup>Pz</sup>H), 3.85 (s, 4H, Pz-CH<sub>2</sub>), 3.07 (sep, <sup>3</sup>J<sub>H,H</sub> = 6.6 Hz, 4 H, <sup>iPr</sup>CH), 3.02-2.95 (m, 8 H, <sup>TACN</sup>CH<sub>2</sub>), 2.92-2.85 (m, 4 H, <sup>TACN</sup>CH<sub>2</sub>), 2.82-2.77 (m, 4 H, <sup>TACN</sup>CH<sub>2</sub>), 2.74-2.66 (m, 8 H, <sup>TACN</sup>CH<sub>2</sub>), 1.42 (d, <sup>3</sup>J<sub>H,H</sub> = 6.6 Hz, 12 H, <sup>iPr</sup>CH<sub>3</sub>), 1.22 (d, <sup>3</sup>J<sub>H,H</sub> = 6.4 Hz, 12 H, <sup>iPr</sup>CH<sub>3</sub>).

<sup>13</sup>C{<sup>1</sup>H}-NMR (125 MHz, (CD<sub>3</sub>)<sub>2</sub>CO): δ (ppm) = 165.0 (q, <sup>1</sup>J<sub>C,B</sub> = 49.6 Hz, *i*-BPhC), 151.3 (<sup>Pz</sup>C), 137.0 (q, <sup>2</sup>J<sub>C,B</sub> = 1.4 Hz, *o*-BPhC), 126.0 (q, <sup>3</sup>J<sub>C,B</sub> = 2.8 Hz, *m*-BPhC), 122.2 (*p*-BPhC), 98.4 (<sup>Pz</sup>CH), 58.3 (<sup>iPr</sup>CH), 55.5 (Pz-CH<sub>2</sub>), 53.2 (<sup>TACN</sup>CH<sub>2</sub>), 51.9 (<sup>TACN</sup>CH<sub>2</sub>), 50.1 (<sup>TACN</sup>CH<sub>2</sub>), 23.0 (<sup>iPr</sup>CH<sub>3</sub>), 19.3 (<sup>iPr</sup>CH<sub>3</sub>).

UV/vis (CH<sub>3</sub>CN solution, *T* = 23 °C): λ<sub>max</sub> [nm] (ε [M<sup>-1</sup>cm<sup>-1</sup>]) = 267 (13289), 274 (11192).

### 7.13.2 [L<sup>1</sup>Cu<sub>2</sub>(O<sub>2</sub>)]BPh<sub>4</sub> · Et<sub>2</sub>O, 0.5 acetone (**2**)

Complex **1** (18.3 mg, 19.0 μmol, 1.00 eq.) was dissolved in acetone (1.8 mL) and in Et<sub>2</sub>O (2.4 mL) and the colorless solution was split into six equal parts and filled into six test tubes, which were placed in a Schlenk tube that was filled with Et<sub>2</sub>O (6.0 mL). Then the Schlenk tube was cooled down to -40 °C. The atmosphere was removed and subsequently dry dioxygen was added. Then the intense purple solution was left for Et<sub>2</sub>O diffusion at -26 °C. After approximately two weeks, the obtained crystalline material was washed with Et<sub>2</sub>O and stored over a mixture of dry argon/O<sub>2</sub> at RT (9.5 mg, 9.5 μmol, 50%).

UV/vis (CH<sub>3</sub>CN solution, *T* = -40 °C): λ<sub>max</sub> [nm] (ε [M<sup>-1</sup> cm<sup>-1</sup>]) = 456 (2615), 527 (4994), 648 (3903).

UV/vis (solid): λ<sub>max</sub> [nm] (reflectance [%]) = 460 (75), 529 (70), 663 (72).

rR (solution, λ<sub>exc</sub> = 633 nm, *T* = -30 °C, *c* = 1 × 10<sup>-2</sup> M, EtCN):  $\tilde{\nu}_{O-O}$  [cm<sup>-1</sup>] = 797 (Δ<sup>16</sup>O<sub>2</sub>-<sup>18</sup>O<sub>2</sub> = 39).

rR (solid, λ<sub>exc</sub> = 633 nm):  $\tilde{\nu}_{O-O}$  [cm<sup>-1</sup>] = 793 (Δ<sup>16</sup>O<sub>2</sub>-<sup>18</sup>O<sub>2</sub> = 41).

### 7.13.3 [L<sup>1</sup>Cu<sub>2</sub>(O<sub>2</sub>)(LiOTf)]<sub>2</sub>(BPh<sub>4</sub>)<sub>2</sub> (**2+Li<sup>+</sup>**)

Complex **1** (9.0 mg, 9.3 μmol, 1.0 eq.) was dissolved in a mixture of acetone (0.3 mL) and of Et<sub>2</sub>O (0.8 mL) and the colorless solution was cooled down to -40 °C. The atmosphere in the headspace was replaced by dry dioxygen and a solution of LiOTf (3.0 mg, 19.2 μmol, 2.0 eq.) in acetone (0.3 mL) was added drop wise and the intense purple color of the solution changed to brown. The solution was left for Et<sub>2</sub>O diffusion at -26 °C. After approximately two weeks the obtained crystalline material was washed with Et<sub>2</sub>O and stored over dry argon (8.4 mg, 7.3 μmol, 78%).

UV/vis (CH<sub>3</sub>CN solution, *T* = -40 °C): λ<sub>max</sub> [nm] (ε [M<sup>-1</sup> cm<sup>-1</sup>]) = 456 (3951), 595 (724).

UV/vis (solid): λ<sub>max</sub> [nm] (reflectance [%]) = 463 (65), 604 (85).

rR (solution, λ<sub>exc</sub> = 633 nm, *T* = -30 °C, *c* = 1 × 10<sup>-2</sup> M, EtCN):  $\tilde{\nu}_{O-O}$  [cm<sup>-1</sup>] = 791 (Δ<sup>16</sup>O<sub>2</sub>-<sup>18</sup>O<sub>2</sub> = 35).

rR (solid, λ<sub>exc</sub> = 633 nm):  $\tilde{\nu}_{O-O}$  [cm<sup>-1</sup>] = 790 (Δ<sup>16</sup>O<sub>2</sub>-<sup>18</sup>O<sub>2</sub> = 36).

### 7.13.4 [L<sup>1</sup>Cu<sub>2</sub>(O<sub>2</sub>)((CH<sub>3</sub>)<sub>2</sub>CO)(KOTf)]<sub>2</sub>(OTf)<sub>2</sub>·0.5 H<sub>2</sub>O (**2+K<sup>+</sup>**)

Precursor **1** (6.8 mg, 7.1 μmol, 1.0 eq.) was dissolved in a mixture of acetone (0.2 mL) and of Et<sub>2</sub>O (0.4 mL). The solution was cooled down to -40 °C and the headspace was replaced by dry dioxygen. Then a solution of KOTf (2.0 mg, 10.6 μmol, 1.5 eq.) in acetone (0.2 mL) was added dropwise at -40 °C, followed by Et<sub>2</sub>O diffusion at -26 °C. The resulting single crystalline material was washed with Et<sub>2</sub>O and stored under dry argon (7.2 mg, 3.3 μmol, 93%).

UV/vis (CH<sub>3</sub>CN solution, *T* = -40 °C): λ<sub>max</sub> [nm] (ε [M<sup>-1</sup> cm<sup>-1</sup>]) = 515 (4826), 624 (2738).

UV/vis (solid): λ<sub>max</sub> [nm] (reflectance [%]) = 511 (60), 615 (65).

rR (solution, λ<sub>exc</sub> = 633 nm, *T* = -30 °C, *c* = 1 × 10<sup>-2</sup> M, EtCN):  $\tilde{\nu}_{O-O}$  [cm<sup>-1</sup>] = 796 (Δ<sup>16</sup>O<sub>2</sub>-<sup>18</sup>O<sub>2</sub> = 40).

rR (solid, λ<sub>exc</sub> = 633 nm):  $\tilde{\nu}_{O-O}$  [cm<sup>-1</sup>] = 790 (Δ<sup>16</sup>O<sub>2</sub>-<sup>18</sup>O<sub>2</sub> = 46).

EA (calculated, found for **2+K<sup>+</sup>**): C (37.93, 38.75), H (5.94, 5.91) N (10.41, 10.33).

### 7.13.5 [L<sup>1</sup>Cu<sub>2</sub>(O<sub>2</sub>)] [(BPh<sub>4</sub>)(SbF<sub>6</sub>)] (**4**)

A solution of **1** (6.5 mg, 6.7 μmol, 1.0 eq.) in acetone (0.4 mL) and in Et<sub>2</sub>O (1.0 mL) was cooled down to -40 °C and the atmosphere in the Schlenk tube was replaced by dry dioxygen. Then a solution of [(<sup>1</sup>Pr<sub>3</sub>TACN)Cu(CH<sub>3</sub>CN)<sub>2</sub>][(SbF<sub>6</sub>)<sub>2</sub>] (7.0 mg, 8.0 μmol, 1.2eq.) in acetone (0.4 mL) was added dropwise to

the purple solution at -40 °C, which immediately turned brown. The solution was left for Et<sub>2</sub>O diffusion at -36 °C. Crystalline material was obtained within a few days (1.4 mg, 1.1 μmol, 17%).

Besides [(<sup>i</sup>Pr<sub>3</sub>TACN)Cu(CH<sub>3</sub>CN)<sub>2</sub>][(SbF<sub>6</sub>)<sub>2</sub>], other oxidants like Cu(OTf)<sub>2</sub>, AgX (X = SbF<sub>6</sub><sup>-</sup>, BF<sub>4</sub><sup>-</sup>) were tested towards the oxidation of complex **2**. Although in all cases a successful oxidation was observed, no suitable crystalline material was obtained during Et<sub>2</sub>O diffusion.

UV/vis (CH<sub>3</sub>CN solution, T = -40 °C): λ<sub>max</sub> [nm] (ε [M<sup>-1</sup> cm<sup>-1</sup>]) = 444 (10100), 600 (2140).

rR (solution, λ<sub>exc</sub> = 457 nm, T = 22 °C, c = 1.4 × 10<sup>-3</sup> M, MeCN):  $\tilde{\nu}_{O-O}$  [cm<sup>-1</sup>] = 1073 (Δ<sup>16</sup>O<sub>2</sub>-<sup>18</sup>O<sub>2</sub> = 60).

IR (ATR): 1595 (m), 1493 (m), 1458 (m), 1373 (m), 1350 (w), 1325 (m), 1293 (w), 1269 (w), 1174 (m), 1138 (m), 1092 (w), 1070 (m), 1048 (m), 998 (w), 975 (w), 951 (m), 898 (vw), 874 (w), 830 (m), 792 (m), 737 (m), 715 (m), 654 (s).

### 7.13.6 [L<sup>1</sup>Cu<sub>2</sub>(OH)(H<sub>2</sub>O)](ClO<sub>4</sub>)<sub>2</sub> (**5**)

To a solution of **HL**<sup>1</sup> (500 mg, 964 μmol, 1.00 eq.) in MeCN/MeOH (3.0 mL MeCN, 2.0 mL MeOH) NaO<sup>t</sup>Bu (130 mg, 1.35 mmol, 1.40 eq.) has been added in one portion at RT. Subsequently, a solution of Cu(ClO<sub>4</sub>)<sub>2</sub>·6H<sub>2</sub>O (710 mg, 1.92 mmol, 1.99 eq.) in MeCN (2.0 mL) was added. The green solution was stirred for 1 h at ambient temperature. The solvent has been removed under reduced pressure and water (150 mL) was added and the resulting mixture was kept in a supersonic bath for 4 h. Then the green solid was filtered off and washed with water (3 x 3.0 mL). The slightly bluish solution was discarded. The solid was dissolved in MeCN (2.0 mL) and a solution of 5 M NaOH (0.2 mL) was added. The bluish solution was stirred for 10 h at RT. Afterwards, the solvent has been removed under reduced pressure and the blue solid was washed with water (3 x 2.0 mL), dried *in vacuo* and subsequently dissolved in MeCN/CHCl<sub>3</sub> (0.2 mL MeCN, 2.0 mL CHCl<sub>3</sub>). The blue solution was left for Et<sub>2</sub>O diffusion at RT. After a few days, blue crystals have been collected which were again crystallized from MeCN/CHCl<sub>3</sub> (340 mg, 369 μmol, 38%).

UV/vis (CH<sub>3</sub>CN, T = -40 °C): λ<sub>max</sub> [nm] (ε [M<sup>-1</sup> cm<sup>-1</sup>]) = 281 (9700), 390 (4600), 690 (800).

UV/vis (H<sub>2</sub>O, T = 22 °C): λ<sub>max</sub> [nm] (ε [M<sup>-1</sup> cm<sup>-1</sup>]) = 278 (10000), 690 (800).

MS (ESI<sup>+</sup>, MeCN): m/z = 330.2 [M - H<sub>2</sub>O]<sup>2+</sup>, 697.3 [M + OH]<sup>+</sup>, 761.3 [M + ClO<sub>4</sub>]<sup>+</sup>.

EA (calculated, found for **5**): C (39.63, 39.62), H (6.88, 6.69), N (12.75, 13.19).

### 7.13.7 Preparation of **HL**<sup>3</sup>

The synthesis of this ligand was reported previously<sup>213</sup>, but has been slightly modified. To a solution of 1,4-Dimethyl-1,4,7-triazonane (1.70 g, 10.8 mmol, 2.5 eq.) in THF (3.0 ml) and trimethylamine (1.96 g, 19.4 mmol, 4.5 eq.) a solution of 3,5-bis(chlorocarbonyl)-1H-pyrazole hydrochloride (0.99 g, 4.31 mmol, 1.0 eq.) in THF (6.0 mL) was added at 0 °C. The mixture was stirred overnight at ambient temperature. Then the mixture was filtered and the residue was washed with THF. Then the solvent

was removed under reduced pressure and  $\text{CHCl}_3$  (10 mL) and a saturated  $\text{Na}_2\text{CO}_3$  solution (5.0 mL) were added. The mixture was stirred for 20 h at RT. Then the organic layer was washed with water (2 x 5.0 mL). The organic layer has been dried over  $\text{MgSO}_4$  and the solvent was removed under reduced pressure and THF (15 mL) was added. Then the solution was added to a suspension of  $\text{LiAlH}_4$  (500 mg, 13.2 mmol, 3.1 eq.) in THF (15 mL) at 0 °C and the mixture was stirred for 20 h at 63 °C. Finally, the excess of  $\text{LiAlH}_4$  was quenched with water at 0 °C. Then the white solid was filtered off and washed with THF (3 x 5.0 mL). The solvent was removed under reduced pressure and  $\text{CHCl}_3$  (50 mL) was added. The organic layer was washed with water (2 x 15 mL) and afterwards dried over  $\text{MgSO}_4$ . The resulting colorless oil was stored under argon for two days. Then hexane (5.0 mL) was added and the solution was filtered over celite. The solvent was removed under reduced pressure and the colorless oil was dried *in vacuo* (455 mg, 1.12 mmol, 26%).

$^1\text{H-NMR}$  (300 MHz, MeOD):  $\delta$  (ppm) = 6.19 (s, 1H,  $\text{P}^z\text{H}$ ), 3.68 (s, 4H,  $\text{P}^z\text{CH}_2$ ), 2.82-2.86 (m, 8H,  $\text{TACNCH}_2$ ), 2.73-2.69 (m, 16H,  $\text{TACNCH}_2$ ), 2.35 (s, 12H,  $\text{CH}_3$ ).

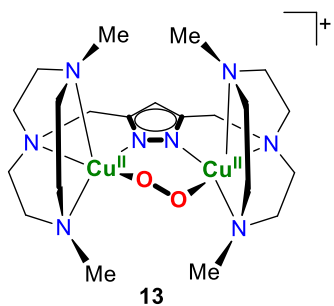
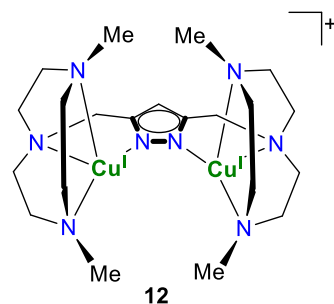
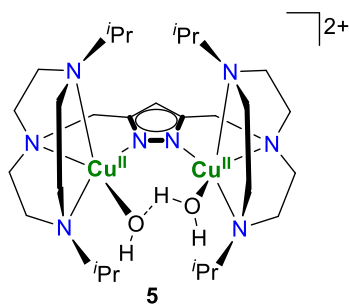
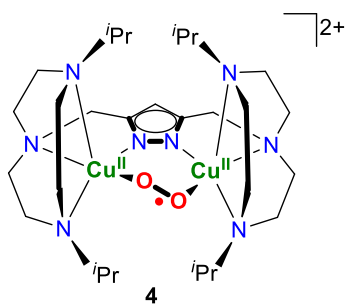
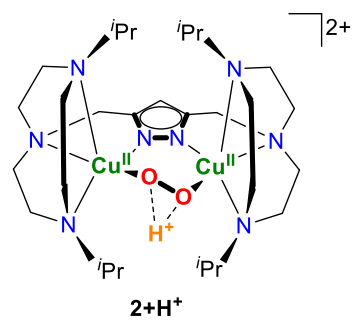
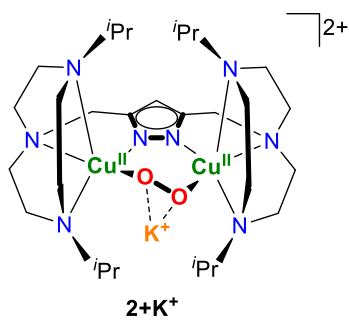
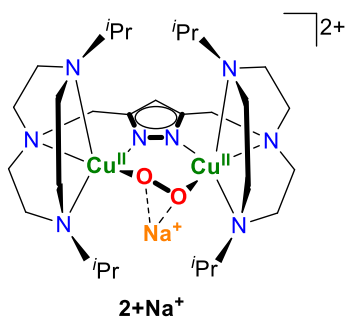
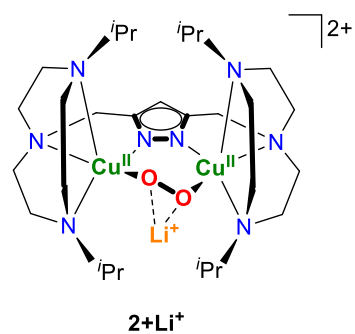
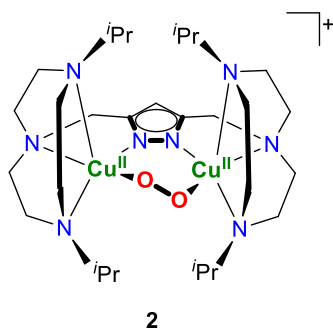
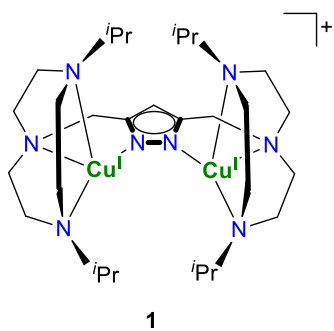
#### 7.13.8 $[\text{L}_3\text{Cu}_2]\text{BPh}_4$ (**12**)

Complex **12** was synthesized according to a previously reported route.<sup>10</sup> To a solution of **HL**<sup>3</sup> (257 mg, 633  $\mu\text{mol}$ , 1.0 eq.) and  $\text{NaO}^t\text{Bu}$  (82.5 mg, 860  $\mu\text{mol}$ , 1.4 eq.) in MeOH (1.0 mL), a solution of  $[\text{Cu}(\text{MeCN})_4]\text{ClO}_4$  (414 mg, 1.27 mmol, 2.00 eq.) in MeOH (12 mL) was added and the slightly yellow solution was stirred for 4 h at RT. Then a solution of  $\text{NaBPh}_4$  (220 mg, 639  $\mu\text{mol}$ , 1.0 eq.) was added and the mixture was stirred for 1 h. Afterwards the white solid was filtered off and washed with MeOH (2 x 1.0 mL) and dried under reduced pressure. The solid was dissolved in acetone and was left for  $\text{Et}_2\text{O}$  diffusion. After 1 d, green oil was separated from a now colorless solution. The colorless solution was taken for a second run of  $\text{Et}_2\text{O}$  diffusion, of which slightly yellow precipitate was obtained after two days (44 mg, 52  $\mu\text{mol}$ , 8%).

Crystallization attempts have also been performed *via*  $\text{Et}_2\text{O}$  diffusion into concentrated solution of MeCN, EtCN (@ RT and @ -34 °C) and THF. However, no crystalline material could be isolated. For all different crystallization conditions, a color change from slightly yellow to a deep brown was observed over time which is attributed to a decomposition of complex **6**. The yellow precipitate obtained from  $\text{Et}_2\text{O}$  diffusion into a concentrated acetone solution was analyzed *via*  $^1\text{H-NMR}$ . Next to complex **6** also unidentifiable impurities were observed (ca. 15%).

$^1\text{H-NMR}$  (300 MHz,  $(\text{CD}_3)_2\text{CO}$ ):  $\delta$  (ppm) = 7.39-7.29 (m, 8H, *o*- $\text{BPh}_4$ ), 6.96-6.88 (m, 8H, *m*- $\text{BPh}_4$ ), 6.80-6.76 (m, 4H, *p*- $\text{BPh}_4$ ) 6.09 (s, 1H,  $\text{P}^z\text{H}$ ), 3.78 (s, 4H,  $\text{P}^z\text{CH}_2$ ), 2.90-2.86 (m, 8H,  $\text{TACNCH}_2$ ), 2.83-2.79 (m, 8H,  $\text{TACNCH}_2$ ), 2.71-2.69 (m, 8H,  $\text{TACNCH}_2$ ), 2.60 (s, 12H,  $\text{CH}_3$ ).

## 7.14 List of Complexes



## 8 REFERENCES

---

- (1) Kaim, W.; Schwederski, B.; Klein, A. *Inorganic Chemistry: A Textbook Series: Bioinorganic Chemistry - Inorganic Elements in the Chemistry of Life: an Introduction and Guide (2)*; Wiley, 2013.
- (2) Garrett, R. H.; Grisham, C. M. *Biochemistry*; Thomson Brooks/Cole: Belmont, 2005.
- (3) Britt, B. M. *J. Biochem. Mol. Biol.* **2004**, *37*, 394.
- (4) Andreini, C.; Bertini, I.; Cavallaro, G.; Holliday, G. L.; Thornton, J. M. *J. Biol. Inorg. Chem.* **2008**, 1205.
- (5) Festa, R. A.; Thiele, D. J. *Curr. Biol.* **2011**, *21*, R877.
- (6) Solomon, E. I.; Heppner, D. E.; Johnston, E. M.; Ginsbach, J. W.; Cirera, J.; Qayyum, M.; Kieber-Emmons, M. T.; Kjaergaard, C. H.; Hadt, R. G.; Tian, L. *Chem. Rev.* **2014**, *114*, 3659.
- (7) Koval, I. A.; Gamez, P.; Belle, C.; Selmeczi, K.; Reedijk, J. *Chem. Soc. Rev.* **2006**, *35*, 814.
- (8) Wilcox, D. E.; Porras, A. G.; Hwang, Y. T.; Lerch, K.; Winkler, M. E.; Solomon, E. I. *J. Am. Chem. Soc.* **1985**, *107*, 4015.
- (9) Guckert, J. A.; Lowery, M. D.; Solomon, E. I. *J. Am. Chem. Soc.* **1995**, *117*, 2817.
- (10) Brinkmeier, A. *Masterarbeit*; Georg-August-Universität Göttingen: Göttingen, 2014.
- (11) Solomon, E. I.; Baldwin, M. J.; Lowery, M. D. *Chem. Rev.* **1992**, *92*, 521.
- (12) Colman, P. M.; Freemna, H. C.; Guss, J. M.; Murata, M.; Norris, V. A.; Ramshaw, J. A. M.; Venkatappa, M. P. *Nature* **1978**, *272*, 319.
- (13) Wijma, H. J.; MacPherson, I.; Farver, O.; Tocheva, E. I.; Pecht, I.; Verbeet, M. P.; Murphy, M. E. P.; Canters, G. W. *J. Am. Chem. Soc.* **2007**, *129*, 519.
- (14) Dennison, C. *Dalt. Trans.* **2005**, 3436.
- (15) Gray, H. B.; Malmström, B. G.; Williams, R. J. P. *J. Biol. Inorg. Chem.* **2000**, *5*, 551.
- (16) Ito, N.; Phillips, S. E. V.; Conrad, S.; Ogel, Z. B.; McPherson, M. J.; Keen, J. N.; Yadav, K. D. S.; Knowles, P. F. *Nature* **1991**, *350*, 87.
- (17) Holm, R. H.; Kennepohl, P.; Solomon, E. I. *Chem. Rev.* **1996**, *96*, 2239.
- (18) Whittaker, J. W. *Chem. Rev.* **2003**, *103*, 2347.
- (19) Whittaker, M. M.; Whittaker, J. W. *J. Biol. Chem.* **1990**, 9610.
- (20) Volbeda, A.; Ho, W. G. J. *J. Mol. Biol.* **1989**, *209*, 249.
- (21) Gaykemat, W. P. J.; Volbeda, A.; Hol, W. G. J. *J. Mol. Biol.* **1985**, *187*, 255.
- (22) Eicken, C.; Krebs, B.; Sacchettini, J. C. *Curr. Opin. Struct. Biol.* **1999**, *9*, 677.
- (23) Decker, H.; Schweikardt, T.; Tuczek, F. *Angew. Chem. Int. Ed.* **2006**, *45*, 4546.
- (24) Decker, H.; Dillinger, R.; Tuczek, F. *Angew. Chem.* **2000**, *112*, 1656.
- (25) Magnus, K. A.; Ton-That, H.; Carpenter, J. E. *Chem. Rev.* **1994**, *94*, 727.
- (26) Metz, M.; Solomon, E. I. *J. Am. Chem. Soc.* **2001**, *123* (21), 4938.
- (27) Magnus, K. A.; Hazes, B.; Ton-That, H.; Bonaventura, C.; Bonaventura, J.; Hol, W. G. J. *Proteins Struct., Funct., Genet* **1994**, *19*, 302.



- (28) Eicken, C.; Zippel, F.; Büldt-Karentzopoulos, K.; Krebs, B. *FEBS Lett.* **1998**, *436*, 293.
- (29) Wigner, E.; Witmer, E. E. *ZS. f. Phys.* **1929**, *57*, 601.
- (30) Bernardi, F.; Bottoni, A.; Casadio, R.; Fariselli, P.; Rigo, A. *Inorg. Chem.* **1996**, *35*, 5207.
- (31) Dalle, K. E.; Gruene, T.; Dechert, S.; Demeshko, S.; Meyer, F. *J. Am. Chem. Soc.* **2014**, *136*, 7428.
- (32) Dalle, K. E. *Dissertation*; Georg-August-Universität Göttingen: Göttingen, 2014.
- (33) Solomon, E. I.; Ginsbach, J. W.; Heppner, D. E.; Kieber-emmons, M. T.; Kjaergaard, C. H.; Smeets, P. J.; Tian, L.; Woertink, J. S. *Farrad. Discuss.* **2011**, *148*, 11.
- (34) Kindermann, N.; Bill, E.; Dechert, S.; Demeshko, S.; Reijerse, E. J.; Meyer, F. *Angew. Chem. Int. Ed.* **2015**, *54*, 1738.
- (35) Bertrand, T.; Jolival, C.; Briozzo, P.; Caminade, E.; Joly, N.; Madzak, C.; Mougin, C. *Biochemistry* **2002**, *41*, 7325.
- (36) Cole, A. P.; Root, D. E.; Mukherjee, P.; Solomon, E. I.; Stack, T. D. P. *Science (80- )*. **1996**, *273*, 1848.
- (37) Solomon, E. I.; Sundaram, U. M.; Machonkin, T. E. *Chem. Rev.* **1996**, *96*, 2563.
- (38) LuBien, C. D.; Winkler, M. E.; Thamann, T. J.; Scott, R. A.; Co, M. S.; Hodgson, K. O.; Solomon, E. I. *J. Am. Chem. Soc.* **1981**, *103*, 7014.
- (39) Yoon, J.; Solomon, E. I. *J. Am. Chem. Soc.* **2007**, *129*, 13127.
- (40) Li, J.; Farrokhnia, M.; Rulisek, L.; Ryde, U. *J. Phys. Chem. B* **2015**, *119*, 8268.
- (41) Augustine, A. J.; Quintanar, L.; Stoji, C. S.; Kosman, D. J.; Solomon, E. I. *J. Am. Chem. Soc.* **2007**, *129*, 13118.
- (42) Elwell, C. E.; Gagnon, N. L.; Neisen, B. D.; Dhar, D.; Spaeth, A. D.; Yee, G. M.; Tolman, W. B. *Chem. Rev.* **2017**.
- (43) Quist, D. A.; Diaz, D. E.; Liu, J. J.; Karlin, K. D. *J. Biol. Inorg. Chem.* **2017**, *22*, 253.
- (44) Mirica, L. M.; Ottenwaelder, X.; Stack, T. D. P. *Chem. Rev.* **2004**, *104*, 1013.
- (45) Aboeella, N. W.; Lewis, E. A.; Reynolds, A. M.; Brennessel, W. W.; Cramer, C. J.; Tolman, W. B. *J. Am. Chem. Soc.* **2002**, *124*, 10660.
- (46) Mahapatra, S.; Halfen, J. A.; Wilkinson, E. C.; Que Jr., L.; Tolman, W. B. *J. Am. Chem. Soc.* **1994**, *116*, 9785.
- (47) Kindermann, N.; Dechert, S.; Demeshko, S.; Meyer, F. *J. Am. Chem. Soc.* **2015**, *137*, 8002.
- (48) Holland, P. L.; Tolman, W. B. *Coord. Chem. Rev.* **1999**, *190–192*, 855.
- (49) Baldwin, M. J.; Root, D. E.; Pate, J. E.; Fujisawa, K.; N., K.; Solomon, E. I. *J. Am. Chem. Soc.* **1992**, *114*, 10421.
- (50) Baldwin, M. J.; Ross, P. K.; Pate, J. E.; Tyeklar, Z.; Karlin, K. D.; Solomon, E. I. *J. Am. Chem. Soc.* **1991**, *113*, 8671.
- (51) Wedler, G. In *Lehrbuch der Physikalischen Chemie*; Wiley-VCH Verlag: Erlangen, 2004; pp 601–610.
- (52) Ross, P. K.; Solomon, E. I. *J. Am. Chem. Soc.* **1991**, *113*, 3246.
- (53) Escuer, A.; Vicence, R.; Goher, M. A. S.; Mautnero, F. A. *Inorg. Chem.* **1995**, *34*, 5707.
- (54) Escuer, A.; Mautner, F. A.; Penalba, E.; Vicente, R. *Inorg. Chem.* **1998**, *37*, 4190.
- (55) Schenker, R.; Kieber-Emmons, M. T.; Riordan, C. G.; Brunold, T. C. *Inorg. Chem.* **2005**, *44*, 1752.

- (56) Henson, M. J.; Mukherjee, P.; Root, D. E.; Stack, T. D. P.; Solomon, E. I. *J. Am. Chem. Soc.* **1999**, *121*, 10332.
- (57) Solomon, E. I.; Dooley, D. M.; Wang, R.-H.; Gray, H. B.; Cerdonio, M.; Mogno, F.; Romani, G. L. *J. Am. Chem. Soc.* **1976**, *98*, 1029.
- (58) Tyeklar, Z.; Jacobson, R. R.; Wei, N.; Murthy, N. N.; Zubieta, J.; Karlin, K. D. *J. Am. Chem. Soc.* **1993**, *115*, 2677.
- (59) Börzel, H.; Comba, P.; Hagen, K. S.; Kerscher, M.; Pritzkow, H.; Schatz, M.; Schindler, S.; Walter, O. *Inorg. Chem.* **2002**, *41*, 5440.
- (60) Berreau, L. M.; Halfen, J. A.; Young Jr., V. G.; Tolman, W. B. *Inorg. Chim. Acta* **2000**, *297*, 115.
- (61) He, C.; Dubois, J. L.; Hedman, B.; Hodgson, K. O.; Lippard, S. J. *Angew. Chem. Int. Ed.* **2001**, *40*, 1484.
- (62) Kariin, K. D.; Tyeklair, Z.; Farooq, A.; Jacobson, R. R.; Sin, E.; Lee, D. W.; Bradshaw, J. E.; Wilson, L. J. *Inorg. Chim. Acta* **1991**, *182*, 1.
- (63) Kitajima, N.; Fujisawa, K.; Fujimoto, C.; Morooka, Y.; Hashimoto, S.; Kitagawa, T.; Toriumi, K.; Tatsumi, K.; Nakamura, A. *J. Am. Chem. Soc.* **1992**, *114* (4), 1277.
- (64) Halfen, J. A.; Mahapatra, S.; Wilkinson, E. C.; Kaderli, S.; Young, V. G.; Que, L.; Zuberbühler, A. D.; Tolman, W. B. *Science (80-. )*. **1996**, *271*, 1397.
- (65) Magnus, K. A.; Ton-That, H.; Carpenter, J. E. *Chem. Rev.* **1994**, 727.
- (66) Magnus, K.; Ton-That, H. J. *Inorg. Biochem.* **1992**, *47*, 20.
- (67) Cuff, M. E.; Miller, K. I.; Vanholde, K. E.; Hendrickson, W. A. *J. Mol. Biol.* **198AD**, *278*, 855.
- (68) Solomon, E. I.; Tuzcek, F.; Root, D. E.; Brown, C. A. *Chem. Rev.* **1994**, *94*, 827.
- (69) Karlin, K. D.; Ghosh, P.; Cruse, R. W.; Farooq, A.; Gultneh, Y.; Jacobson, R. R.; Blackburn, N. J.; Strange, R. W.; Zubieta, J. *J. Am. Chem. Soc.* **1988**, *110*, 6769.
- (70) Blackburn, N. J.; Strange, R. W.; Cruse, R. W.; Karlin, K. D. *J. Am. Chem. Soc.* **1987**, *109*, 1235.
- (71) Karlin, K. D.; Wei, N.; Jung, B.; Kaderli, S.; Zuberbühler, A. D. *J. Am. Chem. Soc.* **1991**, *113*, 5868.
- (72) Kodera, M.; Kita, T.; Miura, I.; Nakayama, N.; Kawata, T.; Kano, K.; Hirota, S. *J. Am. Chem. Soc.* **2001**, *123*, 7715.
- (73) Chen, P.; Fujisawa, K.; Solomon, E. I. *J. Am. Chem. Soc.* **2000**, *122*, 10177.
- (74) Wada, A.; Harata, M.; Hasegawa, K.; Jitsukawa, K.; Masuda, H.; Mukai, M.; Kitagawa, T.; Einaga, H. *Angew. Chemie - Int. Ed.* **1998**, *37*, 798.
- (75) Stewart, L. C.; Klinman, J. P. *Ann. Rev. Biochem.* **1988**, *57*, 551.
- (76) Chen, P.; Root, D. E.; Campochiaro, C.; Fujisawa, K.; Solomon, E. I. *J. Am. Chem. Soc.* **2003**, *125*, 466.
- (77) Cao, R.; Saracini, C.; Ginsbach, J. W.; Kieber-Emmons, M. T.; Siegler, M. A.; Solomon, E. I.; Fukuzumi, S.; Karlin, K. D. *J. Am. Chem. Soc.* **2016**, *138*, 7055.
- (78) Peterson, R. L.; Himes, R. A.; Kotani, H.; Suenobu, T.; Tian, L.; Siegler, M. A.; Solomon, E. I.; Fukuzumi, S.; Karlin, K. D. *J. Am. Chem. Soc.* **2011**, *133*, 1702.
- (79) Lee, J. Y.; Peterson, R. L.; Ohkubo, K.; Garcia-Bosch, I.; Himes, R. A.; Woertink, J.; Moore, C. D.; Solomon, E. I.; Fukuzumi, S.; Karlin, K. D. *J. Am. Chem. Soc.* **2014**, *136*, 9925.

- (80) Woertink, J. S.; Tian, L.; Maiti, D.; Lucas, H. R.; Himes, R. A.; Karlin, K. D.; Neese, F.; Christian, W.; Holthausen, M. C.; Bill, E.; Sundermeyer, J.; Schindler, S.; Solomon, E. I. *Inorg. Chem.* **2010**, *49*, 9450.
- (81) Weitzer, M.; Schatz, M.; Hampel, F.; Heinemann, W.; Schindler, S. *J.C.S. Dalt. Trans.* **2002**, No. 5, 686.
- (82) Weitzer, M.; Schindler, S.; Brehm, G.; Schneider, S.; Hörmann, E.; Jung, B.; Kaderli, S.; Zuberbühler, A. D. *Inorg. Chem.* **2003**, *42*, 1800.
- (83) Zhang, C. X.; Kaderli, S.; Costas, M.; Kim, E.; Neuhold, Y.; Karlin, K. D.; Zuberbühler, A. D. *Inorg. Chem.* **2003**, *42*, 1807.
- (84) Fujisawa, K.; Tanaka, M.; Moro-oka, Y.; Kitajima, N. *J. Am. Chem. Soc.* **1994**, *116*, 12079.
- (85) Becker, M.; Heinemann, F. W.; Schindler, S. *Chem. Eur. J.* **1999**, *5*, 3124.
- (86) Chaudhuri, P.; Hess, M.; Weyhermüller, T.; Wieghardt, K. *Angew. Chem. Int. Ed.* **1999**, *38*, 1095.
- (87) Kunishita, A.; Kubo, M.; Sugimoto, H.; Ogura, T.; Sato, K.; Takui, T.; Itoh, S. *J. Am. Chem. Soc.* **2009**, *131*, 2788.
- (88) Würtele, C.; Gaoutchenova, E.; Harms, K.; Holthausen, M. C.; Sundermeyer, J.; Schindler, S. *Angew. Chem. Int. Ed.* **2006**, *45*, 3867.
- (89) Spencer, D. J. E.; Aboeella, N. W.; Reynolds, A. M.; Holland, P. L.; Tolman, W. B. *J. Am. Chem. Soc.* **2002**, *124*, 2108.
- (90) Kindermann, N.; Günes, C. J.; Dechert, S.; Meyer, F. *J. Am. Chem. Soc.* **2017**, *139*, 9831.
- (91) McMillin, D. R. In *Physical Methods in Bioinorganic Chemistry*; Que Jr., L., Ed.; University Science Books: Sausalito, 2000; pp 1–58.
- (92) Bayliss, N. S.; McRae, E. G. *J. Phys. Chem.* **1954**, *58*, 1002.
- (93) Nafie, L. A.; Freedman, T. B. *J. Chem. Phys.* **1983**, *78*, 7108.
- (94) Werner, M.; Erhan, D. *Spectrochim. Acta* **2017**, *173*, 965.
- (95) Wedler, G. In *Lehrbuch der Physikalischen Chemie*; Wiley-VCH Verlag: Erlangen, 2004; pp 628–634.
- (96) Spiro, T. G.; Czernuszewicz, R. S. In *Physical Methods in Bioinorganic Chemistry*; Que Jr., L., Ed.; University Science Books: Sausalito, 2000; pp 59–120.
- (97) Wedler, G. In *Lehrbuch der Physikalischen Chemie*; Wiley-VCH Verlag: Erlangen, 2004; pp 613–619.
- (98) Wedler, G. In *Lehrbuch der Physikalischen Chemie*; Wiley-VCH Verlag: Erlangen, 2004; pp 623–628.
- (99) Buchler, S. In *Präorganisierte Zweikernkomplexe neuer Pyrazolat-Kompartimentliganden*; Heidelberg, 2002; pp 177–178.
- (100) Solomon, E. I.; Chen, P.; Metz, M.; Lee, S.-K.; Palmer, A. E. *Angew. Chemie Int. Ed.* **2001**, *40*, 4570.
- (101) Leibeling, G.; Demeshko, S.; Dechert, S.; Meyer, F. **2005**, 7111.
- (102) Bang, S.; Lee, Y.-M.; Hong, S.; Cho, K.-B.; Nishida, Y.; Seo, M. S.; Sarangi, R.; Fukuzumi, S.; Nam, W. *Nat. Chem.* **2014**, *6*, 934.
- (103) Fukuzumi, S.; Ohkubo, K.; Lee, Y. M.; Nam, W. *Chem. - A Eur. J.* **2015**, *21*, 17548.
- (104) Bol, J. E.; Driessen, W. L.; Ho, R. Y. N.; Maase, B.; Que Jr., L.; Reedijk, J. *Angew. Chem. Int. Ed.* **1997**, *36*, 998.

- (105) Brinkmeier, A.; Dalle, K. E.; Schulz, R. A.; D'Amore, L.; Dechert, S.; Demeshko, S.; Swart, M.; Meyer, F. *Unpubl. results* **2017**.
- (106) Addison, A. W.; Rao, T. N. *Dalt. Trans.* **1984**, No. 1, 1349.
- (107) Bertran, J. F.; Ballester, L.; Dobrihalova, L.; Sanchez, N.; Arrieta, R. *Spectrochim. Acta* **1968**, 24A, 1765.
- (108) Amat, G.; Pimbert, M. *J. Mol. Spectrosc.* **1965**, 16, 278.
- (109) Henson, M. J.; Vance, M. A.; Zhang, C. X.; Liang, H.; Karlin, K. D.; Solomon, E. I. *J. Am. Chem. Soc.* **2003**, 125, 5186.
- (110) Kahn, O.; Briat, B. *J. Chem. Soc. Trans.* **1975**, 2, 268.
- (111) Kahn, O. *Angew. Chem. Int. Ed. Engl.* **1985**, 24, 834.
- (112) Girerd, J.; Charlot, M.-F.; Kahn, O. *Mol. Phys.* **1977**, 34, 1063.
- (113) Frensch, L. K.; Pröpper, K.; John, M.; Demeshko, S.; Brückner, C.; Meyer, F. *Angew. Chem. Int. Ed.* **2011**, 50, 1420.
- (114) Edward I. Solomon, David E. Heppner, Esther M. Johnston, Jake W. Ginsbach, Jordi Cirera, Munzarin Qayyum, Matthew T. Kieber-Emmons, Christian H. Kjaergaard, Ryan G. Hadt, L. T. *Chem. Rev.* **2014**, 114, 3659.
- (115) Prokofieva, A.; Prikhod'ko, A. I.; Enyedy, E. A.; Farkas, E.; Maringgele, W.; Demeshko, S.; Dechert, S.; Meyer, F. *Inorg. Chem.* **2007**, 46, 4298.
- (116) Driessen, W. L.; Chang, L.; Finazzo, C.; Gorter, S.; Rehorst, D.; Reedijk, J.; Lutz, M.; Spek, A. L. *Inorg. Chim. Acta* **2003**, 350, 25.
- (117) Stoll, S.; Schweiger, A. *J. Magn. Reson* **2006**, 178, 42.
- (118) D'Amore, L.; Swart, M. *Institut de Química Computacional i Catàlisi (IQCC) & Dept. Química, Universitat de Girona; Girona, Spain, 2017*.
- (119) Becke, A. D. *Phys. Rev. A* **1988**, 38, 3098.
- (120) Perdew, J. P. *Phys. Rev. B* **1986**, 34, 7406.
- (121) Grimme, S. *WIREs Comput. Mol. Sci.* **2011**, 1, 211.
- (122) Van Lenthe, E.; Baerends, E. J. *J. Comput. Chem.* **2003**, 24, 1142.
- (123) Baerends, E. J. et al. *SCM* **2016**.
- (124) te Velde, G.; Bickelhaupt, F. M.; Baerends, E. J.; Fonseca Guerra, C.; van Gisbergen, S. J. A.; Snijders, J. G.; Ziegler, T. *J. Comput. Chem.* **2001**, 22, 931.
- (125) Swart, M. *Chem. Phys. Lett.* **2013**, 580, 166.
- (126) Beatty, A. M. *Coord. Chem. Rev.* **2003**, 246, 131.
- (127) Goshe, A. J.; Steele, I. M.; Ceccarelli, C.; Rheingold, A. L.; Bosnich, B. *PNAS* **2002**, 99, 4823.
- (128) Thordarson, P. *Chem. Soc. Rev.* **2011**, 40, 1305.
- (129) Pearson, R. G. *J. Am. Chem. Soc.* **1963**, 85, 3533.
- (130) Lisy, J. M. *Int. Rev. Phys. Chem.* **1997**, 16, 267.
- (131) Wuepper, J. L.; Popov, A. I. *J. Am. Chem. Soc.* **1969**, 4352.

- (132) Cahen, Y. M.; Dye, J. L.; Popov, A. I. *J. Phys. Chem.* **1975**, *79*, 1292.
- (133) Takeda, Y.; Katsuta, K.; Inoue, Y.; Hakushi, T. *Bull. Chem. Soc. Jpn.* 1988, pp 627–632.
- (134) Hopkins, H. P.; Norman, A. B. *J. Phys. Chem.* **1980**, *84*, 309.
- (135) Föppl, H. Z. *Anorg. Allg. Chem.* **1957**, *291*, 12.
- (136) Feher, F.; Wilucki, I.; Dost, G. *Chem. Ber.* **1953**, *86*, 1429.
- (137) Hollemann, A. F.; Wiberg, E.; Wiberg, N. In *Lehrbuch der Anorganischen Chemie*; Walter de Gruyter: Berlin, 2007; p 2003.
- (138) Hollemann, A. F.; Wiberg, E.; Wiberg, N. In *Lehrbuch der Anorganischen Chemie*; Walter de Gruyter: Berlin, 2007; p 509.
- (139) Hoppe, T.; Schaub, S.; Becker, J.; Würtele, C.; Schindler, S. *Angew. Chem.* **2013**, *125*, 904.
- (140) Würtele, C.; Sander, O.; Lutz, V.; Waitz, T.; Tuzek, F.; Schindler, S. *J. Am. Chem. Soc.* **2009**, *131*, 7544.
- (141) Komiyama, K.; Furutachi, H.; Nagatomo, S.; Hashimoto, A.; Hayashi, H.; Fujinami, S.; Suzuki, M.; Kitagawa, T. *Bull. Chem. Soc. Jpn.* **2004**, *77*, 59.
- (142) Schatz, M.; Becker, M.; Walter, O.; Liehr, G.; Schindler, S. *Inorg. Chim. Acta* **2001**, *324*, 173.
- (143) Spiro, T. G.; Stein, P. *Annu. Rev. Phys. Chem.* **1977**, *28*, 501.
- (144) Matsushima, H.; Hamada, H.; Watanabe, K.; Koikawa, M.; Tokii, T. *J. Chem. Soc. Dalton Trans.* **1999**, 971.
- (145) Singh, A. K.; Vlugt, I. Van Der; Demeshko, S.; Dechert, S.; Meyer, F. *Eur. J. Inorg. Chem.* **2009**, 3431.
- (146) Lee, J. Y.; Karlin, K. D. *Curr. Opin. Chem. Biol.* **2015**, *25*, 184.
- (147) Usharani, D.; Wang, B.; Sharon, D. A.; Shaik, S. In *Spin States in Biochemistry and Inorganic Chemistry*; Swart, M., Costas, M., Eds.; Wiley-VCH Verlag, 2016; pp 130–156.
- (148) Stephens, P. J.; Jalkanen, K. J.; Amos, R. D.; Lazzarotti, P.; Zanasi, R. *J. Phys. Chem.* **1990**, *94*, 1811.
- (149) Adamo, C.; Barone, V. *J. Phys. Chem.* **1998**, 664.
- (150) Perdew, J. P. *Phys. Rev. B* **1986**, *33*, 8822.
- (151) Perdew, J. P.; Yue, W. *Phys. Rev. B* **1986**, *33*, 8800.
- (152) Kaljurand, I.; Kütt, A.; Sooväli, L.; Rodima, T.; Mäemets, V.; Leito, I.; Koppel, I. A. *J. Org. Chem.* **2005**, *70*, 1019.
- (153) Kaljurand, I.; Rodima, T.; Leito, I.; Koppel, I. A.; Schwesinger, R. *J. Org. Chem.* **2000**, *65*, 6202.
- (154) Leito, I.; Kaljurand, I.; Koppel, I. A.; Yagupolskii, L. M.; Vlasov, V. M. *J. Org. Chem.* **1998**, *63*, 7868.
- (155) Kovacevic, B.; Maksic, Z. B. *Org. Lett.* **2001**, *3*, 1523.
- (156) Tsui, E. Y.; Tran, R.; Yano, J.; Agapie, T. *Nat. Chem.* **2013**, *5*, 293.
- (157) Kanady, J. S.; Tsui, E. Y.; Day, M. W.; Agapie, T. *Science (80-. )*. **2011**, *333*, 733.
- (158) Fukuzumi, S.; Ohkubo, K. *Chem. Eur. J.* **2000**, *6*, 4532.
- (159) Connelly, N. G.; Geiger, W. E. *Chem. Rev.* **1996**, *96*, 877.
- (160) Yang, L.; Tolman, W. B. *J. Biol. Inorg. Chem.* **2012**, *17*, 285.
- (161) Hirotsu, M.; Kuwamura, N.; Kinoshita, I.; Kojima, M.; Yoshikawa, Y.; Ueno, K. *Dalt. Trans.* **2009**, 7678.

- (162) Neese, F. *WIREs Comput. Mol. Sci.* **2012**, *2*, 73.
- (163) Schäfer, A.; Horn, H.; Ahlrichs, R. *J. Chem. Phys.* **1992**, *97*, 2571.
- (164) Weigend, F.; Ahlrichs, R. *Phys. Chem. Chem. Phys.* **2005**, *7*, 3297.
- (165) Klamt, A.; Schüürmann, G.; *J. Chem. Soc. Perkin Trans. 2* **1993**, *5*, 799. *J. Chem. Soc. Perkin Trans. 2* **1993**, *5*, 799.
- (166) Pye, C. C.; Ziegler, T. *Theor. Chem. Acc.* **1999**, *101*, 396.
- (167) Grimme, S.; Antony, J.; Ehrlich, S.; Krieg, S. H.; 154104. *J. Chem. Phys.* **2010**, *132*, 154104.
- (168) Soda, T.; Kitagawa, Y.; Onishi, T.; Takano, Y.; Shigeta, Y.; Nagao, H.; Yoshioka, Y.; Yamaguchi, K. *Chem. Phys. Lett.* **2000**, *319*, 223.
- (169) Demeshko, S. *Vorlesung Methoden der Chemie II - Magnetismus*; Georg-August-Universität Göttingen: Göttingen, 2014.
- (170) Maiti, D.; Fry, H. C.; Woertink, J. S.; Vance, M. A.; Solomon, E. I.; Karlin, K. D. *J. Am. Chem. Soc.* **2007**, *129*, 264.
- (171) Crespo, A.; Marti, M. A.; Roitberg, A. E.; Amzel, L. M.; Estrin, D. A. *J. Am. Chem. Soc.* **2006**, *128*, 12817.
- (172) Mader, E. A.; Manner, V. W.; Markle, T. F.; Wu, A.; Franz, J. A.; Mayer, J. M. *J. Am. Chem. Soc.* **2009**, *131*, 4335.
- (173) Bordwell, F. G.; Liu, W.-Z. *J. Am. Chem. Soc.* **1996**, *118*, 10819.
- (174) Warren, J. J.; Tronic, T. A.; Mayer, J. M. *Chem. Rev.* **2010**, *110*, 6961.
- (175) Bosque, R.; Sales, J. J. *Chem. Inf. Comput. Sci.* **2003**, *43*, 637.
- (176) Semmelhack, M. F.; Chou, C. S.; Cortes, D. A. *J. Am. Chem. Soc.* **1983**, *105*, 4492.
- (177) Mayer, J. M. *Acc. Chem. Res.* **2011**, *44*, 36.
- (178) Mayer, J. M. *Annu. Rev. Phys. Chem.* **2004**, *55*, 363.
- (179) Eckert, N. A.; Vaddadi, S.; Stoian, S.; Lachicotte, R. J.; Cundari, T. R.; Holland, P. L. *Angew. Chem.* **2006**, *118*, 7022.
- (180) England, J.; Martinho, M.; Farquhar, E. R.; Frisch, J. R.; Bominaar, E. L.; Münck, E.; Que Jr., L. *Angew. Chem.* **2009**, *121*, 3676.
- (181) Marcus, R. A. *J. Phys. Chem.* **1989**, *93*, 3078.
- (182) Chou, M.; Creutz, C.; Sutin, N. *J. Am. Chem. Soc.* **1977**, 5615.
- (183) Meek, S. J.; Pitman, C. L.; Miller, A. J. M. *J. Chem. Educ.* **2016**, *93*, 275.
- (184) Blackmond, D. G. *Angew. Chem. Int. Ed.* **2005**, *44*, 4302.
- (185) Mathew, J. S.; Klusmann, M.; Iwamura, H.; Valera, F.; Futran, A.; Emanuelsson, E. A. C.; Blackmond, D. G. *J. Org. Chem.* **2006**, *71*, 4711.
- (186) Tano, T.; Okubo, Y.; Kunishita, A.; Kubo, M.; Sugimoto, H.; Fujieda, N.; Ogura, T.; Itoh, S. *Inorg. Chem.* **2013**, *52*, 10431.
- (187) Bordwell, F. G.; Cheng, J.-P. *J. Am. Chem. Soc.* **1991**, *113*, 1736.
- (188) Ohkubo, K.; Menon, S. C.; Orita, A.; Otera, J.; Fukuzumi, S. *J. Org. Chem.* **2003**, *68*, 4720.

- (189) Shannon, R. D. *Acta Cryst.* **1976**, A32, 751.
- (190) Tobiszewski, M.; Mechlinska, A.; Namiesnik, J. *Chem. Soc. Rev.* **2010**, 39, 2869.
- (191) Ferlin, F.; Santoro, S.; Ackermann, L.; Vaccaro, L. *Green Chem.* **2017**, 19, 2510.
- (192) Günes, J. In *unpublished results*; Georg-August-University Göttingen, 2017.
- (193) Stojanovic, R. S.; Bond, A. M. *Anal. Chem.* **1993**, 65, 56.
- (194) Sohn, Y. S.; Hendrickson, D. N.; Gray, H. B. *J. Am. Chem. Soc.* **1971**, 3603.
- (195) Vogler, A.; Kunkely, H. *Coord. Chem. Rev.* **2001**, 211, 223.
- (196) Kärkäs, M. D.; Verho, O.; Johnston, E. V.; Åkermark, B. *Chem. Rev.* **2014**, 114, 11863.
- (197) Chow, J.; Kopp, R. J.; Portney, P. R. *Science (80- )*. **2003**, 302, 1528.
- (198) Eisenberg, R.; Gray, H. B. *Inorg. Chem.* **2008**, 47, 1697.
- (199) Chen, Z.; Meyer, T. J. *Angew. Chem. Int. Ed.* **2013**, 52, 700.
- (200) Garrido-Barros, P.; Funes-Ardoiz, I.; Drouet, S.; Benet-Buchholz, J.; Maseras, F.; Llobet, A. *J. Am. Chem. Soc.* **2015**, 137, 6758.
- (201) Barnett, S. M.; Goldberg, K. I.; Mayer, J. M. *Nat. Chem.* **2012**, 4, 498.
- (202) Huang, X.; Groves, J. T. *J. Biol. Inorg. Chem.* **2017**, 22, 185.
- (203) Funes-Ardoiz, I.; Garrido-Barros, P.; Llobet, A.; Maseras, F. *ACS Catal.* **2017**, 7, 1712.
- (204) Praneeth, V. K. K.; Kondo, M.; Woi, P. M.; Okamura, M.; Masaoka, S. *Chempluschem* **2016**, 81, 1123.
- (205) Su, X.; Gao, M.; Jiao, L.; Liao, R.; Siegbahn, P. E. M.; Cheng, J.; Zhang, M. *Angew. Chem. Int. Ed.* **2015**, 54, 4909.
- (206) Nestke, S.; Brinkmeier, A. *synthesized and studied in cooperation (Ak. Prof. Siewert)*; 2017.
- (207) Zhang, M.-T.; Chen, Z.; Kang, P.; Meyer, T. J. *J. Am. Chem. Soc.* **2013**, 135, 2048.
- (208) Wang, J.; Sahoo, P.; Lu, T. *ACS Catal.* **2016**, 6, 5062.
- (209) *The Calibration was determined in cooperation with S. Nestke (Ak. Prof. Siewert)*; 2017.
- (210) Neese, F.; Roy, L. In *Max-Planck Institute for Chemical Energy Conversion, Mülheim/Ruhr, Germany*; 2017.
- (211) Cunningham, C. T.; Cunningham, K. L. H.; Michalec, J. F.; Mcmillin, D. R. *Inorg. Chem.* **1999**, 38, 4388.
- (212) Lum, J. S.; Tahsini, L.; Golen, J. A.; Moore, C.; Rheingold, A. L.; Doerrler, L. H. *Chem. Eur. J.* **2013**, 19, 6374.
- (213) Kindermann, N. *Dissertation*; Georg-August-University Göttingen: Göttingen, 2015.
- (214) Autorenkollektiv. *Organikum*, 22. Auflag.; Wiley-VCH Verlag: Weinheim, 2004.
- (215) Bill, E. *Max-Planck Inst. Chem. Energy Conversion, Mülheim/Ruhr, Ger.* **2008**.
- (216) Beynon, R.; Easterby, J. In *Buffer Solutions*; Taylor and Francis, 2003; pp 1–96.
- (217) Sheldrick, G. M. *Acta Cryst.* **2015**, A71, 3.
- (218) Sheldrick, G. M. *Acta Cryst.* **2015**, C71, 3.
- (219) X-RED; STOE & CIE GmbH: Darmstadt, Germany, 2002.
- (220) Halfen, J. A.; Tolman, W. B.; Weighardt, K. *Inorg. Synth.* **2007**, 32, 75.
- (221) Buchler, S.; Meyer, F.; Kaifer, E.; Pritzkow, H. *Inorg. Chim. Acta* **2002**, 337, 371.

- (222) Schwesinger, R.; Willaredt, J.; Schlemper, H.; Keller, M.; Schmitt, D.; Fritz, H. *Chem. Ber.* **1994**, *127*, 2435.
- (223) Rodima, T.; Mäemets, V.; Koppel, I. *J. Chem. Soc. Perkin Trans. 1* **2000**, 2637.
- (224) Li, Z.; Wu, S.; Ding, H.; Lu, H.; Liu, J.; Huo, Q.; Guan, J.; Kan, Q. *New J. Chem.* **2013**, *37*, 4220.
- (225) Bennur, T. H.; Srinivas, D.; Sivasanker, S. *J. Mol. Catal. A Chem.* **2004**, *207*, 163.

#### Abbreviations

ATR	<b>Attenuated Total Reflection</b>
$^{\circ}\text{P}$	<i>Cis</i> -peroxo dicopper ( <i>cis</i> - $\mu$ -1,2)
CH <sub>3</sub> COOOH	Peracetic acid
°C	degree Celsius
CT	Charge transfer
Cu	Copper
d	day
$\delta$	chemical shift
DMSO	Dimethylsulfoxide
EPR	<b>Electron Paramagnetic Resonance</b>
ESI-MS	<b>Electro Spray Ionization Mass Spectrometry</b>
EtCN	Propionitrile
Et <sub>2</sub> O	Diethyl ether
eq.	equivalent
Fe	Iron
g	gram
h	hour
HBr	Hydrogen bromide
HSAB	principle of <b>Hard and Soft Acids and Bases</b>
Hz	Hertz
IR	<b>Infrared Spectroscopy</b>
K	Kelvin
KBr	Potassium bromide
KO <sup>t</sup> Bu	Potassium <i>tert</i> -butoxide
Li	Lithium
LMCT	<b>Ligand to Metal Charge Transfer</b>
MeCN	acetonitrile
MeOH	methanol
mg	milligram
min	minute



mol	mol
MTBE	Methyl- <i>tert</i> -butylether
Na	Sodium
NaO <sup>t</sup> Bu	Sodium <i>tert</i> -butoxide
NMR	<b>N</b> uclear <b>M</b> agnetic <b>R</b> esonance
rR	Resonance Raman
s	second
<sup>s</sup> P	Side-on peroxo dicopper ( $\mu$ - $\eta^2$ - $\eta^2$ )
SQUID	<b>S</b> uperconducting <b>Q</b> uantum <b>I</b> nterference <b>D</b> evice
<sup>t</sup> BuOOH	<i>Tert</i> -butyl hydroperoxide
TACN	Triazacyclononane
THF	Tetrahydrofuran
TMG	1,1,3,3-Tetramethylguanidine
<sup>T</sup> P	<i>Trans</i> -peroxo dicopper (trans- $\mu$ -1,2)
UV/vis	<b>U</b> ltraviolet/ <b>v</b> isible

## 10 ACKNOWLEDGEMENTS

---

At first I want to thank my supervisor Prof. Dr. Franc Meyer for providing me with this fascinating and challenging topic and for hosting me in his working group during the last three years. Thank you very much for supporting me with good scientific advice and with your motivating manner. I also want to thank Prof. Dr. Sven Schneider for being the second advisor of this work and for the beneficial scientific discussions during the annual status meetings.

I furthermore want to thank everybody, who contributed to this work. I would like to thank Dr. Sebastian Dechert for collecting and handling the X-Ray data and for recording resonance Raman spectra. I would like to thank Dr. Serhiy Demeshko for collecting all the SQUID data with me as well as for his valuable scientific advice during the last three years – this special thanks also goes to Dr. Sebastian Dechert. I would like to thank Dr. Claudia Stückl for recording ESR spectra and for her support with all the administrative issues. In this context I also want to thank Britta Müller. I further would like to thank Lorenzo D'Amore and Prof. Dr. Marcel Swart for carrying out the detailed computational calculations on my peroxo topic. In this context I also would like to mention Dr. Kristian Dalle, who supported me with valuable scientific advice concerning the peroxo topic. I also want to mention Lisa Roy and further members of the Frank Neese group for their computational work on my water oxidation project. I would like to thank our analytical lab for carrying out elemental analyses. I also want to thank Prof. Dr. Inke Siewert and the whole Siewert group for providing me with a lot of valuable scientific advice concerning the water oxidation topic. I would like to thank Jann Odrobina, Jana Lücken, Christoph Schiwiek, Josh Abbenseth, Daniel Delony, Markus Kienauer, Jerome Günes, Roland Schulz and Stefan Resch for many beneficial scientific discussions and again Roland Schulz and Jerome Günes for proofreading parts of this thesis. I further want to thank my former Bachelor students Roland Schulz and Steffen Oevermann and the entire lab students, working for me – thank you for your company and for your valuable scientific contributions. I also want to mention Jörg Teichgräber and Andreas Schwarz for supplying me with diverse technical equipment. I want to thank Dr. Alexander Gers-Barlag and Dr. Oliver Mitevski for introducing me into the technical details of our glove boxes and the whole Meyer group for supporting me and being such a nice company during our lunch breaks.

Last but not least I want to thank my wife Sarah, my family and my friends. Thank you so much for backing me up during the last years. I am very lucky to have so many wonderful people around me. Without your support, this work would not have been possible.

# 11 CURRICULUM VITAE

---

## Personal Details

Name: Alexander Brinkmeier

Date of Birth: 07.07.1988

Place of Birth: Northeim

Nationality: German

## Academic Career

- 09/2014 – Current      Georg-August-Universität Göttingen, Germany  
PhD Thesis under supervision of Prof. Dr. Franc Meyer  
Thesis: „*Bimetallic Copper Complexes for Bioinspired Dioxygen Activation and Catalytic Water Oxidation*“
- Academic Awards  
04/2016 *Nature Chemistry* Best Poster Award (Girona Seminar)  
08/2015 *Inorganic Chemistry* Best Poster Award (IRTG 1422 Final Symposium)
- 04/2012 – 07/2014      Georg-August-Universität Göttingen, Germany  
Master of Science Chemistry (1.4) under supervision of Prof. Dr. Franc Meyer
- Stay Abroad:  
09/2013 – 12/2013  
Research on iron complexes for C-H bond functionalization under supervision of Prof. Dr. Ebbe Nordlander, Lund University
- 10/2008 – 02/2012      Bachelor of Science Chemistry (1.6) under supervision of Prof. Dr. Franc Meyer
- Part-Time Work:  
12/2010 – 03/2011 scientific assistant, Georg-August-Universität Göttingen  
08/2009 – 03/2010 Qualified teacher, Studienkreis Göttingen Mitte